Elucidating Fundamental Structure-Property Relationships of Naphthopyran Mechanophores

Thesis by

Skylar Kathleen Osler

In Partial Fulfillment of the Requirements for the

Degree of

Doctor of Philosophy

CALIFORNIA INSTITUTE OF TECHNOLOGY

Pasadena, California

2026

Defended August 1st, 2025

Skylar Kathleen Osler
ORCID: 0000-0003-1021-7011

Acknowledgements

I am very grateful to the friends and family that have supported me throughout this experience. There is no doubt that the work presented herein would not have been possible without their love and support.

I would like to thank my advisor Professor Maxwell Robb for providing me with opportunities to work on the types of chemistry that I am most excited about, and for constantly challenging me to become a better scientist. Your encouragement and guidance have undoubtedly shaped me as a researcher, and I am incredibly grateful for your mentorship and continued support.

Professors Gregory Fu, Hosea Nelson, and Dennis Dougherty have been amazing thesis committee members, and I am very grateful for their support. The wisdom that they have provided throughout my graduate career has been invaluable. I feel honored to have had the opportunity to share my research and ideas with such an amazing group of scientists.

Molly McFadden and Nathan Ballinger are two incredibly intelligent and driven scientists that I have had the pleasure of working very closely with. Working alongside Molly and Nathan has been inspiring and incredibly rewarding, and I would not be the chemist I am today without their influence. I feel very lucky to have had the opportunity to work with people who I truly believe can do anything they set their minds to.

I joined Maxwell Robb's research group alongside Stella Luo, who I have considered an irreplaceable partner throughout graduate school. Stella is a creative, intelligent, and hardworking scientist that I have the utmost respect for. She has inspired me to become a better scientist, and her love and support have carried me through this experience. Graduate school would have been much dimmer without her presence.

Yan Sun and Audrey Conner have been amazing collaborators during my graduate studies, and I am very grateful for their insightful ideas and suggestions. I have no doubt that both Yan and Audrey will have amazing careers in chemistry, and I am very excited to see what they accomplish in the future.

There are no words to describe how thankful I am to Samir Rezgui and Enric Adillon for their friendship and support throughout the last five years. I feel so lucky to have them in my life, and I would not be here without them. I am grateful to Analiese Wiedenbeck for her steadfast friendship, and for bringing light and laughter to my last few years at Caltech. I am grateful to Madeline Hicks for being a strong, creative, and inspiring friend. My friendships with Molly McFadden, Ross Barber, Yan Sun, and Stella Luo have been fundamental to my graduate school experience, and I am very fortunate to have met them.

I am forever indebted to my family for their unwavering support throughout my time in graduate school. I am a better scientist and person because of their love and encouragement. I am also indebted to Cary Stennett, Jillian Sanzone, Sam Shockley, Sophia Beletsis, and Amanda Knapp for brightening my life outside of Caltech. They are incredible people who inspire me constantly, and their friendship means everything to me.

Abstract

Naphthopyran mechanophores have been identified as a privileged class of molecules due to their synthetic accessibility and structural modularity. In response to mechanical force, naphthopyran mechanophores undergo a ring-opening reaction to generate highly colored merocyanine dyes. Force is transduced to naphthopyran small molecules by covalently attached polymer chains, and naphthopyrans that are incorporated into polymeric materials visually report on macroscopic stress and/or strain. The properties of merocyanine dyes produced under mechanical force have been effectively tuned through straightforward structural modifications on various naphthopyran scaffolds. Additionally, the sensitivity of naphthopyran mechanophores toward mechanochemical ring-opening has been modified through targeted molecular design. The studies discussed herein provide insight into the fundamental relationship between the structure of naphthopyran mechanophores and their mechanochromic properties.

In Chapter 1, the effect of pyran regiochemistry on dye properties is investigated for two angular naphthopyrans. Simple 2*H*-naphthopyran and 3*H*-naphthopyran mechanophores were mechanically activated in soluble linear polymers exposed to ultrasound and in crosslinked siloxane elastomers under tension. The 3*H*-naphthopyran generates a yellow merocyanine dye that is exceedingly thermally unstable and reverts to naphthopyran rapidly under ambient conditions. Mechanical activation of 2*H*-naphthopyran produces a red merocyanine that reverts to colorless naphthopyran an order of magnitude more slowly than 3*H*-derived merocyanine. The relative orientation of the pyran effectively modulates the optical and thermal properties of force-generated dyes.

The reactivity of a multimodal 2*H*-bis-naphthopyran mechanophore in solution-phase ultrasonication experiments is reported in Chapter 2. The 2*H*-bis-naphthopyran mechanophore contains two naphthopyran units that are conjugated through a thiophene linker. Mechanical activation generates a mixture of mono-merocyanine and bis-merocyanine isomers in solution, and a force-mediated ester scission reaction renders mono-merocyanines thermally persistent. An unusual retro-cyclization reaction is implicated in the generation of thermally persistent bis-merocyanine species. The geometry of polymer attachment is critical to the operation of the unexpected reaction pathway.

In Chapter 3, a novel naphthopyran scaffold wherein the pendant aryl rings are constrained as a fluorene group is investigated. The conformational rigidity of fluorenyl naphthopyrans confers precise control over how polymer elongation is coupled to torsional motions that necessarily accompany the ring-opening reaction. Changes in polymer attachment geometry alter how motions associated with the overall chemical transformation are affected under force, resulting in significant difference in mechanochemical activation rate. Results obtained using ultrasonication experiments are supported by an extensive computational investigation using density functional theory calculations.

Chapter 4 discusses the design, synthesis, and reactivity of a novel 3*H*-bis-naphthopyran mechanophore. The multimodal mechanophore was covalently incorporated into siloxane elastomers that were subjected to uniaxial tension. Material deformation produces a dynamic mixture of mono-merocyanine and bis-merocyanine isomers biased by the magnitude of stress and/or stain that is applied. Structural modifications that increase the reversion rate of the associated merocyanines and decrease background coloration were critical to the design of materials with desirable properties.

Published Content and Contributions

1. Osler, S. K.; McFadden, M. E.; Robb, M. J. Comparison of the Reactivity of Isomeric 2*H*- and 3*H*-Naphthopyran Mechanophores. *J. Polym. Sci.* **2021**, *59*, 2537–2544. DOI: 10.1002/pol.20210417
S. K. O. participated in the synthesis of reported compounds, data collection and analysis, and manuscript preparation.

2. Osler, S. K.; McFadden, M. E.; Zeng, T.; Robb, M. J. Mechanochemical Reactivity of a Multimodal 2*H*-Bis-Naphthopyran Mechanophore. *Polym. Chem.* **2023**, *14*, 2717–2723. DOI: 10.1039/d3py00344b
S. K. O. participated in the design of the project, synthesis of reported compounds, data collection and analysis, and manuscript preparation.

3. Osler, S. K.; Ballinger, N. A.; Robb, M. J. The Role of Torsion on the Force-Coupled Reactivity of a Fluorenyl Naphthopyran Mechanophore. *J. Am. Chem. Soc.* **2025**, *147*, 3904–3911. DOI: 10.1021/jacs.4c18395
S. K. O. conceptualized the project and participated in the experimental design, synthesis of reported compounds, data collection and analysis, and manuscript preparation.

4. Osler, S. K.; Conner, A. V.; McFadden, M. E.; Robb, M. J. Strain-Dependent Multicolor Mechanochromism of 3*H*-Bis-Naphthopyran in Solid Polymeric Materials. *Chem. Sci*. **2025**, DOI: 10.1039/D5SC05757D
S. K. O. participated in the design of the project, synthesis of reported compounds, data collection and analysis, and manuscript preparation.

Table of Contents

Chapter 1

Comparison of the Reactivity of Isomeric 2*H*- and 3*H*-Naphthopyran Mechanophores

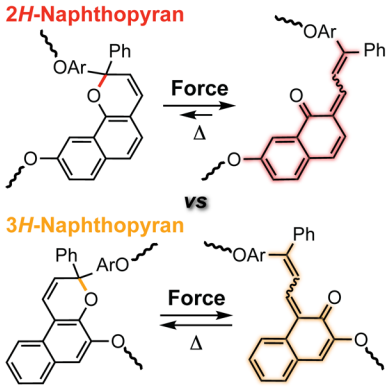

This chapter has been adapted with permission from Osler, S.K.; McFadden, M. E.; Robb, M. J. Comparison of the Reactivity of Isomeric 2*H*- and 3*H*-Naphthopyran Mechanophores. *J. Polym. Sci*. **2021**, *59*, 2537–2544. DOI: 10.1002/pol.20210417

Abstract

Naphthopyrans are molecular switches that produce highly colored merocyanine dyes upon photochemical or mechanochemical activation in polymers. The mechanochromic behavior of these molecular force probes enable the straightforward visualization of stress and/or strain in materials. To date, research on the mechanochemistry of naphthopyran has largely focused on the 3*H*-naphtho[2,1-*b*]pyran (3*H*) scaffold, whereas isomeric 2*H*-naphtho[1,2-*b*]pyrans (2*H*) exhibits complementary properties as suggested from their photochemical reactivity. Here we directly compare the reactivity of two isomeric 2*H*- and 3*H*-naphthopyran mechanophores in solution-phase ultrasonication experiments and in crosslinked

polydimethylsiloxane (PDMS) elastomers subjected to uniaxial tensile deformation. The prototypical 3*H*-naphthopyran mechanophore produces a yellow merocyanine dye that reverts quickly, while the 2*H*-naphthopyran mechanophore generates a red merocyanine dye that reverts significantly slower. The trends in absorption and reversion measured in solution are also reflected in solid polymeric materials activated in tension. Building on recent research into substituent effects, this study identifies naphthopyran isomerism as a simple lever for modulating the mechanochromic properties of the naphthopyran mechanophore used in the development of force responsive polymers.

Introduction

Naphthopyrans are versatile molecular switches that undergo a 6π electrocyclic ring-opening reaction to generate colored merocyanine dyes with an appropriate external stimulus. The photochemical ring-opening reaction of naphthopyrans under UV light has been extensively studied,[1] due in part to significant commercial interest in their use in photochromic lenses.[2] More recently it was discovered that mechanical force, when properly coupled to the C–O pyran bond, also promotes the ring-opening reaction of naphthopyran.[3] The mechanochemical activation of various naphthopyran derivatives covalently incorporated into polymers has been achieved using ultrasound,[4–6] grinding of polymer composites,[7] and in bulk polymeric materials under stress.[3,6,8] The chromogenic behavior of naphthopyran in polymers subjected to mechanical force enables the straightforward visualization of stress and/or strain in a material, and complements the growing repertoire of mechanochromic mechanophores that also includes spiropyran,[9] spirothiopyran,[10] rhodamine,[11,12] oxazine,[13] π-extended anthracene adducts,[14,15] and radical-type mechanophores like diarylbibenzofuranone,[16,17] among others. Naphthopyran mechanophores are particularly

attractive due to their synthetic accessibility combined with a high degree of structural modularity, which allows for precise control of the absorption properties and the lifetime of the mechanochemically generated merocyanine species.[8]

Research into the mechanochemistry of naphthopyrans has largely focused on the 3*H*-naphtho[2,1-*b*]pyran (3*H*) scaffold, with an emphasis on their mechanochromic behavior in solid polymeric materials. An alternative isomeric 2*H*-naphtho[1,2-*b*]pyran (2*H*) scaffold has also been widely developed for photoswitching applications due to its favorable photochromic properties, including relatively slow thermal reversion and unique absorption behavior of the corresponding merocyanine dyes.[1] The parent structures and reactivity of 3*H*- and 2*H*-naphthopyrans are illustrated in Scheme 1.1. We recently reported the first mechanochemical reaction of a 2*H*-naphthopyran mechanophore, revealing an unusual transformation that generates a persistent merocyanine dye locked by an intramolecular H-bonding interaction between the ketone and a β-hydroxyl group that is exposed via a C–O bond scission event.[6] In that case, polymer attachment through an ester group at the 10-position of the naphthopyran was critical to achieve the unique reactivity. More generally, however, 2*H*-naphthopyrans possess desirable properties that are anticipated to complement those of 3*H*-naphthopyrans for the design of

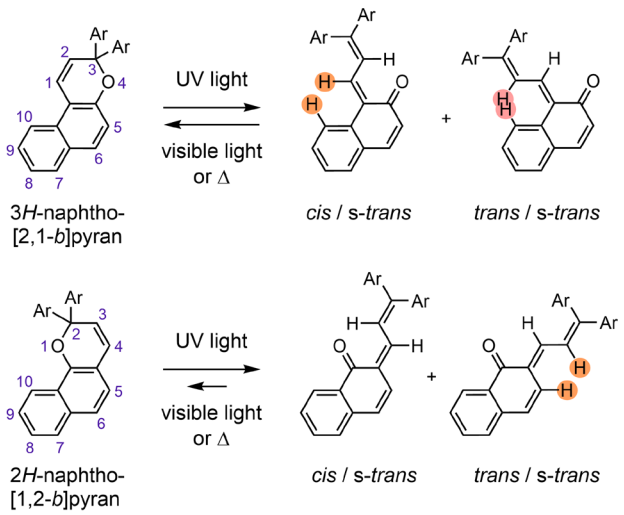

Scheme 1.1. The ring-opening reaction of 3*H*- and 2*H*- naphthopyrans generates merocyanine isomers with varying degrees of steric repulsion, which strongly influence absorption and reversion.

mechanochromic molecular force probes. The photochemical ring-opening reaction of naphthopyran generates multiple merocyanine stereoisomers with varying degrees of steric repulsion.[18] These steric demands differ substantially between merocyanines derived from 2*H*- and 3*H*-naphthopyrans and affect the rate of thermal electrocyclization of the merocyanine dyes, which occurs exclusively from the stereoisomers with *cis* configuration of the exocyclic alkene bond. For merocyanine dyes derived from 2*H*-naphthopyrans, reduced steric crowding results in greater stability and slower electrocyclization, thus leading to a longer-lived merocyanine state and more intense coloration.[18] The reduced steric interactions in merocyanines derived from 2*H*-naphthopyrans also results in greater planarization of the diene portion of the chromophore leading to better conjugation with the quinone and visible absorption features that are bathochromically shifted compared to merocyanine dyes produced from analogous 3*H*-naphthopyrans.[19]

In order to expand and better understand the mechanochemistry of naphthopyrans, here we directly compare the mechanochemical reactivity of two constitutionally isomeric 2*H*- and 3*H*-naphthopyran mechanophores in solution-phase ultrasonication experiments and in bulk polymeric materials. We note that the mechanochemical reactivity of the prototypical 3*H*-naphthopyran mechanophore[3] originally reported by Moore and Sottos is characterized using solution-phase ultrasonication methods for the first time. Consistent with their photochemical behavior, the mechanochromic properties of the mechanophores vary significantly based on isomerism of the naphthopyran nucleus, producing merocyanine dyes with distinct visible absorption and significantly different thermal reversion rates in polymers subjected to mechanical force. These results demonstrate a convenient approach for the

diversification of mechanochromic naphthopyran mechanophores that may find use in stress sensing and other applications.

Results and Discussion

We set out by identifying two isomeric 2*H*- and 3*H*-naphthopyran compounds and incorporating them covalently into polymers to study their mechanochemical reactivity (Scheme 1.2). The positions of polymer attachment to the naphthopyran are critical to enable mechanochemical activity, as force must be applied effectively across the labile C–O pyran bond with a geometry that is congruent with the ring-opening reaction coordinate.[3] On both substrates, a polymer chain is attached at the *para* position of one of the aryl rings connected to the sp^3-hybridized carbon of the pyran ring. For the 3*H*-naphthopyran, attachment of the second polymer chain at the 5-position leads to efficient activation of the ring-opening reaction and merocyanine generation with force. This particular attachment geometry has been employed in every reported mechanophore based on the 3*H*-naphthpoyran scaffold, whereas alternative regiochemistries have been demonstrated to be mechanochemically incompetent.[3] For the 2*H*-naphthopyran, polymer attachment at the 9- and 10-position results in effective alignment between the externally applied force vector and the C–O pyran bond to promote the ring-opening reaction.[6] We chose to investigate the mechanophore with polymer attachment at the 9-position, which produces a reversible merocyanine dye similar to the one generated from the 3*H*-naphthopyran mechanophore. Poly(methyl acrylate) (PMA) polymers containing a chain-centered 2*H*- or 3*H*-naphthopyran mechanophore were synthesized from the corresponding naphthopyran bis-initiators bearing two α-bromoisobutyryl ester functional groups, which were prepared from the reaction of a propargyl alcohol with the appropriately substituted naphthol (see Experimental Details

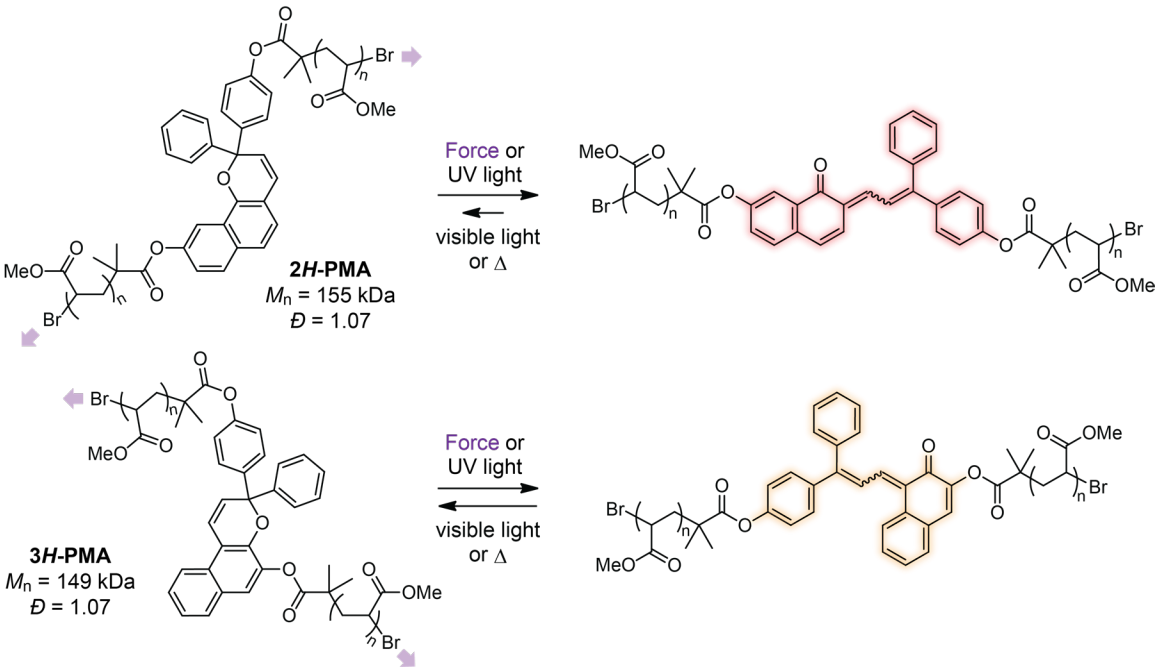

Scheme 1.2. Reversible ring-opening reaction of polymer chain-centered 2*H*-naphtho[1,2-*b*]pyran and 3*H*-naphtho[2,1-*b*]pyran mechanophores is achieved using mechanical force or UV light.

section).[20] Controlled radical polymerization of methyl acrylate using copper wire/Me_6TREN in DMSO[21] furnished polymers **2*H*-PMA** and **3*H*-PMA** with M_n of 155 kDa ($Đ$ = 1.07) and 149 kDa ($Đ$ = 1.07), respectively, as characterized by GPC-MALS.

Density functional theory (DFT) calculations performed using the constrained geometries simulate external force (CoGEF) method[22,23] predict that both the 2*H*- and 3*H*-naphthopyran isomers illustrated in Scheme 1 undergo the desired ring-opening reaction upon mechanical elongation (Figure 1.1). The ring-opening reaction of the 2*H*-naphthopyran substrate in **2*H*-PMA** is predicted to occur at a maximum force (F_{max}) of 4.0 nN, while that of the 3*H*-naphthopyran mechanophore in **3*H*-PMA** occurs at a higher F_{max} of 4.6 nN. These predicted forces, while typically overestimated compared to experimentally measured values, nevertheless provide an indication of the relative mechanochemical activity of mechanophores.[23] The lower F_{max} value calculated for the ring-opening reaction of the 2*H*-

naphthopyran substrate suggests that it is a more active mechanophore than the 3*H*-naphthopyran isomer. We note that the F_{max} value of 4.6 nN calculated for the 3*H*-naphthopyran structure studied here with attachment via an ester group at the 5-position is slightly higher than the F_{max} value of 4.3 nN reported previously for the analogous alkoxy-substituted derivative.[23]

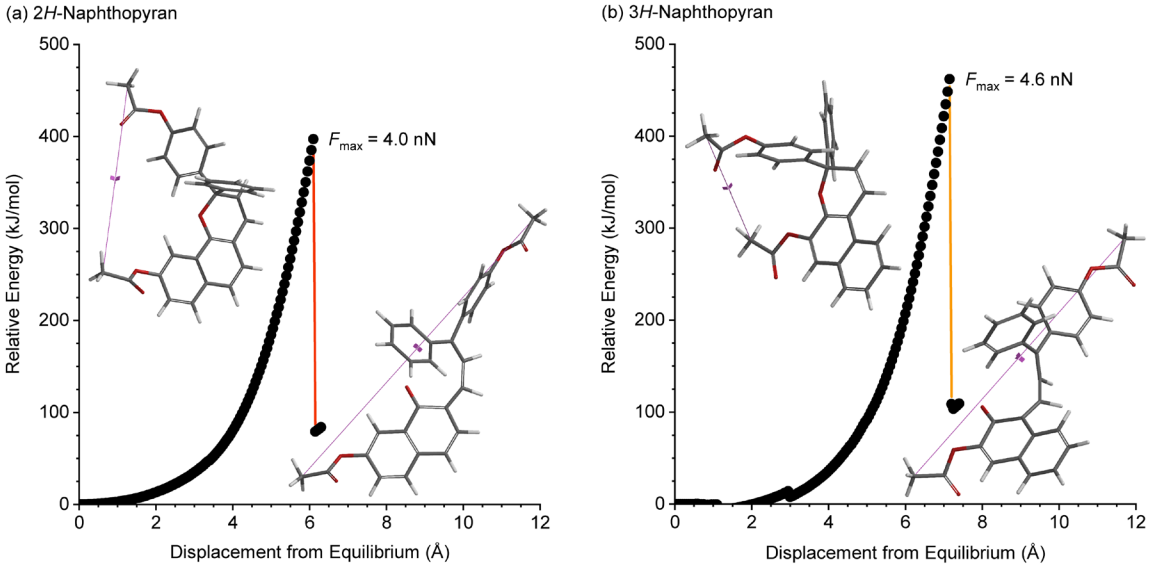

Figure 1.1. DFT calculations using the constrained geometries simulate external force (CoGEF) method performed on truncated models of the mechanophores in (a) **2*H*-PMA** (F_{max} = 4.0 nN) and (b) **3*H*-PMA** (F_{max} = 4.6 nN). Computed structures are shown that correspond to the force-free geometry and the products immediately after the ring-opening reaction. Calculations were performed at the B3LYP/6-31G* level of theory.

The ring-opening reactions of the naphthopyran mechanophores in **2*H*-PMA** and **3*H*-PMA** were initially investigated in solution by first comparing the UV-vis absorption spectra of the merocyanine products obtained from either photochemical or mechanochemical activation (Figure 1.2). Photoirradiation of the polymer solutions (2 mg/mL in THF) with 311 nm UV light for 60 s at ~20 °C produces a red-orange merocyanine dye with a λ_{max} of 485 nm from **2*H*-PMA** and a yellow merocyanine dye with a λ_{max} of 440 nm from **3*H*-PMA**. The absorption spectrum of the merocyanine dye produced from **3*H*-PMA** exhibits a single peak in the visible region, while the absorption spectrum of the merocyanine species generated from **2*H*-PMA** exhibits shorter wavelength features at 390 nm and 410 nm in addition to the primary

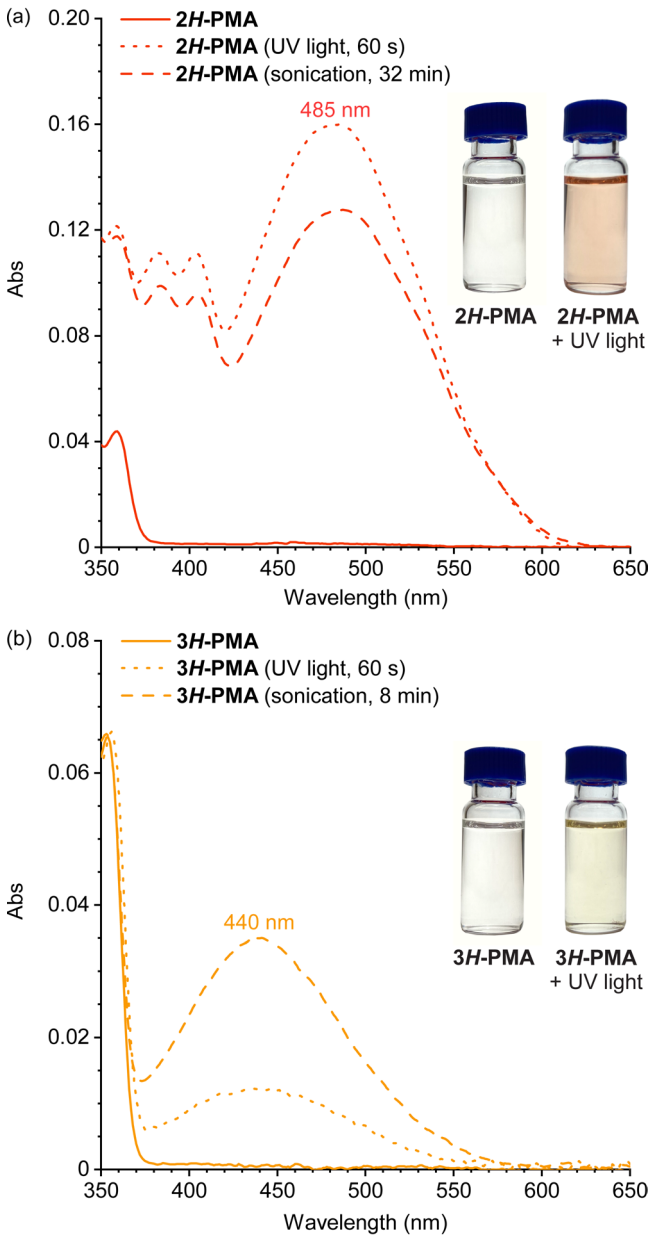

Figure 1.2. UV-vis absorption spectra of (a) **2*H*-PMA** and (b) **3*H*-PMA** (2 mg/mL THF) before and after photochemical activation with UV light (311 nm, ~20 °C) or ultrasound-induced mechanochemical activation (−13 °C). The ring-opening reaction of **2*H*-PMA** produces a merocyanine with a λ_{max} of 485 nm, while activation of **3*H*-PMA** produces a merocyanine with a λ_{max} of 440 nm. Photographs of the same polymer solutions before and after exposure to UV light illustrating the colors of the merocyanines.

visible absorption peak, consistent with typical merocyanines derived from 2*H*-naphthopyran photoswitches.[1,24] Mechanochemical activation of the polymers was studied using ultrasonication, which generates elongational forces on polymer chains in solution that are maximized near the chain midpoint where the naphthopyran mechanophores are installed.[25–27] Solutions of **2*H*-PMA** and **3*H*-PMA** (2 mg/mL in THF containing 30 mM BHT) were subjected to continuous ultrasonication (20 kHz, 8.8 W/cm^2) at −13 °C and reactions were monitored synchronously with UV-vis spectroscopy using a continuous flow setup following previously reported techniques.[5,28] We note that when sonication was performed using only an ice bath, which resulted in an internal solution temperature of ~15 °C, merocyanine formation from **3*H*-PMA** was not observed due to rapid reversion, in contrast to experiments performed on **2*H*-PMA** (Figure S1.5 in Experimental Details section). Lowering the solution temperature to −13 °C using a colder external bath, however, allowed for accumulation of the merocyanine species upon mechanochemical activation of **3*H*-PMA** enabling its characterization. As illustrated in Figure 1.2, the UV-vis absorption spectra obtained after ultrasound-induced mechanical activation of **2*H*-PMA** and **3*H*-PMA** closely match the spectra obtained after photochemical activation, indicating that the same products are generated using UV light and mechanical force.

To further interrogate the mechanochemical reactivity of the 2*H*- and 3*H*-naphthopyran mechanophores, the reversible ring-opening reactions of **2*H*-PMA** and **3*H*-PMA** were followed in real time during and after cessation of ultrasonication (Figure 1.3). The polymers were subjected to ultrasound-induced mechanical force under the same conditions described above and the reactions were monitored at the respective λ_{max} of each merocyanine dye. Polymer solutions were sonicated until the absorption corresponding to each merocyanine species plateaued, at which point sonication was turned off and the thermal reversion of the merocyanine back to the colorless naphthopyran was monitored over time. Rate constants for the observed mechanochemical activation and reversion reactions were obtained by fitting the time dependent absorption data to expressions of first-order kinetics (see Experimental Details section). A significantly higher absorbance is achieved for the mechanochemical reaction of **2*H*-PMA** compared to **3*H*-PMA**, suggesting a greater fraction of merocyanine in the mechanostationary state,[28] although potential differences in the extinction coefficients of the merocyanine dyes will also affect the absorbance plateau value. Likewise,

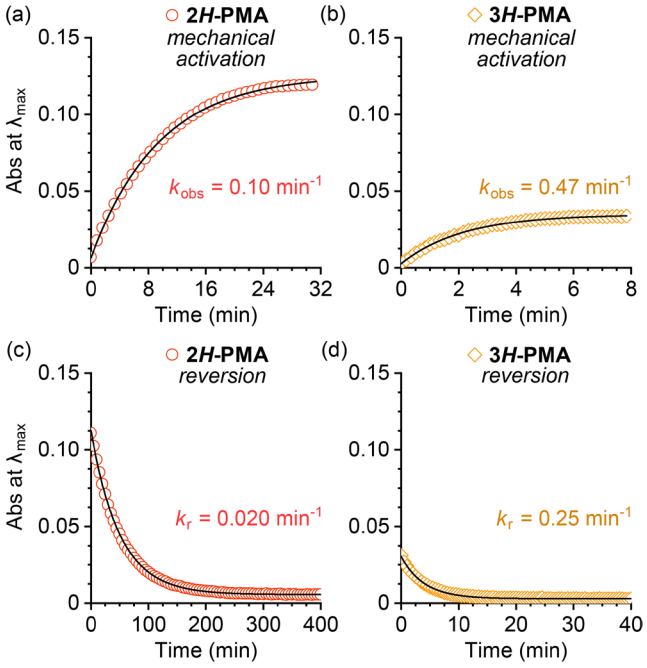

Figure 1.3. Ultrasound-induced mechanical activation and subsequent thermal reversion occur at different rates for **2*H*-PMA** and **3*H*-PMA.** (a,b) Mechanical activation kinetics for polymer solutions (2 mg/mL in THF) measured at −13 °C. (c,d) Kinetics of thermal reversion measured for the same solutions after cessation of ultrasound (−30 °C). Rate constants are averages from duplicate experiments and were determined by fitting the time-dependent merocyanine absorption to expressions of first-order kinetics.

the observed activation rate constant, k_{obs}, for **2*H*-PMA** (k_{obs} = 0.10 min^{-1}) is nearly 5× smaller than that for **3*H*-PMA** (k_{obs} = 0.47 min^{-1}) measured at the same temperature of −13 °C. Both of these observations are consistent with the significantly slower rate of thermal reversion for the merocyanine dye generated from **2*H*-PMA** compared to the merocyanine dye produced from **3*H*-PMA**. In the absence of additional reaction pathways, the observed activation rate constant, k_{obs}, is the sum of the rate constants for the forward ring-opening (k_f) and reverse ring-closing (k_r) reactions. However, nonspecific backbone scission that occurs during ultrasonication results in an irreversible pathway producing mechanophores that cannot be reactivated,[5] which complicates the kinetic analysis. It is also important to point out that upon cessation of ultrasound, the temperature of the polymer solutions quickly equilibrates with the colder external bath to reach an internal temperature of approximately −30 °C (Figure S1.6). Under these experimental conditions, the thermal ring-closing reaction of the merocyanine generated mechanochemically from **2*H*-PMA** occurs with a rate constant of k_r = 0.020 min^{-1} and a corresponding half-life of $t_{1/2}$ = 35 min, while reversion of the merocyanine species generated from **3*H*-PMA** is significantly faster with k_r = 0.25 min^{-1} and a half-life of $t_{1/2}$ = 2.8 min. Separately, rate constants for thermal reversion of each merocyanine dye were determined at −13 °C under otherwise identical conditions after brief photoirradiation of each polymer with UV light (see Experimental Details section). The measured values of k_r for the merocyanine dyes produced from **2*H*-PMA** and **3*H*-PMA** at −13 °C are 0.026 min^{-1} and 0.42 min^{-1}, respectively (Figure S1.7). Nevertheless, irreversible loss of merocyanine due to chain scission combined with the disparate rates of thermal ring-closure and uncertainty in the extinction coefficients of each merocyanine species limit

further quantification of the reaction kinetics, precluding the determination of values of k_f for the two mechanophores.

The mechanochromic behavior of naphthopyran mechanophores makes them useful as molecular forces probes for visualizing stress and/or strain in polymeric materials. Therefore, we were interested in directly comparing the reactivity of the 2*H*- and 3*H*-naphthopyran mechanophores studied above in bulk materials subjected to mechanical force. Analogs of the 2*H*- and 3*H*-naphthopyran mechanophores studied in solution were synthesized with terminal vinyl groups and incorporated as crosslinkers (~1.5 wt% loading) into polydimethylsiloxane (PDMS) elastomers via Pt-catalyzed hydrosilylation[29] to yield materials **2*H*-PDMS** and **3*H*-PDMS** (Figure 1.4a, see Experimental Details section). The difference in stability of each merocyanine species is immediately apparent in the prepared

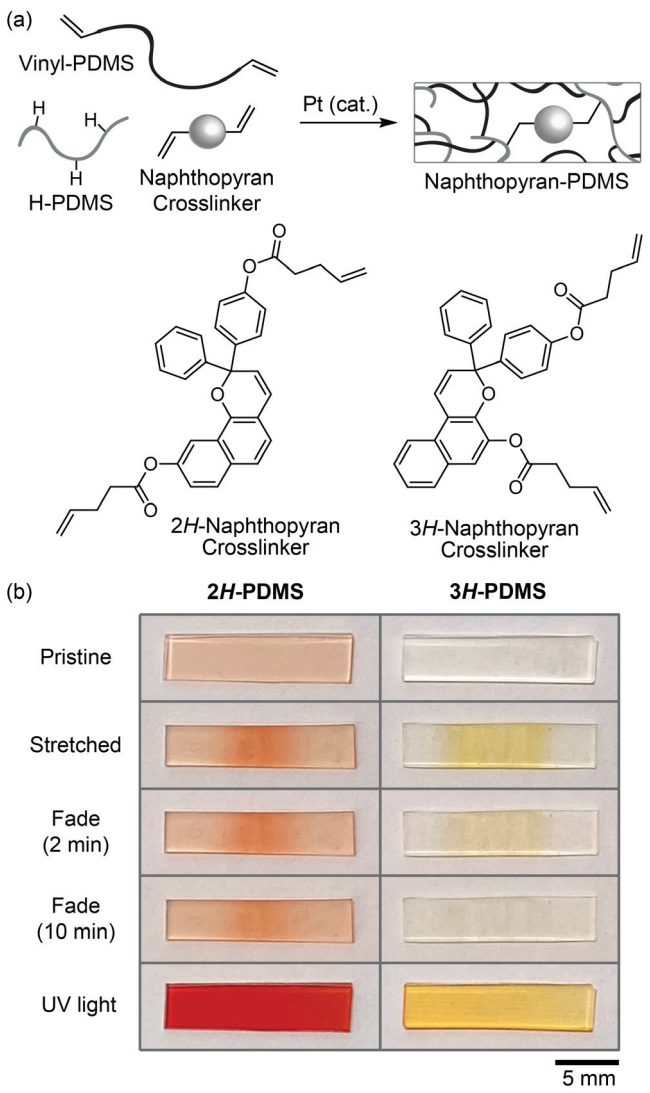

Figure 1.4. Mechanical activation and color fading evaluated in solid polymeric materials. (a) PDMS networks covalently crosslinked with naphthopyran mechanophores (1.5 wt%) are prepared via Pt-catalyzed hydrosilylation. (b) Photographs of **2*H*-PDMS** and **3*H*-PDMS** films immediately after mechanical activation (tension) and subsequent stress relaxation (2 min and 10 min), and after irradiation (λ = 311 nm, 90 s).

PDMS films as **3*H*-PDMS** is completely colorless, while **2*H*-PDMS** exhibits a slightly red background coloration that cannot be fully bleached even upon irradiation with intense visible light. Nonetheless, manual tension applied to each material induces the ring-opening reaction of the naphthopyran mechanophores causing the gauge region to become significantly colored (Figure 1.4b). Consistent with the absorption behavior determined from solution-phase experiments, **2*H*-PDMS** produces a red color while **3*H*-PDMS** produces a yellow color under mechanical force. The relative rate of color fading was assessed after stress relaxation, which also qualitatively matches the behavior of the merocyanine dyes in solution. For **3*H*-PDMS**, the color generated upon mechanical activation nearly completely fades after 10 min following initial stress relaxation, consistent with the relatively rapid reversion of the merocyanine dye generated from the 3*H*-naphthopyran mechanophore observed previously. In contrast, the red color produced in **2*H*-PDMS** upon stretching is more persistent and is still clearly visible 10 min after stress relaxation. Irradiation of the **2*H*-PDMS** and **3*H*-PDMS** materials with UV light (311 nm, 90 s) produces the same red and yellow coloration characteristic of each merocyanine species, but with greater intensity. Building on the recently detailed effects of substitution on the 3*H*-naphthpyran scaffold,[8] these results expand the toolkit for modulating the mechanochromic properties of naphthopyran mechanophores by leveraging simple changes in isomerism.

Conclusions

Naphthopyrans are versatile substrates for the design of mechanophores with a wide range mechanochromic properties. To date, the mechanochemistry of naphthopyran has largely focused on the 3*H*-naphthopyran scaffold; however, the isomeric 2*H*-naphthopyran scaffold exhibits complementary properties for the design of mechanochromic materials. Here we

directly compared the mechanochemical behavior of two isomeric 2*H*- and 3*H*-naphthopyran mechanophores using solution-phase ultrasonication methods and in solid polymeric materials. Naphthopyran mechanophores covalently incorporated into linear poly(methyl acrylate) polymers were activated using ultrasound and the reactions were monitored synchronously with UV-vis absorption spectroscopy. Mechanical activation of the prototypical 3*H*-napthopyran mechanophore was only observed at low temperatures due to the rapid thermal reversion of the merocyanine dye, which reverts approximately one order of magnitude faster than the merocyanine dye generated from the analogous 2*H*-naphthopyran mechanophore. The slower reversion of the merocyanine species derived from the 2*H*-naphthopyran mechanophore leads to a greater fraction of the merocyanine in the mechanostationary state and a higher optical density compared to mechanochemical activation of the 3*H*-naphthopyran mechanophore. The absorption properties of the merocyanine dyes are also distinct, with the 2*H*-naphthopyran substrate producing a red merocyanine dye (λ_{max} = 485 nm) compared to the yellow merocyanine species (λ_{max} = 440 nm) generated from the 3*H*-naphthopyran mechanophore. The mechanochemical behavior of the two naphthopyran isomers measured in solution is also reflected in the mechanochromic behavior of crosslinked elastomer networks. Polydimethylsiloxane (PDMS) materials incorporating the naphthopyran mechanophores as crosslinkers were prepared and mechanically activated under uniaxial tension, resulting in the expected color generation. The more persistent red color produced upon mechanical activation of the PDMS material containing the 2*H*-naphthopyran mechanophore fades much more slowly than the yellow color generated in the material with the 3*H*-naphthopyran isomer, which disappears completely within 10 min of stress relaxation under ambient conditions. The results of this

study expand on the mechanochemistry of naphthopyran and identify naphthopyran isomerism as an additional lever for modulating the absorption and fading behavior of naphthopyran mechanophores used in the development of force-responsive, mechanochromic polymers.

Acknowledgements

Financial support from Caltech is gratefully acknowledged. S.K.O. was supported by an Institute Fellowship from Caltech and M.E.M. was supported by an NSF Graduate Research Fellowship (DGE-1745301). We thank the Center for Catalysis and Chemical Synthesis of the Beckman Institute at Caltech for access to equipment.

Experimental Details

I. General Experimental Details

Reagents from commercial sources were used without further purification unless otherwise stated. Methyl acrylate was passed through a short plug of basic alumina to remove inhibitor immediately prior to use. Copper wire was cleaned by rinsing consecutively with 1 M HCl, water, acetone, and dichloromethane immediately prior to use. Dry THF was obtained from a Pure Process Technology solvent purification system. All reactions were performed under a N_2 or argon atmosphere unless specified otherwise. Column chromatography was performed on a Biotage Isolera system using SiliCycle SiliaSep HP flash cartridges.

NMR spectra were recorded using a 400 MHz Bruker Avance III HD with Prodigy Cryoprobe. All ^{1}H NMR spectra are reported in δ units, parts per million (ppm), and were measured relative to the signals for residual dichloromethane (5.32 ppm), acetone (2.05 ppm), or chloroform (7.26 ppm) in deuterated solvent. All ^{13}C NMR spectra were measured in deuterated solvents and are reported in ppm relative to the signals for chloroform (77.16 ppm). Multiplicity and qualifier abbreviations are as follows: s = singlet, d = doublet, t = triplet, q = quartet, m = multiplet, br = broad, app = apparent.

High resolution mass spectra (HRMS) were obtained from a Waters Corp. LCT Premier XE time-of-flight mass spectrometer equipped with an electrospray ionization (ESI) probe, or a JEOL JMS-600H magnetic sector mass spectrometer equipped with a FAB+ probe.

Analytical gel permeation chromatography (GPC) was performed using an Agilent 1260 series pump equipped with two Agilent PLgel MIXED-B columns (7.5 x 300 mm), an Agilent 1200 series diode array detector, a Wyatt 18-angle DAWN HELEOS light scattering detector, and a Optilab rEX differential refractive index detector. The mobile phase was THF

at a flow rate of 1 mL/min. Molecular weights and molecular weight distributions were calculated by light scattering using a dn/dc value of 0.062 mL/g (25 °C) for poly(methyl acrylate).

UV-vis absorption spectra were recorded on a Thermo Scientific Evolution 220 spectrometer.

Ultrasound experiments were performed using a Vibra Cell 505 liquid processor equipped with a 0.5-inch diameter solid probe (part #630-0217), sonochemical adapter (part #830-00014), and a Suslick reaction vessel made by the Caltech glass shop (analogous to vessel #830-00014 from Sonics and Materials). Polymer solutions were continuously sampled for UV-vis analysis using a Cole Parmer Masterflex L/S pump system (item #EW-77912-10) composed of an L/S pump head (part #77390-00) and L/S precision variable speed drive (part #07528-20) using 4x6 mm PTFE tubing (part #77390-60) and a quartz flow-through cell (Starna, part #583.4-Q-10/Z8.5), which was connected using M6-threaded PTFE tubing (Starna, part #M6-SET).

Photoirradiation with UV light was performed using a Philips PL-S 9W/01/2P UVB bulb with a narrow emission of 305–315 nm and a peak at 311 nm under ambient conditions unless indicated otherwise. Irradiation with blue light was performed using a 470 nm LED (ThorLabs M470L3), driver (ledd1B), and collimator (SM1U25-A).

II. Supplementary Figures

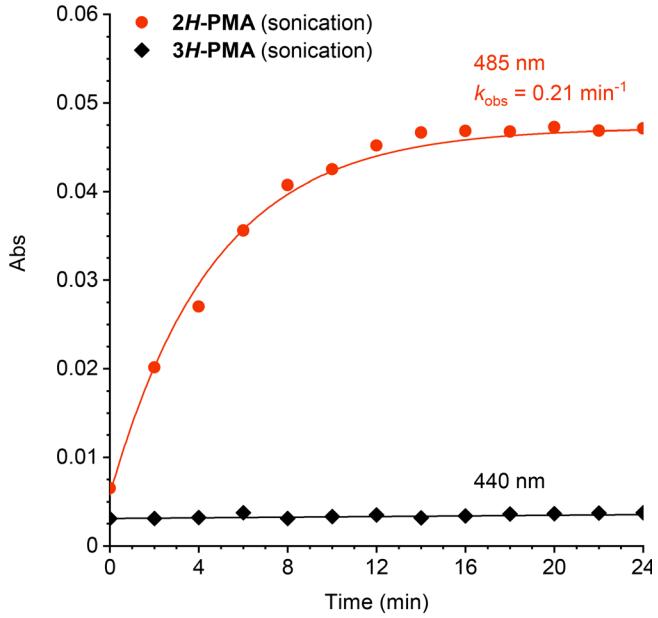

Figure S1.5. Ultrasound-induced mechanical activation of **2*H*-PMA** and **3*H*-PMA** (2 mg/mL in THF with 30 mM BHT) at 15–20 °C (solution temperature), characterized by synchronous UV-vis absorption spectroscopy monitoring at the λ_{max} of each merocyanine. At this temperature, mechanochemical generation of the merocyanine from **3*H*-PMA** is not observed due to rapid thermal reversion. In contrast, mechanochemical activation of **2*H*-PMA** is observed with rate constant k_{obs} = 0.21 min^{-1} due to the longer lifetime of the merocyanine dye.

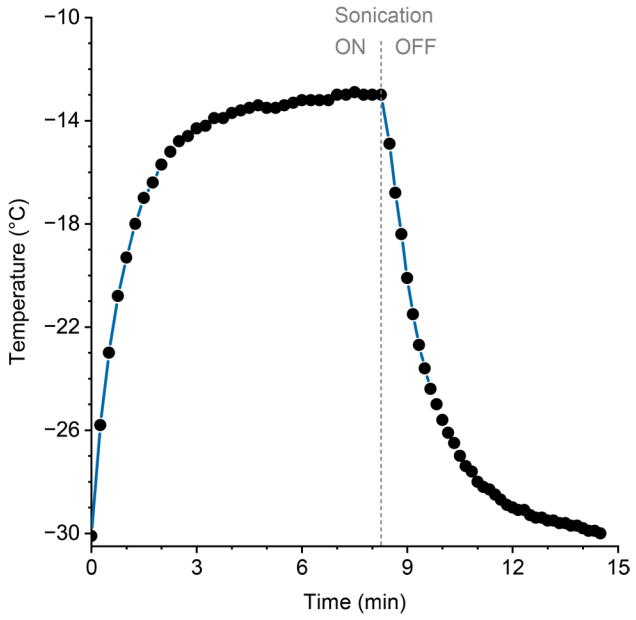

Figure S1.6. Evolution of solution temperature in the sonication vessel during flow. Application of continuous ultrasound (8.8 ± 0.2 W/cm^2) to the vessel starting at a stable initial temperature of –30 °C results in an increase in temperature that reaches a constant value of –13 °C after approximately 5 min. The effect of this temperature increase is eliminated by initiating sonication prior to the injection of a concentrated polymer sample (see Section VII for details). Upon cessation of ultrasound, the solution temperature returns to approximately –30 °C over a period of approximately 7 min.

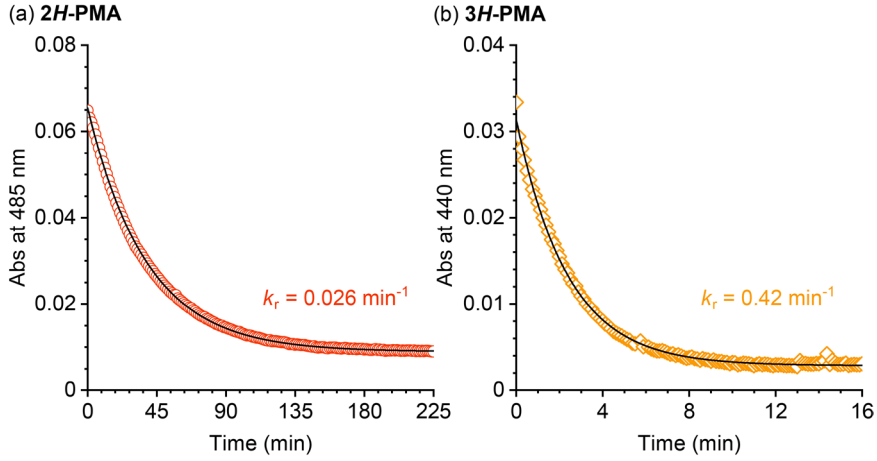

Figure S1.7. Merocyanine reversion at –13 °C in THF after photochemical activation with UV light (311 nm, 2 min) monitored at λ_{max}. (a) The merocyanine derived from **2*H*-PMA** reverts with a rate constant $k_r = 0.026$ min^{-1} and corresponding half-life of $t_{1/2} = 27$ min, while (b) the merocyanine derived from **3*H*-PMA** reverts with a rate constant $k_r = 0.42$ min^{-1} and corresponding half-life of $t_{1/2} = 1.7$ min.

III. Synthetic Details

Scheme S1.3. Synthesis of all compounds used in this study.

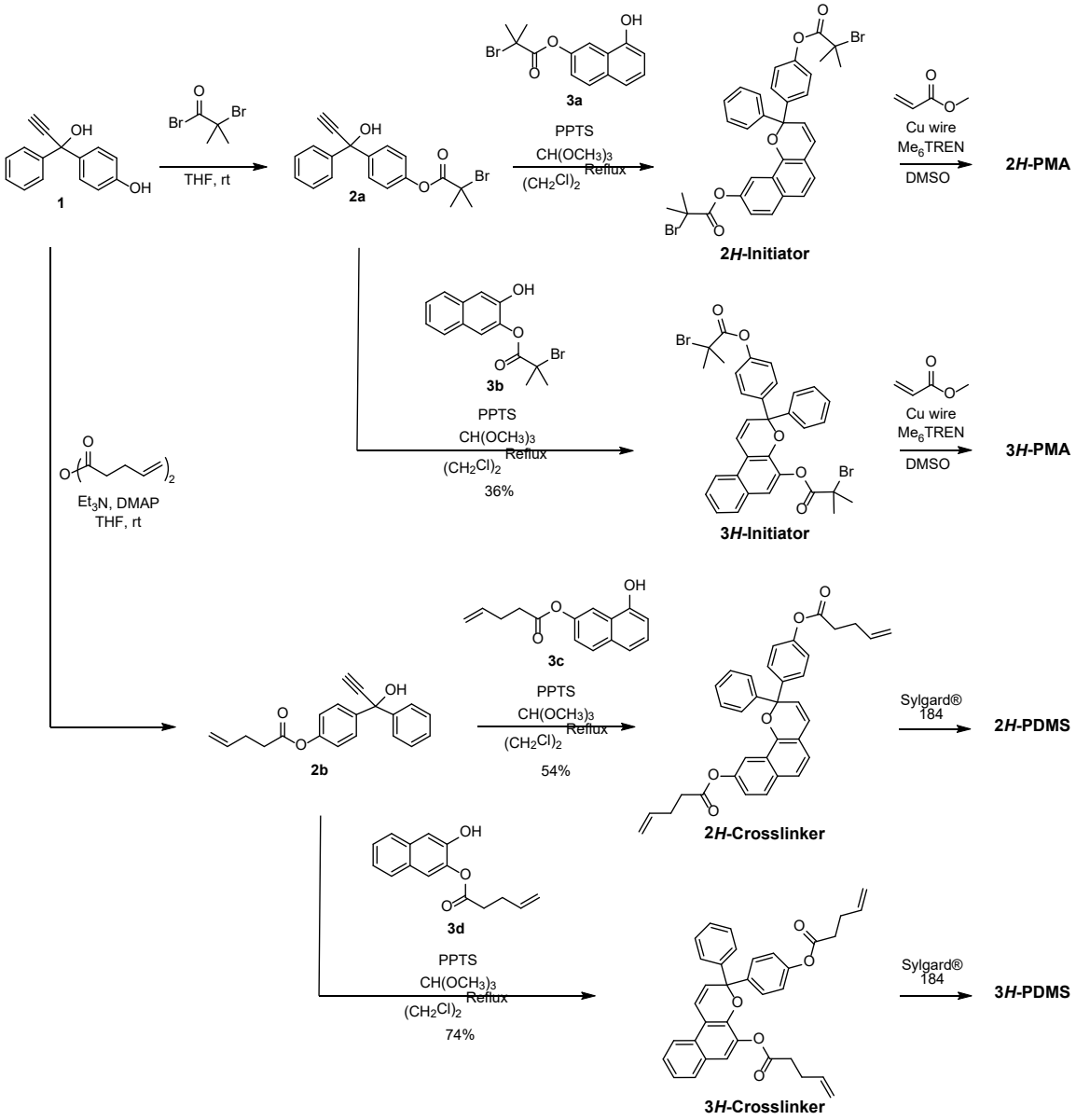

Compounds **1**,[3] **2a**,[6] **2b**,[6] **3a**,[6] **3b**,[5] and **2*H*-Initiator**[6] were prepared according to previously reported procedures.

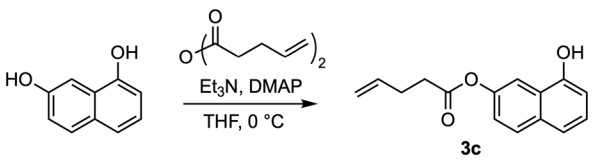

3c

8-hydroxynaphthalen-2-yl pent-4-enoate (3c). To a flame-dried 2-neck 250 mL RBF equipped with a stir bar was added 1,7-dihydroxynaphthalene (2.00 g, 12.5 mmol) and catalytic N,N-dimethylaminopyridine (15.3 mg, 0.125 mmol). The flask was evacuated and backfilled with N_2 three times. Anhydrous THF (50 mL) and triethylamine (2.1 mL, 15.0 mmol) were added sequentially via syringe under N_2. The solution was cooled to 0 °C in ice. Pentenoic anhydride (2.30 mL, 12.5 mmol) was added dropwise via syringe over 10 min at 0 °C. After stirring for 20 h, the reaction was diluted with 100 mL EtOAc, washed with saturated aqueous NH_4Cl (100 mL), saturated aqueous $NaHCO_3$ (100 mL), and brine (100 mL). The organic layer was dried over $MgSO_4$, filtered, and concentrated. The crude material was purified by column chromatography on silica gel (0–50% EtOAc/hexanes). A second chromatographic separation on silica gel (0–35% EtOAc/hexanes with 1% triethylamine) provided the title compound as a brown oil (508 mg, 17%).

TLC (25% EtOAc/hexanes): R_f = 0.36

^{1}H NMR (400 MHz, Acetone-d_6) δ: 9.15 (s, 1H), 7.90 (d, *J* = 2.5 Hz, 1H), 7.86 (d, *J* = 8.9 Hz, 1H), 7.41 (d, *J* = 8.2 Hz, 1H), 7.30 (app dd, *J* = 8.2, 7.5 Hz, 1H), 7.25 (dd, *J* = 8.8, 2.4 Hz, 1H), 6.95 (dd, *J* = 7.5, 1.0 Hz, 1H), 5.97 (ddt, *J* = 16.9, 10.2, 6.5 Hz, 1H), 5.17 (app dq, *J* = 17.2, 1.7 Hz, 1H), 5.06 (ddt, *J* = 10.3, 1.9, 1.3 Hz, 1H), 2.75 td, *J* = 7.3, 0.5 Hz, 2H), 2.55 – 2.47 (m, 2H).

^{13}C{^{1}H} NMR (101 MHz, $CDCl_3$) δ: 172.7, 151.5, 147.8, 136.4, 132.9, 129.3, 125.8, 124.9, 121.5, 120.2, 116.2, 113.4, 109.2, 33.9, 29.0.

HRMS (FAB, *m/z*): calcd for $[C_{15}H_{14}O_3]^+$ $(M)^+$, 242.0943; found, 242.0949.

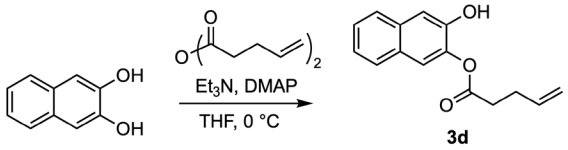

3d

3-hydroxynaphthalen-2-yl pent-4-enoate (3d). To a flame-dried 2-neck 250 mL RBF equipped with a stir bar was added 2,3-dihydroxynaphthalene (721 mg, 4.82 mmol) and catalytic N,N-dimethylaminopyridine (58.9 mg, 0.482 mmol). The flask was evacuated and backfilled with N_2 three times. Anhydrous THF (40 mL) and triethylamine (0.86 mL, 6.2 mmol) were added sequentially via syringe under N_2. The solution was cooled to 0 °C in an ice bath. Pentenoic anhydride (1.0 mL, 5.5 mmol) was added dropwise via syringe over 10 min at 0 °C. After stirring for 16 h, the reaction was diluted with EtOAc (100 mL) and washed sequentially with saturated aqueous NH_4Cl (100 mL), saturated aqueous $NaHCO_3$ (100 mL), and brine (100 mL). The organic layer was dried over $MgSO_4$, filtered, and concentrated. The crude material was purified by column chromatography on silica gel (5–40% EtOAc/hexanes) to provide the title compound as a white solid (892 mg, 76%).

TLC (25% EtOAc/hexanes): $R_f = 0.36$

^{1}H NMR (400 MHz, $CDCl_3$) δ: 7.72 (dd, J = 8.0, 1.4 Hz, 1H), 7.65 (dd, J = 8.3, 1.3 Hz, 1H), 7.58 (d, J = 0.6 Hz, 1H), 7.40 (ddd, J = 8.2, 6.9, 1.4 Hz, 1H), 7.34 (ddd, J = 8.2, 6.9, 1.4 Hz, 1H), 7.30 (s, 1H), 5.97 (ddt, J = 17.2, 10.2, 6.4 Hz, 1H), 5.49 (s, 1H), 5.21 (app dq, J = 17.2, 1.6 Hz, 1H), 5.15 (app dq, J = 10.2, 1.3 Hz, 1H), 2.80 (t, J = 7.3, 0.6 Hz, 2H), 2.63 – 2.53 (m, 2H).

^{13}C{^{1}H} NMR (101 MHz, $CDCl_3$) δ: 171.7, 146.2, 139.3, 136.6, 132.6, 128.6, 127.5, 126.4, 126.3, 124.4, 120.1, 116.4, 112.3, 33.7, 29.0.

HRMS (FAB, *m/z*): calcd for $[C_{15}H_{15}O_3]^+$ $(M+H)^+$, 243.1021; found, 243.1036.

General Procedure A for the Synthesis of Naphthopyrans. Naphthopyrans were synthesized following the procedure by Zhao and Carreira.[20] To a flame-dried 2-neck round bottom flask equipped with a stir bar and reflux condenser was added the appropriate propargyl alcohol, naphthol, and a catalytic amount of pyridinium *p*-toluenesulfonate (PPTS). The flask was evacuated and backfilled with N_2 three times followed by the sequential addition of 1,2-dichloroethane and trimethyl orthoformate via syringe. The reaction was heated to reflux and stirred for the indicated amount of time. Upon completion, the reaction was cooled to room temperature, concentrated with celite, and purified by column chromatography on silica gel.

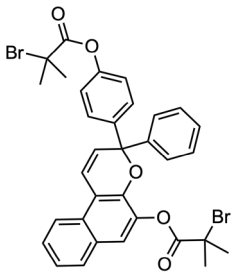

3*H*-Initiator

4-(5-((2-bromo-2-methylpropanoyl)oxy)-3-phenyl-3H-benzo[f]chromen-3-yl)phenyl 2-bromo-2-methylpropanoate (3*H*-Initiator). The title compound was prepared using General Procedure A with compound **2-3b** (311 mg, 1.01 mmol), compound **2-2a** (442 mg, 1.18 mmol) added as a solution in 1,2-dichloroethane, PPTS (35.5 mg, 0.141 mmol), trimethyl orthoformate (0.33 mL, 3.0 mmol), and 1,2-dichloroethane (10 mL). After reacting for 18 h, purification by column chromatography on silica gel (0–35% EtOAc/hexanes) followed by a second chromatographic separation on silica gel (5–15% EtOAc/hexanes) produced the title compound as a pale, peach-colored foamy solid (243 mg, 36%).

TLC (25% EtOAc/hexanes): $R_f = 0.55$

^{1}H NMR (400 MHz, CD_2Cl_2) δ: 8.00 (d, *J* = 8.5, Hz, 1H), 7.73 (d, *J* = 8.2 Hz, 1H), 7.56 – 7.45 (m, 6H), 7.43 – 7.36 (m, 2H), 7.33 (m, 2H), 7.31 – 7.23 (m, 1H), 7.13 – 7.05 (m, 2H), 6.32 (d, *J* = 10.0 Hz, 1H), 2.11 (s, 6H), 2.03 (s, 6H).

$^{13}C\{^{1}H\}$ NMR (101 MHz, $CDCl_3$) δ: 170.2, 170.0, 150.2, 144.1, 142.9, 142.4, 139.2, 128.8, 128.38, 128.36, 128.30, 128.22, 128.20, 127.9, 127.0, 126.7, 124.7, 121.5, 120.74, 120.72, 119.8, 116.0, 83.0, 55.4, 54.9, 31.3, 30.7.

HRMS (FAB, *m/z*): calcd for $[C_{33}H_{28}Br_2O_5]^+$ $(M)^+$, 662.0304; found, 662.0290

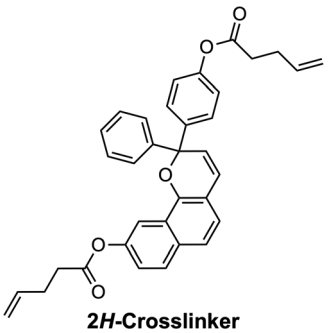

2*H*-Crosslinker

4-(9-(pent-4-enoyloxy)-2-phenyl-2H-benzo[h]chromen-2-yl)phenyl pent-4-enoate (2*H*-Crosslinker). The title compound was prepared using General Procedure A with **2-3c** (145 mg, 0.598 mmol), **2-2b** (220 mg, 0.718 mmol) added as a solution in 1,2-dichloroethane, PPTS (18 mg, 0.072 mmol), trimethyl orthoformate (0.15 mL, 1.4 mmol), and 1,2-dichloroethane (6 mL). After reacting for 4 h, purification by column chromatography on silica gel (0–15% EtOAc/hexanes with 1% triethylamine) followed by a second chromatographic separation on silica gel (10–80% dichloromethane/hexanes) provided the title compound as a red oil (171 mg, 54%).

TLC (25% EtOAc/hexanes): R_f = 0.53

^{1}H NMR (400 MHz, Acetone-d_6) δ: 8.05 (d, J = 2.3 Hz, 1H), 7.84 (d, J = 8.9 Hz, 1H), 7.61 – 7.54 (m, 4H), 7.45 (d, J = 8.5 Hz, 1H), 7.40 – 7.32 (m, 2H), 7.32 – 7.23 (m, 3H), 7.14 – 7.07 (m, 2H), 6.90 (d, J = 9.7 Hz, 1H), 6.46 (d, J = 9.7 Hz, 1H), 5.93 (ddt, J = 16.8, 10.2, 6.5 Hz, 2H), 5.14 (m, 2H), 5.03 (m, 2H), 2.76 (td, J = 7.4, 0.5 Hz, 2H), 2.65 (td, J = 7.3, 0.6 Hz, 2H), 2.54 – 2.47 (m, 2H), 2.46 – 2.39 (m, 2H).

^{13}C{^{1}H} NMR (101 MHz, $CDCl_3$) δ: 171.8, 171.6, 150.1, 148.6, 147.5, 144.8, 142.6, 136.5, 136.4, 132.8, 129.3, 128.34, 128.27, 127.8, 127.7, 127.0, 125.1, 124.5, 123.9, 121.9, 121.3, 120.6, 116.1, 116.0, 113.0, 83.2, 33.8, 33.7, 29.0, 28.98.

HRMS (FAB, *m/z*): calcd for $[C_{35}H_{30}O_5]^+$ $(M)^+$, 530.2093; found, 530.2078

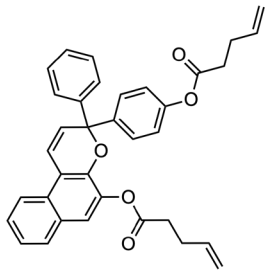

3*H*-Crosslinker

4-(5-(pent-4-enoyloxy)-3-phenyl-3H-benzo[f]chromen-3-yl)phenyl pent-4-enoate (3*H*-Crosslinker). The title compound was prepared using General Procedure A with **2-3d** (300 mg, 1.24 mmol), **2-2b** (455 mg, 1.49 mmol) added as a solution in 1,2-dichloroethane, PPTS (37.3 mg, 0.149 mmol), trimethyl orthoformate (0.31 mL, 2.8 mmol), and 1,2-dichloroethane (12 mL). After reacting for 4 h, purification by column chromatography on silica gel (0–15% EtOAc/hexanes with 1% triethylamine) followed by a second chromatographic separation on silica gel (0–10% Et_2O/CH_2Cl_2:hexanes (1:1)) produced the title compound as an orange oil (484 mg, 74%).

TLC (25% EtOAc/hexanes): R_f = 0.55

^{1}H NMR (400 MHz, CD_2Cl_2) δ: 7.98 (d, *J* = 8.8 Hz, 1H), 7.71 (d, *J* = 8.2 Hz, 1H), 7.53 – 7.43 (m, 6H), 7.42 – 7.31 (m, 4H), 7.31 – 7.24 (m, 1H), 7.08 – 7.00 (m, 2H), 6.32 (d, *J* = 9.9 Hz, 1H), 6.00 – 5.83 (m, 2H), 5.13 (m, 2H), 5.03 (m, 2H), 2.82 – 2.75 (m, 2H), 2.64 (td, *J* = 7.4, 0.8 Hz, 2H), 2.58 – 2.50 (m, 2H), 2.50 – 2.43 (m, 2H).

^{13}C{^{1}H} NMR (101 MHz, $CDCl_3$) δ: 171.5, 171.2, 150.1, 144.2, 143.1, 142.1, 139.4, 136.5, 136.4, 128.8, 128.28, 128.26, 128.24, 128.21, 128.1, 127.8, 127.0, 126.5, 124.5, 121.5, 121.3, 121.0, 119.6, 116.1, 116.0, 115.8, 83.0, 33.7, 33.5, 29.1, 29.0.

HRMS (FAB, *m/z*): calcd for $[C_{35}H_{30}O_5]^+$ $(M)^+$, 530.2093; found, 530.2084

General Procedure B for the Synthesis of Poly(Methyl Acrylate) (PMA) Polymers Incorporating a Chain-Centered Naphthopyran. Polymers were synthesized by controlled radical polymerization following the procedure by Nguyen *et al*.[21] A flame-dried Schlenk flask was charged with freshly cut 20 G copper wire (2 cm), initiator, DMSO, and methyl acrylate. The flask was sealed and the solution was degassed via three freeze-pump-thaw cycles, then backfilled with nitrogen and warmed to room temperature. Me_6TREN was added via microsyringe and the reaction was stirred at room temperature for the indicated amount of time. Upon completion of the polymerization, the flask was opened to atmosphere and diluted with a minimal amount of CH_2Cl_2. The polymer was precipitated 3x into methanol cooled with dry ice and then dried under vacuum.

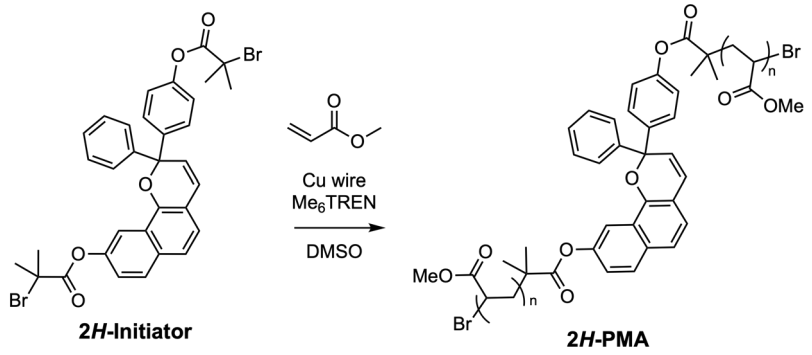

Polymer **2*H*-PMA.** Synthesized using General Procedure B with initiator **2*H*-Initiator** (8.3 mg, 0.012 mmol), methyl acrylate (3.4 mL, 37 mmol), DMSO (3.4 mL), and Me_6TREN (17 µL, 0.063 mmol). Polymerization for 2.5 h provided the title polymer as a tacky pale peach-colored solid (1.4 g, 43%). M_n = 155 kg/mol, $Đ$ = 1.07.

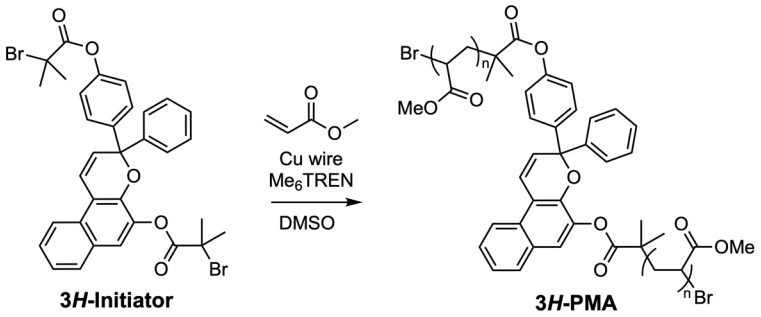

Polymer **3*H*-PMA.** Synthesized using General Procedure B with initiator **3*H*-Initiator** (10.0 mg, 0.015 mmol), methyl acrylate (4.9 mL, 54 mmol), DMSO (4.9 mL), and Me_6TREN (20 µL, 0.075 mmol). Polymerization for 3 h provided the title polymer as a tacky colorless solid (1.6 g, 34%). M_n = 149 kg/mol, $Đ$ = 1.07.

IV. Characterization of Linear PMA Polymers

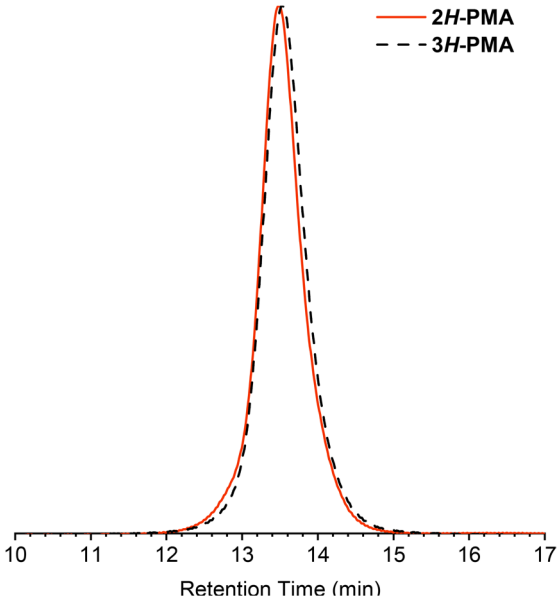

Figure S1.8. GPC traces (refractive index response) normalized to peak height for **2*H*-PMA** and **3*H*-PMA**.

V. Preparation of PDMS Materials

PDMS materials incorporating naphthopyran (~1.5 wt%) were prepared following previously reported procedures using the two-part Sylgard® 184 elastomer kit (Dow Corning).[3,29] PDMS films approximately 0.5 mm thick were cut into 3 x 15 mm strips for testing.

General Procedure C for the Preparation of PDMS Materials. The naphthopyran crosslinker was dissolved in a minimal amount of xylene in a 20 mL scintillation vial. Sylgard® 184 prepolymer base was added and the contents were thoroughly mixed in a vortex mixer with intermittent gentle heating to form a homogeneous dispersion. Sylgard® 184 curing agent was added and the contents were mixed thoroughly using a vortex mixer. The mixture was pipetted onto a clean 5 cm x 5 cm delrin plate, which was placed inside a vacuum chamber and evacuated under high vacuum (~30 mTorr) for 4 h. The delrin plate

was then transferred to an oven and cured at 80 °C overnight. After curing, the plate was removed from the oven and the PDMS film was peeled off and cut into strips.

2*H*-PDMS was synthesized using General Procedure C with **2*H*-Crosslinker** (30.7 mg, 0.058 mmol), xylenes (0.2 mL), Sylgard® 184 prepolymer base (1.956 g), and Sylgard® 184 curing agent (0.195 g). After curing, the films were irradiated with blue light (470 nm) for 30 min to reduce initial coloration.

3*H*-PDMS was synthesized using General Procedure C with **3*H*-Crosslinker** (31.4 mg, 0.059 mmol), xylenes (0.2 mL), Sylgard® 184 prepolymer base (1.975 g), and Sylgard® 184 curing agent (0.197 g).

VI. DFT Calculations (CoGEF)

CoGEF calculations were performed using Spartan ′18 Parallel Suite according to previously reported methods.[22,23] Ground state energies were calculated using DFT at the B3LYP/6-31G* level of theory. Truncated models of each mechanophore with terminal acetoxy groups were used in the calculations. For each structure, the equilibrium conformations of the unconstrained molecule were initially calculated using molecular mechanics (MMFF) followed by optimization of the equilibrium geometries using DFT (B3LYP/6-31G*). Starting from the equilibrium geometry of the unconstrained molecules (energy = 0 kJ/mol), the distance between the terminal methyl groups of the truncated structures was increased in increments of 0.05 Å and the energy was minimized at each step. The maximum force associated with the mechanochemical reaction was calculated from the slope of the curve immediately prior to bond cleavage using the final two contiguous data points.

VII. Details for Photoirradiation and Sonication Experiments

In order to continuously monitor reaction progress by UV-vis absorption spectroscopy, a previously described experimental setup[5,28] was assembled using a peristaltic pump to transport solution from the reaction vessel through a quartz flow cell in a UV-vis spectrometer and return the solution to the reaction vessel. The flow rate through the system was maintained at 8 mL/min, corresponding to a setting of 50 RPM on the peristaltic pump at the selected occlusion. The UV-vis spectrometer was programmed to acquire either full spectra or absorbance at predefined wavelengths at regular time intervals. Absorbance measurements at wavelengths of 440, 485, and 700 nm were acquired every 10 s during continuous photoirradiation or sonication of polymer solutions. The absorbance values measured at 700 nm were subtracted from the absorbance values monitored at 440 or 485 nm at each time point to account for drift during the experiments.

General Procedure for Sonication Experiments. A sonication vessel was placed onto the sonication probe and allowed to cool under a stream of N_2. The vessel was charged with THF, which contained 30 mM BHT (19.0 mL) to avoid decomposition side reactions resulting from free radicals generated during sonication.[30] An additional 6.2 mL of stabilized THF was pumped into the dead space of the circulatory setup. Teflon inlet and outlet tubes were inserted into the solution in the sonication vessel through punctured septa, and the pump was engaged to start the flow of solution through the system. The sonication vessel was submerged in either an ethanol bath maintained at −45 ± 2 °C with an immersion chiller or an ice bath maintained at 0 ± 2 °C, and the solution was sparged with N_2 for 30 min. The system was then maintained under an inert atmosphere for the duration of the experiment. Continuous sonication at 20 kHz (8.8 ± 0.2 W/cm^2) was initiated and run for approximately

5 min to allow the temperature inside the reaction vessel to equilibrate to –13 °C (ethanol bath) or 15–20 °C (ice bath), as measured by a thermocouple inserted into the solution (Digi-Sense EW-91428-02 thermometer with Digi-Sense probe EW-08466-83). Separately, a concentrated solution of polymer (1.0 mL, 52.4 mg/mL in stabilized THF) was sparged with N_2 for 30 min. This solution was then injected into the sonication vessel to provide a total system volume of 26.2 mL (2.0 mg/mL of polymer) and reaction progress was monitored by UV-vis absorption spectroscopy. Sonication intensity was calibrated via the literature method.[25] The entire system was kept in the dark for the duration of the experiment. Complete experimental data for the ultrasound-induced mechanochemical generation and reversion of merocyanine dyes derived from **2*H*-PMA** and **3*H*-PMA** are provided in Figures S1.9 and S1.10 below.

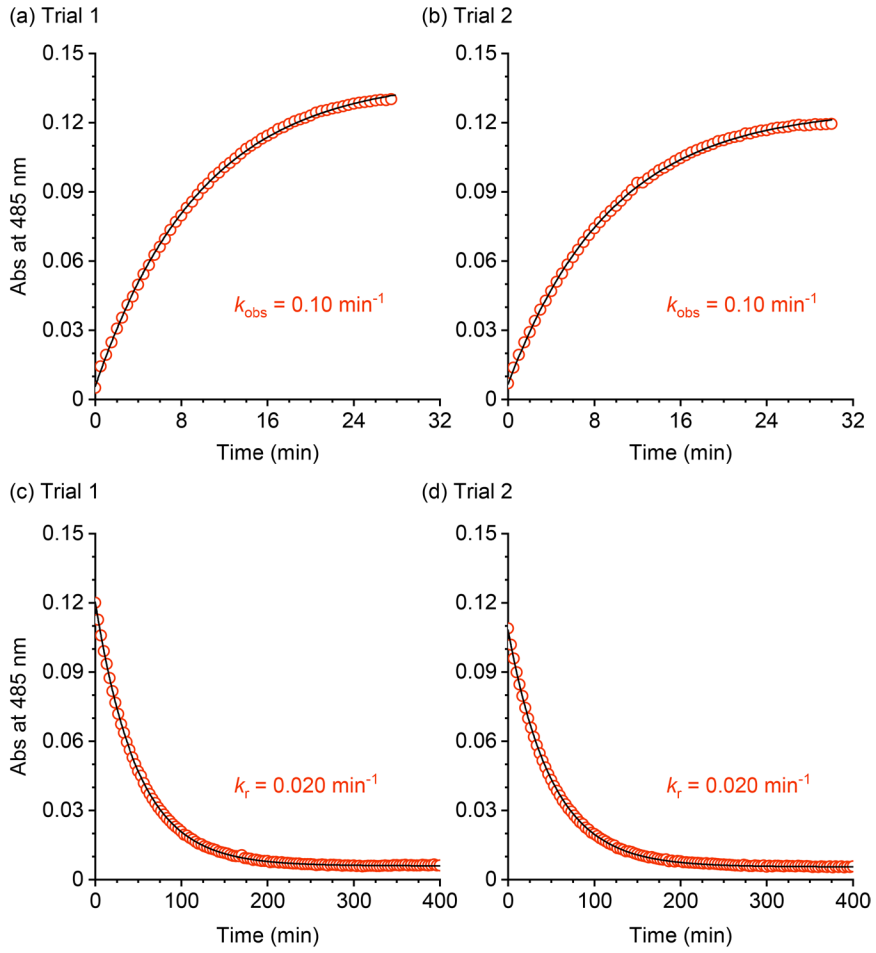

Figure S1.9. Ultrasound-induced mechanical activation of **2*H*-PMA** (2 mg/mL in THF with 30 mM BHT) at –13 °C and subsequent thermal reversion at approximately –30 °C, monitored at λ_{max} = 485 nm. (a,b) The forward reaction occurs with an observed rate constant of k_{obs} = 0.10 min^{-1} averaged over two replicate experiments. (c,d) Thermal reversion of the merocyanine at –30 °C measured from the same polymer solutions after cessation of ultrasound occurs with an average rate constant of k_r = 0.020 min^{-1} corresponding to a half-life of $t_{1/2}$ = 35 min. Note that the temperature of the polymer solution quickly equilibrates to approximately –30 °C when the ultrasound is turned off (see Figure S1.6).

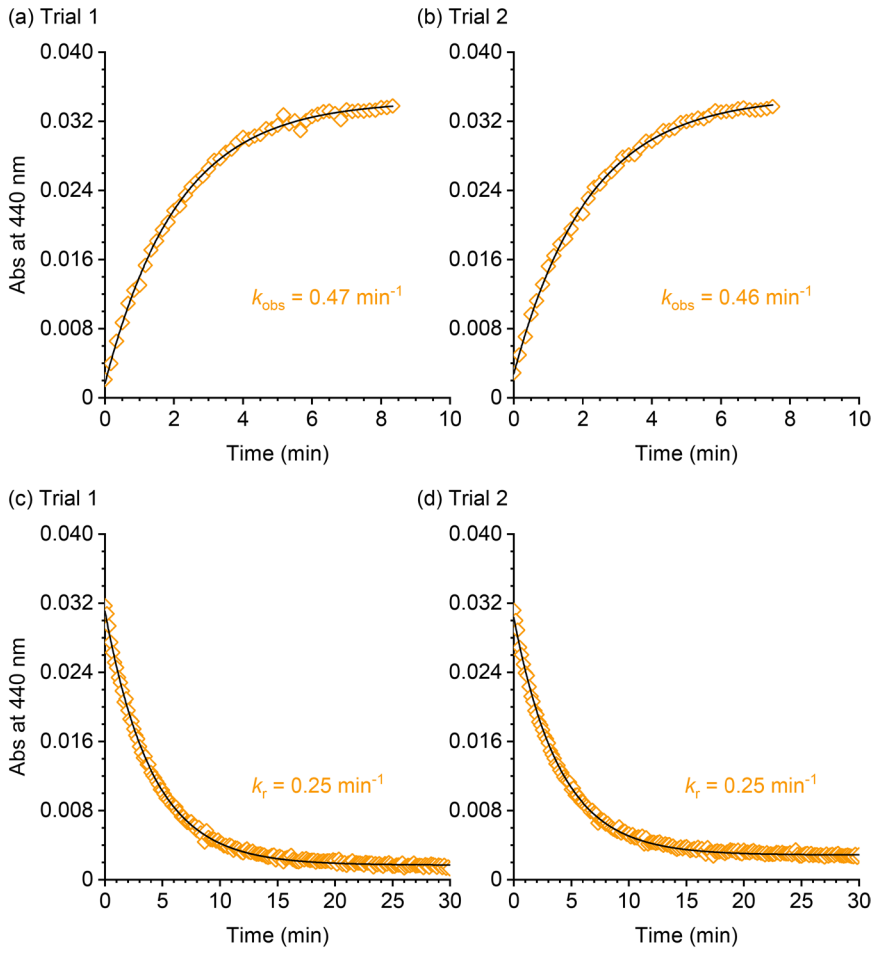

Figure S1.10. Ultrasound-induced mechanical activation of **3*H*-PMA** (2 mg/mL in THF with 30 mM BHT) at –13°C and subsequent thermal reversion at approximately –30 °C, monitored at λ_{max} = 440 nm. (a,b) The forward reaction occurs with an observed rate constant of k_{obs} = 0.47 min^{-1} averaged over two replicate experiments. (c,d) Thermal reversion of the merocyanine at –30 °C measured from the same polymer solutions after cessation of ultrasound occurs with an average rate constant of k_r = 0.25 min^{-1} corresponding to a half-life of $t_{1/2}$ = 2.8 min. Note that the temperature of the polymer solution quickly equilibrates to approximately –30 °C when the ultrasound is turned off (see Figure S1.6).

General Procedure for Photoirradiation Experiments. Absorption spectra of photochemically generated merocyanines were measured at room temperature (~20 °C) by exposing a solution of the polymer (2.0 mg/mL in THF) in a two-sided quartz cuvette to a UV light source (λ = 311 nm) positioned ~2 inches away for 60 s. The cuvette was immediately placed into the spectrometer and the absorption spectrum was collected. To

monitor thermal reversion of photochemically generated merocyanines at –13 °C, an identical procedure as the one used for sonication experiments was employed with continuous flow and synchronous UV-vis measurements, except a 20% ethanol/ethylene glycol dry ice bath maintained at −30 ± 2 °C was used to cool the reaction vessel containing the polymer solution. The temperature of the solution inside the reaction vessel equilibrated to –13 °C as measured by a thermocouple inserted into the solution (Digi-Sense EW-91428-02 thermometer with Digi-Sense probe EW-08466-83). The solution was exposed to a UV light source (λ = 311 nm) positioned ~3.5 inches away for 2 min, and then the thermal reversion of the photochemically generated merocyanine was monitored by UV-vis absorption spectroscopy. The entire system was kept under an inert atmosphere in the dark for the duration of the experiment.

VIII. Kinetic Analysis

Determination of reaction kinetics from UV-vis spectroscopy. The kinetics of the ring-opening reaction under sonication, or thermal ring-closure after sonication or UV irradiation, was evaluated by fitting time-dependent absorbance traces monitored at λ_{max} to expressions of first-order kinetics using OriginPro 2020. Data corresponding to product formation is fit to eq S1.1:

$$A(t) = A(1 - e^{-kt}) + c \tag{S1.1}$$

For characterizing the rate of thermal ring-closure, the time-dependent absorbance signal is fit to eq S1.2:

$$A(t) = A(e^{-kt}) + c \tag{S1.2}$$

^{1}H and ^{13}C NMR Spectra

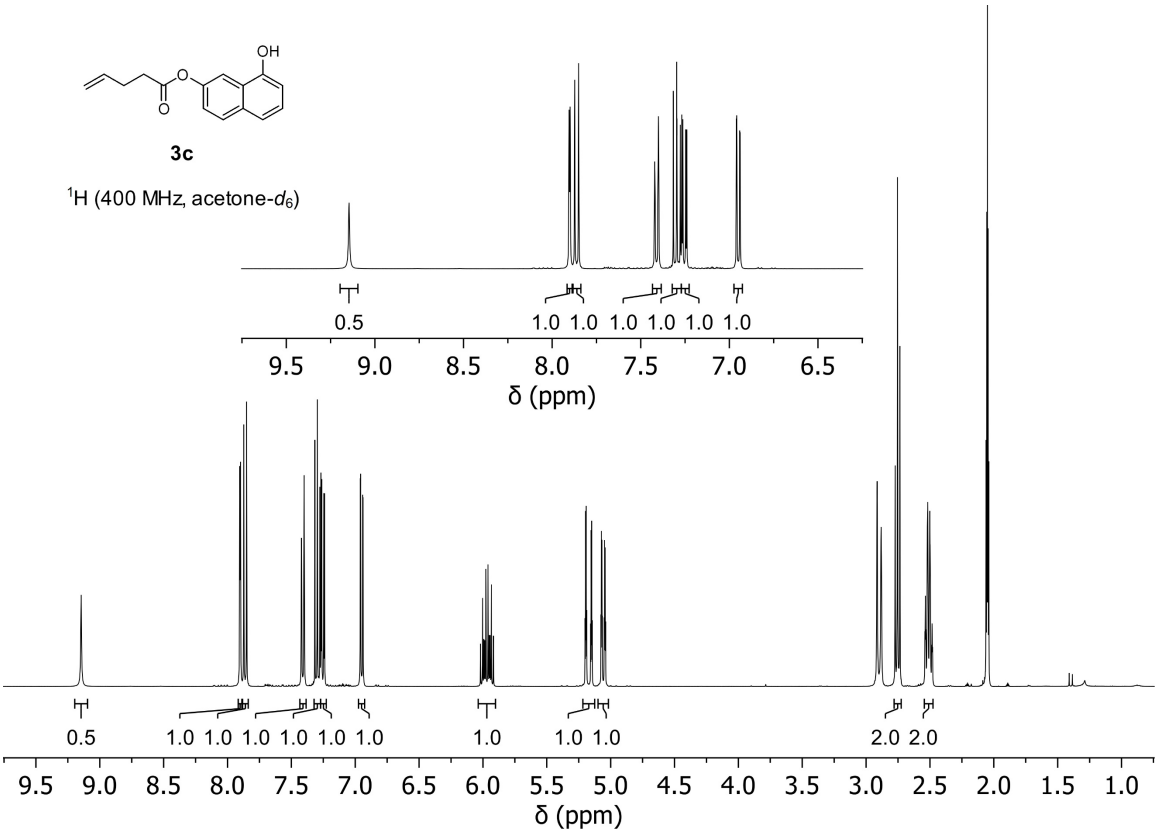

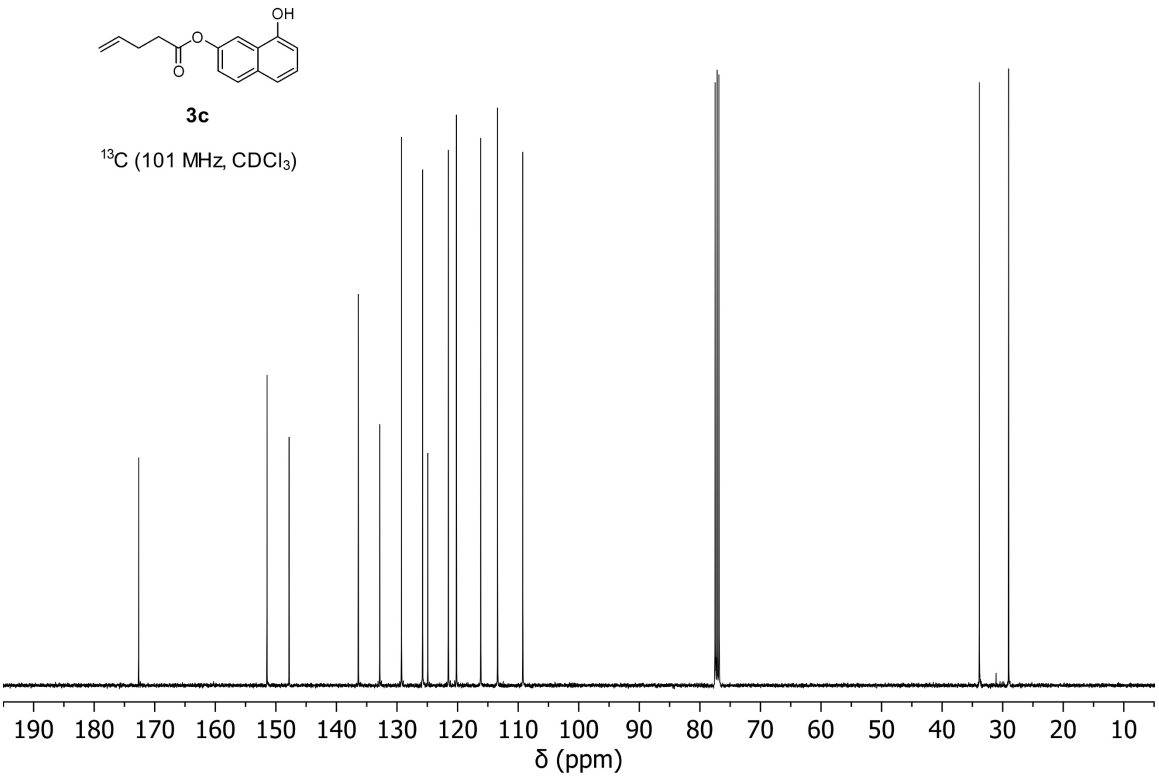

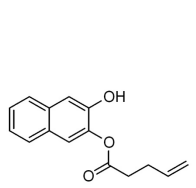

3d

^{1}H (400 MHz, $CDCl_3$)

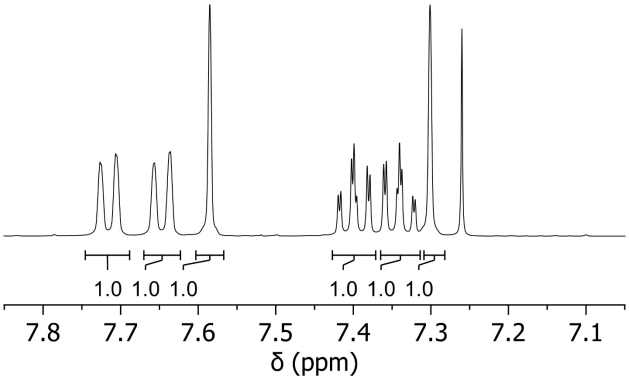

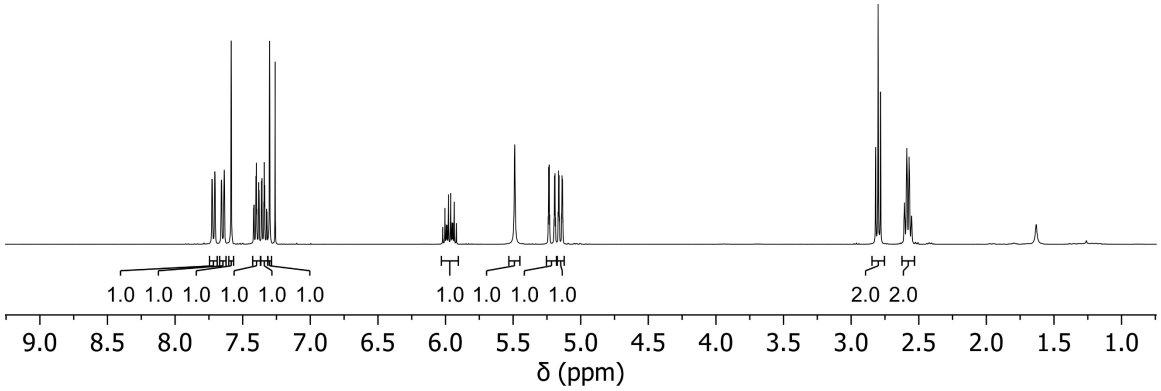

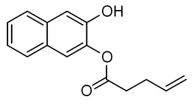

3d

^{13}C (101 MHz, $CDCl_3$)

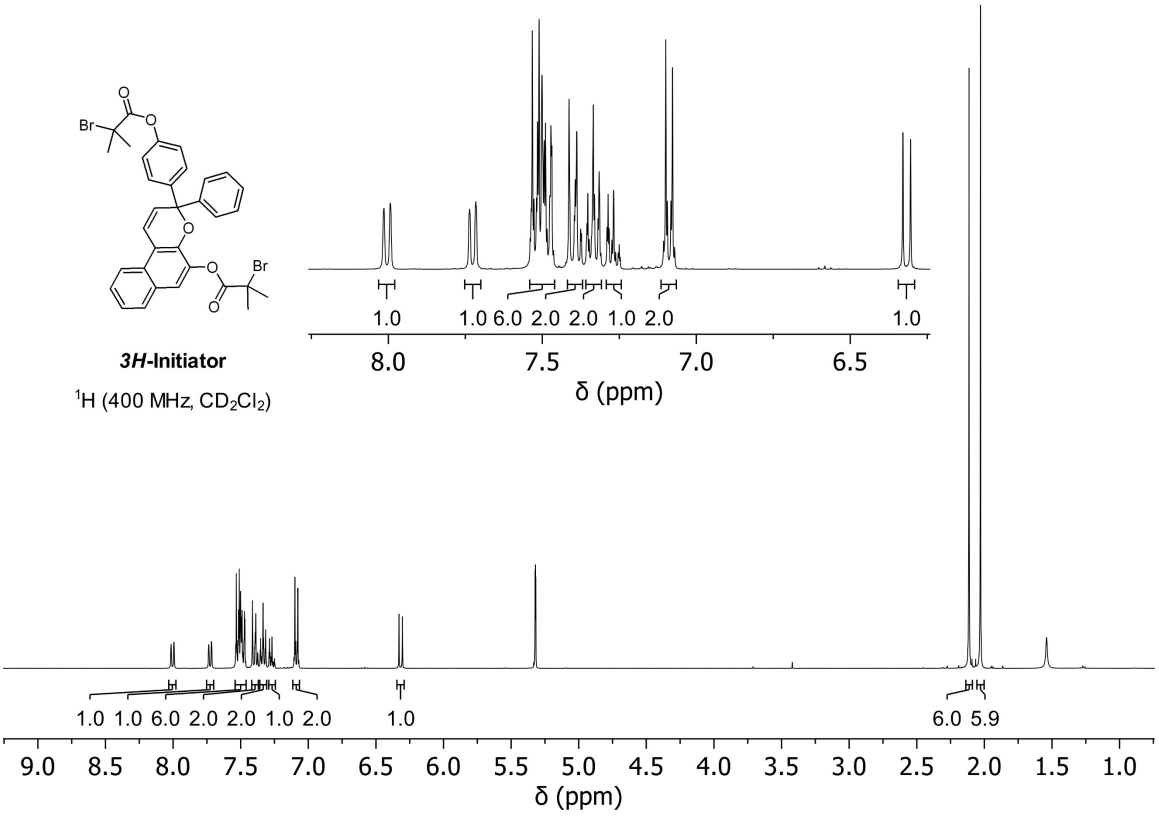

***3H*-Initiator**

^{1}H (400 MHz, CD_2Cl_2)

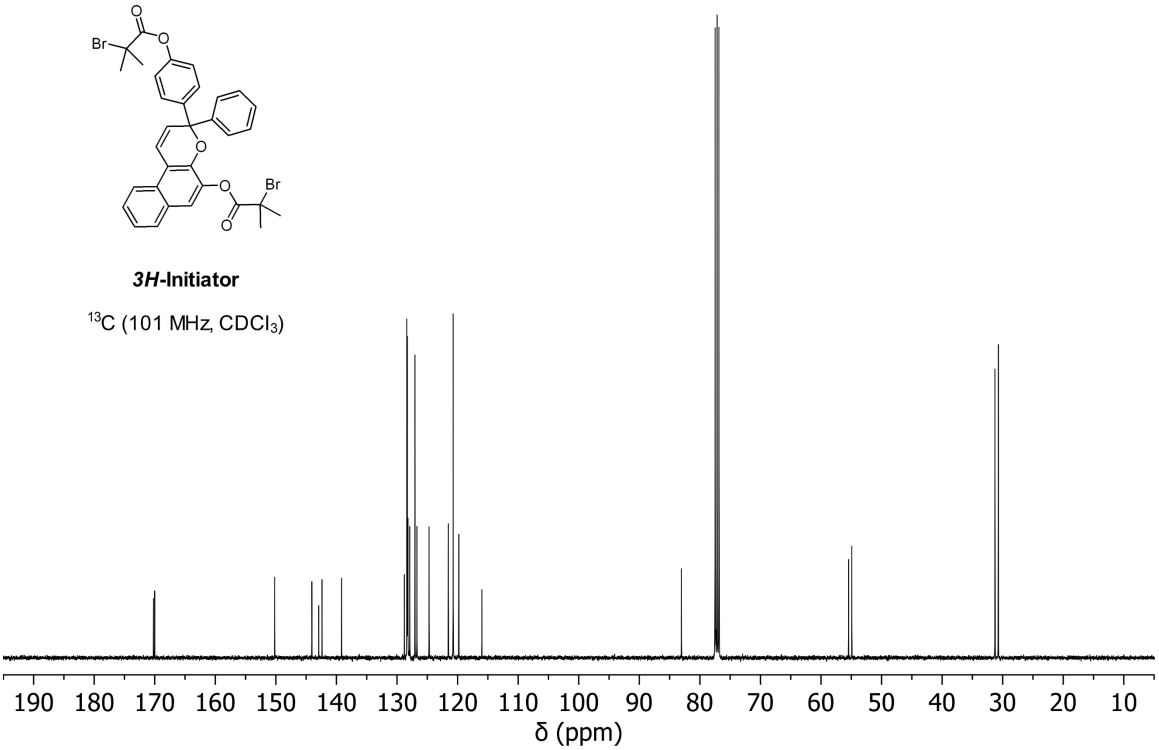

***3H*-Initiator**

^{13}C (101 MHz, $CDCl_3$)

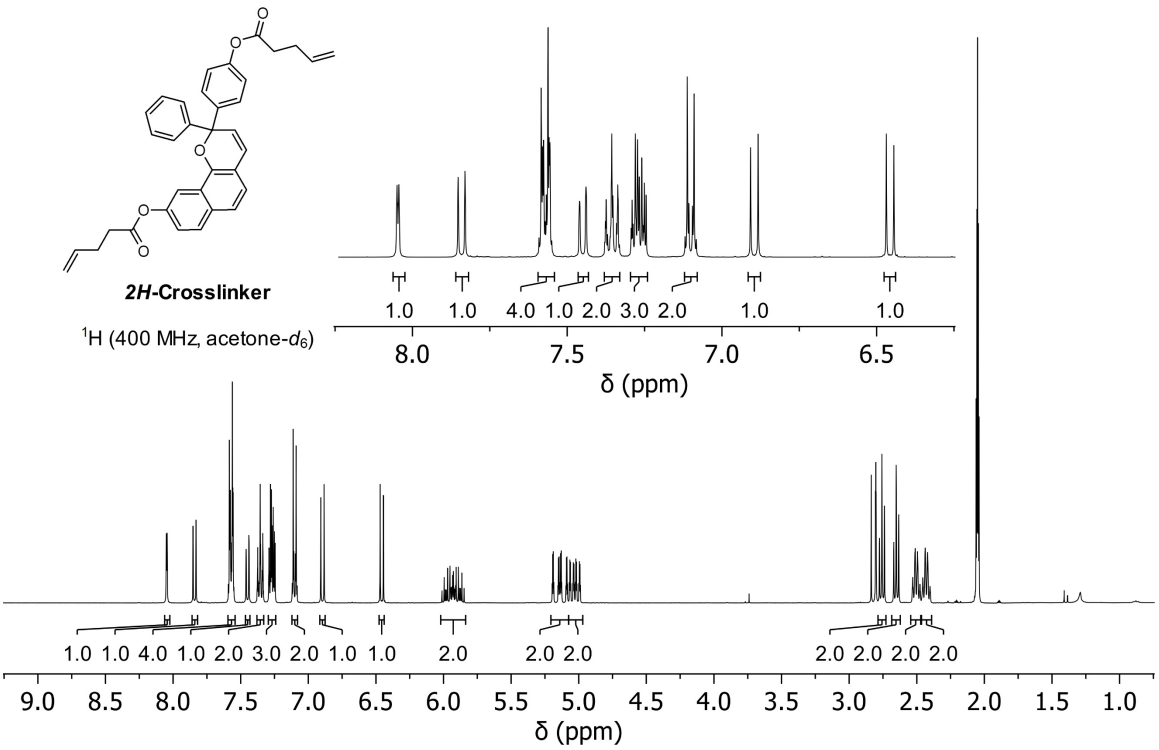
2H-Crosslinker
1H (400 MHz, acetone-d6)
1.0 1.0 4.0 1.0 2.0 3.0 2.0 1.0 1.0
8.0 7.5 7.0 6.5
δ (ppm)
1.0 1.0 4.0 1.0 2.0 3.0 2.0 1.0 1.0 2.0 2.0 2.0 2.0 2.0 2.0 2.0
9.0 8.5 8.0 7.5 7.0 6.5 6.0 5.5 5.0 4.5 4.0 3.5 3.0 2.5 2.0 1.5 1.0
δ (ppm)

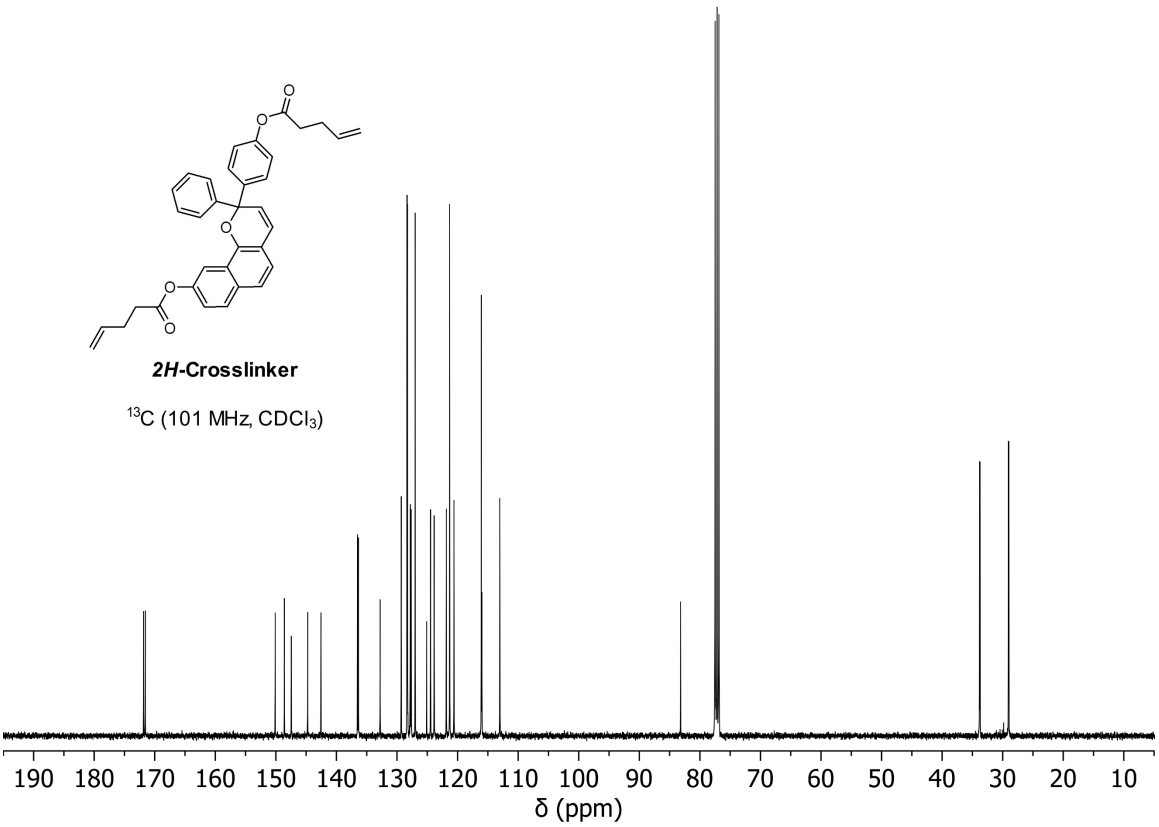
2H-Crosslinker
13C (101 MHz, CDCl3)
190 180 170 160 150 140 130 120 110 100 90 80 70 60 50 40 30 20 10
δ (ppm)

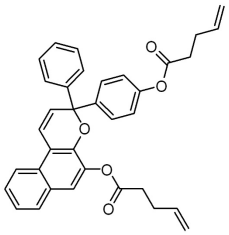

***3H*-Crosslinker**

^{1}H (400 MHz, CD_2Cl_2)

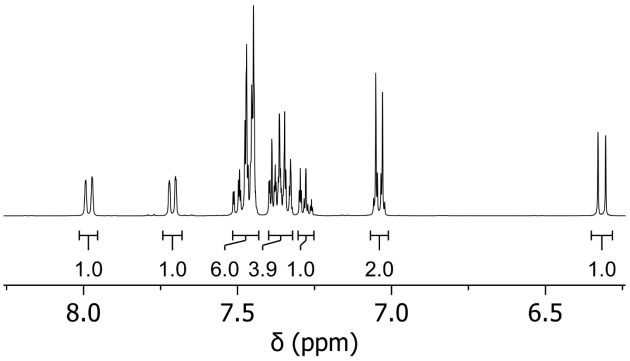

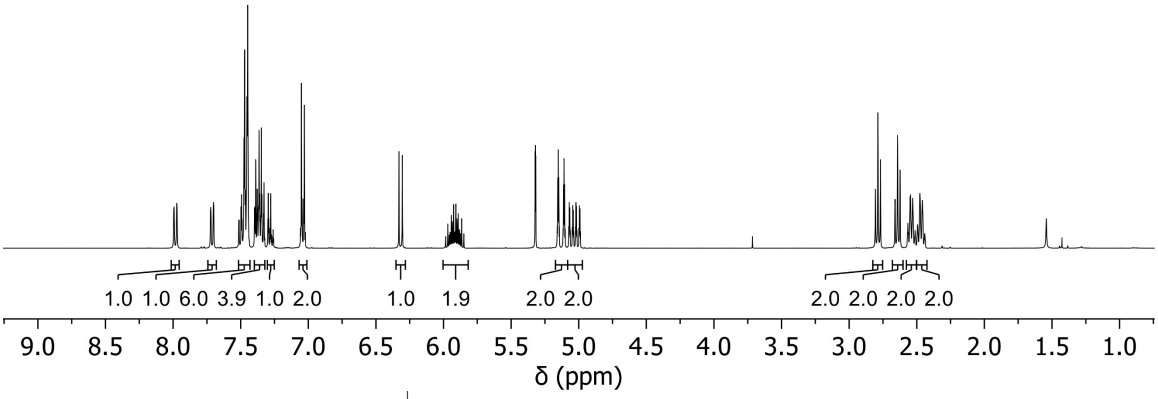

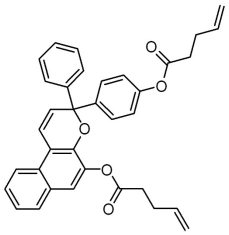

***3H*-Crosslinker**

^{13}C (101 MHz, $CDCl_3$)

References

(1) Hepworth, J. D.; Heron, B. M. Photochromic Naphthopyrans. In *Functional Dyes*; Elsevier, 2006; pp 85–135.

(2) Nigel Corns, S.; Partington, S. M.; Towns, A. D. Industrial Organic Photochromic Dyes. *Color. Technol.* **2009**, *125*, 249–261.

(3) Robb, M. J.; Kim, T. A.; Halmes, A. J.; White, S. R.; Sottos, N. R.; Moore, J. S. Regioisomer-Specific Mechanochromism of Naphthopyran in Polymeric Materials. *J. Am. Chem. Soc.* **2016**, *138*, 12328–12331.

(4) Kim, G.; Lau, V. M.; Halmes, A. J.; Oelze, M. L.; Moore, J. S.; Li, K. C. High-Intensity Focused Ultrasound-Induced Mechanochemical Transduction in Synthetic Elastomers. *Proc. Natl. Acad. Sci. U.S.A.* **2019**, *116*, 10214–10222.

(5) McFadden, M. E.; Robb, M. J. Force-Dependent Multicolor Mechanochromism from a Single Mechanophore. *J. Am. Chem. Soc.* **2019**, *141*, 11388–11392.

(6) McFadden, M. E.; Robb, M. J. Generation of an Elusive Permanent Merocyanine via a Unique Mechanochemical Reaction Pathway. *J. Am. Chem. Soc.* **2021**, *143*, 7925–7929.

(7) Kosuge, T.; Zhu, X.; Lau, V. M.; Aoki, D.; Martinez, T. J.; Moore, J. S.; Otsuka, H. Multicolor Mechanochromism of a Polymer/Silica Composite with Dual Distinct Mechanophores. *J. Am. Chem. Soc.* **2019**, *141*, 1898–1902.

(8) Versaw, B. A.; McFadden, M. E.; Husic, C. C.; Robb, M. J. Designing Naphthopyran Mechanophores with Tunable Mechanochromic Behavior. *Chem. Sci.* **2020**, *11*, 4525–4530.

(9) Davis, D. A.; Hamilton, A.; Yang, J.; Cremar, L. D.; Van Gough, D.; Potisek, S. L.; Ong, M. T.; Braun, P. V.; Martínez, T. J.; White, S. R.; Moore, J. S.; Sottos, N. R. Force-Induced Activation of Covalent Bonds in Mechanoresponsive Polymeric Materials. *Nature* **2009**, *459*, 68–72.

(10) Zhang, H.; Gao, F.; Cao, X.; Li, Y.; Xu, Y.; Weng, W.; Boulatov, R. Mechanochromism and Mechanical-Force-Triggered Cross-Linking from a Single Reactive Moiety Incorporated into Polymer Chains. *Angew. Chem. Int. Ed.* **2016**, *55*, 3040–3044.

(11) Wang, Z.; Ma, Z.; Wang, Y.; Xu, Z.; Luo, Y.; Wei, Y.; Jia, X. A Novel Mechanochromic and Photochromic Polymer Film: When Rhodamine Joins Polyurethane. *Adv. Mat.* **2015**, *27*, 6469–6474.

(12) Wang, T.; Zhang, N.; Dai, J.; Li, Z.; Bai, W.; Bai, R. Novel Reversible Mechanochromic Elastomer with High Sensitivity: Bond Scission and Bending-Induced Multicolor Switching. *ACS Appl. Mater. Interfaces* **2017**, *9*, 11874–11881.

(13) Qian, H.; Purwanto, N. S.; Ivanoff, D. G.; Halmes, A. J.; Sottos, N. R.; Moore, J. S. Fast, Reversible Mechanochromism of Regioisomeric Oxazine Mechanophores: Developing In Situ Responsive Force Probes for Polymeric Materials. *Chem.* **2021**, *7*, 1080–1091.

(14) Göstl, R.; Sijbesma, R. P. π-Extended Anthracenes as Sensitive Probes for Mechanical Stress. *Chem. Sci.* **2016**, *7*, 370–375.

(15) Baumann, C.; Stratigaki, M.; Centeno, S. P.; Göstl, R. Multicolor Mechanofluorophores for the Quantitative Detection of Covalent Bond Scission in Polymers. *Angew. Chem. Int. Ed.* **2021**, *60*, 13287–13293.

(16) Imato, K.; Irie, A.; Kosuge, T.; Ohishi, T.; Nishihara, M.; Takahara, A.; Otsuka, H. Mechanophores with a Reversible Radical System and Freezing-Induced Mechanochemistry in Polymer Solutions and Gels. *Angew. Chem. Int. Ed.* **2015**, *54*, 6168–6172.
(17) Imato, K.; Kanehara, T.; Ohishi, T.; Nishihara, M.; Yajima, H.; Ito, M.; Takahara, A.; Otsuka, H. Mechanochromic Dynamic Covalent Elastomers: Quantitative Stress Evaluation and Autonomous Recovery. *ACS Macro Lett.* **2015**, *4*, 1307–1311.
(18) Gemert, B. V.; Kumar, A.; Knowles, D. B. Naphthopyrans. Structural Features and Photochromic Properties. *Mol. Cryst. Liq. Cryst.* **1997**, *297*, 131–138.
(19) Kumar, A.; Van Gemert, B.; Knowles, D. B. Color Tunability in Photochromic Naphthopyrans. *Mol. Cryst. Liq. Cryst.* **2000**, *344*, 217–222.
(20) Zhao, W.; Carreira, E. M. Facile One-Pot Synthesis of Photochromic Pyrans. *Org. Lett.* **2003**, *5*, 4153–4154.
(21) Nguyen, N. H.; Rosen, B. M.; Lligadas, G.; Percec, V. Surface-Dependent Kinetics of Cu(0)-Wire-Catalyzed Single-Electron Transfer Living Radical Polymerization of Methyl Acrylate in DMSO at 25 °C. *Macromolecules* **2009**, *42*, 2379–2386.
(22) Beyer, M. K. The Mechanical Strength of a Covalent Bond Calculated by Density Functional Theory. *J. Chem. Phys.* **2000**, *112*, 7307–7312.
(23) Klein, I. M.; Husic, C. C.; Kovács, D. P.; Choquette, N. J.; Robb, M. J. Validation of the CoGEF Method as a Predictive Tool for Polymer Mechanochemistry. *J. Am. Chem. Soc.* **2020**, *142*, 16364–16381.
(24) Jockusch, S.; Turro, N. J.; Blackburn, F. R. Photochromism of 2 *H* -Naphtho[1,2-b]pyrans: A Spectroscopic Investigation. *J. Phys. Chem. A* **2002**, *106*, 9236–9241.
(25) Berkowski, K. L.; Potisek, S. L.; Hickenboth, C. R.; Moore, J. S. Ultrasound-Induced Site-Specific Cleavage of Azo-Functionalized Poly(ethylene glycol). *Macromolecules* **2005**, *38*, 8975–8978.
(26) Caruso, M. M.; Davis, D. A.; Shen, Q.; Odom, S. A.; Sottos, N. R.; White, S. R.; Moore, J. S. Mechanically-Induced Chemical Changes in Polymeric Materials. *Chem. Rev.* **2009**, *109*, 5755–5798.
(27) Li, J.; Nagamani, C.; Moore, J. S. Polymer Mechanochemistry: From Destructive to Productive. *Acc. Chem. Res.* **2015**, *48*, 2181–2190.
(28) May, P. A.; Munaretto, N. F.; Hamoy, M. B.; Robb, M. J.; Moore, J. S. Is Molecular Weight or Degree of Polymerization a Better Descriptor of Ultrasound-Induced Mechanochemical Transduction? *ACS Macro Lett.* **2016**, *5*, 177–180.
(29) Gossweiler, G. R.; Hewage, G. B.; Soriano, G.; Wang, Q.; Welshofer, G. W.; Zhao, X.; Craig, S. L. Mechanochemical Activation of Covalent Bonds in Polymers with Full and Repeatable Macroscopic Shape Recovery. *ACS Macro Lett.* **2014**, *3*, 216–219.
(30) Yang, J.; Horst, M.; Werby, S. H.; Cegelski, L.; Burns, N. Z.; Xia, Y. Bicyclohexene-*peri* -naphthalenes: Scalable Synthesis, Diverse Functionalization, Efficient Polymerization, and Facile Mechanoactivation of Their Polymers. *J. Am. Chem. Soc.* **2020**, *142*, 14619–14626.

Chapter 2

Mechanochemical Reactivity of a Multimodal 2*H*-Bis-Naphthopyran Mechanophore

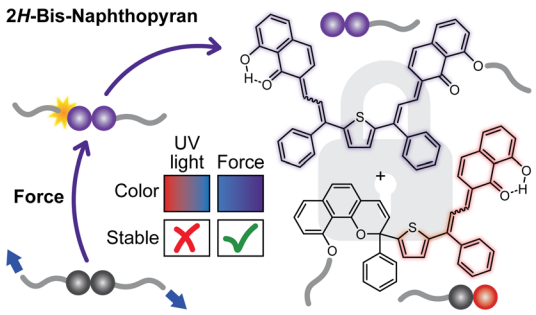

This chapter has been adapted with permission from Osler, S.K.; McFadden, M. E.; Zeng, T.; Robb, M. J. Mechanochemical Reactivity of a Multimodal 2*H*-Bis-Naphthopyran Mechanophore. *Polym. Chem.* **2023**, *14*, 2717–2723. DOI: 10.1039/d3py00344b

Abstract

Multimodal mechanophores that react under mechanical force to produce discrete product states with uniquely coupled absorption properties are interesting targets for the design of force-sensing polymers. Herein, we investigate the reactivity of a 2H-bis-naphthopyran mechanophore that generates thermally persistent mono-merocyanine and bis-merocyanine products upon mechanical activation in solution using ultrasonication, distinct from the thermally reversible products generated photochemically. We demonstrate that a force-mediated ester C(O)−O bond scission reaction following ring opening establishes an intramolecular hydrogen bond, locking one merocyanine subunit in the open form. Model compound studies suggest that this locked subunit confers remarkable thermal stability to

bis-merocyanine isomers possessing a trans exocyclic alkene on the other subunit, implicating the formation of an unusual trans merocyanine isomer as the product of mechanochemical activation. Density functional theory calculations unexpectedly predict a thermally reversible retro-cyclization reaction of the bis-merocyanine species that could explain the mechanochemical generation of the unusual trans merocyanine isomer.

Introduction

Naphthopyrans are a class of molecular switches that undergo a ring-opening reaction upon photochemical or mechanochemical activation to generate a highly colored merocyanine dye. While the photochemical reactivity of naphthopyran has been studied extensively,[1] the mechanochemical reactivity of naphthopyran has only recently been investigated within the nascent field of polymer mechanochemistry.[2–9] Mechanical force is transduced to naphthopyrans covalently incorporated into polymers by the application of stress to bulk materials,[2–5] or by solution-phase ultrasonication,[6–9] leading to merocyanine formation. Naphthopyran is thus a versatile mechanochromic force probe capable of reporting on stress and/or strain colorimetrically. Interestingly, the mechanochemical

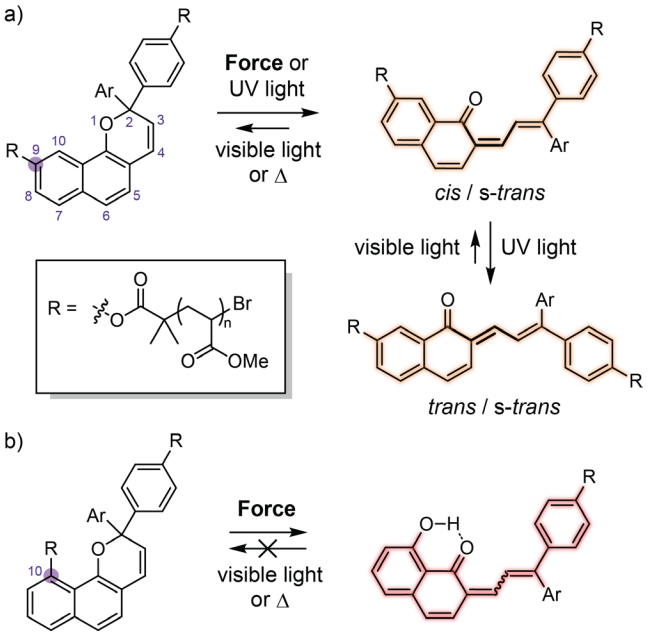

Scheme 2.1. Reactions of 2*H*-naphthopyran-containing poly(methyl acrylate) polymers and the structures of the merocyanine dyes produced upon mechanochemical or photochemical activation.

reactivity of naphthopyran mechanophores often diverges from their photochemical behavior.[6,7,9]

Extended UV photoirradiation of naphthopyrans generates a mixture of merocyanine isomers with *cis* and *trans* alkene geometry at the exocyclic olefin (Scheme 2.1a).[10–19] Merocyanines with *trans* exocyclic olefin geometry are more thermally stable, while the *cis* isomers readily revert to the naphthopyran under ambient conditions. In contrast to the photochemical reactions, the thermal reversion behavior of most mechanochemically generated naphthopyran-derived merocyanines suggests that only the isomer with *cis* stereochemistry of the exocyclic alkene is produced using force.[2–8] Recently, our group discovered a 2*H*-naphthopyran mechanophore scaffold that generates a persistent merocyanine dye after mechanical activation (Scheme 2.1b).[7] Rather than *cis–trans* isomerization, a unique intramolecular hydrogen bonding mechanism is implicated in the persistent color generation whereby the scission of a C(O)–O ester bond following pyran ring opening establishes a β-hydroxy ketone that prevents merocyanine reversion.

Mechanochromic mechanophores possessing multiple reactive sites are theoretically capable of a more complex colorimetric response, accessing distinct states under mechanical force that are coupled to unique changes in optical properties.[20] For example, a bis-naphthopyran mechanophore previously developed in our group displays force-dependent multicolor mechanochromism due to a force-modified dynamic equilibrium that is established between two different merocyanine states.[6] In contrast to the photochemical reaction, which proceeds via sequential ring-opening reactions of each pyran unit,[21–24] mechanical activation was found to simultaneously open both pyran rings to generate the bis-merocyanine species. Because the mono-merocyanine product is formed via thermal reversion, increasing the

amount of force applied to the mechanophore increases the rate of bis-merocyanine formation relative to mono-merocyanine and shifts the relative distribution of the two distinctly colored dyes. Naphthodipyran[9] and diketopyrrolopyrrole[25,26] mechanophores also display multicolor mechanochromism under force; however, the dyes produced from these mechanophores are either transient and revert to their original state after stress is removed, or require a trapping agent for persistent color generation. In bulk materials, spiropyran[27,28] and rhodamine[29] mechanophores have been shown to generate uniquely colored states under active tension and after stress relaxation. Notably, mechanophores that display multicolor mechanochromism and generate persistent coloration remain limited.[26,30]

We were interested in exploring the mechanochromism of a bis-naphthopyran mechanophore potentially capable of generating persistent coloration via the same intramolecular hydrogen bonding mechanism associated with the 2*H*-naphthopyran mechanophore described above (Scheme 2.2). In analogy to our previously studied 3*H*-bis-naphthopyran mechanophore,[6] we imagined that the two pyran rings of a 2*H*-bis-naphthopyran (2*H*-BNP) mechanophore would open simultaneously upon ultrasound-induced mechanical activation to generate bis-merocyanine **2*H*-BNP$_{oo}$** (open–open), followed by rapid

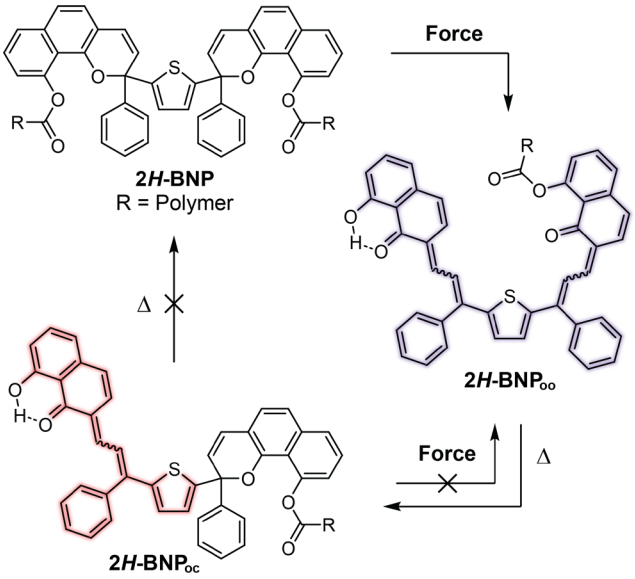

Scheme 2.2. The anticipated mechanochemical reactivity of 2*H*-BNP wherein mechanical force induces a dual ring-opening reaction accompanied by ester scission leading to a transient bis-merocyanine intermediate (2*H*-BNP$_{oo}$), which thermally reverts to form a stable mono-merocyanine dye (2*H*-BNP$_{oc}$).

scission of a C(O)–O ester bond on one of the merocyanine units. This bond cleavage would position the mechanophore at the end of the polymer chain, precluding further mechanochemical reaction.[31] The merocyanine unit with an intact ester linkage would be expected to undergo a thermal ring-closing reaction to produce persistent mono-merocyanine **2*H*-BNP$_{oc}$** (open–closed). Here, we study the mechanochemical reactivity of this 2*H*-BNP mechanophore in dilute polymer solutions using ultrasonication. While mechanical activation results in the anticipated ring-opening reactions accompanied by ester cleavage, the reactivity is unexpectedly complex. A multifaceted experimental and computational approach provides insights into the unusual reactivity of this 2*H*-BNP mechanophore.

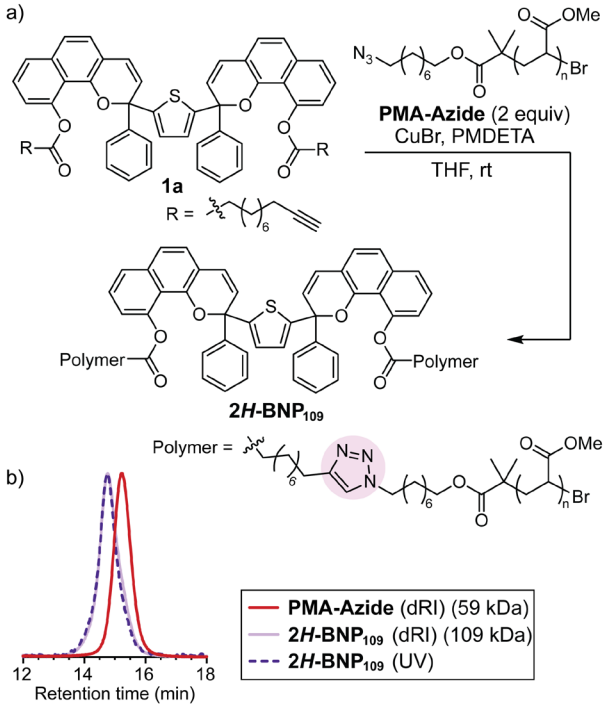

Figure 2.1. Synthesis and characterization of **2*H*-BNP$_{109}$**. (a) Synthesis of a poly(methyl acrylate) polymer (109 kDa, $Đ$ = 1.17) containing a chain-centered 2*H*-bis-naphthopyran mechanophore unit via CuAAC. (b) Characterization by GPC-MALS with differential refractive index (dRI) and in-line UV detection (345 nm) confirms 2*H*-bis-naphthopyran functionalization near the chain center.

Results and Discussion

We investigated the mechanochemical reactivity of the 2*H*-BNP mechanophore through solution-phase ultrasonication experiments.[31,32] Polymer attachment at the 10-position of each naphthopyran subunit is critical to form the persistent hydrogen-bonded merocyanine dye.[7] Polymer **2*H*-BNP$_{109}$** (M_n = 109 kDa, $Đ$ = 1.17) was synthesized by a Cu(I)-catalyzed

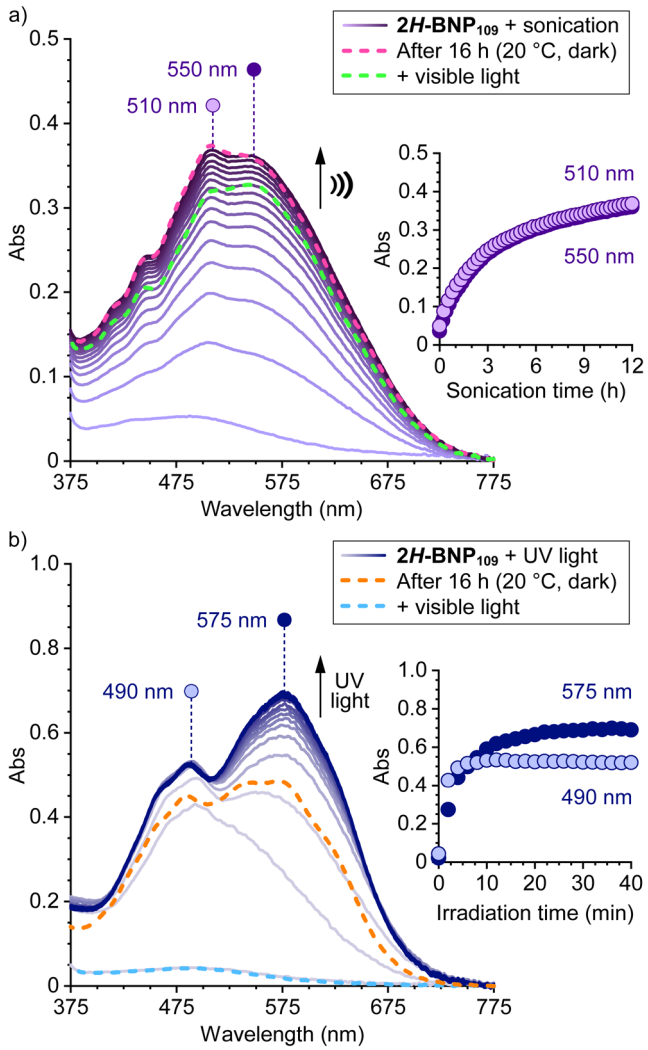

Figure 2.2. Ultrasonication and photoirradiation experiments performed on **2*H*-BNP$_{109}$**. (a) Ultrasound-induced mechanochemical activation (12 h, 20 °C) of **2*H*-BNP$_{109}$** generates a product mixture with absorption maxima at approximately 510 and 550 nm. After incubation at 20 °C for 16 h in the dark, the spectrum remains essentially unchanged. Irradiation with 565 nm light (150 min) results in minimal bleaching. (b) Photoirradiation of **2*H*-BNP$_{109}$** with 365 nm UV light (40 min, 20 °C) generates a product mixture with absorption maxima at ~490 and 575 nm. Some attenuation of the absorbance is observed after 16 h in the dark (20 °C). Irradiation with 565 nm light (180 min) results in nearly complete bleaching. Insets show time-dependent absorbance at the specified wavelengths.

azide-alkyne cycloaddition (CuAAC) reaction between bis-alkyne **1a** and two equivalents of azide-terminated poly(methyl acrylate) (PMA) polymer **PMA-Azide** (M_n = 59 kDa, $Đ$ = 1.10) (Figure 2.1a).[33] Characterization by GPC-MALS with in-line UV absorption detection confirmed that the 2*H*-BNP mechanophore was incorporated near the chain-center where mechanical force is maximized (Figure 2.1b).[31,34,35]

To investigate the mechanochemical activation of the 2*H*-BNP mechanophore, a solution of **2*H*-BNP$_{109}$** (2 mg/mL in THF containing 30 mM BHT) maintained at ~20 °C was subjected to continuous ultrasonication (20 kHz, 8.2 W/cm^2) for 12 h (see Experimental Details section). Generation of colored merocyanine products was monitored

by synchronous UV-vis absorption spectroscopy using a continuous flow setup.[6,36] Ultrasound-induced mechanochemical activation of **2*H*-BNP$_{109}$** produces an absorption spectrum with two local maxima at 510 and 550 nm (Figure 2.2a). The absorption spectrum of the mechanochemical reaction products remains essentially unchanged 16 h after the cessation of ultrasound, indicating that mechanical activation produces a thermally persistent merocyanine species. Extended irradiation with intense visible light (565 nm, 150 min) causes a slight attenuation of the absorption features, but does not induce significant bleaching (Figure S2.6), consistent with the formation of a permanent merocyanine dye locked via an intramolecular H-bonding interaction.[7] To our surprise, however, even the longer wavelength absorption features attributed to the bis-merocyanine are largely persistent under these conditions, indicating the presence of an unusually stable bis-merocyanine species. Notably, the simultaneous cleavage of both C(O)–O ester linkages is unlikely. Thus, this persistent bis-merocyanine species likely contains a single intact ester group on one merocyanine subunit, consistent with the structure of **2*H*-BNP$_{oo}$** shown in Scheme 2.2. The slight attenuation of the absorption spectrum after irradiation with visible light is consistent with *trans*-to-*cis* isomerization of the exocyclic alkene in the merocyanine subunit containing the intramolecular H-bond (Figures S2.7 and S2.8, see the ESI for additional details).[12] Control experiments demonstrate that the absorption spectrum generated from photochemical activation of **2*H*-BNP$_{109}$** is distinct from the spectrum obtained during sonication experiments (Figure 2.2b and Figure S2.9). Furthermore, in contrast to the products of mechanochemical activation, the colored species produced under UV light undergo significant reversion under ambient conditions and completely revert to the colorless state upon irradiation with visible light. Together, these data suggest that the thermally

persistent species produced upon ultrasound-induced mechanochemical activation of **2*H*-BNP$_{109}$** are neither the expected mono-merocyanine locked by an intramolecular H-bond, nor the bis-merocyanine product with two intact ester linkages.

To identify the persistent mechanochemical product(s) of **2*H*-BNP$_{109}$** activation, small molecule model compound **M1** was synthesized and characterized by ^{1}H NMR and UV-vis absorption spectroscopy (Figure 2.3). Consistent with prior studies of a related 2*H*-naphthopyran mechcanophore,[7] deprotection of the 10-hydroxyl group on the bis-naphthopyran precursor results in spontaneous thermal equilibration to the mono-merocyanine form. Characteristic proton resonances in the 13–14 ppm region of the ^{1}H NMR spectrum of **M1** are attributed to the hydrogen-bonded OH proton (H^a) on various merocyanine stereoisomers

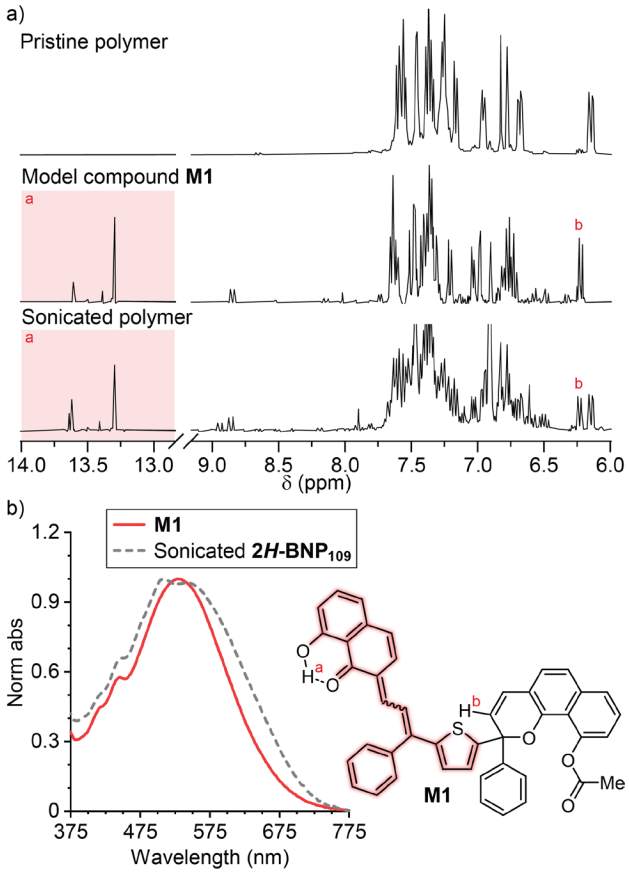

Figure 2.3. Characterization of sonicated **2*H*-BNP$_{109}$**. (a) Characteristic resonances in the ^{1}H NMR (THF-d_8, 400 MHz) spectrum of model compound **M1** are also observed in the product mixture generated from ultrasound-mediated mechanical activation of **2*H*-BNP$_{109}$**. (b) The absorption spectrum generated during the sonication of **2*H*-BNP$_{109}$** is not consistent with pristine **M1**. The long wavelength feature is bathochromically shifted from the absorption maximum of **M1**.

(Figure 3.3a). These diagnostic signals are also observed in the ^{1}H NMR spectrum of **2*H*-BNP$_{109}$** after ultrasonication. The intact pyran ring on the naphthopyran subunit of **M1** is

identified by a doublet at 6.40 ppm (H^b, J = 9.5 Hz). This resonance is also observed in the ^{1}H NMR spectrum of **2*H*-BNP$_{109}$** after ultrasound-induced mechanical activation, along with a pair of overlapping doublets at 6.14 and 6.15 ppm (J = 9.6 Hz) corresponding to pyran protons of residual unreacted **2*H*-BNP**. While signatures of the mono-merocyanine species with a single β-hydroxy ketone motif are clearly visible in the ^{1}H NMR spectrum of **2*H*-BNP$_{109}$** after ultrasonication, further analysis by NMR spectroscopy is obscured by overlapping peaks in the aromatic region. The UV-vis absorption spectrum of **M1** contains a single peak with a maximum at 530 nm, which is notably distinct from the spectrum obtained after mechanochemical activation of **2*H*-BNP$_{109}$** (Figure 2.3b). The absorption spectrum acquired after sonication of **2*H*-BNP$_{109}$** has an absorption edge that is bathochromically shifted from that of **M1**, further suggesting that the sonication product mixture contains a persistent bis-merocyanine species with longer wavelength absorption in addition to mono-merocyanine isomers.

Further structural elucidation of the mechanochemical product mixture was achieved by photochemical activation of model compound **M1** to generate the bis-merocyanine species. A solution of **M1** (0.01 mg/mL in THF) was irradiated with UV light (365 nm, 8 min) at 20 °C using the same analytical flow setup as above (Figure 2.4a). Immediately following

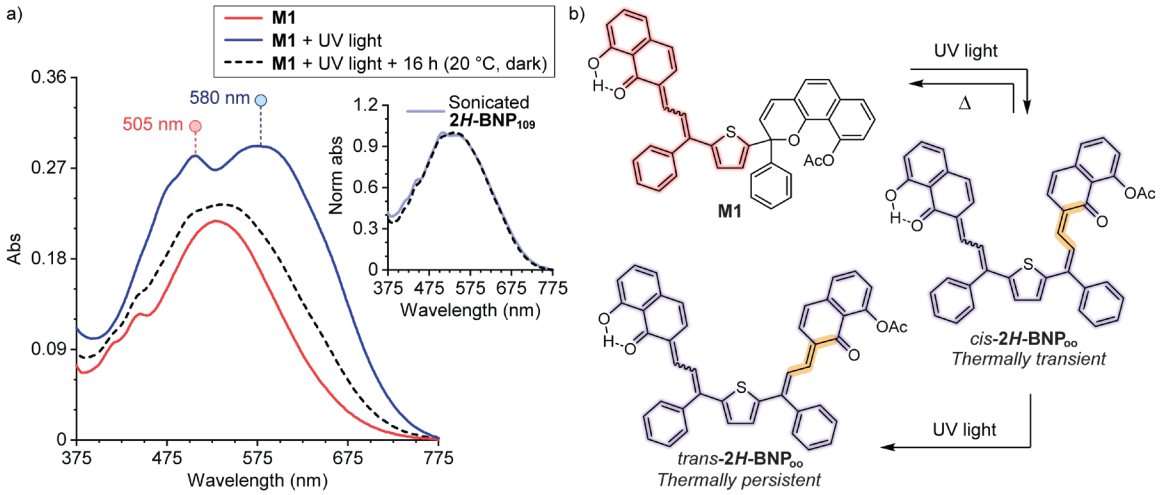

Figure 2.4. Photoirradiation of model compound **M1**. (a) Photoirradiation of **M1** with UV light (345 nm, 8 min) results in a bathochromic shift in absorption with maxima at 505 and 580 nm. Upon cessation of photoirradiation and 16 h in the dark (20 °C), the spectrum evolves to closely match the final absorption spectrum obtained upon sonication of **2*H*-BNP$_{109}$** (inset). (b) Reaction scheme illustrating the formation of a mixture of thermally transient and persistent bis-merocyanine isomers with *cis* and *trans* exocyclic alkene geometry on the ester-containing subunit upon exposure of **M1** to UV light.

photoirradiation, the absorption spectrum exhibits two local maxima at 505 and 580 nm. This extended UV irradiation generates a substantial amount of bis-merocyanine, resulting in significant absorption in the longer wavelength region. However, after an extended period under ambient conditions in the dark (16 h, 20 °C), the absorption spectrum evolves to ultimately match that obtained from ultrasonication of polymer **2*H*-BNP$_{109}$** (Figure 2.4a, inset). Partial retention of the longer wavelength absorption features suggests that photoirradiation of **M1** generates a mixture of thermally transient and thermally persistent bis-merocyanine isomers (Figure 2.4b). We identify the thermally transient bis-merocyanine species as having *cis* exocyclic alkene geometry on the merocyanine unit with an intact ester linkage at the 10-position (*cis*-**2*H*-BNP$_{oo}$**).[18] The thermally persistent bis-merocyanine species is attributed to isomers with *trans* exocyclic alkene geometry on the merocyanine subunit with an intact ester linkage at the 10-position (*trans*-**2*H*-BNP$_{oo}$**). Increasing exposure of **M1** to UV light results in a greater proportion of thermally persistent *trans*-**2*H*-BNP$_{oo}$**,

consistent with the expected photochemical *cis*-to-*trans* isomerization of the exocyclic alkene (Figure S2.10).[18,19] Visible light irradiation is known to accelerate *trans*-to-*cis* isomerization, which must occur before electrocyclization to regenerate the naphthopyran.[11,12,18,19] However, photochemical activation of **M1** produces products that do not bleach appreciably under visible light, similar to the mechanochemically-generated products of **2*H*-BNP$_{109}$** (Figure S2.11). On the other hand, complete reversion of photochemically produced merocyanines is possible using visible light when both ester linkages at the 10-position are intact (Figure 2.2b). These results suggest that the unique persistence of ***trans*-2*H*-BNP$_{oo}$** relies on having one merocyanine subunit locked in the open form via the intramolecular hydrogen bond.

The results presented above indicate that the photochemical activation of **M1** and the mechanochemical activation of **2*H*-BNP$_{109}$** generate similar product mixtures. An important implication is that the mechanochemical ring-opening reaction of the 2*H*-BNP mechanophore produces a mixture of bis-merocyanine isomers with both *cis* and *trans* geometry of the exocyclic alkene on the merocyanine subunit with an intact ester linkage at the 10-position. For typical naphthopyran-derived merocyanines, thermal *cis*-to-*trans* isomerization of the exocyclic alkene is rare.[16,19] As discussed above, the mechanochemical generation of merocyanines with a *trans* exocyclic olefin is unusual from naphthopyran mechanophores. Consistent with the mechanical activation of **2*H*-BNP$_{109}$**, sonication experiments performed on analogous polymers with lower (**2*H*-BNP$_{44}$**: M_n = 44 kDa, $Đ$ = 1.25) and higher (**2*H*-BNP$_{317}$:** M_n = 317 kDa, $Đ$ = 1.17) molar mass result in product mixtures with similar absorption maxima at 510 and 550 nm, suggesting that the ratio of mechanically-generated *cis* and *trans* merocyanine products is not force-dependent (Figure

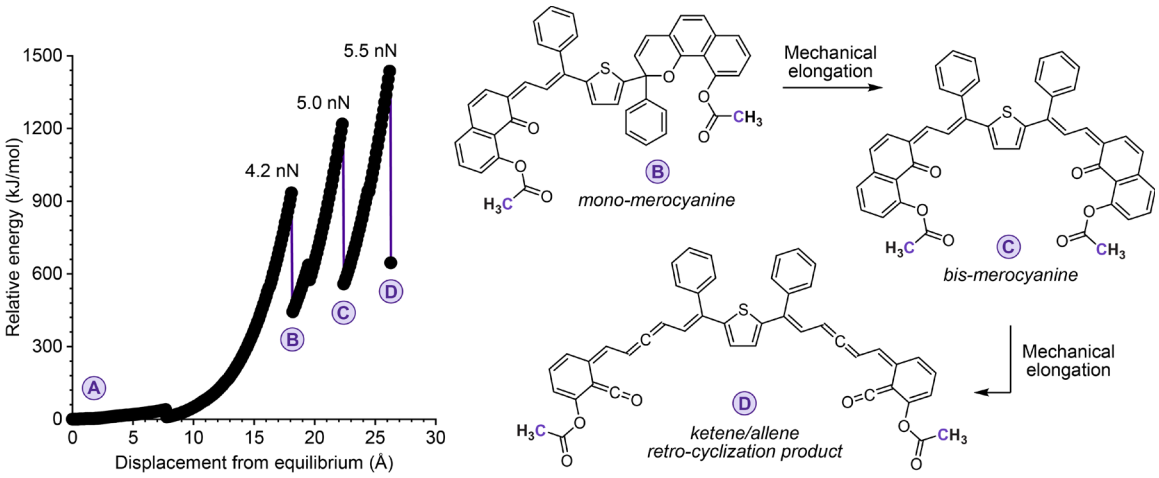

Figure 2.5. Density functional theory (DFT) calculations using the constrained geometries simulate external force (CoGEF) method performed on a truncated model of **2*H*-BNP** predict an unusual retro-cyclization reaction upon extended mechanical elongation to generate two sets of ketene and allene motifs. Structures are shown that correspond to the computed products of pyran ring opening (B and C) and the retro-cyclization reaction (D) on the CoGEF profile. Calculations were performed at the B3LYP/6-31G* level of theory. The purple carbon atoms of the terminal methyl groups define the distance constraint.

S2.12 and S2.13).[37] Notably, low-temperature sonication of **2*H*-BNP$_{317}$** results in the detectable accumulation of a thermally transient bis-merocyanine species due to the increased reaction rate,[36] confirming that mechanical activation of 2*H*-BNP does generate ***cis*-2*H*-BNP$_{oo}$** in addition to the thermally persistent *trans* isomers analogous to the photochemical pathway illustrated in Figure 3.4b (Figure S2.14).

Density functional theory (DFT) calculations using the constrained geometries simulate external force (CoGEF) method[38,39] performed on a truncated model offer an intriguing explanation for the unique mechanochemical generation of merocyanine isomers from 2*H*-BNP that possess a *trans* alkene in the ester-containing subunit (Figure 2.5). Molecular elongation first results in the expected ring-opening reactions to form the bis-merocyanine product; however, extended elongation does not result in the C(O)–O ester bond scission that

was observed previously for the analogous 2*H*-naphthopyran.[7] Instead, a retro-cyclization reaction is predicted to occur simultaneously on both merocyanine subunits to generate two sets of ketene and allene moieties. Electrocyclic ketene-forming reactions have been reported under thermal[40] and photochemical[41,42] conditions, providing some precedent for this unusual transformation. If such a retro-cyclization reaction occurs in practice, the species would be predicted to undergo rapid thermal cyclization[42] upon chain relaxation to regenerate a mixture of merocyanines with *cis* and *trans* exocyclic alkene geometry. Notably, this unusual retro-cyclization reaction is not predicted by CoGEF for a 2*H*-BNP model with ester groups at the 9-position of the two naphthopyran subunits (Figure S2.15). Consistent with these computational predictions, ultrasonication experiments performed on a polymer containing a chain-centered 2*H*-BNP mechanophore connected at the 9-position via ester linkages on each subunit does not generate any thermally persistent merocyanine isomers (Figure S2.16).

Conclusions

In summary, we have investigated the mechanochemical reactivity of a 2*H*-bis-naphthopyran mechanophore (2*H*-BNP). Instead of the expected force-dependent multicolor mechanochromism, which is predicated on a dynamic equilibrium involving the thermal reversion of the bis- merocyanine product,[6] we find that ultrasound-induced mechanochemical activation of 2*H*-BNP results in an unexpectedly persistent bis-merocyanine species. Scission of a C(O)–O ester bond at the 10-position on one naphthopyran subunit establishes an intramolecular hydrogen bond that locks one merocyanine subunit open. In contrast to previously reported naphthopyran mechanophores that appear to exclusively produce the *cis* merocyanine product upon ring opening, mechanical activation of 2*H*-BNP generates a mixture of merocyanine isomers with *cis* and

trans geometry of the exocyclic alkene on the merocyanine subunit with an intact ester linkage. Supported by small molecule model studies, the bis-merocyanine isomers with a *trans* exocyclic alkene on the ester-containing subunit are thermally persistent and resist bleaching under visible light irradiation. Density functional calculations implicate an unusual, thermally reversible mechanochemical retro-cyclization reaction of the bis-merocyanine species that is plausibly responsible for the formation of the *trans* merocyanine isomer, rather than a direct mechanically facilitated *cis*-to-*trans* isomerization. Efforts within our group are currently underway to experimentally probe the possibility of this unusual transformation.

Acknowledgements

Financial support from Caltech and an NSF CAREER award (CHE-2145791) is gratefully acknowledged. S.K.O. was supported by an Institute Fellowship from Caltech. M.E.M. was supported by an NSF Graduate Research Fellowship (DGE- 1745301) and a Barbara J. Burger Fellowship. We thank the Center for Catalysis and Chemical Synthesis of the Beckman institute at Caltech for access to equipment. M.J.R. is an Alfred P. Sloan Research Fellow and a Camille Dreyfus Teacher-Scholar.

Experimental Details

I. General Experimental Details

Reagents from commercial sources were used without further purification unless otherwise stated. Methyl acrylate was passed through a short plug of basic alumina to remove inhibitor immediately prior to use. Copper wire was soaked in 1 M HCl for 10 min and then rinsed consecutively with water, acetone, and dichloromethane immediately prior to use. Dry THF was obtained from a Pure Process Technology solvent purification system. All reactions were performed under a N_2 atmosphere unless specified otherwise. Column chromatography was performed on a Biotage Isolera system using SiliCycle SiliaSep HP flash cartridges.

NMR spectra were recorded using either a 400 MHz Bruker Avance III HD with Prodigy Cryoprobe or a 600 MHz Varian spectrometer with 5 mm triple resonance inverse probe. All ^{1}H NMR spectra are reported in δ units, parts per million (ppm), and were measured relative to the signals for residual chloroform (7.26 ppm), acetone (2.05 ppm), dichloromethane (5.32 ppm), THF (3.58 ppm), or benzene (7.16 ppm) in deuterated solvent. All ^{13}C NMR spectra were measured in deuterated solvents and are reported in ppm relative to the signals for chloroform (77.16 ppm), acetone (206.26 ppm), or dichloromethane (53.84 ppm). Multiplicity and qualifier abbreviations are as follows: s = singlet, d = doublet, t = triplet, m = multiplet, br = broad, app = apparent.

High resolution mass spectra (HRMS) were obtained from a Waters Corp. LCT Premier XE time-of-flight mass spectrometer equipped with an electrospray ionization (ESI) probe, a JEOL JMS-600H magnetic sector mass spectrometer equipped with a FAB+ probe, or via direct injection on an Agilent 1260 Infinity II Series HPLC coupled to a 6230 LC/TOF system in electrospray ionization (ESI+) mode.

Analytical gel permeation chromatography (GPC) was performed using an Agilent 1260 series pump equipped with two Agilent PLgel MIXED-B columns (7.5 x 300 mm), an Agilent 1200 series diode array detector, a Wyatt 18-angle DAWN HELEOS light scattering detector, and a Optilab rEX differential refractive index detector. The mobile phase was THF at a flow rate of 1 mL/min. Molecular weights and molecular weight distributions were calculated by light scattering using a dn/dc value of 0.062 mL/g (25 °C) for poly(methyl acrylate).

UV-vis absorption spectra were recorded on a Thermo Scientific Evolution 220 spectrometer.

Ultrasound experiments were performed using a Vibra Cell 505 liquid processor equipped with a 0.5-inch diameter solid probe (part #630-0217), sonochemical adapter (part #830-00014), and a Suslick reaction vessel made by the Caltech glass shop (analogous to vessel #830-00014 from Sonics and Materials). Polymer solutions were continuously sampled for UV-vis analysis using a Cole Parmer Masterflex L/S pump system (item #EW-77912-10) composed of an L/S pump head (part #77390-00) and L/S precision variable speed drive (part #07528-20) using 4x6 mm PTFE tubing (part #77390-60) and a quartz flow-through cell (Starna, part #583.4-Q-10/Z8.5), which was connected using M6-threaded PTFE tubing (Starna, part #M6-SET). Either an ice bath or a Thermo Scientific EK45 Immersion Cooler (part #3281452) was used to maintain a constant temperature bath for sonication experiments. Photoirradiation with UV light was performed using either a DR/9W-UVA 365 nm lamp or a Philips PL-S 9W/01/2P UVB bulb with a narrow emission of 305–315 nm and a peak at 311 nm under ambient conditions unless indicated otherwise. Irradiation with

yellow-green light filtered through a 425 nm bandpass filter was applied to sample solutions using a 565 nm LED (ThorLabs M565L3), driver (ledd1B), and collimator (SM1U25-A).

Compounds **Mono-M1** and **5c** were synthesized following the procedures reported in the literature.[7]

II. Supplementary Figures

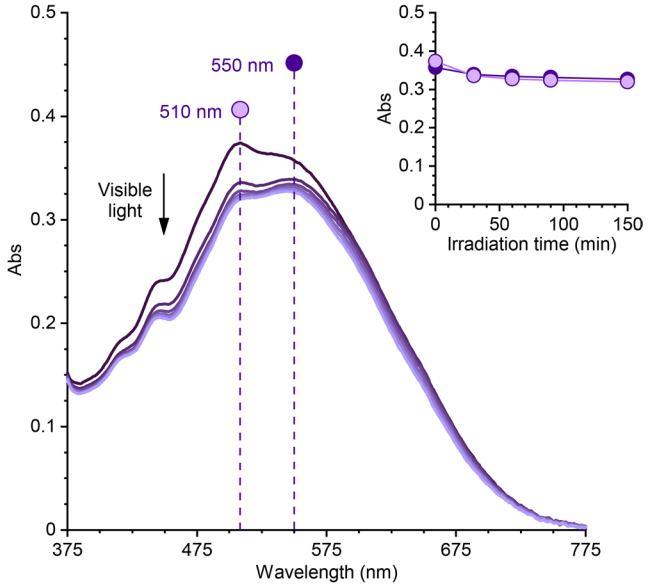

Figure S2.6. Photoirradiation (565 nm visible light) of the final product mixture resulting from mechanochemical activation of **2*H*-BNP$_{109}$** produces minimal bleaching. See Section VII for experimental details.

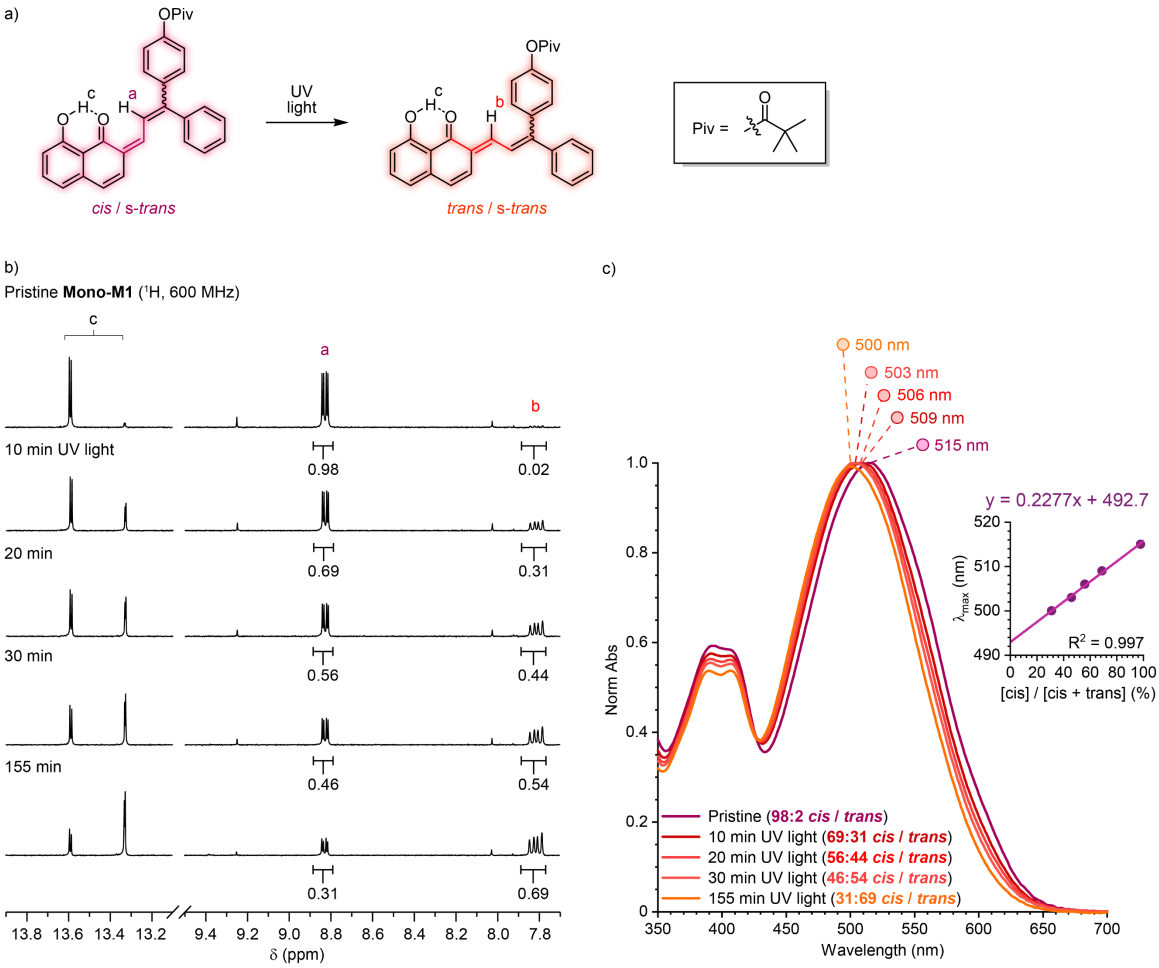

Figure S2.7. Photoirradiation with UV light induces *cis*-to-*trans* isomerization of the exocyclic olefin. (a) Photoirradiation of **Mono-M1** for varying amounts of time with 311 nm UV light results in a different distribution of *cis* and *trans* merocyanine isomers with respect to the exocyclic alkene, as evidenced by (b) ^{1}H NMR (600 MHz, THF-d_8) and (c) UV-vis absorption spectroscopy. There is a linear relationship between the percent *cis* configuration at the exocyclic alkene determined by ^{1}H NMR spectroscopy and the wavelength of the absorption maximum (inset). See Section VIII for details.

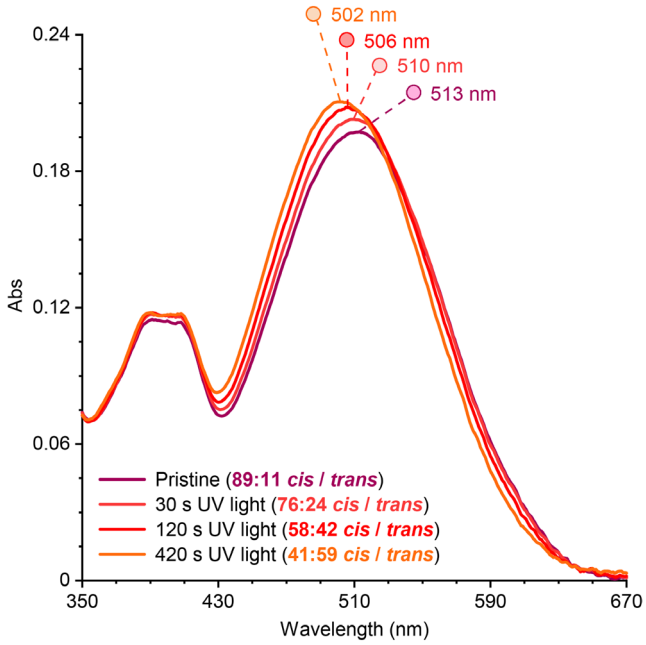

Figure S2.8. UV-vis absorption spectra measured in a sealed cuvette upon varying exposure of a solution of **Mono-M1** (10 μM, THF) to 311 nm UV light. The relative amount of *cis* and *trans* merocyanine isomers was determined using the calibration curve in Figure S2.7. An increase in the relative amount of the *trans* merocyanine isomer is coupled to a hypsochromic shift in λ_{max} and an increase in absorbance due to the higher absorptivity of the *trans* merocyanine isomer. See Section VIII for details.

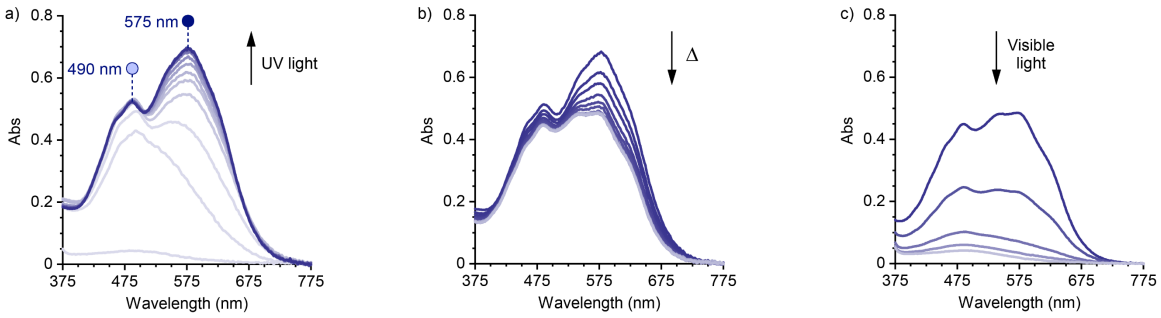

Figure S2.9. UV-vis absorption spectra measured in the flow setup (a) during photoirradiation using 365 nm UV light (40 min) of polymer **2*H*-BNP$_{109}$** (2 mg/mL in THF, 20 °C) and (b) following cessation of photoirradiation in the dark (20 °C, 18 hours). (c) Photoirradiation of the residual thermally persistent product with 565 nm visible light (180 min) results in nearly complete bleaching.

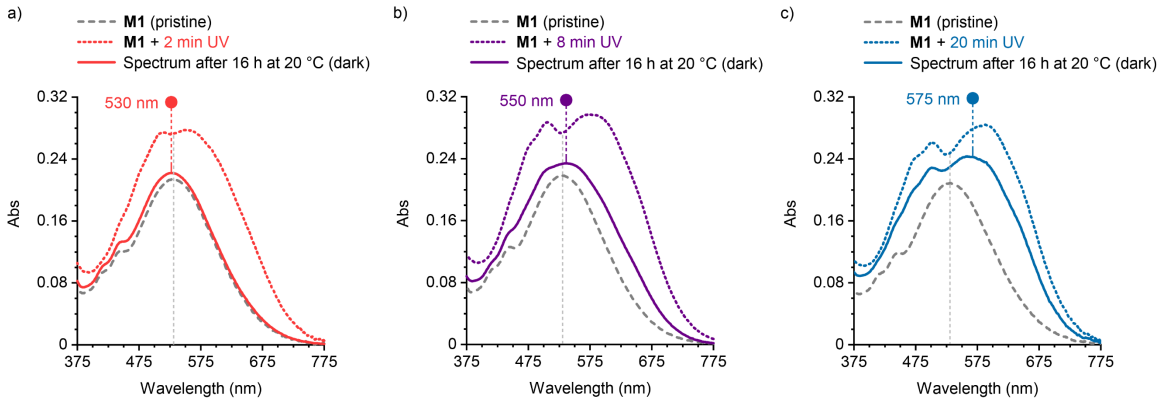

Figure S2.10. UV-vis absorption spectra measured after exposure of three separate solutions of **M1** (0.01 mg/mL in THF, 20 °C) to 365 nm UV light for (a) 2 min, (b) 8 min, or (c) 20 min in the continuous flow setup. Longer exposure to UV light is correlated with a bathochromic shift in the final absorption spectrum following a period in the dark (16 h, 20 °C), indicating the generation of increasing amounts of thermally stable bis-merocyanine isomers.

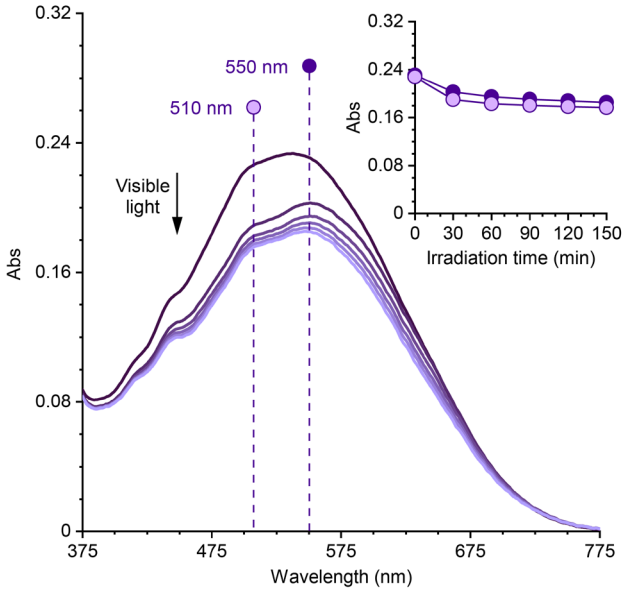

Figure S2.11. Photoirradiation (565 nm visible light) of the final product mixture resulting from photochemical activation of **M1** (365 nm UV light, 8 min) produces minimal bleaching. See section VII for details.

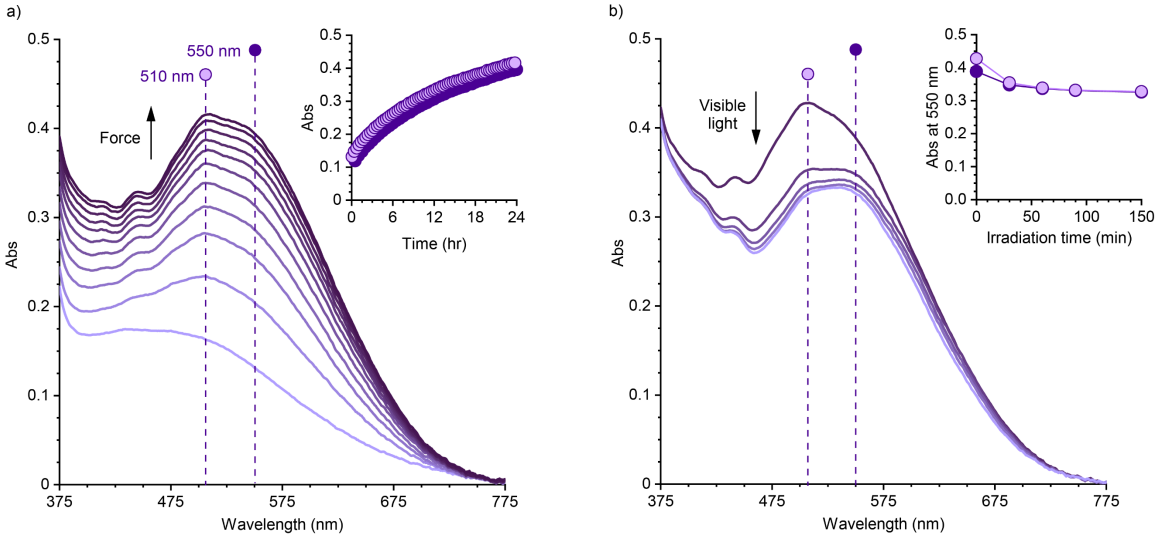

Figure S2.12. Ultrasonication of polymer **2*H*-BNP$_{44}$**. (a) Absorption spectra acquired during ultrasound-induced mechanochemical activation of polymer **2*H*-BNP$_{44}$** with M_n = 44 kDa (24 h sonication at –15 °C, 2 mg/mL in THF containing 30 mM BHT). (b) Photoirradiation of the final mechanochemical product mixture with 565 nm visible light results in minimal bleaching. See section VII for details.

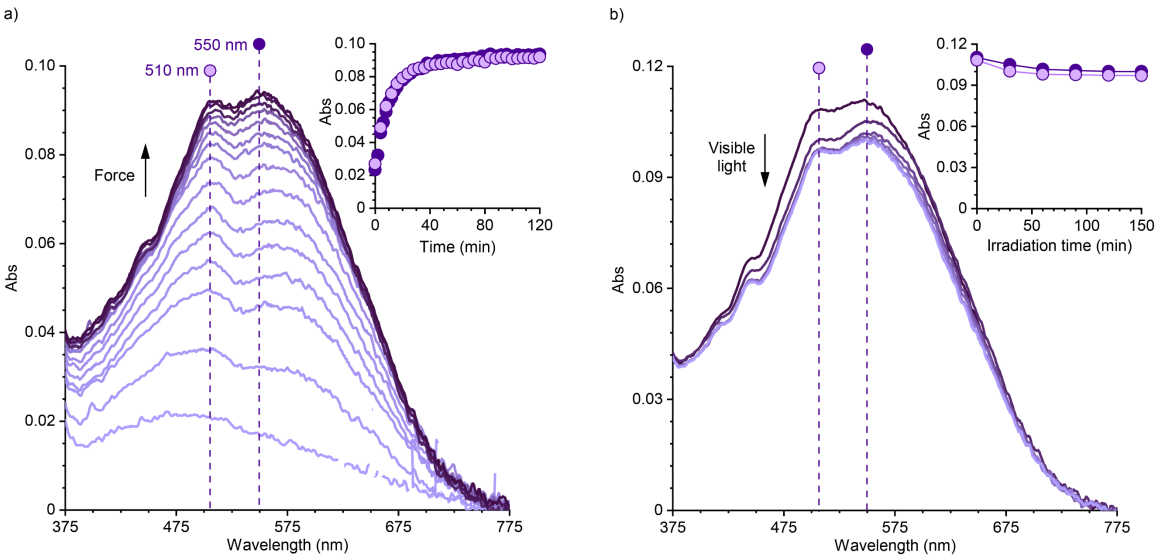

Figure S2.13. Ultrasonication of polymer **2*H*-BNP$_{317}$**. (a) Absorption spectra acquired during ultrasound-induced mechanochemical activation of polymer **2*H*-BNP$_{317}$** with M_n = 317 kDa (2 h sonication at 20 °C, 2 mg/mL in THF containing 30 mM BHT). (b) Photoirradiation of the final mechanochemical product mixture with 565 nm visible light results in minimal bleaching. See section VII for details.

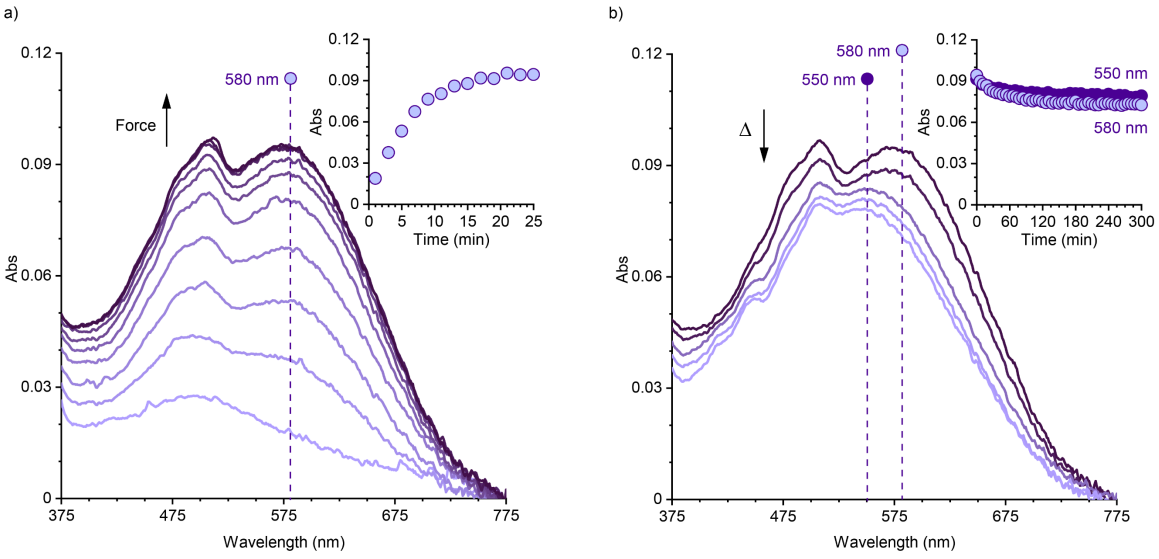

Figure S2.14. Low temperature ultrasonication of polymer **2*H*-BNP$_{317}$**. (a) Absorption spectra acquired during ultrasound-induced mechanochemical activation of **2*H*-BNP$_{317}$** (25 min sonication at –15 °C, 2 mg/mL in THF containing 30 mM BHT). (b) UV-vis absorption spectra measured after cessation of sonication illustrating a slight attenuation of absorbance and a hypsochromic shift of the peak maximum from 580 to 550 nm. See section VII for details.

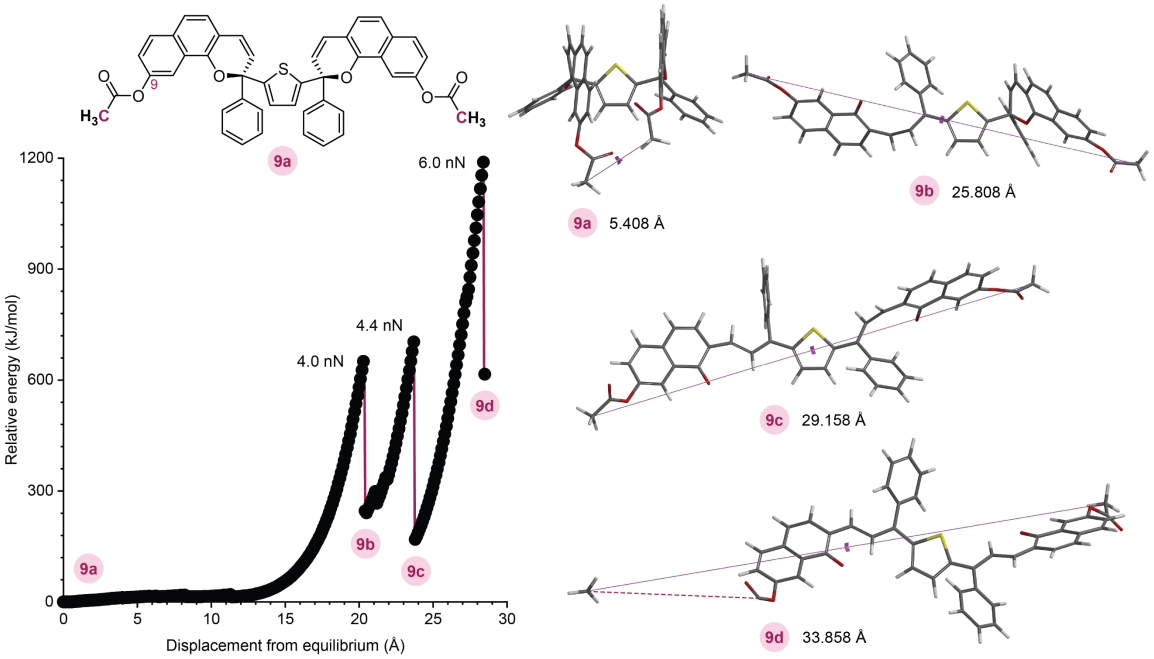

Figure S2.15. Density functional theory (DFT) calculations using the constrained geometries simulate external force (CoGEF) method performed on a truncated model of an analog of the 2*H*-BNP mechanophore with attachment points at the 9-position of each naphthopyran subunit instead of the 10-position. Computed structures are shown at right that correspond to the indicated points in the CoGEF profile along with the associated constraint distance between the terminal methyl groups (pink carbon atoms designate the anchor points defining the distance constraint). The first and second ring-opening reactions are predicted to occur at a maximum force of 4.0 and 4.4 nN, respectively. Scission of a C–C(O) bond of one of the ester groups is predicted to occur with a force of 6.0 nN. Calculations were performed at the B3LYP/6-31G* level of theory.

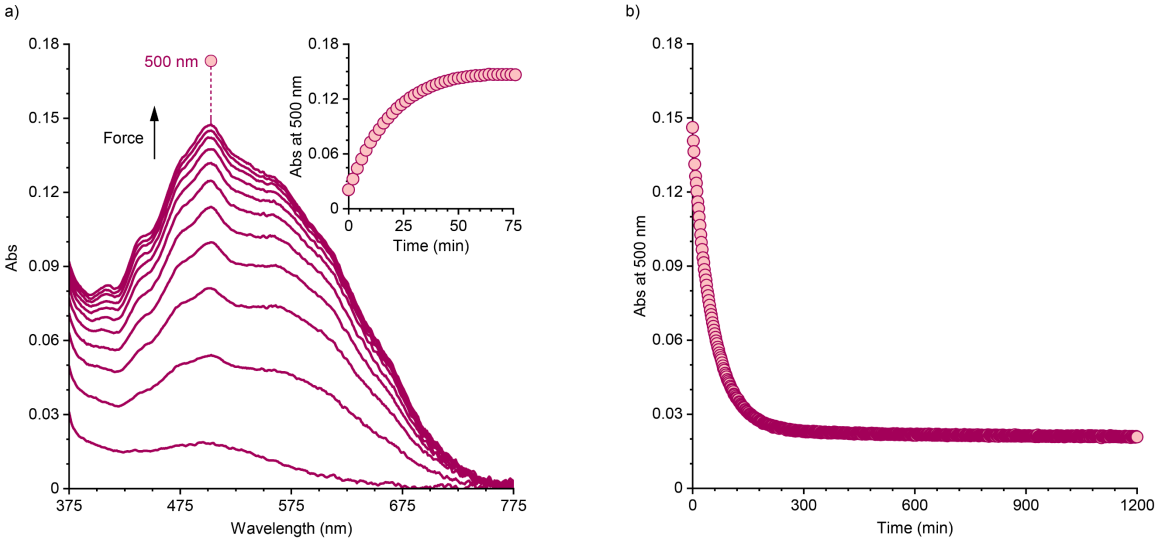

Figure S2.16. Ultrasonication of polymer **(9)-2*H*-BNP$_{104}$**. (a) UV-vis absorption spectra acquired during ultrasound-induced mechanochemical activation of control polymer **(9)-2*H*-BNP$_{104}$** (75 min sonication at –15 °C, 2 mg/mL in THF containing 30 mM BHT). Polymer **(9)-2*H*-BNP$_{104}$** contains polymer attachment points at the 9-position of each naphthopyran subunit. (b) Time-dependent absorbance at 500 nm acquired after cessation of sonication illustrating nearly complete reversion of the mechanically generated merocyanine species, in contrast to the thermally persistent species produced upon mechanical activation of the 2*H*-BNP mechanophore with polymer attachment at the 10-position of each naphthopyran subunit.

III. Synthetic Details

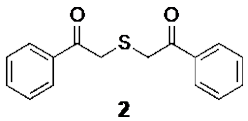

2,2'-Thiobis(1-phenylethan-1-one) (2). A 250 mL two-neck round bottom flask equipped with a stir bar was charged with 2-bromo-1-phenylethan-1-one (11.5 g, 57.8 mmol). The flask was evacuated and backfilled with N_2 (2x), followed by the addition of acetone (125 mL). The solution was cooled to 0 °C in an ice bath and sodium sulfide nonahydrate (7.0 g, 29.0 mmol) in deionized water (15 mL) was added slowly via syringe. The reaction was stirred at 0 °C for 1 h, then warmed to room temperature and stirred for 16 h. The reaction mixture was concentrated under reduced pressure and the resulting aqueous solution was washed with dichloromethane (3 x 150 mL). The organic layers were combined, dried over $MgSO_4$, filtered, and concentrated. The crude material was purified by column chromatography on silica gel (30% EtOAc/hexanes) and subsequently recrystallized from dichloromethane/hexanes to provide the title compound as a pale tan crystalline powder (3.15 g, 40%).

^{1}H NMR (400 MHz, $CDCl_3$) δ: 8.02 – 7.92 (m, 4H), 7.63 – 7.54 (m, 2H), 7.51 – 7.44 (m, 4H), 3.99 (s, 4H).

^{13}C NMR (101 MHz, $CDCl_3$) δ: 194.3, 135.5, 133.7, 128.9, 128.8, 37.7.

TLC (25% EtOAc/hexanes): R_f = 0.50

HRMS (ESI *m/z*): calcd for $[C_{16}H_{15}O_2S]^+$ $(M+H)^+$, 271.0793; found 271.0792.

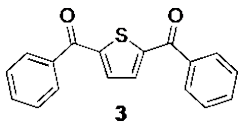

Thiophene-2,5-diylbis(phenylmethanone) (3). A flame-dried 100 mL two-neck round bottom flask equipped with a stir bar and condenser was charged with 2,3-dihydroxy-1,4-dioxane (460 g, 3.83 mmol). The flask was evacuated and backfilled with N_2 (3x), followed by the addition of anhydrous methanol (20

mL). The mixture was heated to reflux for 2 h to generate glyoxal. A separate flame-dried 50 mL round bottom flask equipped with a stir bar was charged with sodium metal (0.170 g, 7.40 mmol) and evacuated/backfilled with N_2 (3x). The flask was cooled to 0 °C in an ice bath and anhydrous methanol (8.5 mL) was added via syringe to form sodium methoxide. The flask containing glyoxal was removed from the heating bath and compound **2** (1.67 g, 6.18 mmol) in anhydrous dichloromethane (5 mL) was added under nitrogen to the warm glyoxal solution via syringe, followed by the dropwise addition of the sodium methoxide solution by syringe. The reaction mixture was returned to reflux (turning dark red) and stirred for 18 h. The reaction was cooled to room temperature, concentrated under reduced pressure, and dissolved in EtOAc (250 mL). The organic layer was washed consecutively with 1 M aqueous HCl (100 mL), deionized water (100 mL), saturated aqueous $NaHCO_3$ (100 mL), 1 M aqueous NaOH (100 mL), and brine (100 mL). The organic layer was dried over $MgSO_4$, filtered, and concentrated under reduced pressure. The crude material was purified by column chromatography on silica gel (5–40% EtOAc/hexanes) and subsequently recrystallized from dichloromethane/hexanes to provide the title compound as off-white crystalline powder (0.879 g, 49%).

^{1}H NMR (400 MHz, $CDCl_3$) δ: 7.94 – 7.89 (m, 4H), 7.68 (s, 2H), 7.67 – 7.61 (m, 2H), 7.56 – 7.50 (m, 4H).

^{13}C NMR (101 MHz, $CDCl_3$) δ: 188.2, 148.6, 137.4, 133.9, 133.1, 129.5, 128.8.

TLC (25% EtOAc/hexanes): R_f = 0.58

HRMS (ESI *m/z*): calcd for $[C_{18}H_{13}O_2S]^+$ $(M+H)^+$, 293.0636; found 293.0631.

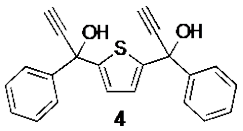

4

1,1'-(Thiophene-2,5-diyl)bis(1-phenylprop-2-yn-1-ol) (4). A flame-dried 500 mL two-neck round bottom flask equipped with a stir bar was evacuated/backfilled with N_2 (3x) and charged with anhydrous THF (50 mL) and ethynyltrimethylsilane (2.84 mL, 20.5 mmol). The flask was cooled to 0 °C in an ice bath and n-butyllithium (2.5 M in hexanes, 7.92 mL, 19.8 mmol) was added dropwise via syringe. The reaction was stirred at 0 °C for 80 min. Compound **3** (2.067 g, 7.07 mmol) in anhydrous THF (30 mL) was added to the reaction mixture via syringe under N_2. The reaction was stirred at 0 °C for 1 h, and then allowed to warm to room temperature. After stirring for 18 h, the solution was cooled to 0 °C in an ice bath and methanol (40 mL) was added to the reaction mixture. The reaction was warmed to room temperature and stirred for 8 h. The reaction mixture was cooled to 0 °C in an ice bath, neutralized by the slow addition of 1 M aqueous HCl, and extracted into EtOAc (300 mL). The organic layer was washed with deionized water (100 mL), saturated aqueous NH_4Cl (300 mL), saturated aqueous $NaHCO_3$ (2 x 300 mL), and brine (150 mL). The organic layer was dried over $MgSO_4$, filtered, and concentrated under reduced pressure. The crude material was purified by column chromatography on silica gel (5–40% EtOAc/hexanes) to give the title compound (mixture of diastereomers) as a colorless crystalline solid (2.22 g, 91%).

^{1}H NMR (400 MHz, $CDCl_3$) δ: 7.68 (dt, *J* = 8.0, 1.6 Hz, 4H), 7.39 – 7.28 (m, 6H), 6.89 (s, 1H), 6.85 (s, 1H), 2.95 (s, 2H), 2.86 (s, 2H).

^{13}C NMR (101 MHz, $CDCl_3$) δ: 150.1, 150.0, 143.4, 143.3, 128.46, 128.45, 128.42, 125.84, 125.78, 125.1, 125.0, 85.6, 85.5, 75.31, 75.28, 71.88, 71.86.

TLC (25% EtOAc/hexanes): R_f = 0.32

HRMS (ESI *m/z*): calcd for $[C_{22}H_{17}O_2S]^+$ $(M-OH)^+$, 327.0838; found 327.0865.

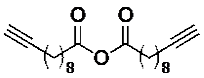

10-Undecynoic anhydride. A flame-dried 100 mL two-neck round bottom flask equipped with a stir was charged with *N*,*N*′-dicyclohexylcarbodiimide (2.95 g, 14.3 mmol) and evacuated/backfilled with N_2 (3x). Anhydrous dichloromethane (25 mL) was added to the flask. A solution of 10-undecynoic acid (5.11 g, 28.0 mmol) in anhydrous dichloromethane (25 mL) under N_2 was added to the reaction flask via syringe. The reaction was stirred at room temperature for 24 h, filtered through a glass frit, and concentrated under reduced pressure to give the title compound as a white solid (4.81 g, 99%). The crude material was carried forward without further purification.

Crude ^{1}H NMR (400 MHz, Acetone) δ: 2.51 (t, *J* = 7.3 Hz, 4H), 2.30 (t, *J* = 2.7 Hz, 2H), 2.17 (td, *J* = 7.0, 2.7 Hz, 4H), 1.69 – 1.28 (m, 24H).

Crude ^{13}C NMR (101 MHz, $CDCl_3$) δ: 169.7, 84.8, 68.3, 35.4, 29.2, 29.0, 28.9, 28.7, 28.5, 24.3, 18.5.

HRMS (FD *m/z*): calcd for $[C_{22}H_{35}O_3]^+$ $(M+H)^+$, 347.2586; found 347.2582.

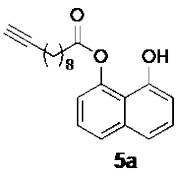

5a

8-hydroxynaphthalen-1-yl undec-10-ynoate (5a). A flame-dried 250 mL two-neck round bottom flask equipped with a stir bar was charged with 1,8-dihydroxynaphthalene (2.24 g, 14.0 mmol) and 4-dimethylaminopyridine (0.171 g, 1.40 mmol). The flask was evacuated/backfilled with N_2 (3x), and anhydrous THF (50 mL) was added. Triethylamine (2.55 mL, 18.3 mmol) was added via syringe, and then the solution was cooled to 0 °C in an ice bath. A solution of 10-undecynoic anhydride (4.85 g, 14.0 mmol) in anhydrous THF (50 mL) was added dropwise over 30 minutes under N_2. The reaction was warmed to room temperature and stirred for 16 h. The reaction was diluted

with EtOAc (400 mL) and the organic layer was washed with saturated aqueous NH_4Cl (3 x 300 mL), saturated aqueous $NaHCO_3$ (300 mL), and brine (300 mL). The organic layer was dried over $MgSO_4$, filtered, and concentrated under reduced pressure. The crude material was purified by column chromatography on silica gel (0–25% EtOAc/hexanes) and subsequently recrystallized from dichloromethane/hexanes to give the product as a colorless crystalline solid (2.80 g, 62%).

^{1}H NMR (400 MHz, $CDCl_3$) δ: 7.69 (dd, *J* = 8.3, 1.1 Hz, 1H), 7.43 – 7.28 (m, 4H), 7.18 (dd, *J* = 7.6, 1.1 Hz, 1H), 6.88 (dd, *J* = 7.5, 1.2 Hz, 1H), 2.69 (t, *J* = 7.5 Hz, 2H), 2.20 (td, *J* = 7.0, 2.6 Hz, 2H), 1.95 (t, *J* = 2.6 Hz, 1H), 1.81 (p, *J* = 7.5 Hz, 2H), 1.59 – 1.50 (m, 2H), 1.48 – 1.31 (m, 8H).

^{13}C NMR (101 MHz, $CDCl_3$) δ: 171.2, 152.0, 146.0, 137.0, 127.2, 126.5, 125.5, 120.4, 118.5, 117.0, 111.5, 84.9, 68.3, 34.8, 29.2, 29.1, 29.0, 28.8, 28.5, 24.8, 18.5.

TLC (25% EtOAc/hexanes): R_f = 0.50

HRMS (ESI *m/z*): calcd for $[C_{21}H_{23}O_3]^-$ $(M-H)^-$, 323.1653; found 323.1648.

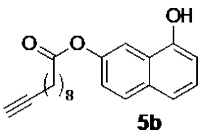

5b

8-hydroxynaphthalen-2-yl undec-10-ynoate (5b). A flame-dried 250 mL two-neck round bottom flask equipped with a stir bar was charged with 1,7-dihydroxynaphthalene (2.18 g, 13.6 mmol) and 4-dimethylaminopyridine (0.170 g, 1.39 mmol). The flask was evacuated/backfilled with N_2 (3x), and anhydrous THF (50 mL) was added. Triethylamine (2.50 mL, 17.9 mmol) was added via syringe, and then the solution was cooled to 0 °C in an ice bath. A solution of 10-undecynoic anhydride (4.70 g, 13.6 mmol) in anhydrous THF (50 mL) was added dropwise over 30 minutes under N_2. The reaction was warmed to room temperature and stirred for 16 h. The reaction was diluted with EtOAc (400

mL) and the organic layer was washed with saturated aqueous NH_4Cl (3 x 300 mL), saturated aqueous $NaHCO_3$ (300 mL), and brine (300 mL). The organic layer was dried over $MgSO_4$, filtered, and concentrated under reduced pressure. The crude material was purified by column chromatography on silica gel (0–55% EtOAc + 1% triethylamine/hexanes) to give the product as a pale pink solid (0.568 mg, 13%).

^{1}H NMR (400 MHz, $CDCl_3$) δ: 7.85 (d, *J* = 2.4 Hz, 1H), 7.77 (d, *J* = 8.9 Hz, 1H), 7.35 (d, *J* = 8.3 Hz, 1H), 7.22 – 7.15 (m, 2H), 6.68 (d, *J* = 7.5 Hz, 1H), 5.77 (s, 1H), 2.63 (t, *J* = 7.5 Hz, 2H), 2.20 (td, *J* = 7.1, 2.7 Hz, 2H), 1.96 (t, *J* = 2.7 Hz, 1H), 1.81 (p, *J* = 7.5 Hz, 2H), 1.59 – 1.50 (m, 2H), 1.47 – 1.33 (m, 8H).

^{13}C NMR (101 MHz, $CDCl_3$) δ: 173.3, 151.4, 147.9, 132.8, 129.3, 125.7, 124.9, 121.7, 120.3, 113.4, 109.2, 84.9, 68.3, 34.6, 29.3, 29.2, 29.0, 28.8, 28.6, 25.1, 18.5.

TLC (25% EtOAc/hexanes): R_f = 0.47

HRMS (ESI *m/z*): calcd for $[C_{21}H_{23}O_3]^-$ $(M-H)^-$, 323.1653; found 323.1654.

General Procedure A for the Synthesis of Bis-naphthopyrans. Bis-naphthopyrans were synthesized according to the literature[43] following the general procedure developed by Zhao and Carreira.[23,44] To a flame-dried two-neck round bottom flask equipped with a stir bar and reflux condenser was added bis-propargyl alcohol **4**, the appropriate naphthol, and a catalytic amount of pyridinium *p*-toluenesulfonate (PPTS). The flask was evacuated and backfilled with N_2 (3x) followed by the sequential addition of 1,2-dichloroethane and trimethyl orthoformate via syringe. The reaction was heated to reflux and stirred for the indicated amount of time. Upon completion, the reaction was cooled to room temperature, concentrated with celite, and purified by column chromatography on silica gel.

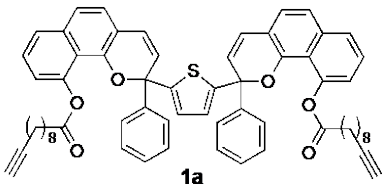

Thiophene-2,5-diylbis(2-phenyl-2*H*-benzo[*h*]chromene-2,10-diyl) bis(undec-10-ynoate) (1a). Synthesized according to General Procedure A with compound **4** (0.400 g, 1.16 mmol), compound **5a** (0.870 g, 2.68 mmol), PPTS (0.032 g, 0.127 mmol), 1,2-dichloroethane (10 mL), and trimethyl orthoformate (0.57 mL, 5.2 mmol). The reaction was stirred at reflux for 1.75 h. Purification by column chromatography on silica gel (0–15% Et_2O/CH_2Cl_2:hexanes (1:1)), followed by a second chromatographic separation on silica gel (0–40% EtOAc + 1% triethylamine/hexanes) afforded the title compound (mixture of diastereomers) as a dark red oil (0.195 g, 18%). We note that later column fractions were contaminated with the mono-merocyanine species, which was characterized by its reversion behavior under visible light irradiation to regenerate bis-naphthopyran **1a** (see Figure S12 below).

^{1}H NMR (400 MHz, C_6D_6) δ: 7.67 – 7.60 (m, 4H), 7.30 – 7.24 (m, 2H), 7.13 – 7.07 (m, 4H), 7.07 – 6.99 (m, 8H), 6.93 (s, 1H), 6.88 (s, 1H), 6.74 (dd, *J* = 8.3, 5.4 Hz, 2H), 6.20 (d, *J* = 9.6, 1H), 6.18 (d, *J* = 9.6, 1H), 5.81 (d, *J* = 9.6 Hz, 1H), 5.76 (d, *J* = 9.6 Hz, 1H), 2.25 – 2.06 (m, 4H), 2.03 – 1.96 (m, 4H), 1.84 – 1.80 (m, 2H), 1.53 – 1.42 (m, 4H), 1.41 – 1.31 (m, 4H), 1.29 – 1.18 (m, 4H), 1.13 – 1.01 (m, 12H).

^{13}C NMR (101 MHz, Acetone) δ: 173.1, 173.0, 150.9, 150.7, 147.98, 147.96, 147.69, 147.67, 145.1, 144.9, 138.0, 137.9, 128.97, 128.95, 128.91, 128.89, 128.6, 127.6, 127.3, 127.2, 127.06, 127.05, 126.2, 124.8, 124.7, 122.4, 121.2, 120.1, 117.9, 117.8, 85.0, 82.4, 82.3, 69.9, 34.49, 34.47, 29.93, 29.90, 29.72, 29.71, 29.68, 29.4, 29.33, 29.32, 25.2, 18.8.

TLC (25% EtOAc/hexanes): R_f = 0.53

HRMS (ESI *m/z*): calcd for $[C_{64}H_{61}O_6S]^+$ $(M+H)^+$, 957.4183; found 957.4217.

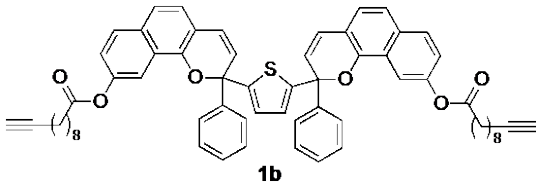

1b

Thiophene-2,5-diylbis(2-phenyl-2*H*-benzo[*h*]chromene-2,9-diyl) bis(undec-10-ynoate) (1b). Synthesized according to General Procedure A with compound **3-4** (0.145 g, 0.421 mmol), compound **5b** (0.328 g, 1.01 mmol), PPTS (0.012 g, 0.048 mmol), 1,2-dichloroethane (5 mL), and trimethyl orthoformate (0.21 mL, 1.9 mmol). The reaction was stirred at reflux for 2 h. Purification by column chromatography on silica gel (0–15% Et_2O/CH_2Cl_2:hexanes (1:1)), followed by a second chromatographic separation on silica gel (0–40% EtOAc + 1% triethylamine/hexanes) afforded the title compound (mixture of diastereomers) as a dark red oil (0.022 g, 5.5%).

^{1}H NMR (400 MHz, Acetone) δ: 7.95 (ddd, *J* = 8.8, 2.3, 1.2 Hz, 2H), 7.83 (dd, *J* = 8.9, 1.8 Hz, 2H), 7.62 – 7.57 (m, 4H), 7.44 (ddd, *J* = 8.5, 2.7, 0.8 Hz, 2H), 7.35 – 7.22 (m, 10H), 6.84 – 6.79 (m, 4H), 6.39 (d, *J* = 9.7 Hz, 1H), 6.38 (d, *J* = 9.7 Hz, 1H), 2.63 (t, *J* = 7.5 Hz, 4H), 2.31 (t, *J* = 2.7 Hz, 2H), 2.16 (td, *J* = 6.9, 2.8 Hz, 4H), 1.79 – 1.69 (m, 4H), 1.55 – 1.32 (m, 20H).

^{13}C NMR (101 MHz, CD_2Cl_2) δ: 172.7, 150.73, 150.70, 149.20, 149.18, 147.41, 147.39, 144.33, 144.31, 133.0, 129.47, 129.46, 128.6, 128.37, 128.35, 127.71, 127.68, 126.5, 126.1, 126.0, 125.3, 124.7, 124.30, 124.27, 122.47, 122.45, 121.15, 121.12, 116.4, 116.3, 113.28, 113.25, 85.1, 81.6, 81.5, 68.3, 34.7, 29.55, 29.50, 29.48, 29.47, 29.39, 29.33, 29.1, 28.9, 25.2, 18.7.

TLC (25% EtOAc/hexanes): R_f = 0.58

HRMS (ESI *m/z*): calcd for $[C_{64}H_{61}O_6S]^+$ $(M+H)^+$, 957.4183; found 957.4197.

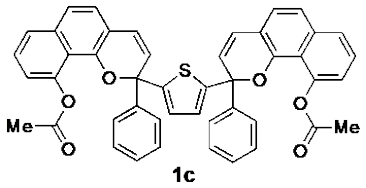

1c

Thiophene-2,5-diylbis(2-phenyl-2*H*-benzo[*h*]chromene-2,10-diyl) diacetate (1c). Synthesized according to General Procedure A with compound **4** (0.435 g, 1.26 mmol), compound **5c** (0.588 g, 2.91 mmol), PPTS (0.035 g, 0.139 mmol), 1,2-dichloroethane (10 mL), and trimethyl orthoformate (0.57 mL, 5.2 mmol). The reaction was stirred at reflux for 2.5 h. Purification by column chromatography on silica gel (0–15% Et_2O/CH_2Cl_2:hexanes (1:1)) afforded the title compound (mixture of diastereomers) as a dark red oil (0.098 g, 11%).

^{1}H NMR (400 MHz, Acetone) δ: 7.69 (dd, J = 8.3, 1.2 Hz, 2H), 7.65 – 7.59 (m, 4H), 7.48 – 7.39 (m, 4H), 7.38 – 7.29 (m, 6H), 7.27 (dd, J = 8.3, 3.3 Hz, 2H), 7.07 (ddd, J = 7.5, 2.0, 1.2 Hz, 2H), 6.87 (s, 1H), 6.83 (s, 1H), 6.81 (d, J = 9.6, 1H), 6.79 (d, J = 9.6, 1H), 6.30 (d, J = 9.6 Hz, 1H), 6.27 (d, J = 9.5 Hz, 1H), 1.61 (m, 6H).

^{13}C NMR (101 MHz, Acetone) δ: 170.34, 170.25, 151.0, 150.9, 147.88, 147.86, 147.6, 144.9, 144.8, 137.9, 129.0, 128.88, 128.85, 128.62, 128.57, 127.7, 127.6, 127.51, 127.46, 127.11, 127.07, 127.05, 126.22, 126.18, 125.0, 124.9, 122.37, 122.35, 121.13, 121.11, 120.1, 120.0, 118.0, 82.3, 82.2, 20.8, 20.6.

TLC (25% EtOAc/hexanes): R_f = 0.36

HRMS: calcd for $[C_{46}H_{33}O_6S]^+$ $(M+H)^+$, 713.1992; found 713.2018.

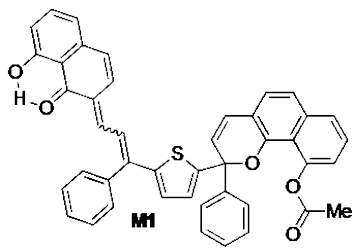

2-(5-(3-(8-hydroxy-1-oxonaphthalen-2(1*H*)-ylidene)-1-phenylprop-1-en-1-yl)thiophen-2-yl)-2-phenyl-2*H*-benzo[*h*]chromen-10-yl acetate (M1). Lithium diisopropylamine was freshly prepared in a flame-dried 50 mL round bottom flask. Anhydrous THF (9.5 mL) and diisopropylamine (0.145 mL, 1.035 mmol) were added via syringe under N_2. The flask was cooled to –78 °C and n-butyllithium (2.5 M in hexanes, 0.410 mL, 1.025 mmol) was added via syringe under N_2. The reaction was stirred for 2 h. To a separate flame dried 50 mL 2-neck round bottom flask equipped with a stir bar was added **1c** (73.0 mg, 0.1025 mmol) and the vessel was evacuated and backfilled with N_2 (3x). Anhydrous THF (5 mL) was added via syringe under N_2, the solution was cooled to –78 °C, and the LDA solution (4.5 mL, 0.49 mmol) was added dropwise via syringe over the course of 8 h in 0.5–1.0 mL portions. After complete addition, the reaction was removed from the cooling bath and immediately diluted with EtOAc (50 mL) and saturated aqueous NH_4Cl solution (50 mL). The organic layer was washed with saturated aqueous NH_4Cl solution (2 x 50 mL) and then brine (50 mL), dried over $MgSO_4$, filtered, and concentrated under reduced pressure. The crude material was purified by column chromatography on silica gel (0–50% EtOAc/hexanes) followed by a reverse-phase chromatographic separation on a C18 column (80–100% acetonitrile/H_2O). An additional chromatographic separation on silica gel (0–30% EtOAc/hexanes) afforded the title compound as a dark red-purple oil (0.013 g, 19%). The product is a mixture of merocyanine stereoisomers that readily interconvert (Figures S2 and S3, and Section VIII).

^{1}H NMR (400 MHz, CD_2Cl_2) δ: 13.67 (s, 0.08H), 13.39 (s, 0.06H), 13.29 (s, 0.52H), 8.91 (d, J = 12.4, 0.004H), 8.89 (d, J = 12.4, 0.006H), 8.74 (d, J = 12.2, 0.08H), 8.72 (d, J = 12.2,

0.02H), 8.42 (d, *J* = 12.1 Hz, 0.01H), 8.10 (d, *J* = 12.5, 0.06H), 7.72 – 6.61 (m, 25H), 6.57 (d, *J* = 9.3 Hz, 0.11H), 6.44 (d, *J* = 9.5 Hz, 0.11H), 6.28 (d, *J* = 9.6 Hz, 0.06H), 6.204 (d, *J* = 9.6, 0.21H), 6.198 (d, *J* = 9.6, 0.50H), 1.91 – 1.76 (m, 3H).

^{1}H NMR (400 MHz, THF-d_8) δ: 13.61 (s, 0.12H), 13.50 (s, 0.01H), 13.39 (s, 0.09H), 13.30 (s, 0.59H), 8.85 (d, *J* = 12.3 Hz, 0.13H), 8.80 (d, *J* = 12.1 Hz, 0.01H), 8.54 (d, *J* = 12.3 Hz, 0.01H), 8.14 (d, *J* = 12.7 Hz, 0.07H), 7.76 – 7.71 (m, 0.13H), 7.68 – 6.67 (m, 25H), 6.57 (d, *J* = 9.4 Hz, 0.11H), 6.47 (d, *J* = 9.5 Hz, 0.12H), 6.33 (d, *J* = 9.6 Hz, 0.06H), 6.24 (d, *J* = 9.6 Hz, 0.15H), 6.22 (d, *J* = 9.6 Hz, 0.68H), 1.84 – 1.80 (m, 3H).

^{13}C NMR (101 MHz, CD_2Cl_2) δ: 189.3, 170.7, 164.8, 164.5, 152.5, 149.7, 147.3, 146.9, 144.0, 143.9, 139.7, 139.0, 137.4, 137.2, 136.6, 136.4, 131.4, 130.79, 130.77, 130.69, 130.3, 130.1, 129.7, 129.52, 129.49, 129.1, 128.80, 128.76, 128.75, 128.73, 128.62, 128.59, 128.57, 128.5, 127.6, 127.5, 127.4, 127.31, 127.29, 126.9, 126.8, 126.6, 125.8, 125.6, 125.3, 125.0, 124.8, 124.1, 123.3, 122.1, 121.4, 120.54, 120.53, 119.4, 117.43, 117.41, 116.8, 116.1, 81.8, 32.3, 30.09, 30.06, 23.1, 20.9, 14.3.

TLC (25% EtOAc/hexanes): R_f = 0.45

HRMS: calcd for $[C_{44}H_{31}O_5S]^+$ $(M+H)^+$, 671.1887; found 671.1879.

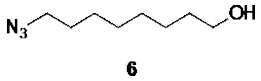

6

8-Azidooctan-1-ol (6). A flame-dried 100 mL two-neck round bottom flask equipped with a stir bar and reflux condenser was evacuated and backfilled with N_2 (3x). The flask was charged with anhydrous DMF (15 mL) and 8-bromooctan-1-ol (1.00 mL, 5.83 mmol) and the solution was cooled to 0 °C in an ice bath. Sodium azide (0.760 g, 11.7 mmol) was added to the reaction flask as a solid in a single portion. The reaction flask was warmed to room temperature, then heated to 80 °C and stirred

for 18 h. The reaction mixture was cooled to room temperature and diluted with EtOAc (300 mL). Ice cold water (150 mL) was added, the organic layer was separated and then washed consecutively with saturated aqueous $NaHCO_3$ (2 x 150 mL), 10% aqueous lithium chloride (5 x 200 mL), and brine (200 mL). The organic layer was dried over $MgSO_4$, filtered, and concentrated under reduced pressure. The crude material was purified by column chromatography on silica gel (0–50% EtOAc/hexanes) to give the title compound as a colorless liquid (0.933 g, 93%).

^{1}H NMR (400 MHz, $CDCl_3$) δ: 3.64 (t, J = 6.6 Hz, 2H), 3.25 (t, J = 7.0 Hz, 2H), 1.63 – 1.52 (m, 4H), 1.40 – 1.30 (m, 9H).

^{13}C NMR (101 MHz, $CDCl_3$) δ: 63.1, 51.6, 32.8, 29.4, 29.2, 28.9, 26.7, 25.7.

TLC (25% EtOAc/hexanes): R_f = 0.46

HRMS (ESI *m/z*): calcd for $[C_8H_{18}N_3O]^+$ $(M+H)^+$, 172.1450; found 172.1448.

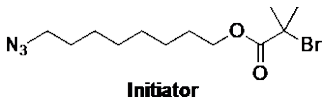

Initiator

8-Azidooctyl 2-bromo-2-methylpropanoate (Initiator). A flame-dried 50 mL two-neck round bottom flask equipped with a stir bar was evacuated and backfilled with N_2 (3x). The flask was charged with anhydrous THF (10 mL). A solution of **6** (0.870 g, 5.08 mmol) in anhydrous THF (10 mL) was added via syringe. The solution was cooled 0 °C in an ice bath, followed by the sequential addition of triethylamine (0.95 mL, 6.8 mmol) and α-bromoisobutyryl bromide (0.75 mL, 6.07 mmol). The reaction was warmed to room temperature and stirred for 24 h. The mixture was diluted with EtOAc (200 mL) and the organic layer was washed consecutively with deionized water (200 mL), saturated aqueous $NaHCO_3$ (2 x 200 mL), and brine (200 mL). The organic layer was dried over $MgSO_4$, filtered, and concentrated under reduced pressure. The crude

material was purified by column chromatography on silica gel (0–50% EtOAc/hexanes) to give the title compound as a colorless liquid (1.535 g, 94%).

^{1}H NMR (400 MHz, $CDCl_3$) δ: 4.17 (t, J = 6.6 Hz, 2H), 3.25 (t, J = 7.0 Hz, 2H), 1.93 (s, 6H), 1.72 – 1.64 (m, 2H), 1.63 – 1.55 (m, 2H), 1.44 – 1.29 (m, 8H).

^{13}C NMR (101 MHz, $CDCl_3$) δ: 171.9, 66.2, 56.1, 51.6, 30.9, 29.14, 29.12, 28.9, 28.4, 26.7, 25.8.

TLC (25% EtOAc/hexanes): R_f = 0.86

HRMS (FD *m/z*): calcd for $[C_{12}H_{23}BrN_3O_2]^+$ $(M+H)^+$, 320.09736; found 320.09787.

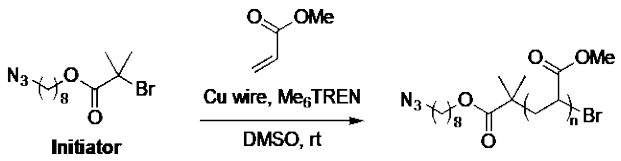

General Procedure B for the Synthesis of Poly(Methyl Acrylate) (PMA) Polymers Incorporating a Terminal Azide. Polymers were synthesized by controlled radical polymerization following the procedure by Nguyen *et al.*[45] A flame-dried Schlenk flask equipped with a stir bar was charged with freshly cut 20 G copper wire (2 cm), **Initiator**, DMSO, and methyl acrylate. The flask was sealed and the solution was degassed via three freeze-pump-thaw cycles, then backfilled with N_2 and warmed to room temperature. Tris[2-(dimethylamino)ethyl]amine (Me_6TREN) was added via microsyringe and the reaction was stirred at room temperature for the indicated amount of time. Upon completion of polymerization, the flask was opened to atmosphere and diluted with a minimal amount of CH_2Cl_2. The polymer was precipitated (3x) into methanol cooled with dry ice and then dried under vacuum.

PMA-Azide$_{22}$. Synthesized using General Procedure B with **Initiator** (57.0 mg, 0.178 mmol), methyl acrylate (4.0 mL, 44 mmol), DMSO (2.0 mL), and Me_6TREN (60 μL, 0.22 mmol). Polymerization for 60 min provided the title polymer as a tacky colorless solid (2.4 g, 61%). M_n = 22 kg/mol, $Đ$ = 1.13.

PMA-Azide. Synthesized using General Procedure B with **Initiator** (19.4 mg, 0.061 mmol), methyl acrylate (4.1 mL, 45 mmol), DMSO (4.1 mL), and Me_6TREN (33 μL, 0.12 mmol). Polymerization for 80 min provided the title polymer as a tacky colorless solid (2.3 g, 64%). M_n = 59 kg/mol, $Đ$ = 1.10.

PMA-Azide$_{194}$. Synthesized using General Procedure B with **Initiator** (3.3 mg, 0.010 mmol), methyl acrylate (2.8 mL, 31 mmol), DMSO (5.6 mL), and Me_6TREN (4.2 μL, 0.016 mmol). Polymerization for 4 h provided the title polymer as a tacky colorless solid (1.3 g, 67%). M_n = 194 kg/mol, $Đ$ = 1.09.

General Procedure C for the Synthesis of Polymers Incorporating a Chain-Centered Bis-naphthopyran. Polymers were synthesized by a Cu-catalyzed azide-alkyne cycloaddition (CuAAC) reaction based on a procedure adapted from the literature.[46] A flame dried Schlenk flask equipped with a stir bar was charged with azide-terminated PMA polymer and pentamethyldiethylenetriamine (PMDETA). The flask was evacuated and backfilled with N_2 (3x) and brought into a glovebox. A solution of bis-alkyne functionalized bis-naphthopyran (**1a** or **1b**) in anhydrous THF was added to the flask, followed by copper(I) bromide. Additional THF was introduced to achieve a final polymer concentration of 50

mg/mL. The flask was sealed and the solution was stirred at room temperature in the glovebox for the indicated amount of time. After removal from the glovebox, the solution was filtered through a plug of basic alumina and concentrated under reduced pressure, and the residue was dissolved in a minimal amount of CH_2Cl_2. The polymer was precipitated (3x) into methanol cooled with dry ice and then dried under vacuum.

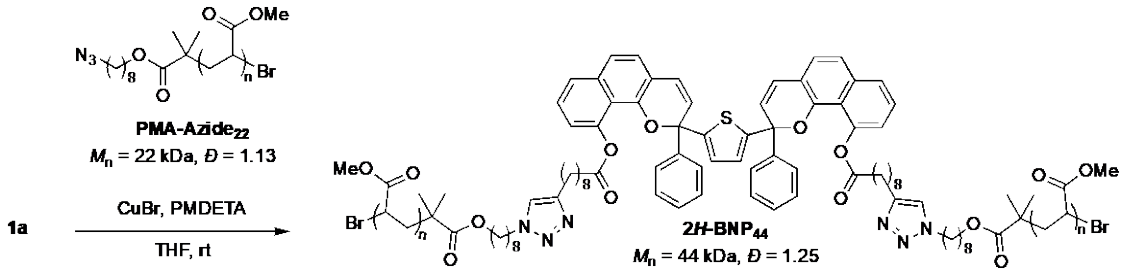

2*H*-BNP$_{44}$. Synthesized using General Procedure C with **PMA-Azide$_{22}$** (0.916 g, 0.042 mmol), PMDETA (40 μL, 0.19 mmol), **1a** (19.9 mg, 0.021 mmol), copper(I) bromide (18.0 mg, 0.125 mmol), and THF (16.4 mL) for 72 h of reaction time. The title polymer was isolated as a tacky purple solid (0.53 g, 58%). M_n = 44 kg/mol, $Đ$ = 1.25.

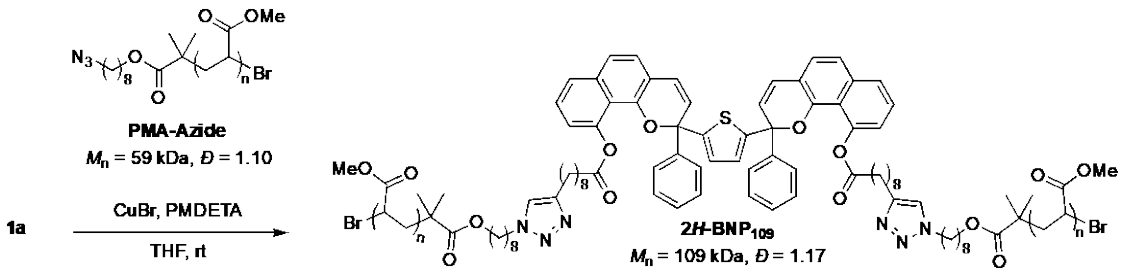

2*H*-BNP$_{109}$. Synthesized using General Procedure C with **PMA-Azide** (0.980 g, 0.0166 mmol), PMDETA (16 μL, 0.077 mmol), **1a** (7.9 mg, 0.0083 mmol), copper(I) bromide (7.1 mg, 0.050 mmol), and THF (18 mL) for 60 h of reaction time. The title polymer was isolated as a tacky pale purple solid (0.65 g, 66%). M_n = 109 kg/mol, $Đ$ = 1.17.

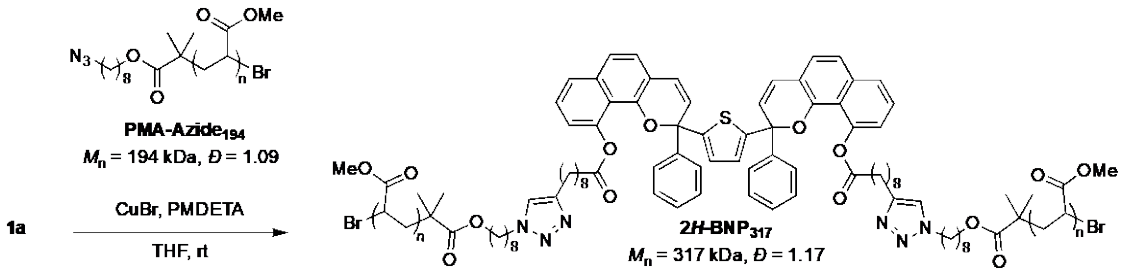

2*H*-BNP$_{317}$. Synthesized using General Procedure C with **PMA-Azide$_{194}$** (1.095 g, 0.0056 mmol), PMDETA (5.3 μL, 0.025 mmol), **1a** (2.7 mg, 0.0028 mmol), copper(I) bromide (2.5 mg, 0.017 mmol), and THF (20 mL) for 60 h of reaction time. The title polymer was isolated as a tacky pale purple solid (0.79 g, 72%). M_n = 317 kg/mol, $Đ$ = 1.17.

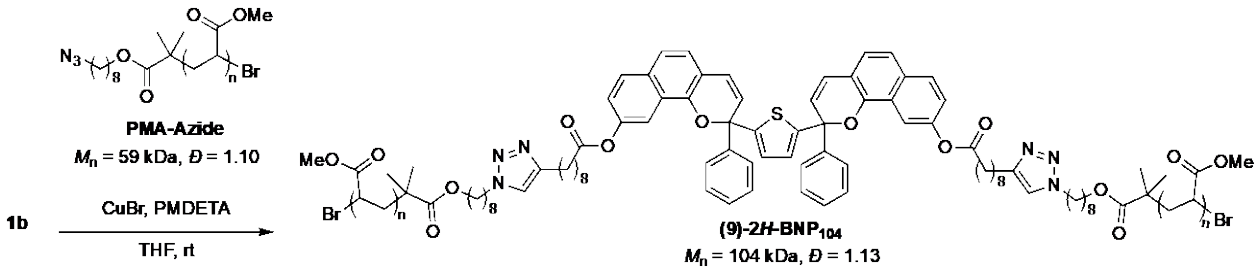

(9)-2*H*-BNP$_{104}$. Synthesized using General Procedure C with **PMA-Azide** (0.864 g, 0.0146 mmol), PMDETA (14 μL, 0.067 mmol), **1b** (7.0 mg, 0.0073 mmol), copper(I) bromide (7.0 mg, 0.049 mmol), and THF (16 mL) for 48 h of reaction time. The title polymer was isolated as a tacky pale pink solid (0.60 g, 70%). M_n = 104 kg/mol, $Đ$ = 1.13.

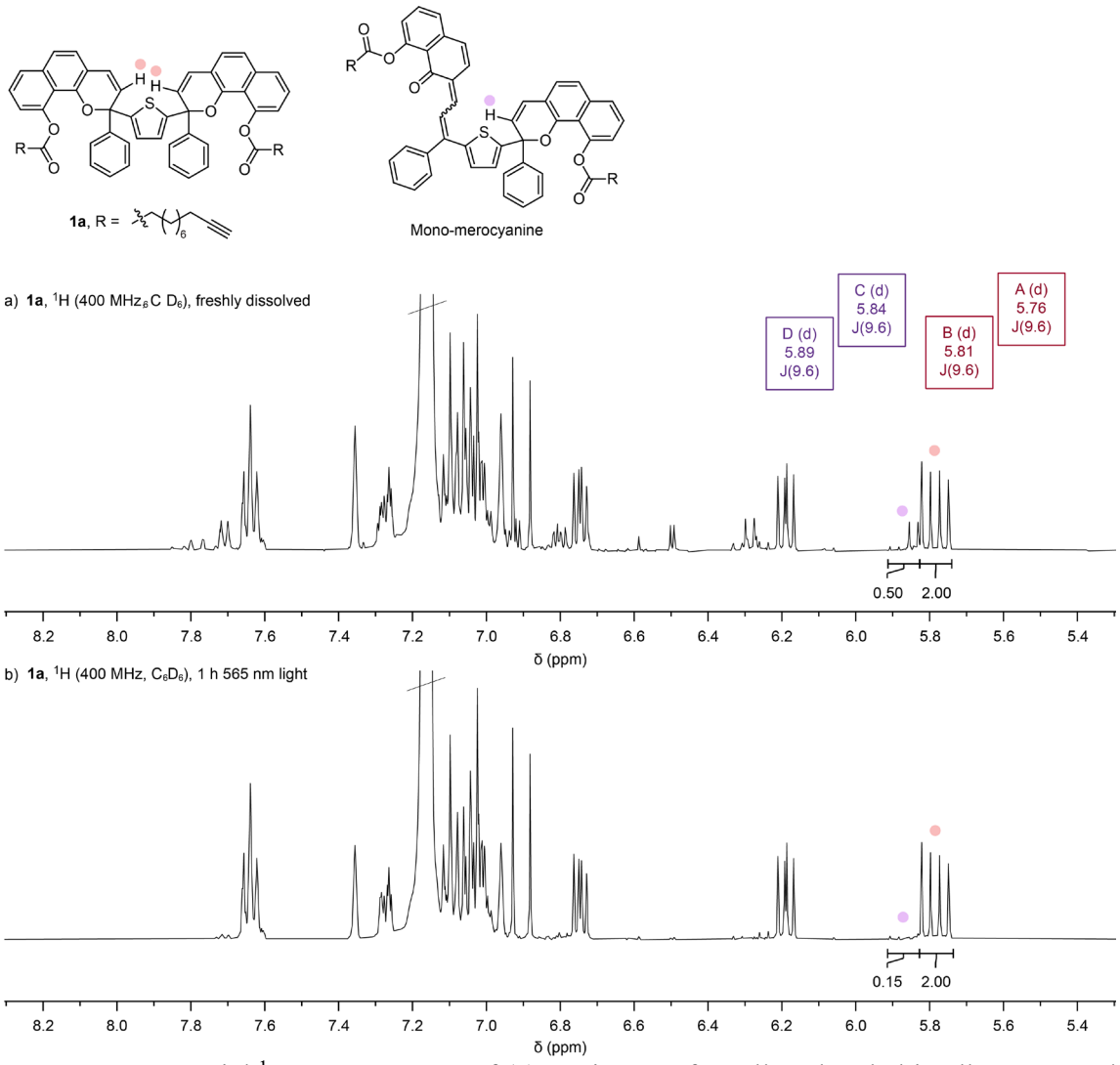

Figure S2.17. Partial ^{1}H NMR spectra of (a) a mixture of small molecule bis-alkyne **1a** and the mono-merocyanine species in C_6D_6, and (b) the same solution following 1 h of irradiation with 565 nm visible light. The bis-naphthopyran **1a** is characterized by a pair of doublets at 5.76 and 5.81 ppm (J = 9.6 Hz, 2H) corresponding to pyran protons on various diastereomers. The mono-merocyanine compound is characterized by a pair of doublets at 5.84 and 5.89 ppm (J = 9.6 Hz, 2H) corresponding to pyran protons on various isomers. Before irradiation with visible light, resonances associated with the mono-merocyanine species are present, and visible light irradiation results in the significant attenuation of these peaks.

V. Characterization of PMA Polymers

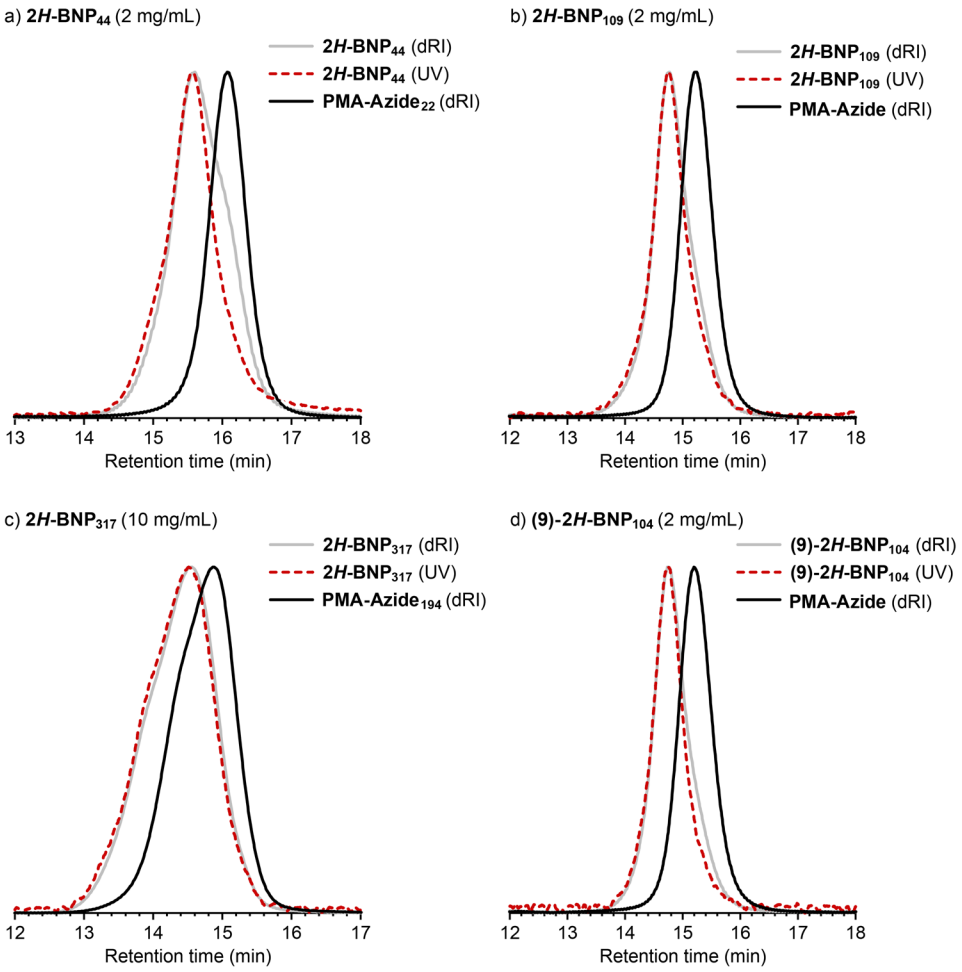

Figure S2.18. GPC chromatograms measured with differential refractive index (dRI) and UV absorption (345 nm) detectors for **2*H*-BNP44** (2 mg/mL in THF, M_n = 44 kDa, $Đ$ = 1.25), **2*H*-BNP109** (2 mg/mL in THF, M_n = 109 kg/mol, $Đ$ = 1.17), **2*H*-BNP317** (10 mg/mL in THF, M_n = 317 kg/mol, $Đ$ = 1.17), and **(9)-2*H*-BNP104** (2mg/mL in THF, M_n = 104 kg/mol, $Đ$ = 1.13) overlaid with the GPC chromatograms of their respective azide-terminated poly(methyl acrylate) polymers at the same concentration.

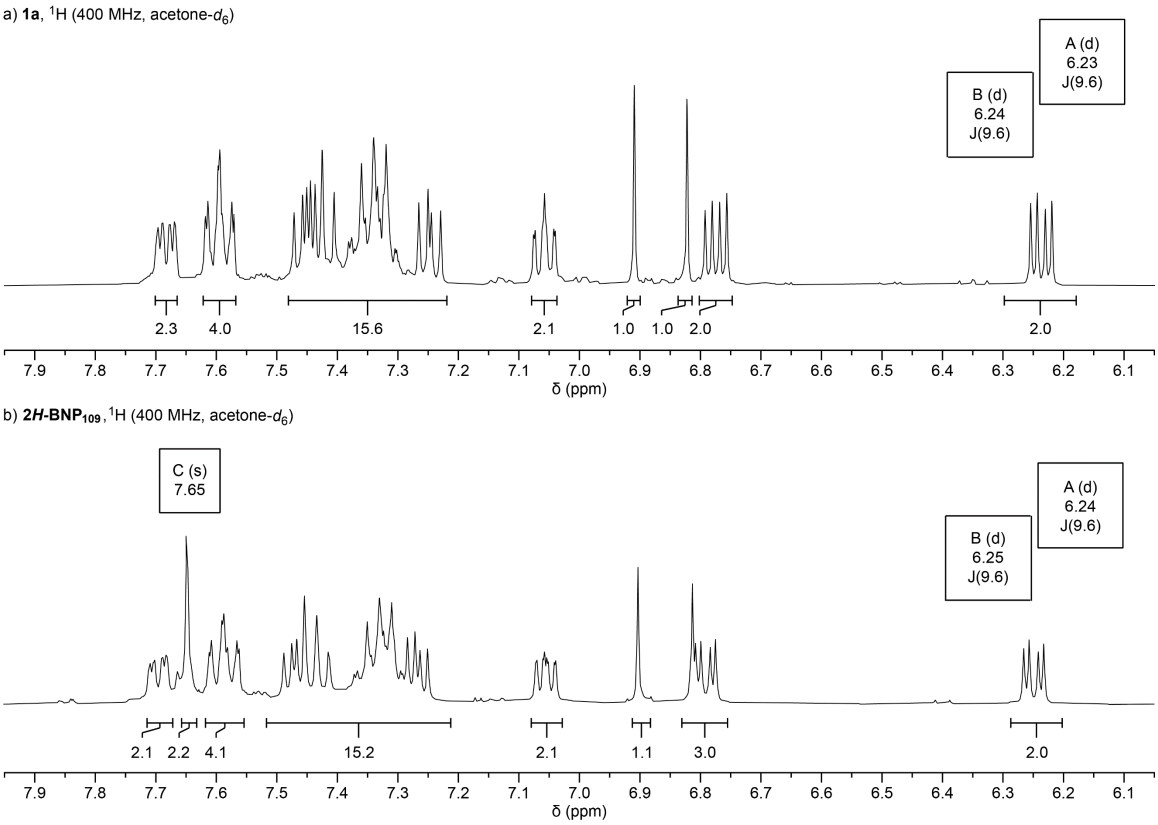

Figure S2.19. Partial ^{1}H NMR spectra of (a) small molecule bis-alkyne **1a**, and (b) polymer **2*H*-BNP$_{109}$** demonstrating successful coupling of the bis-naphthopyran unit and the polymer chains. The bis-naphthopyran at the center of polymer **2*H*-BNP$_{109}$** is characterized by a pair of overlapping doublets at 6.24 and 6.25 ppm (J = 9.6 Hz, 2H) corresponding to pyran protons on various diastereomers. A new singlet (7.65 ppm, 2H) corresponds to the triazole protons generated in the CuAAC reaction. Overintegration of the overlapping signals from 7.2 to 7.5 ppm (15H versus the expected 12H) is likely due to a small amount of the merocyanine species (See section IV).

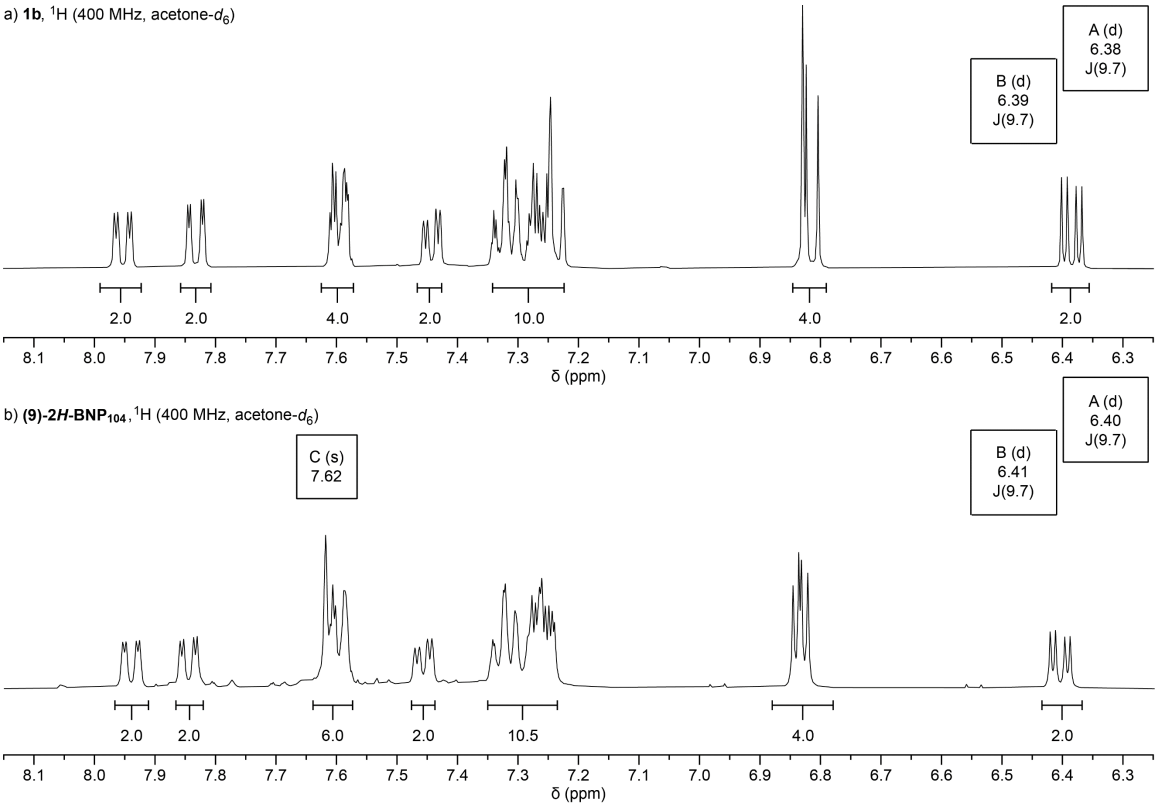

Figure S2.20. Partial ^{1}H NMR spectra of (a) small molecule bis-alkyne **1b**, and (b) polymer **(9)-2*H*-BNP$_{104}$** demonstrating successful coupling of the bis-naphthopyran unit and the polymer chains. The bis-naphthopyran at the center of polymer **(9)-2*H*-BNP$_{104}$** is characterized by a pair of overlapping doublets at 6.40 and 6.41 ppm (J = 9.7 Hz, 2H) corresponding to pyran protons on various diastereomers. A new singlet (7.62 ppm, 2H) corresponds to the triazole protons generated in the CuAAC reaction.

VI. DFT Calculations (CoGEF)

CoGEF calculations were performed using Spartan ′20 Parallel Suite according to previously reported methods.[38,47] Ground state energies were calculated using DFT at the B3LYP/6-31G* level of theory. Truncated models of each mechanophore with terminal acetoxy groups were used in the calculations. For each structure, the equilibrium conformations of the unconstrained molecule were initially calculated using molecular mechanics (MMFF) followed by optimization of the equilibrium geometries using DFT (B3LYP/6-31G*). Starting from the equilibrium geometry of the unconstrained molecules (energy = 0 kJ/mol),

the distance between the terminal methyl groups of the truncated structures was increased in increments of 0.05 Å and the energy was minimized at each step. The maximum force associated with the mechanochemical reaction was calculated from the slope of the curve immediately prior to bond cleavage using the final two contiguous data points.

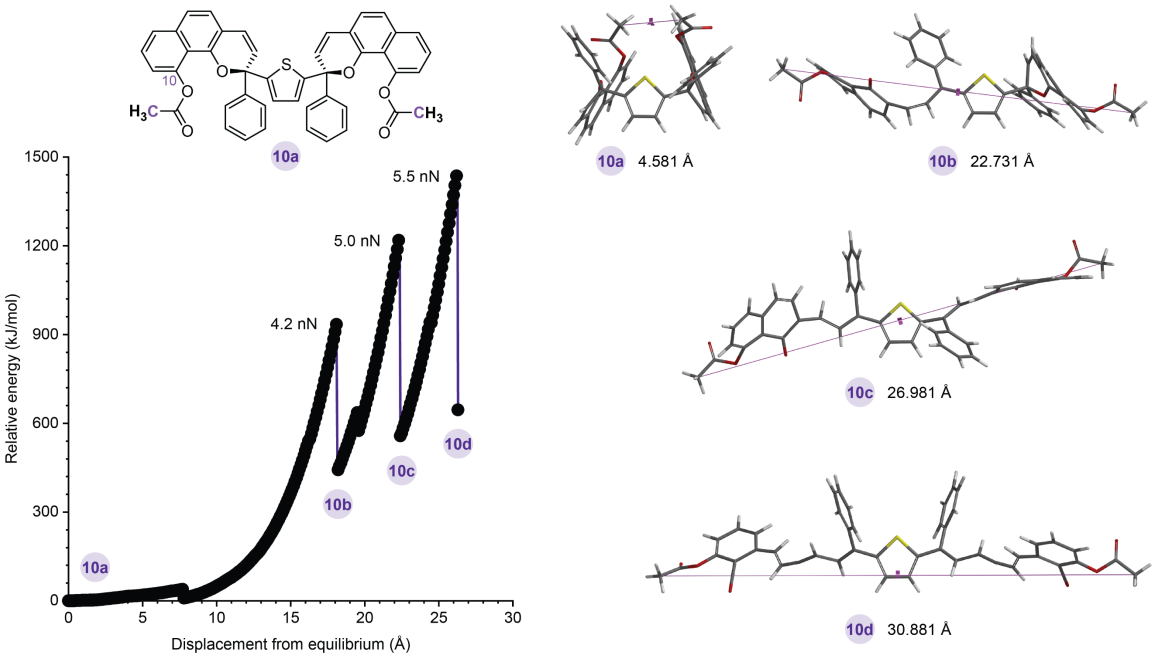

Figure S3.21. Density functional theory (DFT) calculations using the constrained geometries simulate external force (CoGEF) method performed on a truncated model of the 2*H*-BNP mechanophore with attachment points at the 10-position of each naphthopyran subunit. Computed structures are shown at right that correspond to the indicated points in the CoGEF profile along with the associated constraint distance between the terminal methyl groups (purple carbon atoms designate the anchor points defining the distance constraint). The first and second ring-opening reactions are predicted to occur at a maximum force of 4.2 nN and 5.0 nN, respectively. Upon further extension, an atypical ring-opening reaction is predicted to occur on both merocyanine subunits simultaneously at 5.5 nN, generating a pair of ketene and allene units as described in the main text. Calculations were performed at the B3LYP/6-31G* level of theory.

VII. Details for Photoirradiation and Sonication Experiments

Reaction progress was continuously monitored by UV-vis absorption spectroscopy using a previously described experimental setup[43] assembled using a peristaltic pump to transport

solution from the reaction vessel through a quartz flow cell in a UV-vis spectrometer and return the solution to the reaction vessel. The flow rate through the system was maintained at 8 mL/min, corresponding to a setting of 50 RPM on the peristaltic pump at the selected occlusion. The UV-vis spectrometer was programmed to acquire full spectra at regular time intervals. Absorbance values were measured at 790 nm and subtracted from the absorbance values at all other wavelengths to account for drift during the experiments.

General Procedure for Sonication Experiments. A sonication vessel was placed onto the sonication probe and charged with anhydrous THF (18 mL) that contained 30 mM BHT to avoid decomposition side reactions resulting from free radicals generated during sonication.[48,49] An additional 6.2 mL of stabilized THF was pumped into the dead space of the circulatory setup. Teflon inlet and outlet tubes were inserted into the solution in the sonication vessel through punctured septa, and the pump was engaged to start the flow of solution through the system. The sonication vessel was submerged in either an ethanol bath maintained at −45 ± 2 °C with an immersion chiller or an ice bath maintained at 0 ± 2 °C, and the solution was sparged with N_2 for 30 min. The system was then maintained under an inert atmosphere for the duration of the experiment. Continuous sonication at 20 kHz (20% amplitude, 6.8 ± 0.5 W/cm^2) was initiated and run for approximately 5 min to allow the temperature inside the reaction vessel to equilibrate to –15 °C (ethanol bath) or 15–20 °C (ice bath), as measured by a thermocouple inserted into the solution (Digi-Sense EW-91428-02 thermometer with Digi-Sense probe EW-08466-83). Separately, a concentrated solution of polymer (2.0 mL, 26.2 mg/mL in stabilized THF) was sparged with N_2 for 30 min. This solution was then injected into the sonication vessel to provide a total system volume of 26.2 mL (2.0 mg/mL of polymer) and reaction progress was monitored by UV-vis

absorption spectroscopy. Sonication intensity was calibrated via the literature method.[34] After completion of the sonication experiment, ultrasound was turned off and the temperature of the solution in the sonication vessel was allowed to equilibrate (–30 °C if the ethanol bath was used, 20 °C if an ice bath was used), after which the solution was monitored by UV-vis absorption spectroscopy for 16–20 h in the dark. The entire system was protected from external light and kept under an inert atmosphere for the duration of the experiment. A 1 mL aliquot of the sonication solution was transferred to a cuvette for bleaching experiments with visible light.

The rate of mechanochemical reactions is typically increased at lower temperatures due to the effects of decreased solvent vapor pressure on cavitation.[32,50] Additionally, the rate of mechanochemical reactions of a chain-centered mechanophore scales with polymer chain length.[51] In ultrasonication experiments of naphthopyran, low temperatures are known to slow merocyanine reversion significantly, enabling the accumulation and observation of thermally transient species.[8] During the sonication of **2*H*-BNP$_{317}$** at low temperatures (–15 °C), the relative rates of mechanochemical ring opening (fast) and merocyanine reversion (slow) are such that accumulation of *cis*-**2*H*-BNP$_{oo}$** is observed (Figure S2.14).

General Procedure for Photoirradiation Experiments. Photoirradiation experiments were performed under conditions that closely mimic those of the ultrasonication experiments. A sonication vessel was placed onto the sonication probe and charged with anhydrous THF (18 mL) and an additional 6.2 mL of THF was pumped into the dead space of the circulatory setup. Teflon inlet and outlet tubes were inserted into the solution in the sonication vessel through punctured septa, and the pump was engaged to start the flow of solution through the system. The sonication vessel was lowered into an empty metal Dewar, and the solution was

sparged with N_2 for 10 min. The system was then maintained under an inert atmosphere for the duration of the experiment. A solution of either polymer **2*H*-BNP$_{109}$** (2 mL, 26.2 mg/mL in THF) or model compound **M1** (2 mL, 0.13 mg/mL) was sparged with N_2 for 10 minutes. This solution was then injected into the sonication vessel to provide a total system volume of 26.2 mL (2.0 mg/mL of **2*H*-BNP$_{109}$** or 0.01 mg/mL of **M1**). The vessel was exposed to a UV light source (λ = 365 nm) positioned ~2 in from the vessel for the indicated amount of time, and merocyanine formation at room temperature (20 °C) was monitored by UV-vis absorption spectroscopy. Once the UV light was turned off, absorption spectra were collected to monitor thermal reversion of the photochemically generated merocyanines. The entire system was protected from external light and kept under an inert atmosphere for the duration of the experiment. A 1 mL aliquot of the solution was transferred into a cuvette for bleaching experiments with visible light.

General Procedure for Bleaching Experiments with Visible Light. Absorption spectra of photobleached samples were measured at room temperature (20 °C) by exposing a sample solution (2.0 mg/mL of polymer in THF or 0.01 mg/mL of **M1** in THF) in a quartz cuvette to a visible light source (λ = 565 nm) positioned ~3 in from the cuvette for 30 min. The cuvette was immediately placed into the spectrometer and the absorption spectrum was collected. After a 10 min period in the dark, the cuvette was placed under the visible light source for another 30 min. This procedure was repeated until the sample had been irradiated with visible light for either 150 min or 180 min total.

VIII. Properties of H-bonded Merocyanines with *Cis* and *Trans* Exocyclic Alkenes

Naphthopyran **Mono-M1** containing a β-hydroxy ketone motif and a terminal pivalate ester exists primarily as a mixture of merocyanine species with *cis* exocyclic olefin geometry

under ambient conditions (see Figure S2.7).[7] Irradiation with UV light promotes *cis*-to-*trans* alkene isomerization.[52] To evaluate the variability in the absorption properties of the merocyanine locked with an intramolecular H-bond as a function of stereoisomer distribution, a freshly dissolved sample of **Mono-M1** in THF-d_8 was irradiated with UV light. Changes in the relative amount of exocyclic *cis* and exocyclic *trans* merocyanine isomers were monitored by ^{1}H NMR spectroscopy (600 MHz), while changes in absorption were monitored using UV-vis spectroscopy. The ^{1}H NMR spectrum of an unirradiated sample of **Mono-M1** contains a doublet at 8.83 ppm (J = 12.3 Hz) characteristic of a proton on the *cis* exocyclic alkene (H^a),[7] and a pair of overlapping doublets at 7.81 ppm (J = 12.8 Hz) that correspond to a proton (H^b) of the merocyanine bridge on the exocyclic *trans* isomers.[52] The relative integrations of these two signals suggest that when freshly dissolved in THF-d_8, the exocyclic alkene of the mono-merocyanine has predominantly *cis* geometry (98%).

One drop of the above sample was diluted with non-deuterated THF and analyzed by UV-vis spectroscopy to reveal an absorption maximum at 515 nm (see Figure S2.7). The original sample was then irradiated with 311 nm UV light and periodically analyzed by ^{1}H NMR. After each NMR spectrum was collected, one drop of the NMR sample was again diluted with non-deuterated THF and analyzed by UV-vis spectroscopy. Conversion of the *cis* merocyanine is monitored by the attenuation of the doublet at 8.83 ppm (proton H^a) and concomitant generation of the *trans* merocyanine is monitored by an increase in the signals at 7.81 ppm (proton H^b). An increase in the relative amount of *trans* exocyclic alkene isomers also induces a hypsochromic shift in the absorption maximum of the merocyanine mixture (Figure S3.7). After 155 min of irradiation with UV light, the ^{1}H NMR spectrum suggests

that only 31% of the merocyanine species have *cis* geometry of the exocyclic olefin, while 69% of merocyanines have *trans* geometry. This change in alkene isomerism corresponds to a shift in the absorption maximum from 515 to 500 nm.

To evaluate the impact of *cis* and *trans* isomerism of the exocyclic alkene on the observed extinction coefficient at a given wavelength, a ~10 μM solution of **Mono-M1** in THF was prepared and transferred to a sealed cuvette (see Figure S2.8). The sample was irradiated with 311 nm UV light and analyzed by UV-vis absorption spectroscopy. Using the quantitative ^{1}H NMR data described in Figure S2, a linear relationship between *cis* exocyclic alkene content and absorption maximum was determined (Figure S2.7c, inset). Using this relationship, the relative ratio of merocyanine isomers with *cis* and *trans* exocyclic alkenes was determined based on the absorption maximum of the mixture. The mixture was converted from 89% to 41% *cis* geometry after exposure to UV light for 420 s. Concurrently, the absorbance at λ_{max} of the sample increased by approximately 7%, from 0.197 to 0.211. The data presented in Figures S2 and S3 indicate that merocyanine isomers containing a single intramolecular H-bond and a *cis* exocyclic alkene have a smaller extinction coefficient and exhibit a bathochromically shifted absorption maximum compared to the *trans* isomer. Notably, *cis*-to-*trans* isomerization of **Mono-M1** is also observed in the dark in the presence of small amounts of water (Figure S2.22).

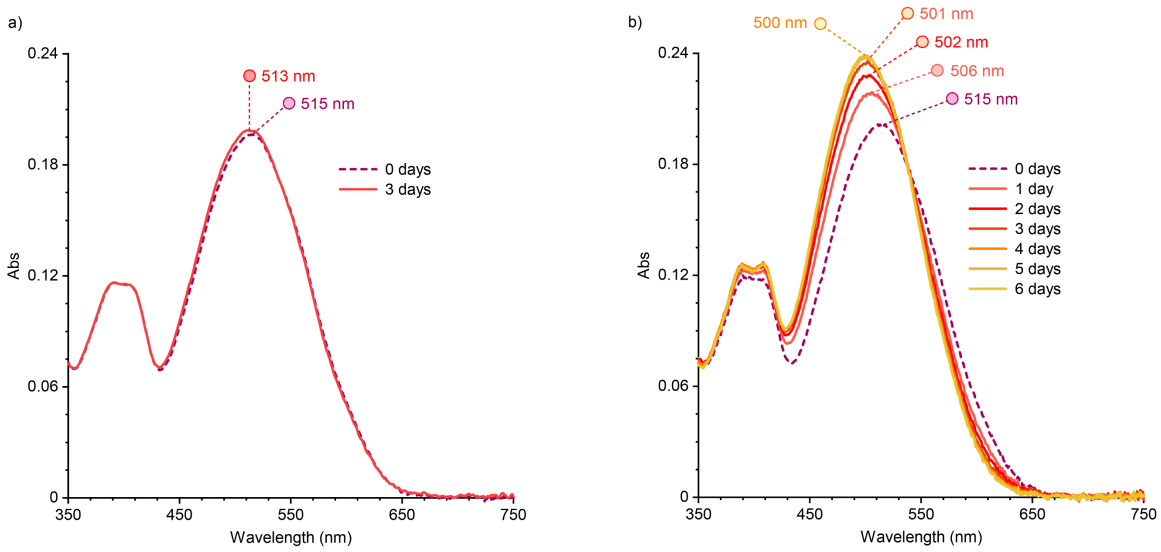

Figure S2.22. UV-vis absorption spectra of **Mono-M1** in THF (10 μM) illustrating *cis*-to-*trans* isomerization of the exocyclic alkene in the presence of a small amount of water. (a) Minimal change is observed in the absorption spectrum of a freshly prepared solution of **Mono-M1** after storage for 3 days at 20 °C in the dark. (b) The absorption spectrum of a solution of **Mono-M1** containing 4.3% water (by volume) changes significantly over a period of six days. A hypsochromic shift of λ_{max} is accompanied by an increase in absorbance. These spectral changes correspond to a change in the distribution of merocyanine isomers from 98% to 32% *cis*.

The ^{1}H NMR spectra of **2*H*-BNP$_{109}$** before and after ultrasonication are illustrated in Figure S3.23, along with the ^{1}H NMR spectrum of model compound **M1**. The bis-naphthopyran unit in polymer **2*H*-BNP$_{109}$** is characterized by a pair of overlapping doublets at 6.14 and 6.15 ppm (J = 9.6 Hz) corresponding to pyran protons on various diastereomers. The pyran ring in model compound **M1** is characterized by a doublet at 6.22 ppm (J = 9.6 Hz). Signals attributed to the OH proton of various merocyanine isomers appear in the 13.0–14.0 ppm region in the spectra of **M1** and **2*H*-BNP$_{109}$** after mechanochemical activation. Photoisomerization of **Mono-M1** (see Figure S2.7) suggests that the singlet at 13.30 ppm belongs to H-bonded merocyanine isomers with *trans* configuration of the exocyclic olefin, and the singlets at 13.62 and 13.64 ppm belong to *cis* isomers. The minor sets of doublets at 8.86 and 8.94 ppm (J = 12.3 and J = 12.4 Hz, respectively) are attributed to protons on various

isomers of the H-bonded merocyanine subunit with *cis* configuration of the exocyclic alkene and account for approximately 32% of the total H-bonded merocyanine present in the sample of **2*H*-BNP$_{109}$** after ultrasonication. We note that this does not necessarily reflect the actual product distribution from the mechanochemical reaction due to the spontaneous *cis*-to-*trans* isomerization that is observed in the presence of water (see Figure S2.22).

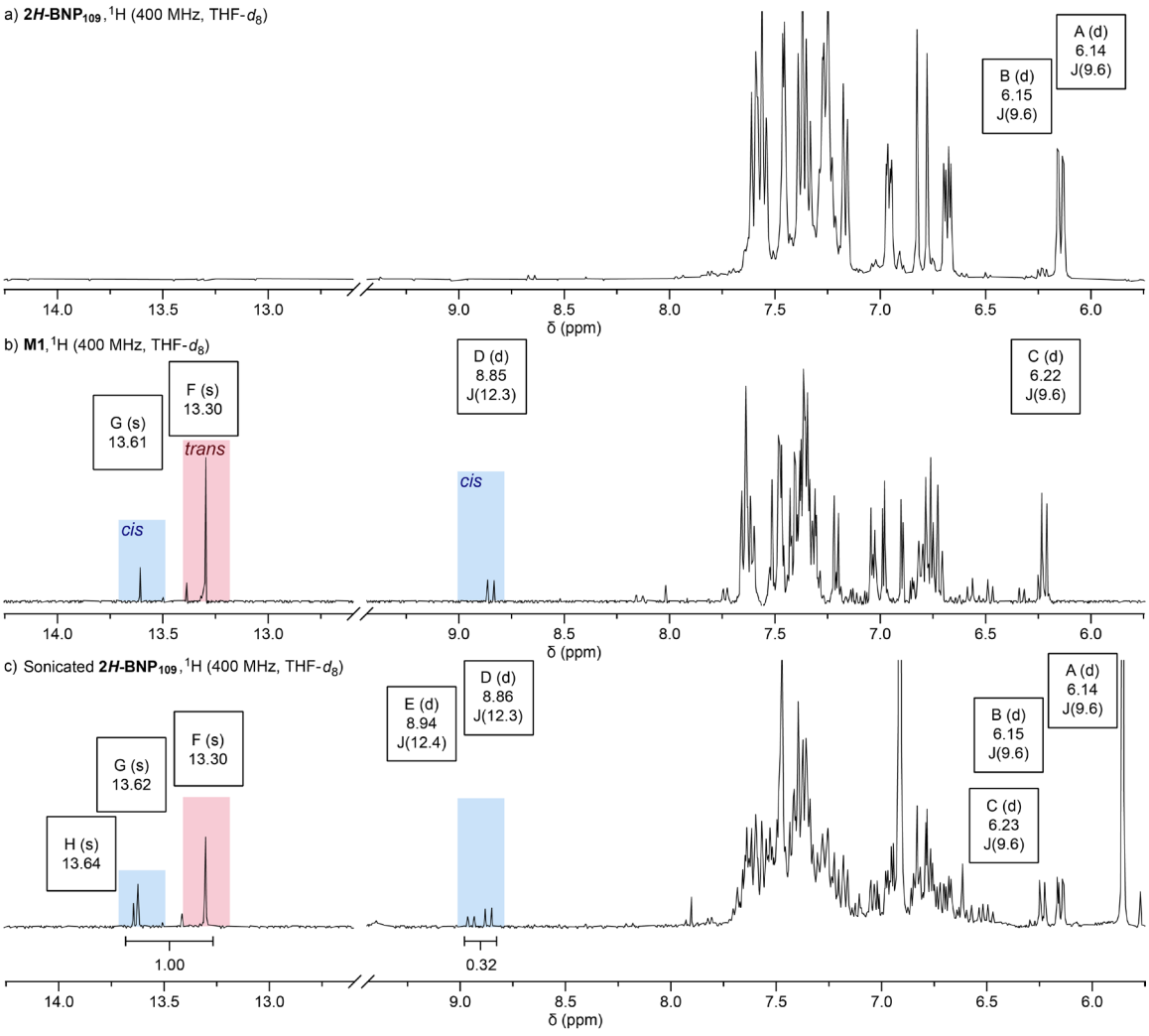

Figure S2.23. Partial ^{1}H NMR spectra of (a) **2*H*-BNP$_{109}$**, (b) model compound **M1**, and (c) **2*H*-BNP$_{109}$** after mechanochemical activation (12 h of continuous ultrasonication, 30 mM BHT in THF, 20 °C).

^{1}H and ^{13}C NMR Spectra

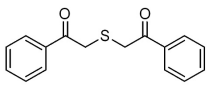

2

^{1}H (400 MHz, $CDCl_3$)

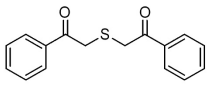

2

^{13}C (101 MHz, $CDCl_3$)

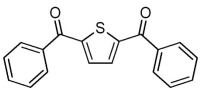

3

^{1}H (400 MHz, $CDCl_3$)

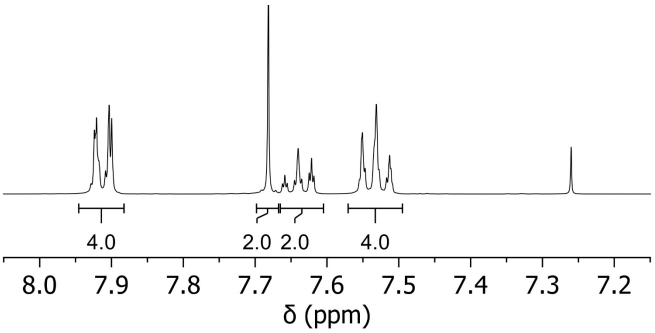

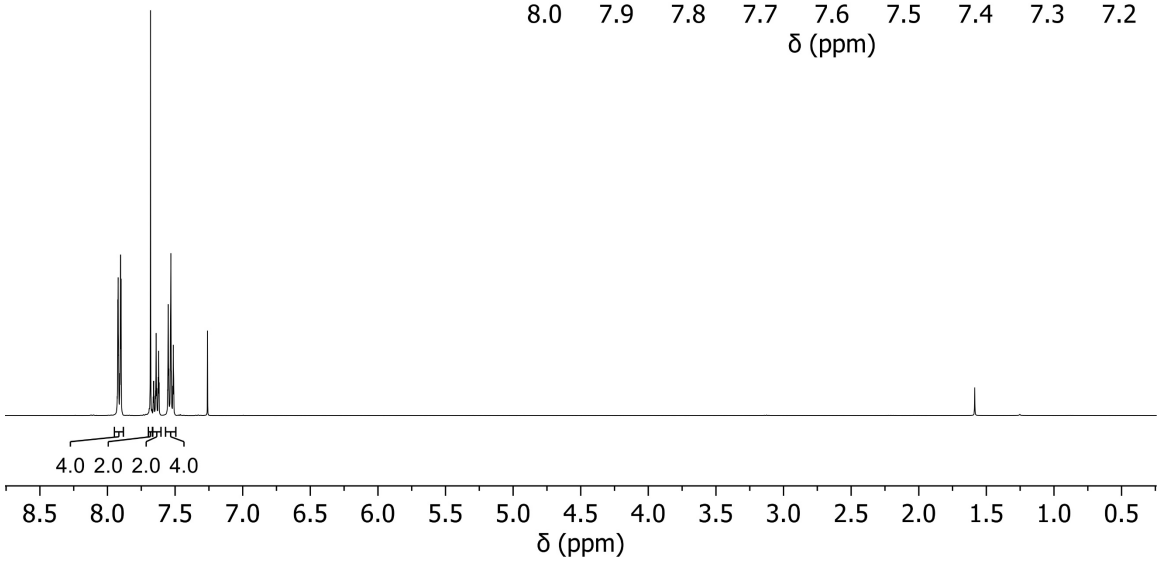

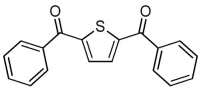

3

^{13}C (101 MHz, $CDCl_3$)

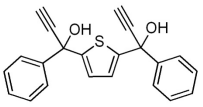

4

^{1}H (400 MHz, $CDCl_3$)

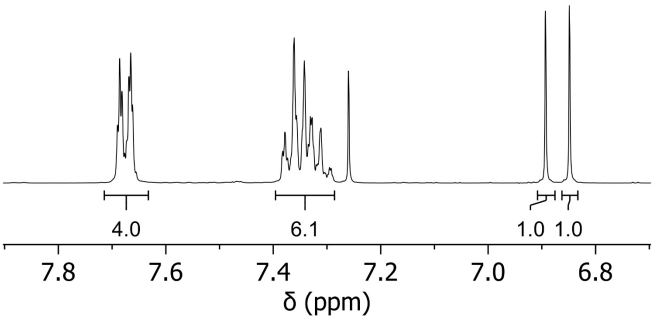

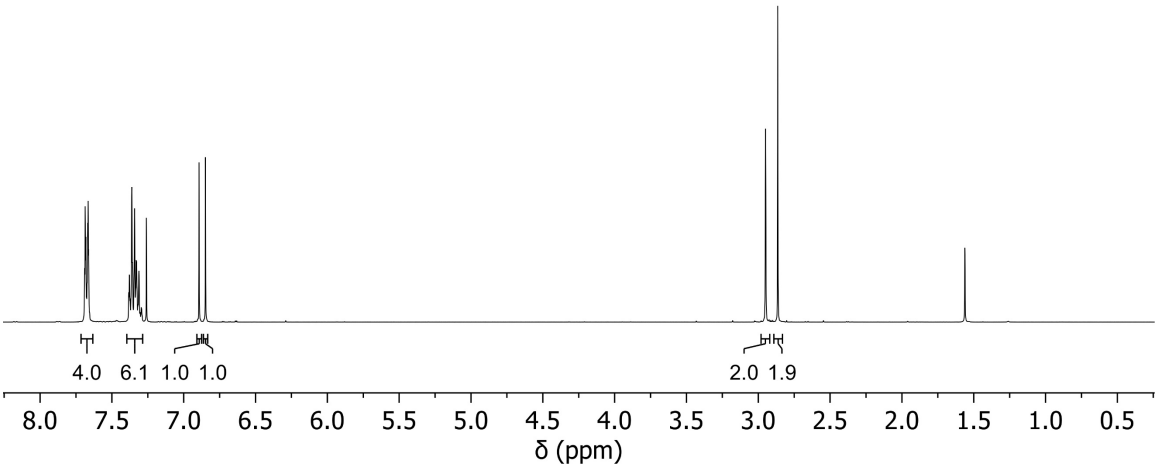

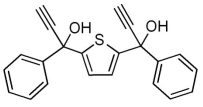

4

^{13}C (101 MHz, $CDCl_3$)

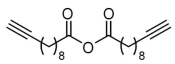

10-Undecynoic acid

^{1}H (400 MHz, acetone-d_6)

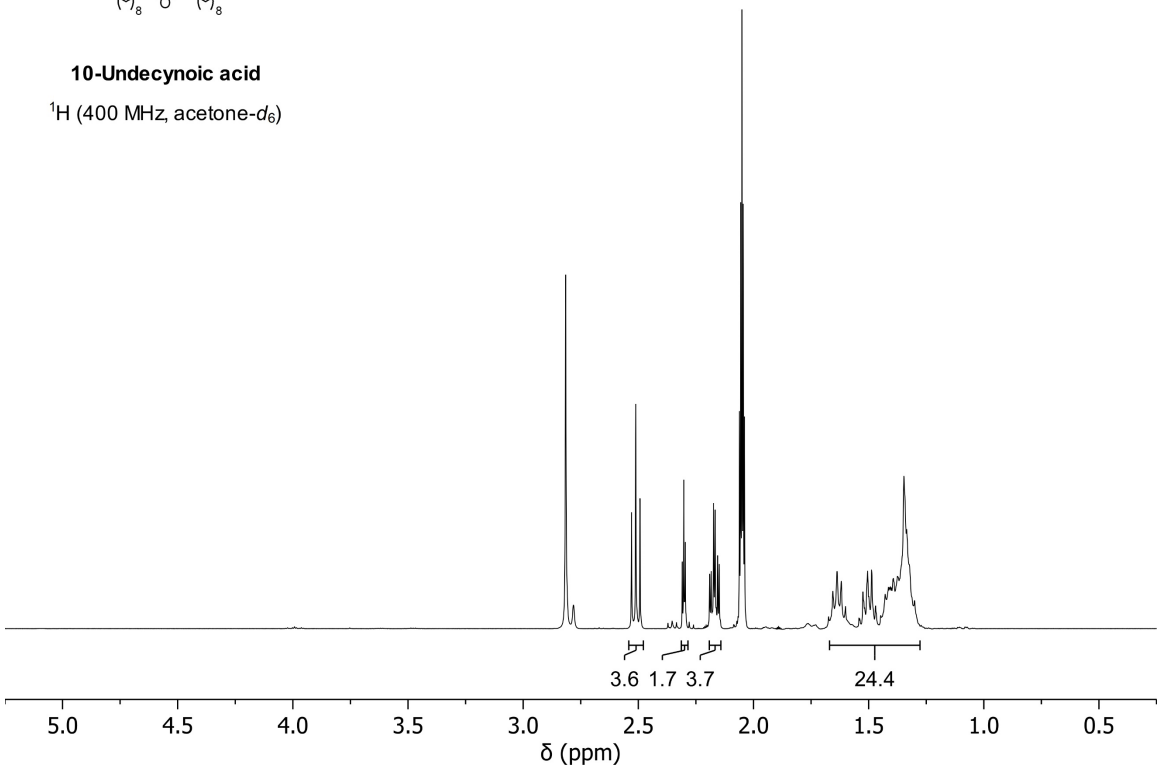

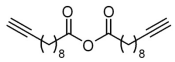

10-Undecynoic acid

^{13}C (101 MHz, $CDCl_3$)

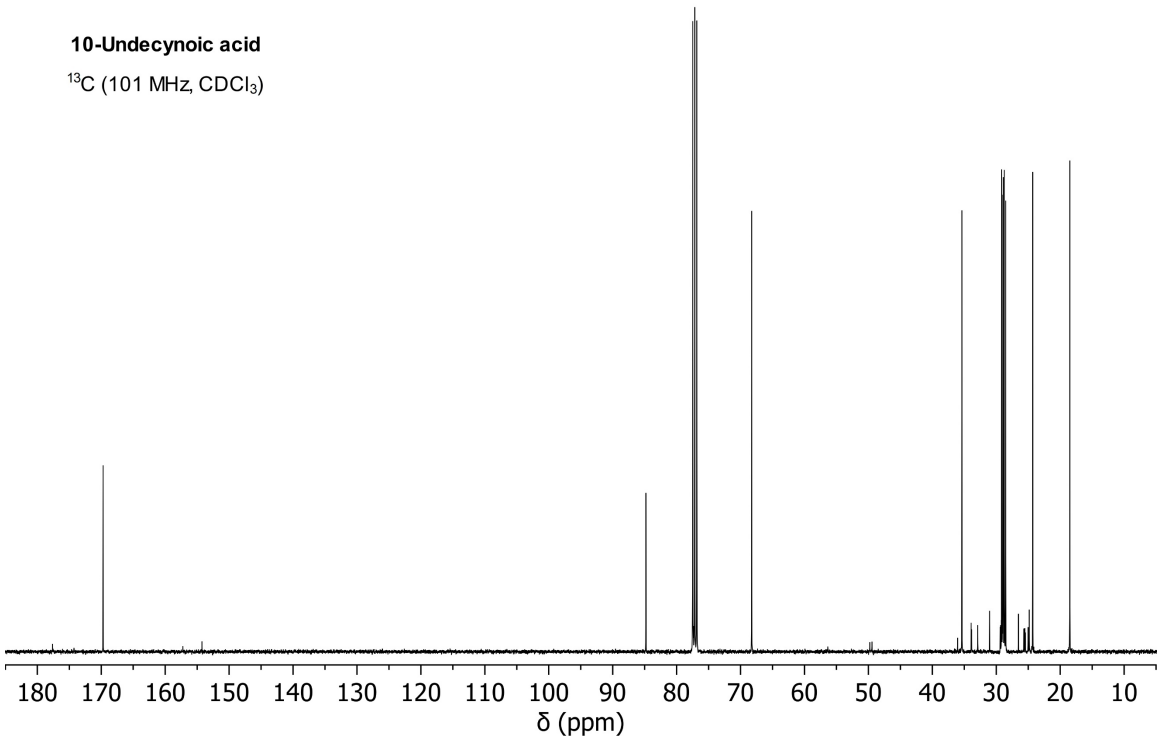

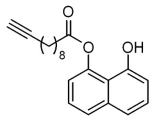

5a

^{1}H (400 MHz, $CDCl_3$)

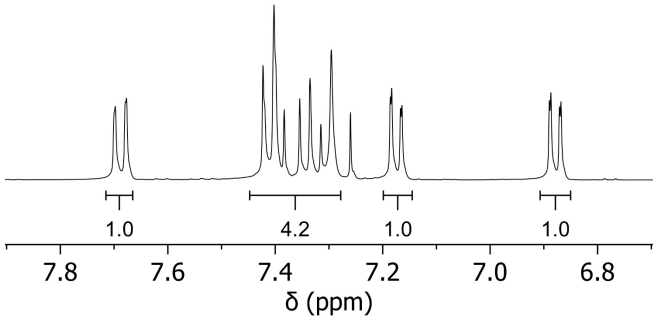

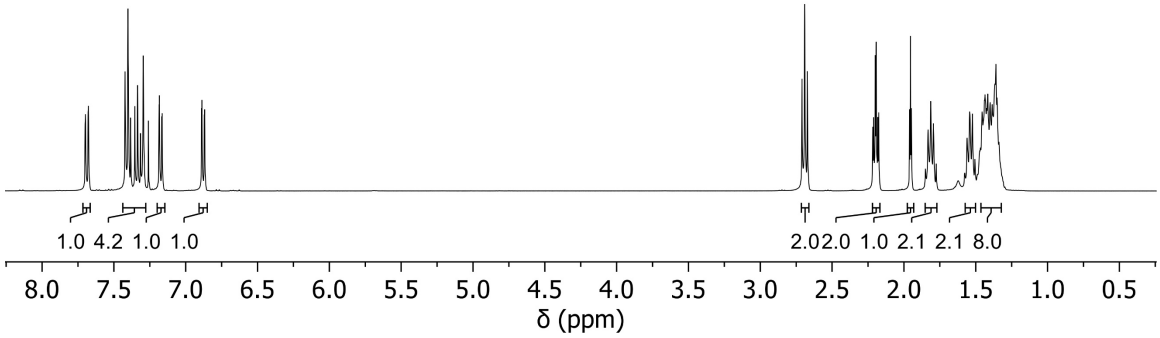

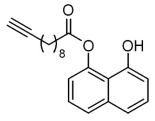

5a

^{13}C (101 MHz, $CDCl_3$)

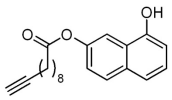

5b

^{1}H (400 MHz, $CDCl_3$)

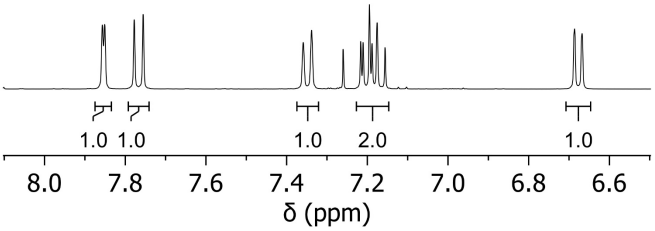

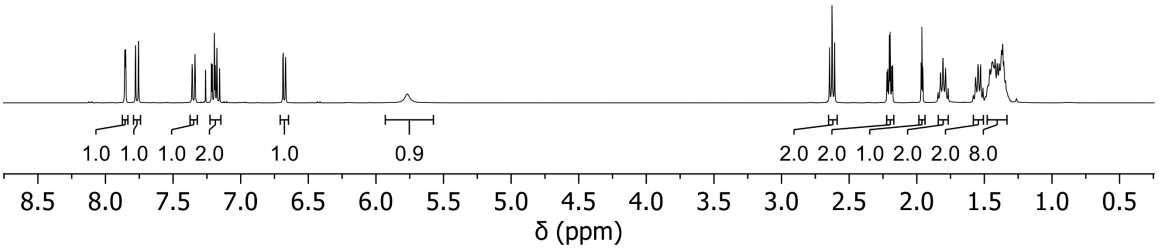

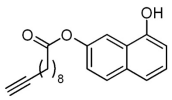

5b

^{13}C (101 MHz, $CDCl_3$)

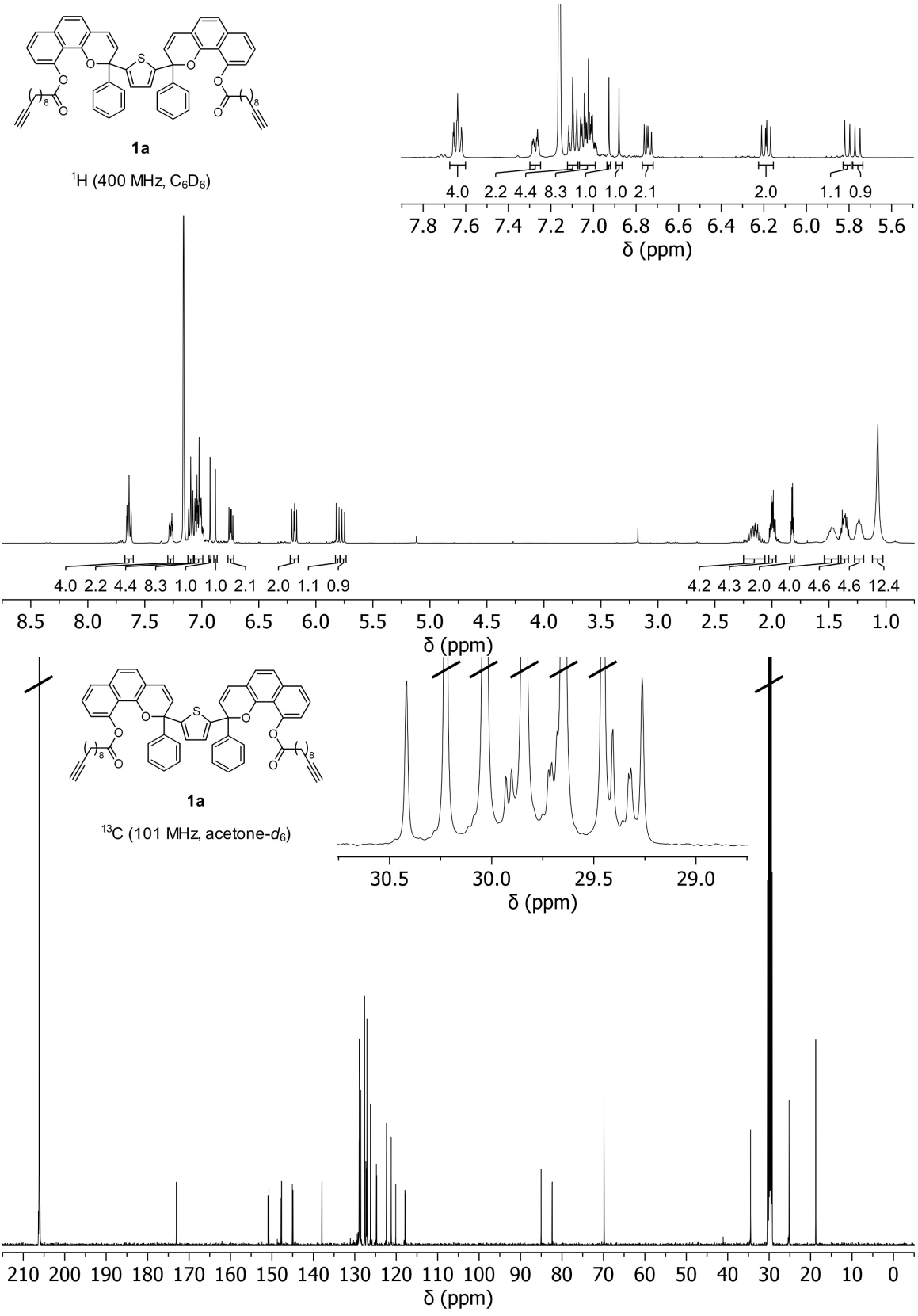
1a
^{1}H (400 MHz, C_6D_6)
4.0 2.2 4.4 8.3 1.0 1.0 2.1 2.0 1.1 0.9
7.8 7.6 7.4 7.2 7.0 6.8 6.6 6.4 6.2 6.0 5.8 5.6
δ (ppm)
4.0 2.2 4.4 8.3 1.0 1.0 2.1 2.0 1.1 0.9
4.2 4.3 2.0 4.0 4.6 4.6 12.4
8.5 8.0 7.5 7.0 6.5 6.0 5.5 5.0 4.5 4.0 3.5 3.0 2.5 2.0 1.5 1.0
δ (ppm)
1a
^{13}C (101 MHz, acetone-d_6)
30.5 30.0 29.5 29.0
δ (ppm)
210 200 190 180 170 160 150 140 130 120 110 100 90 80 70 60 50 40 30 20 10 0
δ (ppm)

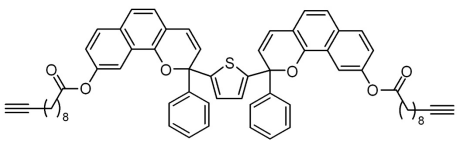

1b

^{1}H (400 MHz, acetone-d_6)

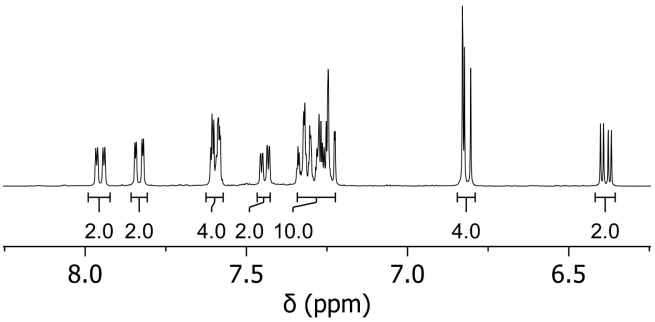

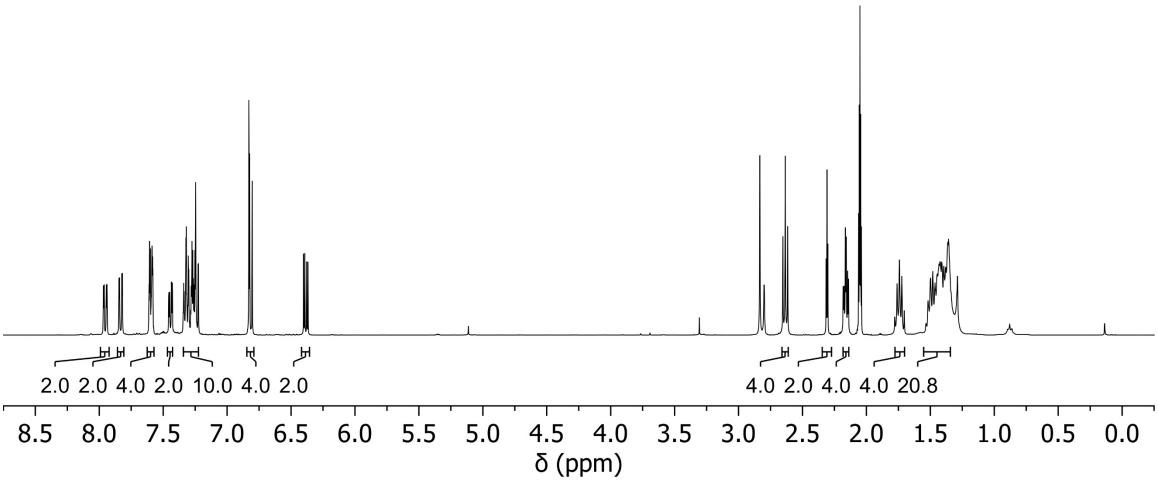

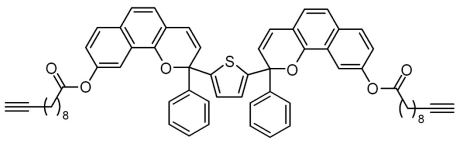

1b

^{13}C (101 MHz, CD_2Cl_2)

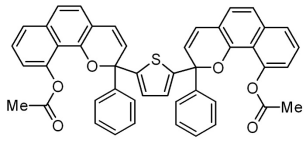

1c

^{1}H (400 MHz, acetone-d_6)

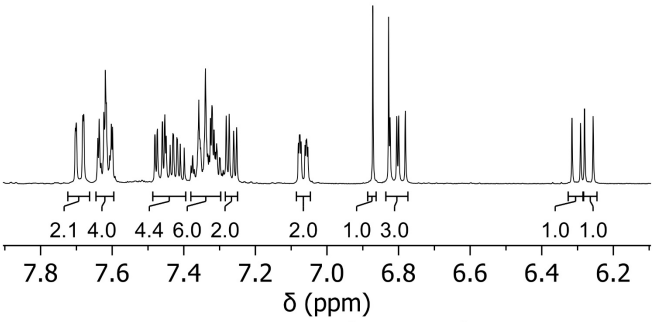

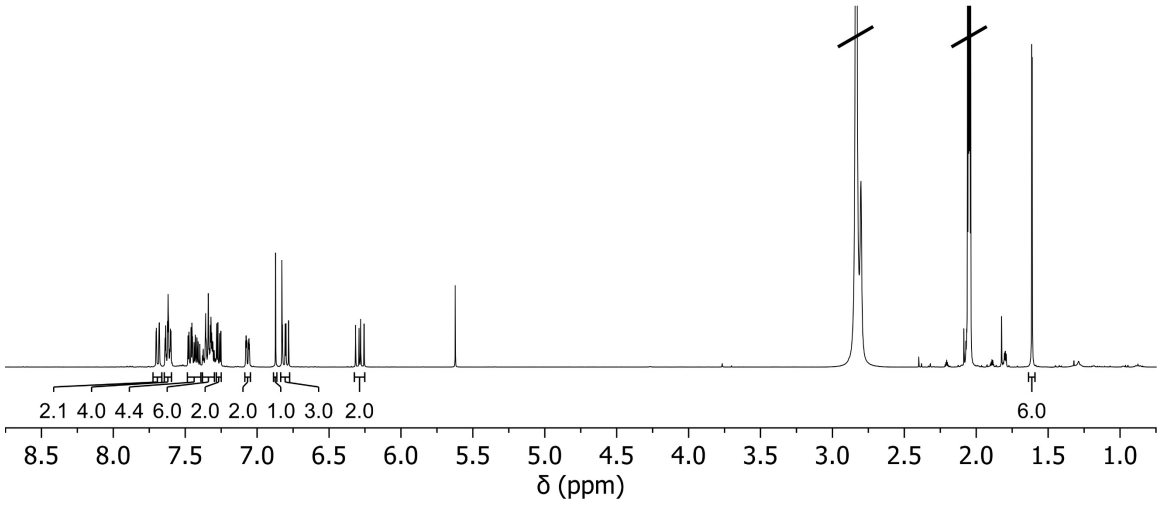

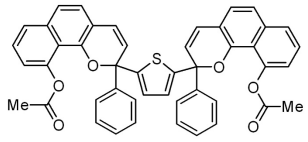

1c

^{13}C (101 MHz, acetone-d_6)

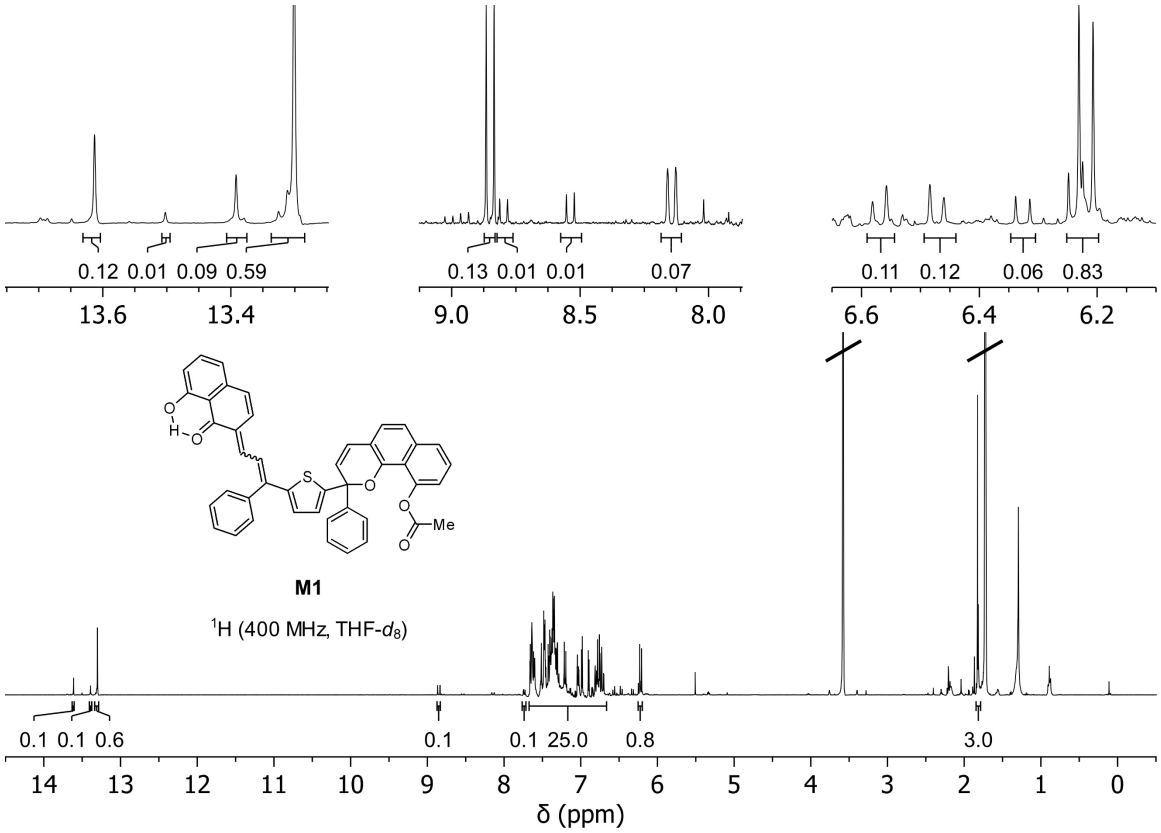
0.12 0.01 0.09 0.59
0.13 0.01 0.01 0.07
0.11 0.12 0.06 0.83
M1
^{1}H (400 MHz, THF-d_8)
0.1 0.1 0.6
0.1
0.1 25.0
0.8
3.0
δ (ppm)

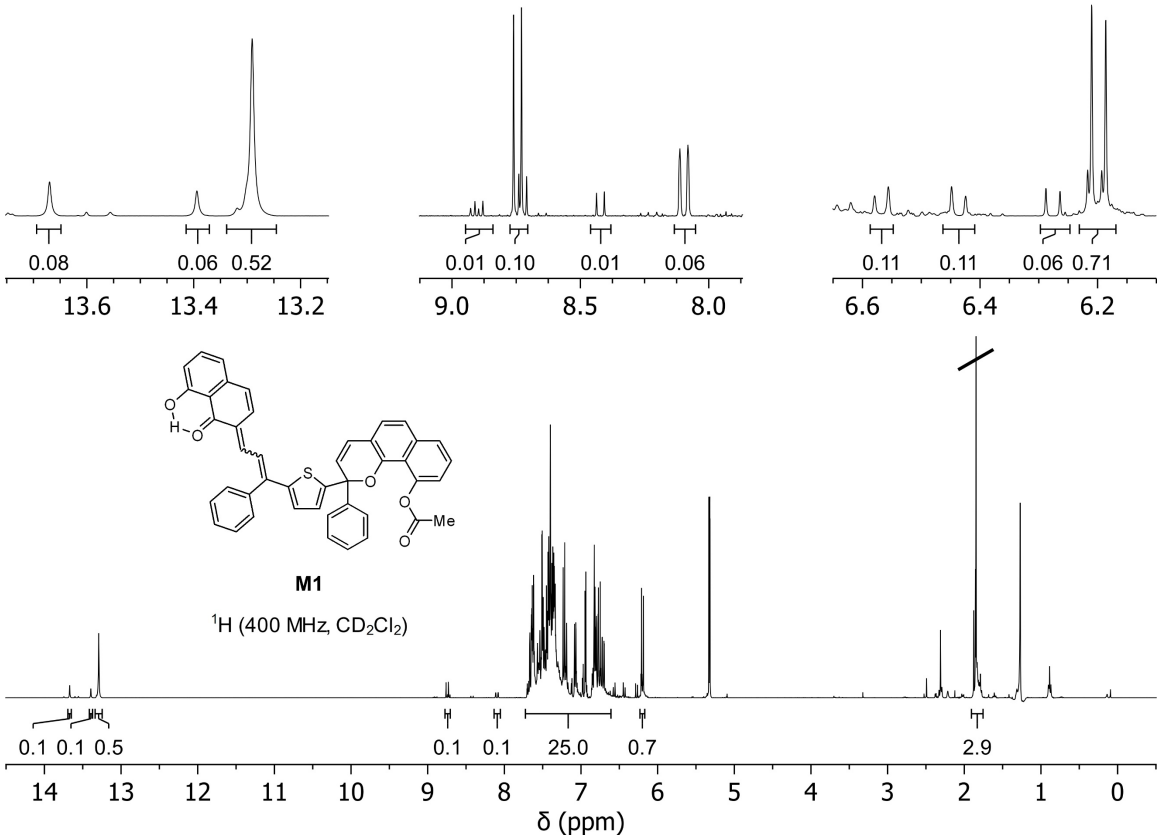
0.08
0.06 0.52
0.01 0.10 0.01 0.06
0.11 0.11 0.06 0.71
M1
^{1}H (400 MHz, CD_2Cl_2)
0.1 0.1 0.5
0.1 0.1
25.0
0.7
2.9
δ (ppm)

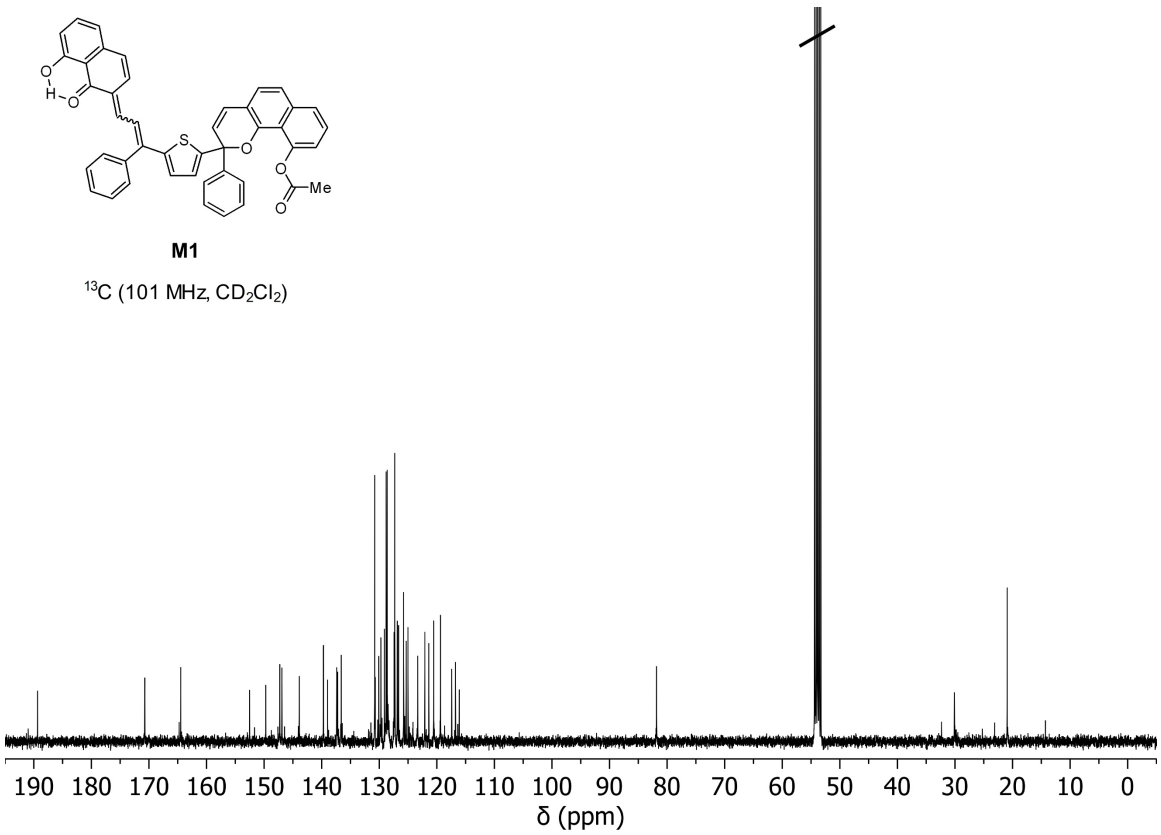
O
H
O
S
O
O
Me
O
M1
13C (101 MHz, CD2Cl2)
190 180 170 160 150 140 130 120 110 100 90 80 70 60 50 40 30 20 10 0
δ (ppm)

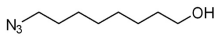

6

^{1}H (400 MHz, $CDCl_3$)

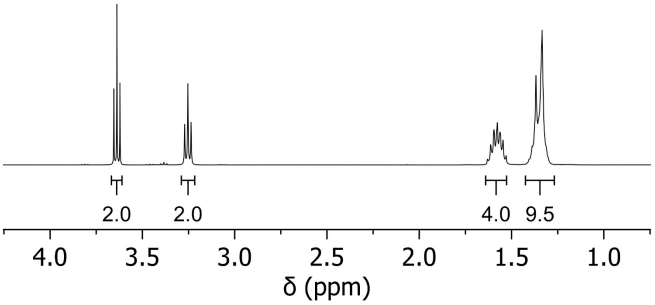

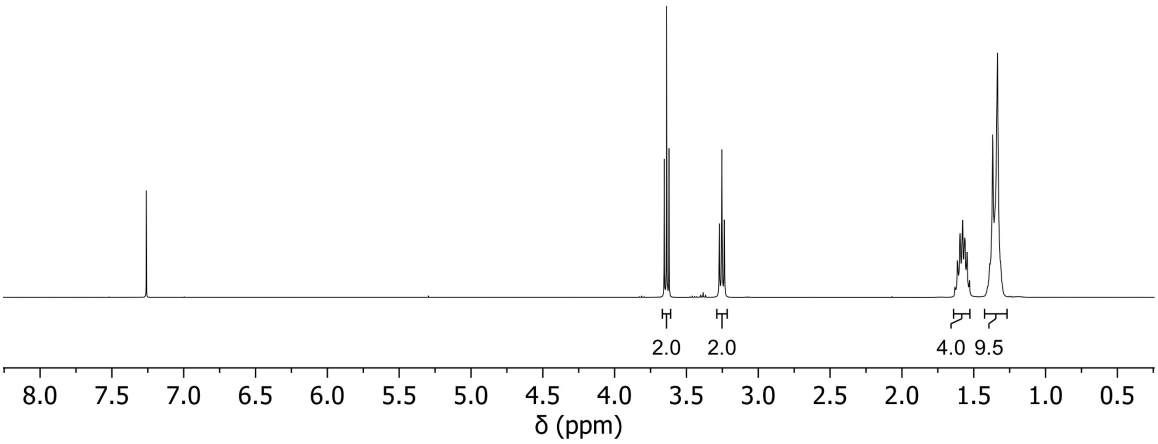

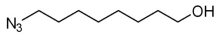

6

^{13}C (101 MHz, $CDCl_3$)

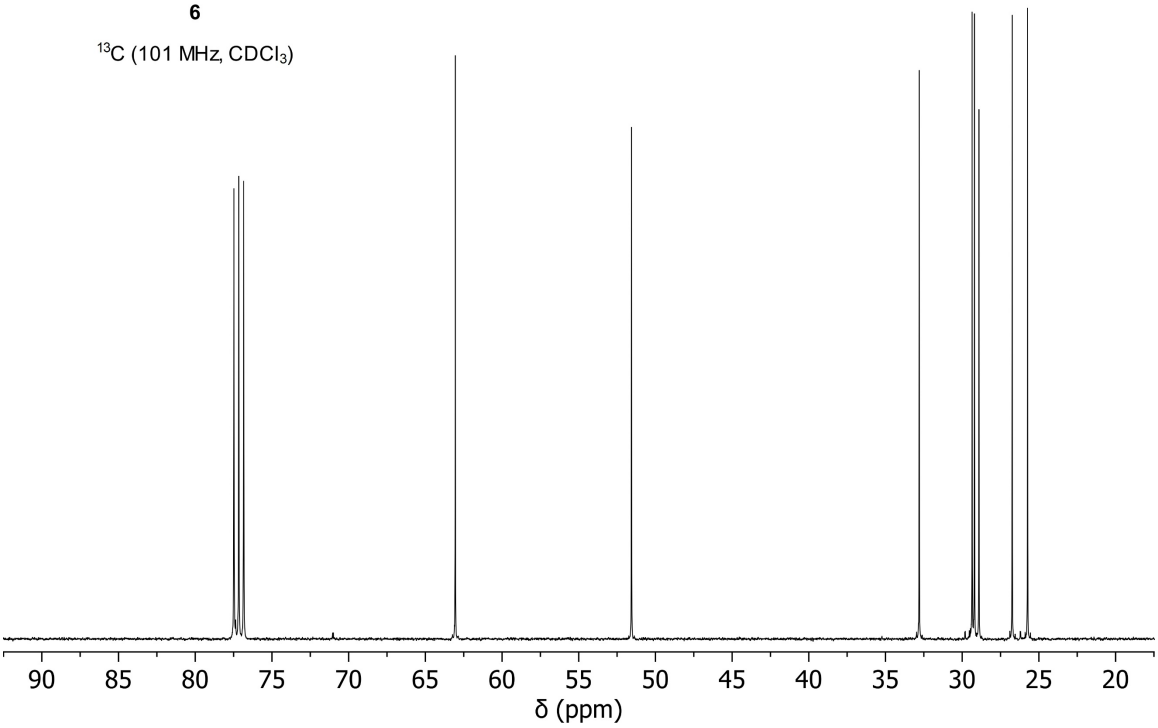

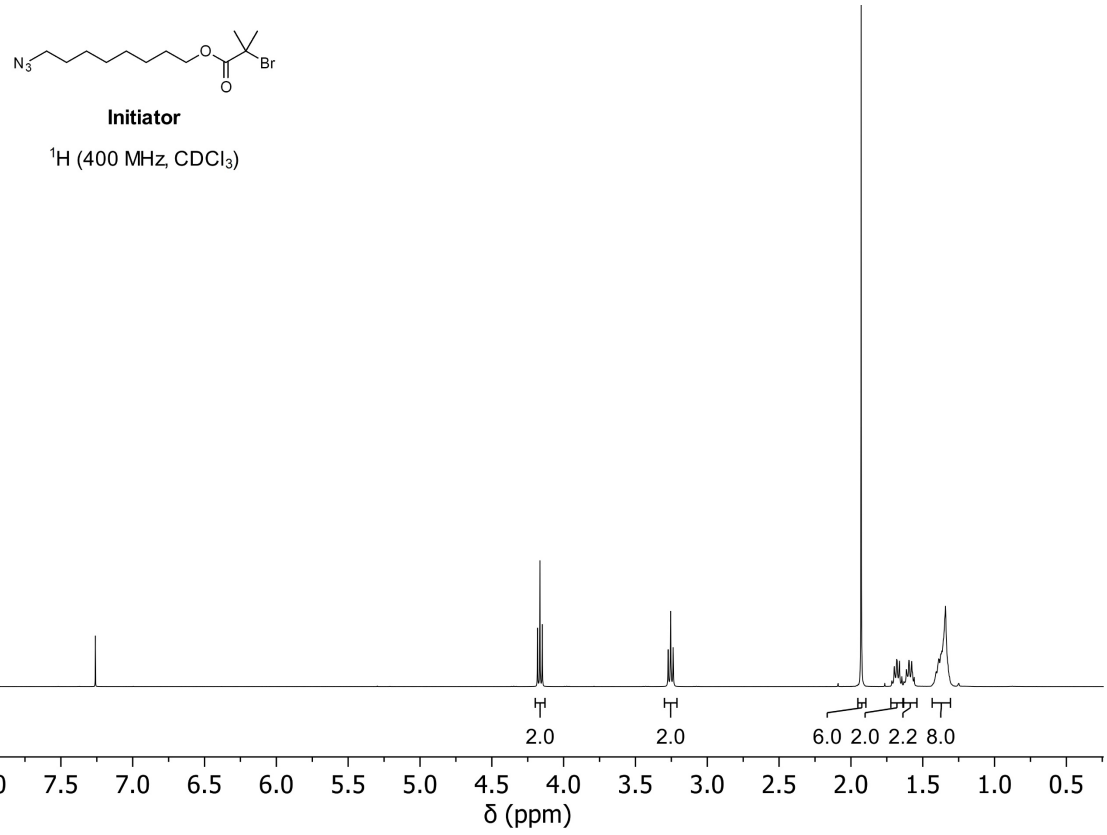
N3
O
O
Br
Initiator
1H (400 MHz, CDCl3)
2.0
2.0
6.0 2.0 2.2 8.0
8.0 7.5 7.0 6.5 6.0 5.5 5.0 4.5 4.0 3.5 3.0 2.5 2.0 1.5 1.0 0.5
δ (ppm)

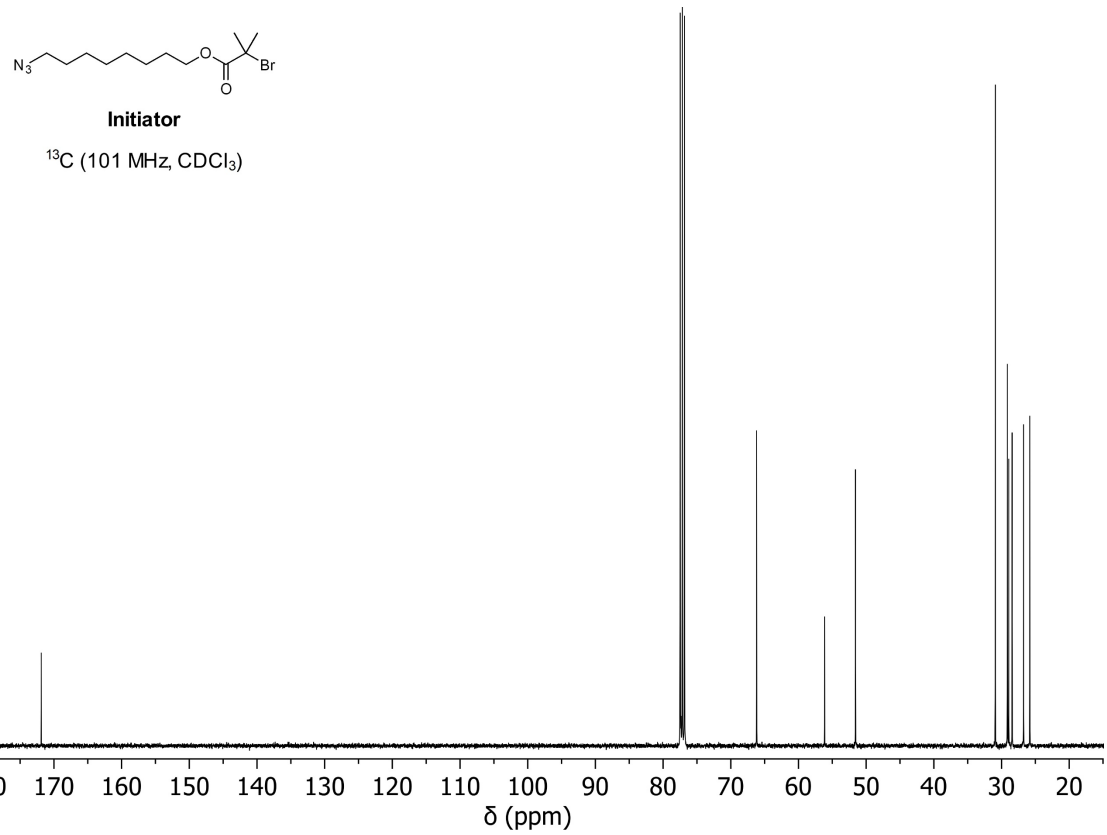
N3
O
O
Br
Initiator
13C (101 MHz, CDCl3)
180 170 160 150 140 130 120 110 100 90 80 70 60 50 40 30 20
δ (ppm)

References

(1) Hepworth, J. D.; Heron, B. M. Photochromic Naphthopyrans. In *Functional Dyes*; Elsevier, 2006; pp 85–135.

(2) Robb, M. J.; Kim, T. A.; Halmes, A. J.; White, S. R.; Sottos, N. R.; Moore, J. S. Regioisomer-Specific Mechanochromism of Naphthopyran in Polymeric Materials. *J. Am. Chem. Soc.* **2016**, *138*, 12328–12331.

(3) Kim, G.; Lau, V. M.; Halmes, A. J.; Oelze, M. L.; Moore, J. S.; Li, K. C. High-Intensity Focused Ultrasound-Induced Mechanochemical Transduction in Synthetic Elastomers. *Proc. Natl. Acad. Sci. U.S.A.* **2019**, *116*, 10214–10222.

(4) Kosuge, T.; Zhu, X.; Lau, V. M.; Aoki, D.; Martinez, T. J.; Moore, J. S.; Otsuka, H. Multicolor Mechanochromism of a Polymer/Silica Composite with Dual Distinct Mechanophores. *J. Am. Chem. Soc.* **2019**, *141*, 1898–1902.

(5) Versaw, B. A.; McFadden, M. E.; Husic, C. C.; Robb, M. J. Designing Naphthopyran Mechanophores with Tunable Mechanochromic Behavior. *Chem. Sci.* **2020**, *11*, 4525–4530.

(6) McFadden, M. E.; Robb, M. J. Force-Dependent Multicolor Mechanochromism from a Single Mechanophore. *J. Am. Chem. Soc.* **2019**, *141*, 11388–11392.

(7) McFadden, M. E.; Robb, M. J. Generation of an Elusive Permanent Merocyanine via a Unique Mechanochemical Reaction Pathway. *J. Am. Chem. Soc.* **2021**, *143*, 7925–7929.

(8) Osler, S. K.; McFadden, M. E.; Robb, M. J. Comparison of the Reactivity of Isomeric 2*H*- and 3*H*-Naphthopyran Mechanophores. *J. Polym. Sci.* **2021**, *59*, 2537–2544.

(9) McFadden, M. E.; Osler, S. K.; Sun, Y.; Robb, M. J. Mechanical Force Enables an Anomalous Dual Ring-Opening Reaction of Naphthodipyran. *J. Am. Chem. Soc.* **2022**, 22391–22396.

(10) Delbaere, S.; Luccioni-Houze, B.; Bochu, C.; Teral, Y.; Campredon, M.; Vermeersch, G. Kinetic and Structural Studies of the Photochromic Process of 3*H*-Naphthopyrans by UV and NMR Spectroscopy. *J. Chem. Soc., Perkin Trans. 2* **1998**, *2*, 1153–1158.

(11) Ottavi, G.; Favaro, G.; Malatesta, V. Spectrokinetic Study of 2,2-Diphenyl-5,6-benzo(2H)chromene: A Thermoreversible and Photoreversible Photochromic System. *J. Photochem. Photobiol. A* **1998**, *115*, 123–128.

(12) Jockusch, S.; Turro, N. J.; Blackburn, F. R. Photochromism of 2 *H* -Naphtho[1,2-b]pyrans: A Spectroscopic Investigation. *J. Phys. Chem. A* **2002**, *106*, 9236–9241.

(13) Arnall-Culliford, J. C.; Teral, Y.; Sgarabotto, P.; Campredon, M.; Giusti, G. New Halogenated Diphenyl-2*H*-benzo[h]chromene Derivatives: Synthesis and Optical Properties. *J. Photochem. Photobiol. A* **2003**, *159*, 7–16.

(14) Delbaere, S.; Vermeersch, G. NMR Characterization of Allenyl-Naphthol in the Photochromic Process of 3,3-Diphenyl-[3*H*]-naphtho[2-1,b]pyran. *J. Photochem. Photobiol. A* **2003**, *159*, 227–232.

(15) Delbaere, S.; Micheau, J.-C.; Vermeersch, G. NMR Kinetic Investigations of the Photochemical and Thermal Reactions of a Photochromic Chromene. *J. Org. Chem.* **2003**, *68*, 8968–8973.

(16) Delbaere, S.; Micheau, J.-C.; Frigoli, M.; Vermeersch, G. Unexpected Halogen Substituent Effects on the Complex Thermal Relaxation of Naphthopyrans after UV Irradiation. *J. Org. Chem.* **2005**, *70*, 5302–5304.

(17) Aiken, S.; Booth, K.; Gabbutt, C. D.; Mark Heron, B.; Rice, C. R.; Charaf-Eddin, A.; Jacquemin, D. The First Structural and Spectroscopic Characterisation of a Ring-Opened Form of a 2*H*-Naphtho[1,2-b]pyran: A Novel Photomerocyanine. *Chem. Commun.* **2014**, *50*, 7900–7903.
(18) Brazevic, S.; Nizinski, S.; Szabla, R.; Rode, M. F.; Burdzinski, G. Photochromic Reaction in 3 *H* -Naphthopyrans Studied by Vibrational Spectroscopy and Quantum Chemical Calculations. *Phys. Chem. Chem. Phys.* **2019**, *21*, 11861–11870.
(19) Brazevic, S.; Baranowski, M.; Sikorski, M.; Rode, M. F.; Burdziński, G. Ultrafast Dynamics of the Transoid- *cis* Isomer Formed in Photochromic Reaction from 3 *H* -Naphthopyran. *Chem. Phys. Chem.* **2020**, *21*, 1402–1407.
(20) Kim, D.; Kwon, M. S.; Lee, C. W. Mechanochromic Polymers with a Multimodal Chromic Transition: Mechanophore Design and Transduction Mechanism. *Polym. Chem.* **2022**, *13*, 5177–5187.
(21) Zhao, W.; Carreira, E. M. A Smart Photochromophore through Synergistic Coupling of Photochromic Subunits. *J. Am. Chem. Soc.* **2002**, *124*, 1582–1583.
(22) Zhao, W.; Carreira, E. M. Synthesis and Photochromism of Novel Phenylene-Linked Photochromic Bispyrans. *Org. Lett.* **2006**, *8*, 99–102.
(23) Zhao, W.; Carreira, E. M. Oligothiophene-Linked Bisnaphthopyrans: Sequential and Temperature-Dependent Photochromism. *Chem. Eur. J.* **2007**, *13*, 2671–2685.
(24) Lu, X.; Dong, Q.; Dong, X.; Zhao, W. Synthesis and Sequential Photochromism of Thiophene-Linked Bis-Pyrans. *Tetrahedron* **2015**, *71*, 4061–4069.
(25) Raisch, M.; Maftuhin, W.; Walter, M.; Sommer, M. A Mechanochromic Donor-Acceptor Torsional Spring. *Nat. Commun.* **2021**, *12*, 4243.
(26) Hertel, R.; Maftuhin, W.; Walter, M.; Sommer, M. Conformer Ring Flip Enhances Mechanochromic Performance of *ansa* -Donor–Acceptor–Donor Mechanochromic Torsional Springs. *J. Am. Chem. Soc.* **2022**, *144*, 21897–21907.
(27) Gossweiler, G. R.; Hewage, G. B.; Soriano, G.; Wang, Q.; Welshofer, G. W.; Zhao, X.; Craig, S. L. Mechanochemical Activation of Covalent Bonds in Polymers with Full and Repeatable Macroscopic Shape Recovery. *ACS Macro Lett.* **2014**, *3*, 216–219.
(28) Kim, T. A.; Robb, M. J.; Moore, J. S.; White, S. R.; Sottos, N. R. Mechanical Reactivity of Two Different Spiropyran Mechanophores in Polydimethylsiloxane. *Macromolecules* **2018**, *51*, 9177–9183.
(29) Wang, T.; Zhang, N.; Dai, J.; Li, Z.; Bai, W.; Bai, R. Novel Reversible Mechanochromic Elastomer with High Sensitivity: Bond Scission and Bending-Induced Multicolor Switching. *ACS Appl. Mater. Interfaces* **2017**, *9*, 11874–11881.
(30) He, W.; Yuan, Y.; Wu, M.; Li, X.; Shen, Y.; Qu, Z.; Chen, Y. Multicolor Chromism from a Single Chromophore through Synergistic Coupling of Mechanochromic and Photochromic Subunits. *Angew. Chem. Int. Ed.* **2023**, *62*, e202218785.
(31) Li, J.; Nagamani, C.; Moore, J. S. Polymer Mechanochemistry: From Destructive to Productive. *Acc. Chem. Res.* **2015**, *48*, 2181–2190.
(32) May, P. A.; Moore, J. S. Polymer Mechanochemistry: Techniques to Generate Molecular Force via Elongational Flows. *Chem. Soc. Rev.* **2013**, *42*, 7497–7506.
(33) Nixon, R.; De Bo, G. Three Concomitant C–C Dissociation Pathways During the Mechanical Activation of an N-Heterocyclic Carbene Precursor. *Nat. Chem.* **2020**, *12*, 826–831.

(34) Berkowski, K. L.; Potisek, S. L.; Hickenboth, C. R.; Moore, J. S. Ultrasound-Induced Site-Specific Cleavage of Azo-Functionalized Poly(ethylene glycol). *Macromolecules* **2005**, *38*, 8975–8978.
(35) Caruso, M. M.; Davis, D. A.; Shen, Q.; Odom, S. A.; Sottos, N. R.; White, S. R.; Moore, J. S. Mechanically-Induced Chemical Changes in Polymeric Materials. *Chem. Rev.* **2009**, *109*, 5755–5798.
(36) May, P. A.; Munaretto, N. F.; Hamoy, M. B.; Robb, M. J.; Moore, J. S. Is Molecular Weight or Degree of Polymerization a Better Descriptor of Ultrasound-Induced Mechanochemical Transduction? *ACS Macro Lett.* **2016**, *5*, 177–180.
(37) Odell, J. A.; Keller, A. Flow-Induced Chain Fracture of Isolated Linear Macromolecules in Solution. *J. Polym. Sci. B Polym. Phys.* **1986**, *24*, 1889–1916.
(38) Beyer, M. K. The Mechanical Strength of a Covalent Bond Calculated by Density Functional Theory. *J. Chem. Phys.* **2000**, *112*, 7307–7312.
(39) Klein, I. M.; Husic, C. C.; Kovács, D. P.; Choquette, N. J.; Robb, M. J. Validation of the CoGEF Method as a Predictive Tool for Polymer Mechanochemistry. *J. Am. Chem. Soc.* **2020**, *142*, 16364–16381.
(40) Smallman, H. R.; Leitch, J. A.; McBride, T.; Ley, S. V.; Browne, D. L. Formation and Utility of Reactive Ketene Intermediates Under Continuous Flow Conditions. *Tetrahedron* **2021**, *93*, 132305.
(41) Boch, R.; Bradley, J. C.; Durst, T.; Scaiano, J. C. Z □ E Photoisomerization of Benzylidenebenzocyclobutenones via Ketene-Allene Intermediates. A Laser Flash Photolysis Study. *Tet. Lett.* **1994**, *35*, 19–22.
(42) Parker, J. K.; Davis, S. R. Photochemical Reaction of Ozone and Benzene: An Infrared Matrix Isolation Study. *J. Am. Chem. Soc.* **1999**, *121*, 4271–4277.
(43) McFadden, M. E.; Robb, M. J. Force-Dependent Multicolor Mechanochromism from a Single Mechanophore. *J. Am. Chem. Soc.* **2019**, *141*, 11388–11392.
(44) Zhao, W.; Carreira, E. M. Facile One-Pot Synthesis of Photochromic Pyrans. *Org. Lett.* **2003**, *5*, 4153–4154.
(45) Nguyen, N. H.; Rosen, B. M.; Lligadas, G.; Percec, V. Surface-Dependent Kinetics of Cu(0)-Wire-Catalyzed Single-Electron Transfer Living Radical Polymerization of Methyl Acrylate in DMSO at 25 °C. *Macromolecules* **2009**, *42*, 2379–2386.
(46) Nixon, R.; De Bo, G. Three Concomitant C–C Dissociation Pathways During the Mechanical Activation of an N-Heterocyclic Carbene Precursor. *Nat. Chem.* **2020**, *12*, 826–831.
(47) Klein, I. M.; Husic, C. C.; Kovács, D. P.; Choquette, N. J.; Robb, M. J. Validation of the CoGEF Method as a Predictive Tool for Polymer Mechanochemistry. *J. Am. Chem. Soc.* **2020**, *142*, 16364–16381.
(48) Yang, J.; Horst, M.; Werby, S. H.; Cegelski, L.; Burns, N. Z.; Xia, Y. Bicyclohexene-*peri* -naphthalenes: Scalable Synthesis, Diverse Functionalization, Efficient Polymerization, and Facile Mechanoactivation of Their Polymers. *J. Am. Chem. Soc.* **2020**, *142*, 14619–14626.
(49) Overholts, A. C.; McFadden, M. E.; Robb, M. J. Quantifying Activation Rates of Scissile Mechanophores and the Influence of Dispersity. *Macromolecules* **2022**, *55*, 276–283.

(50) Caruso, M. M.; Davis, D. A.; Shen, Q.; Odom, S. A.; Sottos, N. R.; White, S. R.; Moore, J. S. Mechanically-Induced Chemical Changes in Polymeric Materials. *Chem. Rev.* **2009**, *109*, 5755–5798.
(51) May, P. A.; Munaretto, N. F.; Hamoy, M. B.; Robb, M. J.; Moore, J. S. Is Molecular Weight or Degree of Polymerization a Better Descriptor of Ultrasound-Induced Mechanochemical Transduction? *ACS Macro Lett.* **2016**, *5*, 177–180.
(52) Aiken, S.; Booth, K.; Gabbutt, C. D.; Mark Heron, B.; Rice, C. R.; Charaf-Eddin, A.; Jacquemin, D. The First Structural and Spectroscopic Characterisation of a Ring-Opened Form of a 2*H*-Naphtho[1,2-b]pyran: A Novel Photomerocyanine. *Chem. Commun.* **2014**, *50*, 7900.

Chapter 3

The Role of Torsion on the Force-Coupled Reactivity of a Fluorenyl Naphthopyran Mechanophore

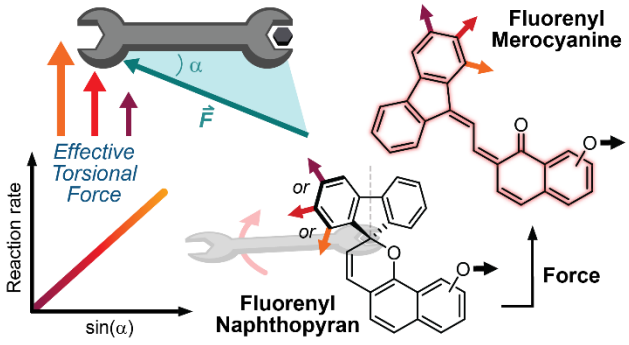

This chapter has been adapted with permission from Osler, S. K.; Ballinger, N. A.; Robb, M. J. The Role of Torsion on the Force-Coupled Reactivity of a Fluorenyl Naphthopyran Mechanophore. *J. Am. Chem. Soc.* **2025**, *147*, 3904–3911. DOI: 10.1021/jacs.4c18395

Abstract

The unique reactivity of molecules under force commands an understanding of structure–mechanochemical activity relationships. While conceptual frameworks for understanding force transduction in many systems are established, systematic investigations into force-coupled molecular torsions are limited. Here, we describe a novel fluorenyl naphthopyran mechanophore for which mechanical force is uniquely coupled to the torsional motions associated with the overall chemical transformation as a result of the conformational rigidity imposed by the fluorene group. Using a combined experimental and theoretical approach, we demonstrate that variation in the pulling geometry on the fluorene subunit results in significant differences in mechanochemical activity due to pronounced changes in how force

is coupled to distinct torsional motions and their coherence with the nuclear motions that accompany the force-free ring-opening reaction. Notably, subtle changes in polymer attachment position lead to a >50% difference in the rate of mechanochemical activation in ultrasonication experiments. Our results offer new insights into the structural and geometric factors that influence mechanochemical reactivity by describing how mechanical force is coupled to a reaction that principally involves torsional motions.

Introduction

Mechanophores are stress-sensitive molecules that undergo productive chemical transformations in response to mechanical force, which is transduced *via* covalently-bound polymer chains.[1–3] Over the past two decades, a wide variety of mechanophores have been developed that can be harnessed to design force-responsive polymers and materials capable of myriad functions such as changes in color or luminescence,[4–7] small molecule release,[8–13] conductivity switching,[14,15] and catalysis.[16,17] Remarkably, the reaction pathways promoted by mechanical force often diverge from those under more conventional thermal or photochemical modes of activation.[18–20] Canonical examples include the mechanochemical ring-opening reactions of benzocyclobutene[21] and *gem*-dihalocyclopropanes,[22] which follow pathways that formally violate classical orbital symmetry rules.

The unique reactivity of molecules under the bias of mechanical force has inspired extensive investigations into structure–mechanochemical activity relationships.[23] At a fundamental level, mechanical force effectively reduces a reaction barrier by coupling mechanical work to the atomic motions inherent to the reaction coordinate.[24] Because force is a vector, the directional nature of mechanical force is a critical factor that influences reactivity. The regiochemistry[25–30] and stereochemistry[22,31] by which the polymers are

connected to the mechanophore dictates the directionality of force transduction, and more specifically, how effectively mechanical force is coupled to elongation of the target scissile bond. Even relatively remote changes in the regiochemistry of polymer attachment on a diphenyl-substituted cyclobutane mechanophore were recently shown to significantly impact reactivity.[32] Likewise, a lever-arm effect associated with both polymer conformation[33] and the stereochemistry of alkene substituents adjacent to the mechanophore[34] reduces the force required for mechanochemical activation by increasing the efficiency of force transduction. A similar effect was implicated in the mechanochemical *cis*-to-*trans* isomerization of tetrahydrofuran-flanked C–C double bonds;[35] however, systematic investigations into force-coupled molecular rotations remain limited. For mechanophore reactions that principally involve rotational motions, we reasoned that effectively coupling external force to torsion would result in more efficient force transduction and greater mechanochemical reactivity.

Naphthopyran mechanophores undergo a ring-opening reaction under mechanical force to generate a colored merocyanine dye (Scheme 3.1a).[19] The tetrahedral carbon center of the pyran ring is typically substituted with two aryl groups, which are oriented perpendicular to the naphthalene core. The conversion of naphthopyran to the merocyanine product is accompanied by rehybridization at that position from Csp3 to Csp2. In effect, mechanical

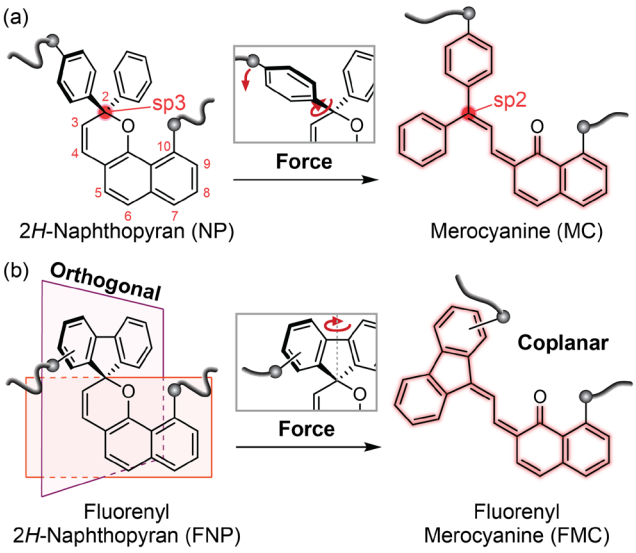

Scheme 3.1. Mechanically activated ring-opening reactions of (a) typical diaryl naphthopyrans, and (b) a conformationally restricted fluorenyl naphthopyran.

force causes a rotation at this diaryl-substituted carbon leading to a new coplanar arrangement in the merocyanine. However, modeling (and intuition) supports that the reaction actually proceeds with significant geometric distortion about the tetrahedral center. The regiochemistry of polymer attachment in archetypal naphthopyrans putatively influences force transduction to the scissile C–O pyran bond by controlling its alignment with the external force vector.[27] We hypothesized, however, that tethering the diaryl substituents at C2 in the form of a fluorene group would increase the conformational rigidity and enable more effective coupling of mechanical force to the torsional motion that accompanies the overall ring-opening reaction (Scheme 3.1b). Furthermore, we reasoned that varying the position of polymer attachment on the fluorene unit would modulate the degree to which mechanical force is coupled to this torsional motion, thereby leading to significant differences in reactivity.

Results and Discussion

We identified three fluorenyl 2*H*-naphthopyran (FNP) structures with polymer attachment *via* an ester linkage at the 10-position and either the *ortho*, *meta*, or *para* position on the fluorene subunit with respect to the pyran ring (Figure 3.1a). We first sought to assess the relative mechanochemical reactivity of the three FNP congeners by performing density functional theory (DFT) calculations using the constrained geometries simulate external force (CoGEF) method on truncated models at the B3LYP/6-31G* level of theory (Figure 3.1b).[23,36] All three FNP regioisomers are predicted to undergo the anticipated ring-opening reaction upon mechanical elongation but at markedly different rupture forces (F_{max}), which span from a relatively low value of 3.7 nN for the *ortho*-FNP isomer to 4.9 nN for the *para*-FNP isomer (Figure 3.1c, Figures S3.6–S3.8). A similar range of F_{max} values (1.1 nN) is

predicted for the mechanochemical ring-opening reactions of an analogous series of FNP structures with polymer attachment *via* an ester linkage at the 9-position of the naphthopyran scaffold (Figures S3.9–S3.11). These results are consistent with the hypothesis that the position of polymer attachment on the fluorene group, rather than on the naphthalene core, differentiates reactivity. Notably, if the aryl substituents at C2 are not constrained by the biaryl bond, not only is a much smaller difference in reactivity predicted with values of F_{max} ranging from 4.1 to 4.5 nN, but the *para*-substituted compound is predicted to be the most reactive (Figures S3.12–S3.14).

To understand the differences in reactivity predicted for the FNP congeners, we examined the geometries of the computed structures from CoGEF calculations immediately prior to C–O bond cleavage to assess how changing the site of polymer attachment on the fluorene group influences mechanochemical coupling. In solid mechanics, the magnitude of the force that contributes to torsion is equal to the component of the incident force vector in

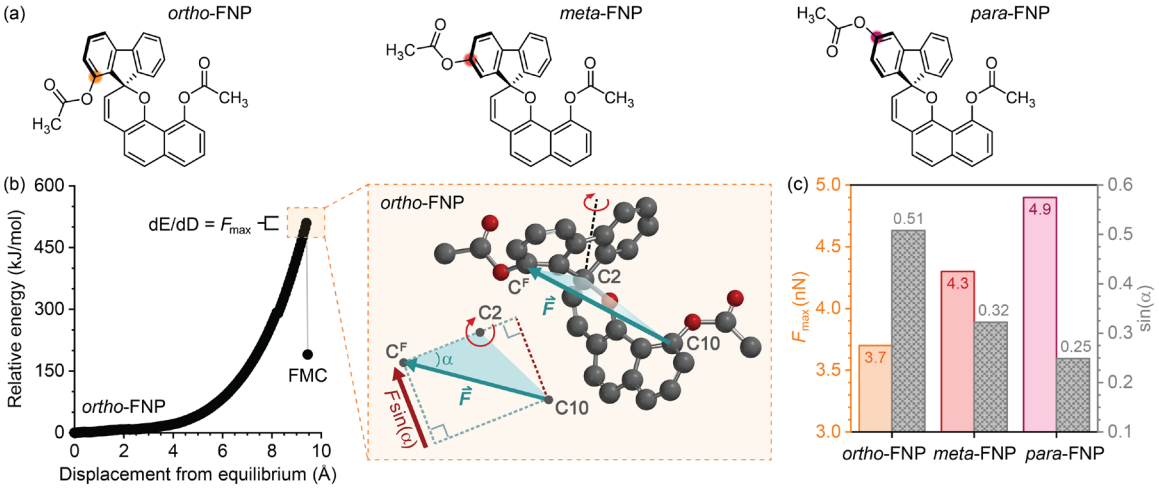

Figure 3.1. Initial geometric analysis performed on model structures of fluorenyl naphthopyran mechanophores. (a) Truncated models of fluorenyl naphthopyrans with polymer attachment at the *ortho*, *meta*, or *para* position on the fluorene subunit. (b) CoGEF calculations (B3LYP/6-31G*) were used to assess the relative reactivity of the fluorenyl naphthopyrans (representative data for the *ortho*-FNP congener shown). Angle α was determined from the computed structures immediately prior to C–O bond cleavage. (c) Relationship between predicted values of F_{max} and the effective torsional force as represented by the magnitude of sin(α).

the plane of rotation perpendicular to the lever arm, or $F\sin(\alpha)$, as illustrated in Figure 3.1b.[37] In this case, the lever arm is defined by the line connecting C2 of the pyran ring and the carbon atom of the fluorene unit (C^F) bearing the ester group, which rotates in the plane defined by C2, C^F, and C10. Carbon atoms C10 and C^F were used to approximate the externally applied force vector (see Experimental Details section).[27] This geometric analysis reveals that the effective torsional force scales linearly with the quantity $\sin(\alpha)$, which is strongly correlated with the trend in reactivity represented by the predicted values of F_{max} (Figure 3.1c). The progressively smaller values of $\sin(\alpha)$ for *ortho*, *meta*, and *para* substitution illustrate the diminishing proportion of the externally applied force that contributes effectively to torsion of the fluorene unit, thereby requiring correspondingly greater force applied to the molecule to achieve the ring-opening reaction. In particular, mechanical force is most efficiently coupled to rotation of the fluorene group in the *ortho*-FNP isomer, which is also expected to have the lowest activation barrier for merocyanine formation under force (*vide infra*). We note that a complete description of torque in this system would involve multiplying the quantity $F\sin(\alpha)$ by the length of the lever arm, r. Using the more complete geometric descriptor of $r\cdot\sin(\alpha)$ produces a similar trend as above with the predicted values of F_{max} (Figure S3.15). To further evaluate the generality of this method, we also performed a similar analysis on two different spiropyran mechanophores that are envisioned to undergo a rotational motion in their ring-opening reactions analogous to that of fluorenyl naphthopyrans.[26] We find that values of $\sin(\alpha)$, $r\cdot\sin(\alpha)$, and F_{max} are similarly correlated (Figure S3.16). Furthermore, the predicted trend in reactivity for the FNP congeners is inversely correlated with the degree of alignment between the external force vector and the pyran C–O bond (Figure S3.17). This observation further supports that the

mechanochemical reactivity of fluorenyl naphthopyran is strongly influenced by force-coupled torsional motions rather than the extensional motions typically considered to drive reactivity in most mechanophores. We return to this idea with a more complete discussion below.

We next set out to experimentally investigate the relative mechanochemical reactivity of the FNP isomers using solution-phase ultrasonication.[1,38] Poly(methyl acrylate) (PMA) polymers ***ortho*-FNP**, ***meta*-FNP**, and ***para*-FNP** were prepared *via* a Cu(I)-catalyzed azide-alkyne cycloaddition (CuAAC) reaction between two equivalents of azide-terminated PMA (**PMA-N$_3$**, M_n = 89.3 kDa; M_p = 98.0 kDa; $Đ$ = 1.08) and the corresponding bis-alkyne-functionalized fluorenyl naphthopyrans (Figure 3.2, see Experimental Details section). Importantly, this convergent synthetic strategy yields mechanophore chain-centered polymers with essentially identical molar mass and molar mass distribution, ensuring that uniform force is applied to each mechanophore during ultrasonication and enabling the direct comparison of mechanophore activation kinetics.[39]

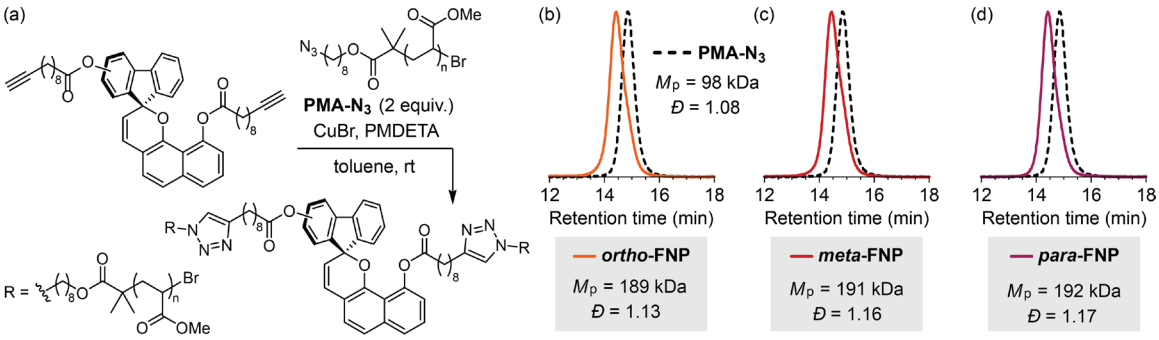

Figure 3.2. Synthesis and characterization of polymers. (a) Synthesis of poly(methyl acrylate) polymers containing a chain-centered FNP mechanophore via Cu-catalyzed azide-alkyne cycloaddition (CuAAC) "click" coupling. Characterization by GPC (RI response shown) confirms successful coupling reactions to generate chain-centered polymers (b) ***ortho*-FNP**, (c) ***meta*-FNP**, and (d) ***para*-FNP**.

Dilute solutions of ***ortho*-FNP**, ***meta*-FNP**, and ***para*-FNP** (2 mg/mL in THF, 30 mM BHT) were subjected to pulsed ultrasonication (−70 ± 5 °C, 1s on / 3 s off, 20 kHz, 6.5 ± 0.1 W cm^{-2}) for 90 min and aliquots were periodically removed for characterization by UV-vis absorption spectroscopy to measure merocyanine accumulation (Figures 3.3a and 3.3b, Figure S3.18). Ultrasound-induced mechanochemical activation of the FNP-containing polymers is expected to generate a persistent merocyanine dye *via* scission of the naphthyl C(O)–O ester bond that accompanies the ring-opening reaction, as observed previously for related naphthopyran scaffolds.[40,41] Nevertheless, we also verified that thermal reversion of the merocyanine dye containing an intact ester group does not occur at these low temperatures, thus guaranteeing the irreversible accumulation of all possible merocyanine products in the sonication experiments (Figure S3.19). The absorption spectra of the mechanochemical reaction products are unchanged 90 min after sonication, further confirming that no merocyanine reversion occurs under the experimental conditions (Figure 3.3b and Figure S3.18). Finally, the absorption spectra obtained upon mechanochemical activation of ***ortho*-FNP**, ***meta*-FNP**, and ***para*-FNP** closely match the spectra of independently prepared small molecule model compounds, indicating that each FNP mechanophore produces the anticipated merocyanine dye (Figure S3.20).

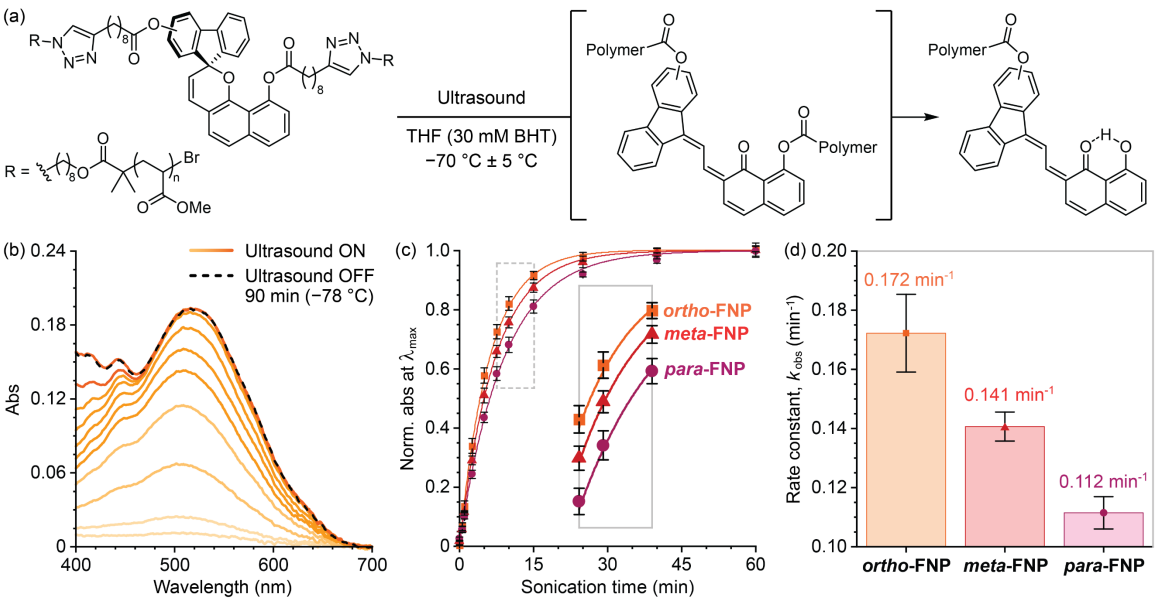

Figure 3.3. Ultrasonication experiments performed on ***ortho*-FNP**, ***meta*-FNP**, and ***para*-FNP**. (a) Ultrasound-induced mechanochemical activation of fluorenyl naphthopyrans results in a ring-opening reaction and ester scission to generate a permanent merocyanine dye. (b) Representative UV-vis absorption spectra acquired during and after the sonication of ***ortho*-FNP**. (c) Absorbance monitored at l_{max} as a function of sonication time for ***ortho*-PMA** (510 nm), ***meta*-PMA** (520 nm), and ***para*-PMA** (525 nm) fit to first order kinetics and normalized to the plateau value. Data points and error bars represent average values and standard deviation from 3–4 replicate trials. (d) Rate constants (k_{obs}) for merocyanine accumulation determined from the data in (c).

The rate of mechanochemical merocyanine formation for each mechanophore was determined by fitting the time-dependent absorbance values at the observed λ_{max} to an expression of simple first-order kinetics (Figure 3.3c, see Experimental Details section). Average values of the observed rate constant, k_{obs}, for each mechanophore were determined from 3–4 replicate trials (Figure 3.3d). The relative rate of merocyanine formation follows the order ***ortho*-FNP** (most reactive) > ***meta*-FNP** > ***para*-FNP** (least reactive), in agreement with the trend predicted from CoGEF calculations. Analysis using an unpaired *t* test confirms that the differences in the measured rate constants are statistically significant ($p < 0.05$). Control experiments also confirm that the observed kinetics are not convoluted by either the secondary ester scission reaction or variation in the rate of nonspecific backbone scission.

Reaction rates for an analogous series of FNP mechanophores with polymer attachment at the 9-position of the naphthopyran, which do not undergo ester scission to generate a persistent merocyanine,[40,41] follow the same trend as above with rate constants for the *ortho*- and *para*-substituted mechanophores closely matching those of ***ortho*-FNP** and ***para*-FNP**, respectively, while the *meta*-substituted mechanophore reacts at an intermediate rate (Figure S3.21–S3.23). Notably, k_{obs} represents the sum of the rate constants for mechanophore activation and nonspecific backbone scission, which is always a competing pathway.[42,43] GPC measurements further confirmed that the rate of nonspecific backbone scission is invariant with changes in the attachment geometry on the fluorene group (Figure S3.24, see Experimental Details section). Mechanochemical activation rates were also determined for another series of polymers with M_p ~ 150 kDa incorporating chain-centered *ortho*-FNP, *meta*-FNP, and *para*-FNP mechanophores, revealing the same trend in reactivity with average values of k_{obs} of 0.128, 0.107, and 0.082 min^{-1}, respectively (Figure S3.25, see Experimental Details section). These results further support that the significant differences in mechanochemical activity for the regioisomeric FNP mechanophores are conserved across different batches of polymers and for polymers of substantially different molar mass.

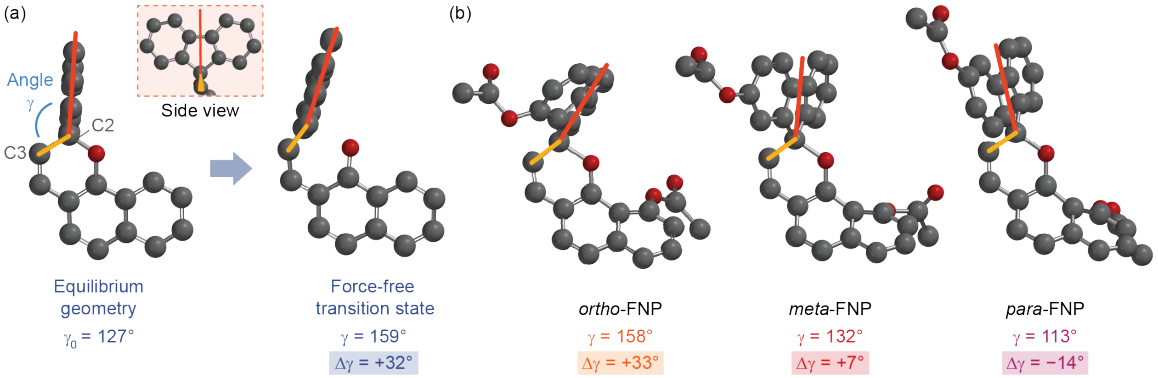

Figure 3.4. Geometric analysis of angle γ from DFT calculations. (a) Optimized geometries calculated by DFT for unsubstituted fluorenyl naphthopyran and the force-free transition state structure (B3LYP/6-31G*). (b) Truncated models of ***ortho*-FNP**, ***meta*-FNP**, and ***para*-FNP** from CoGEF calculations immediately prior to C–O bond cleavage. The angle γ is defined by a line bisecting the fluorene group and the bond between carbons C2 and C3.

To better understand the impact of polymer attachment position on the mechanochemical reactivity of the FNP mechanophore system, we consider the changes in molecular geometry associated with the force-free ring-opening reaction that are distinct from the rotational motions considered previously (Figure 3.4). Progression from the equilibrium geometry of fluorenyl naphthopyran to the force-free transition state is accompanied by a significant increase (+32°) in the angle γ defined by a line that bisects the fluorene group and the C2–C3 bond (Figure 3.4a). Ring opening of the pyran is accompanied by rehybridization of C2 from Csp3 to Csp2, which causes an increase in angle γ approaching 180° in the merocyanine product. Interestingly, CoGEF calculations predict this same torsional motion to be well-coupled to mechanical elongation of the *ortho*-FNP mechanophore; γ is similarly increased by 33° in the structure immediately prior to C–O bond cleavage relative to the starting material (Figure 3.4b, Figure S3.26). In contrast, only a slight increase in g of 7° is observed for the *meta*-FNP analogue, while mechanical elongation of the *para*-FNP model actually decreases γ from 127° to 113° prior to bond rupture. The correlation between the rate of

mechanophore activation and Δγ suggests that the pulling geometry not only dictates the efficiency with which mechanical force is coupled to the rotation of the fluorene group as described earlier, but secondary structural effects[44–46] strongly influence the coherence with which the torsional motions under applied tension mimic the natural nuclear motions associated with the ring-opening reaction and thus mechanochemical coupling. We note that similar secondary structural effects from rehybridization have been previously reported by Craig and coworkers to describe the mechanochemical dissociation of phenyl benzyl ether, for example, which is less labile than expected due to an overall molecular contraction that occurs during C–O bond elongation that is poorly coupled to an applied force of tension.[44]

The structures obtained from CoGEF calculations immediately prior to C–O bond cleavage offer a compelling snapshot of the mechanochemical reaction, but fail to quantitatively describe the energetic and geometric changes that occur over the relevant range of forces. Therefore, we performed DFT calculations using the external force is explicitly included (EFEI) method[47,48] on the same truncated models used in the CoGEF calculations to quantify how the reaction barriers and molecular geometries, including angle γ, evolve as a function of external force (Figure 3.5, see Experimental Details section). In agreement with the experimental kinetic data and CoGEF calculations, the EFEI calculations predict that the barrier ($\Delta E^{\ddagger}$) of the naphthopyran ring-opening reaction is lowest for *ortho*-FNP and highest for *para*-FNP at all forces (Figure 3.5a). The dashed grey line in Figure 3.5a represents the activation barrier (6.3 kcal/mol) below which the thermal ring-opening reaction is expected to occur rapidly on the microsecond timescale of cavitation-induced chain extension during ultrasonication at −70 °C (see Experimental Details section).[38,49] At this threshold of $\Delta E^{\ddagger}$, the ring-opening reaction requires approximately 2.1, 2.5, and 3.0 nN

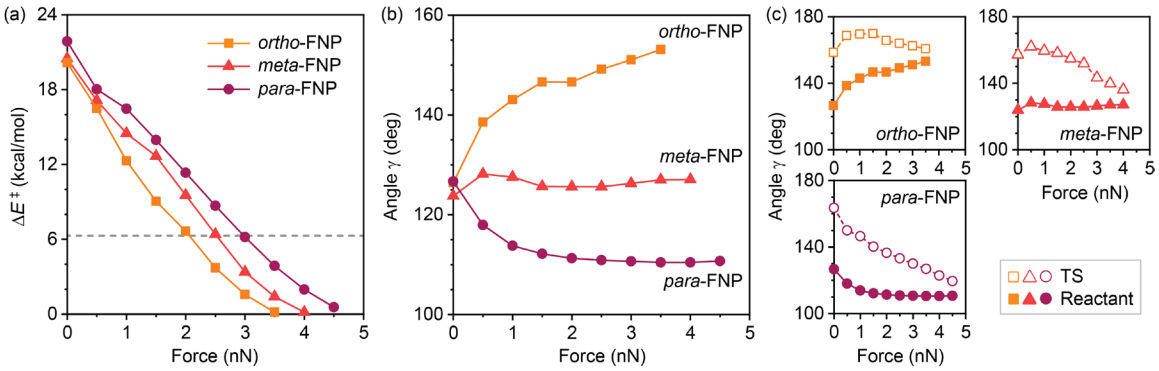

Figure 3.5. EFEI calculations performed on truncated models of the fluorenyl naphthopyrans. (a) Calculated barrier height ($\Delta E^{\ddagger}$) for naphthopyran ring opening as a function of applied force from EFEI calculations (uB3LYP-D3BJ/def2-TZVPP). The dashed grey line represents the activation barrier (6.3 kcal/mol) below which the thermal ring-opening reaction is expected to occur rapidly at −70 °C. (b) Angle γ in each fluorenyl naphthopyran congener, and (c) comparison of angle γ between the transition state (TS) and reactant structures as a function of applied force.

of force for *ortho*-FNP, *meta*-FNP, and *para*-FNP, respectively. Thus, the calculated barriers support that the mechanochemical reactivity of FNP mechanophores follows the order *ortho*-FNP > *meta*-FNP > *para*-FNP consistent with the experimental observations and CoGEF calculations.

To confirm that the secondary structural effects involving the torsional motion of the fluorene group illustrated in Figure 3.4 are not merely a consequence of varying degrees of distortion at different forces resulting from changes in the pulling geometry, we examined how angle γ evolves as a function of applied force in structures from the EFEI calculations (Figure 3.5b). At low force (0.5 nN), a sharp increase in angle γ from 126° to 139° is observed for *ortho*-FNP, which continues to increase toward linearity reaching 153° at 3.5 nN of applied force. This trend is consistent with the CoGEF predictions described above and replicates the geometric changes associated with the expected rehybridization at C2 from sp3 to sp2 that accompanies the naphthopyran ring-opening reaction. In contrast, only a small

increase in angle γ of 4° is observed for *meta*-FNP at 0.5 nN, and γ remains relatively constant across the range of forces studied up to 4 nN. For *para*-FNP, angle γ decreases from 127° to 118° at 0.5 nN and steadily reaches a minimum of 110° at 4.5 nN of applied force. Again, the force-induced nuclear distortions of *para*-FNP oppose the natural torsional motions of the fluorene group that accompany rehybridization at C2. These observations strongly support the results from CoGEF calculations above and confirm that the highly differentiated changes in reactant geometry for each FNP congener are evident across the entire range of relevant forces.

Results of the EFEI calculations also provide further insight into the force-modified potential energy surface by illustrating how the transition state geometries of the FNP mechanophores evolve relative to the reactant structures as a function of applied force (Figure 3.5c). Similar to the transition state structure of the unsubstituted fluorenyl naphthopyran model illustrated in Figure 4.4a, angle γ is approximately 160° in the force-free transition state structure of each FNP regioisomer. Upon increasing the applied force from 0.5 nN to 4.5 nN, the difference in angle g between respective reactant and transition state structures decreases as the transition state geometries become more "reactant-like".[25] That is, consistent with Hammond's postulate, angle γ converges as the reactant and transition state structures of each FNP mechanophore become exceedingly similar upon lowering the reaction barrier with increasing applied force; the force at which angle γ converges reflects the relative mechanochemical activity of each FNP congener. This convergent behavior further supports that the changes in angle γ describe a motion that is coupled to the naphthopyran ring-opening reaction.

Finally, we sought to further understand the importance of torsion by examining other factors that may contribute to the force-coupled reactivity of fluorenyl naphthopyran mechanophores. Using structures from the EFEI calculations, we interrogated alternative molecular motions including torsion of the pyran ring as well as the naphthalene core; however, these molecular distortions are poorly coupled to either external force or the natural atomic motions accompanying the thermal ring-opening reaction, respectively (Figure S3.27–S3.28). We further examined the FNP mechanophores in the context of other popular methods for describing mechanochemical coupling. As mentioned above, force vector alignment analysis[27] reveals that *para*-FNP exhibits the best alignment between the external force vector and the labile C–O bond while *ortho*-FNP exhibits the poorest alignment (see Figure S3.17). While only qualitative, this trend is nevertheless in direct contrast to the theoretically predicted and experimentally observed relative reactivities of the FNP mechanophores and suggests that the externally applied force is not directly coupled to the elongation and rupture of the C–O pyran bond to induce the ring-opening reaction. Activation length ($\Delta x^{\ddagger}$) is a more quantitative descriptor of mechanochemical coupling[24] that has been used extensively to describe the relative activity of various mechanophores including *gem*-dihalocyclopropanes,[33,34] benzocyclobutenes,[50] spiropyrans,[26] and furan–maleimide Diels–Alder adducts[51]. The activation length reflects the extension in the transition state relative to the reactant structure projected along the external force vector. For reactions with similar force-free activation energies, such as the case of the FNP mechanophores, a transformation that is better coupled to a force of tension would be expected to have a larger value of $\Delta x^{\ddagger}$ and exhibit a faster rate of reaction at a given force or under similar experimental conditions. Notably, activation length analysis reveals similar values of $\Delta x^{\ddagger}$ for *ortho*-FNP, *meta*-FNP,

and *para*-FNP (0.57, 0.45, and 0.45 Å, respectively) despite the significant differences in measured mechanochemical activation rates (Figure S3.29, see Experimental Details section). In particular, the identical values of $\Delta x^{\ddagger}$ for *meta*-FNP and *para*-FNP strongly suggests that mechanochemical coupling does not arise from the direct elongational activation of the C–O pyran bond for the fluorenyl naphthopyran mechanophores. Taken together, the inconsistency of these models with the theoretically predicted and experimentally determined activities of the fluorenyl naphthopyran mechanophores further supports that mechanochemical reactivity in this system is differentiated by changes in force-coupled torsional motions distinct from more conventional frameworks for describing mechanochemical coupling.

Conclusions

In summary, we describe the mechanochemical reactivity of a series of regioisomeric fluorenyl naphthopyran mechanophores. Unlike typical diaryl naphthopyrans, the conformational rigidity of the fluorene group enforces well-defined torsional motions in the ring-opening reaction leading to the merocyanine product. Our results demonstrate that the efficiency with which external force is coupled to the rotation of the fluorene unit varies systematically depending on the position of polymer attachment. Moreover, variation in pulling geometry is shown to significantly impact the torsional motion of the fluorene group with respect to its coherence with the natural nuclear motions associated with the force-free ring-opening reaction. These aspects are fundamental in dictating mechanochemical coupling, and therefore the relative mechanochemical reactivity of the fluorenyl naphthopyran mechanophores. This study offers new insights into the structural features that

govern mechanochemical reactions and, in particular, how mechanical work is coupled to chemical transformations that principally involve torsional motions.

Acknowledgements

Financial support from an NSF CAREER award (CHE-2145791) and the Rose Hills Foundation Innovator Award is gratefully acknowledged. We thank Molly E. McFadden, Soren Holm, and Ilia Kevlishvili for helpful discussions. We thank the Center for Catalysis and Chemical Synthesis of the Beckman Institute at Caltech for access to equipment and the Resnick High Performance Computing Center, a facility supported by Resnick Sustainability Institute at Caltech. M.J.R. gratefully acknowledges the Alfred P. Sloan Foundation for a Sloan Research Fellowship and the Camille and Henry Dreyfus Foundation for a Camille Dreyfus Teacher-Scholar Award.

Experimental Details

I. General Experimental Details

Reagents from commercial sources were used without further purification unless otherwise stated. Methyl acrylate was passed through a short plug of basic alumina to remove inhibitor immediately prior to use. Copper wire was soaked in 1 M HCl for 10 min and then rinsed consecutively with water, acetone, and dichloromethane immediately prior to use. Dry THF was obtained from a Pure Process Technology solvent purification system. All reactions were performed under a N_2 atmosphere unless specified otherwise. Column chromatography was performed on a Biotage Isolera system using SiliCycle SiliaSep HP flash cartridges.

NMR spectra were recorded using either a 400 MHz Bruker Avance III HD with Prodigy Cryoprobe or a 600 MHz Varian spectrometer with 5 mm triple resonance inverse probe. All

^{1}H NMR spectra are reported in δ units, parts per million (ppm), and were measured relative to the signals for residual chloroform (7.26 ppm), acetone (2.05 ppm), or dichloromethane (5.32 ppm) in deuterated solvent. All ^{13}C NMR spectra were measured in deuterated solvents and are reported in ppm relative to the signals for chloroform (77.16 ppm), acetone (206.26 ppm), or dichloromethane (53.84 ppm). Multiplicity and qualifier abbreviations are as follows: s = singlet, d = doublet, t = triplet, m = multiplet, br = broad, app = apparent.

High resolution mass spectra (HRMS) were obtained via direct injection on an Agilent 1260 Infinity II Series HPLC coupled to a 6230 LC/TOF system in electrospray ionization (ESI+ or ESI-) mode.

Analytical gel permeation chromatography (GPC) was performed using an Agilent 1260 series pump equipped with two Agilent PLgel MIXED-B columns (7.5 x 300 mm), an Agilent 1200 series diode array detector, a Wyatt miniDAWN 3-angle light scattering detector, and an Optilab differential refractive index detector. The mobile phase was THF at a flow rate of 1 mL/min. Molecular weights and molecular weight distributions were calculated by light scattering using a dn/dc value of 0.062 mL/g (25 °C) for poly(methyl acrylate).

UV-vis absorption spectra were recorded on a Thermo Scientific Evolution 220 spectrometer.

Ultrasound experiments were performed using a Vibra Cell 505 liquid processor equipped with a 0.5-inch diameter solid probe (part #630-0217), sonochemical adapter (part #830-00014), and a Suslick reaction vessel made by the Caltech glass shop (analogous to vessel #830-00014 from Sonics and Materials). A dry ice/acetone bath was used to maintain a constant temperature for sonication experiments. Photoirradiation with UV light was

performed using a DR/9W-UVA 365 nm lamp under ambient conditions unless indicated otherwise.

PMA-N_3, **PMA-N_3-79**, 10-undecynoic anhydride, 8-hydroxynaphthalen-1-yl undec-10-ynoate, and 8-hydroxynaphthalen-2-yl undec-10-ynoate were synthesized according to the reported literature method.[41]

II. Supplementary Figures

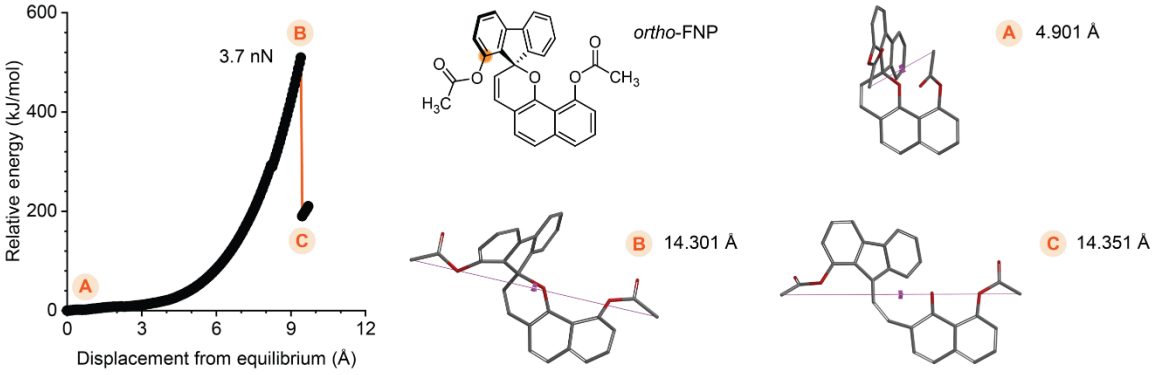

Figure S3.6. Density functional theory (DFT) calculations using the constrained geometries simulate external force (CoGEF) method performed on a truncated model of the *ortho*-FNP mechanophore with attachment points at the *ortho*-position of the fluorene subunit and the 10-position of the naphthopyran. Computed structures are shown at right that correspond to the indicated points in the CoGEF profile along with the associated constraint distance between the terminal methyl groups. The ring-opening reaction is predicted to occur at a maximum force of 3.7 nN. Calculations were performed at the B3LYP/6-31G* level of theory.

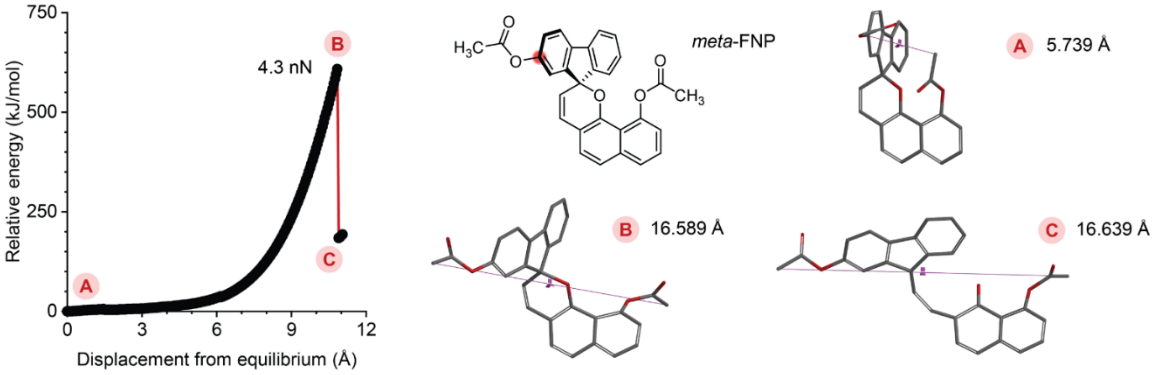

Figure S3.7. Density functional theory (DFT) calculations using the constrained geometries simulate external force (CoGEF) method performed on a truncated model of the *meta*-FNP mechanophore with attachment points at the *meta*-position of the fluorene subunit and the 10-position of the naphthopyran. Computed structures are shown at right that correspond to the indicated points in the CoGEF profile along with the associated constraint distance between the terminal methyl groups. The ring-opening reaction is predicted to occur at a maximum force of 4.3 nN. Calculations were performed at the B3LYP/6-31G* level of theory.

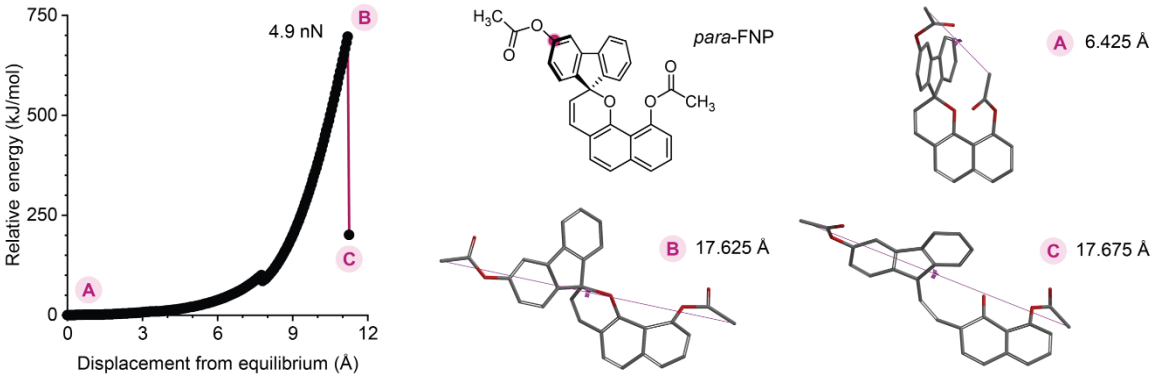

Figure S3.8. Density functional theory (DFT) calculations using the constrained geometries simulate external force (CoGEF) method performed on a truncated model of the *para*-FNP mechanophore with attachment points at the *para*-position of the fluorene subunit and the 10-position of the naphthopyran. Computed structures are shown at right that correspond to the indicated points in the CoGEF profile along with the associated constraint distance between the terminal methyl groups. The ring-opening reaction is predicted to occur at a maximum force of 4.9 nN. Calculations were performed at the B3LYP/6-31G* level of theory.

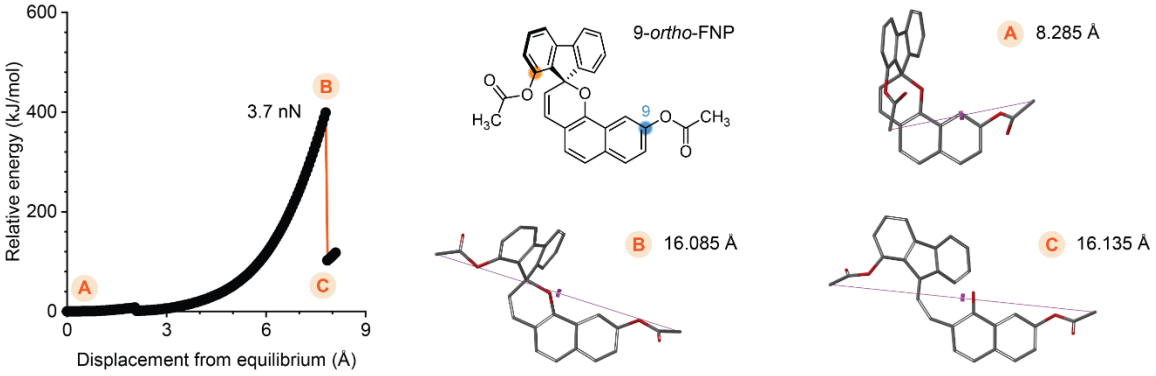

Figure S3.9. Density functional theory (DFT) calculations using the constrained geometries simulate external force (CoGEF) method performed on a truncated model of the 9-*ortho*-FNP mechanophore with attachment points at the *ortho*-position of the fluorene subunit and the 9-position of the naphthopyran. Computed structures are shown at right that correspond to the indicated points in the CoGEF profile along with the associated constraint distance between the terminal methyl groups. The ring-opening reaction is predicted to occur at a maximum force of 3.7 nN. Calculations were performed at the B3LYP/6-31G* level of theory.

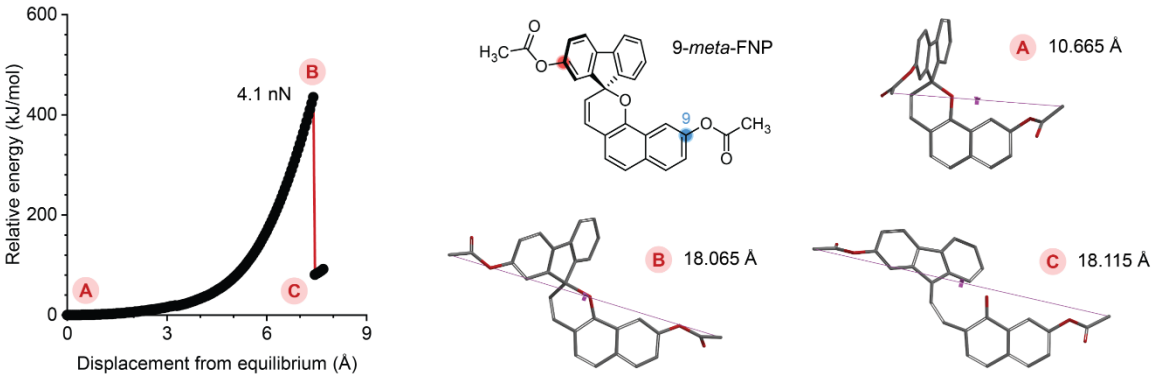

Figure S3.10. Density functional theory (DFT) calculations using the constrained geometries simulate external force (CoGEF) method performed on a truncated model of the 9-*meta*-FNP mechanophore with attachment points at the *meta*-position of the fluorene subunit and the 9-position of the naphthopyran. Computed structures are shown at right that correspond to the indicated points in the CoGEF profile along with the associated constraint distance between the terminal methyl groups. The ring-opening reaction is predicted to occur at a maximum force of 4.1 nN. Calculations were performed at the B3LYP/6-31G* level of theory.

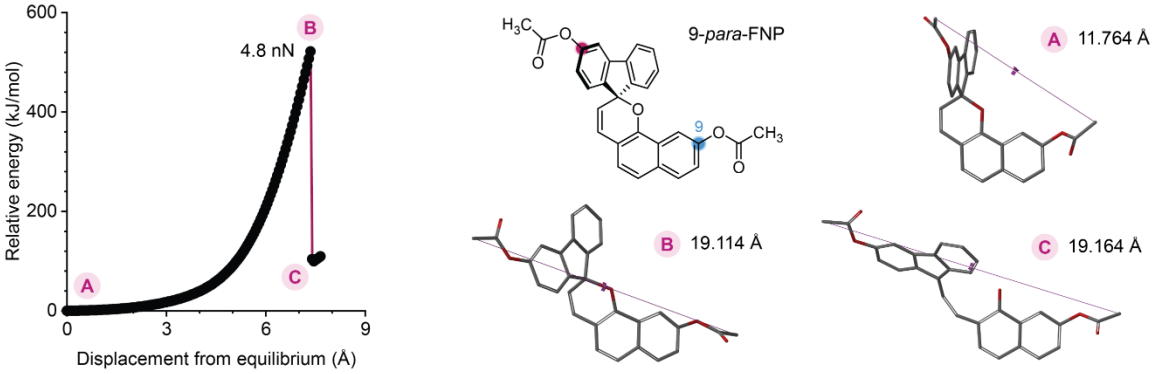

Figure S3.11. Density functional theory (DFT) calculations using the constrained geometries simulate external force (CoGEF) method performed on a truncated model of the 9-*para*-FNP mechanophore with attachment points at the *para*-position of the fluorene subunit and the 9-position of the naphthopyran. Computed structures are shown at right that correspond to the indicated points in the CoGEF profile along with the associated constraint distance between the terminal methyl groups. The ring-opening reaction is predicted to occur at a maximum force of 4.8 nN. Calculations were performed at the B3LYP/6-31G* level of theory.

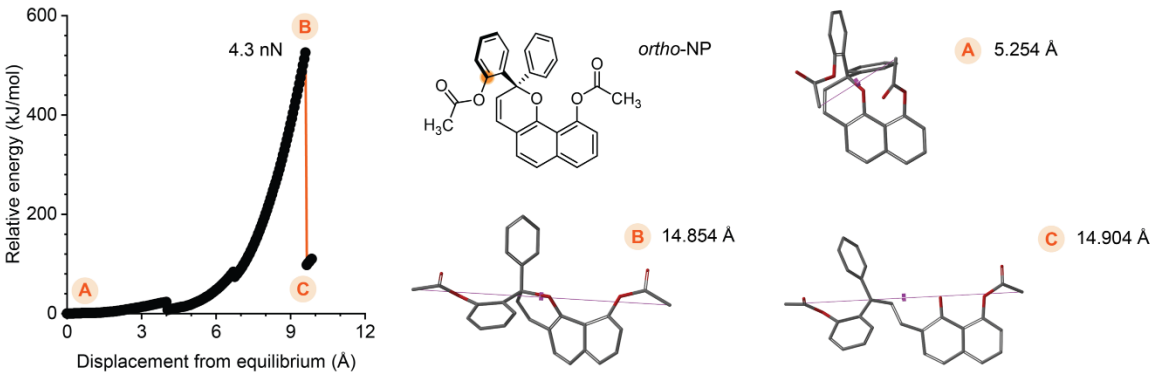

Figure S3.12. Density functional theory (DFT) calculations using the constrained geometries simulate external force (CoGEF) method performed on a truncated model of the *ortho*-NP mechanophore (lacking the biaryl bond) with attachment points at the *ortho*-position of one of one of the aryl groups at C2 and the 10-position of the naphthopyran. Computed structures are shown at right that correspond to the indicated points in the CoGEF profile along with the associated constraint distance between the terminal methyl groups. The ring-opening reaction is predicted to occur at a maximum force of 4.3 nN. Calculations were performed at the B3LYP/6-31G* level of theory.

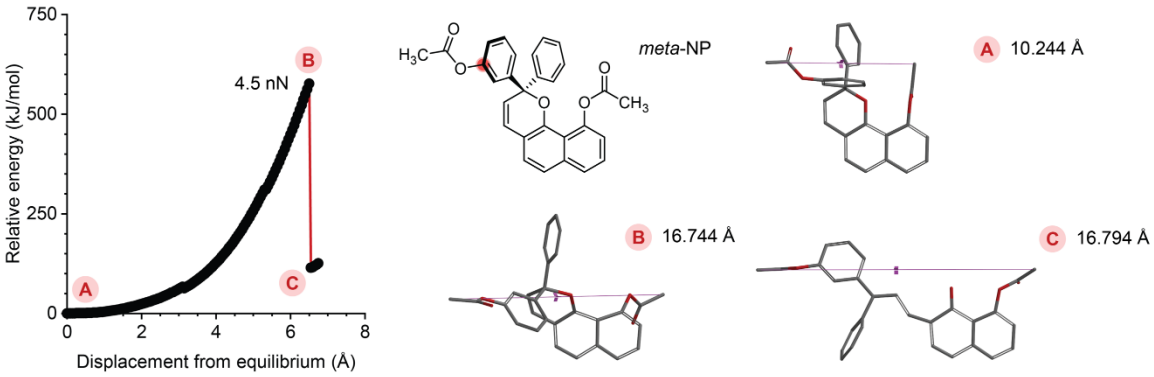

Figure S3.13. Density functional theory (DFT) calculations using the constrained geometries simulate external force (CoGEF) method performed on a truncated model of the *meta*-NP mechanophore (lacking the biaryl bond) with attachment points at the *meta*-position of one of one of the aryl groups at C2 and the 10-position of the naphthopyran. Computed structures are shown at right that correspond to the indicated points in the CoGEF profile along with the associated constraint distance between the terminal methyl groups. The ring-opening reaction is predicted to occur at a maximum force of 4.5 nN. Calculations were performed at the B3LYP/6-31G* level of theory.

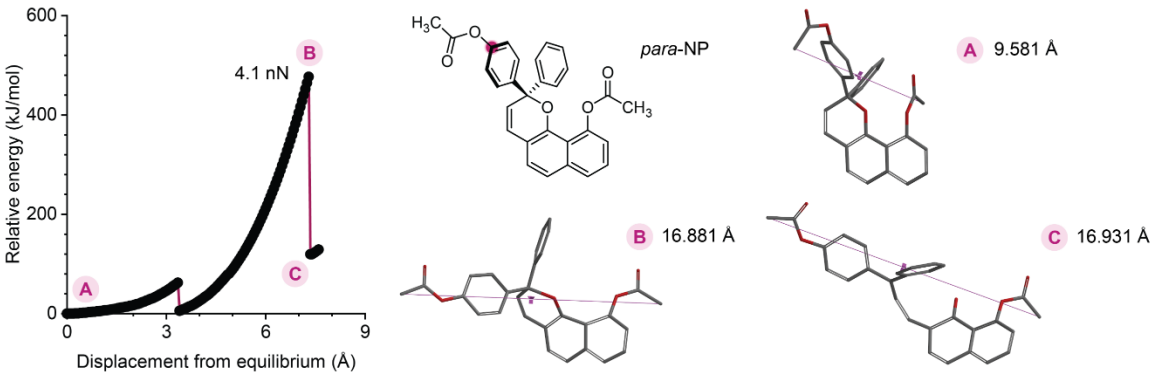

Figure S3.14. Density functional theory (DFT) calculations using the constrained geometries simulate external force (CoGEF) method performed on a truncated model of the *para*-NP mechanophore (lacking the biaryl bond) with attachment points at the *para*-position of one of one of the aryl groups at C2 and the 10-position of the naphthopyran. Computed structures are shown at right that correspond to the indicated points in the CoGEF profile along with the associated constraint distance between the terminal methyl groups. The ring-opening reaction is predicted to occur at a maximum force of 4.1 nN. Calculations were performed at the B3LYP/6-31G* level of theory.

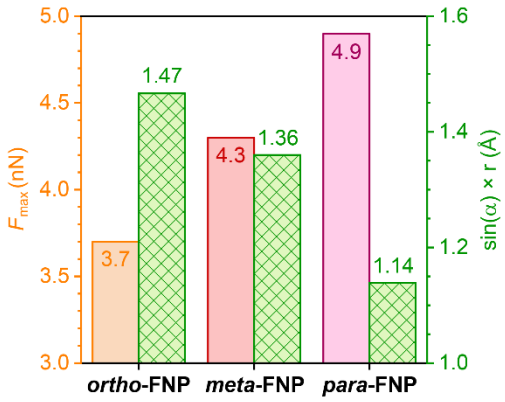

Figure S3.15. Relationship between predicted values of F_{max} and the complete geometric force descriptor as represented by the magnitude of sin(α) × r. See Section III for additional details.

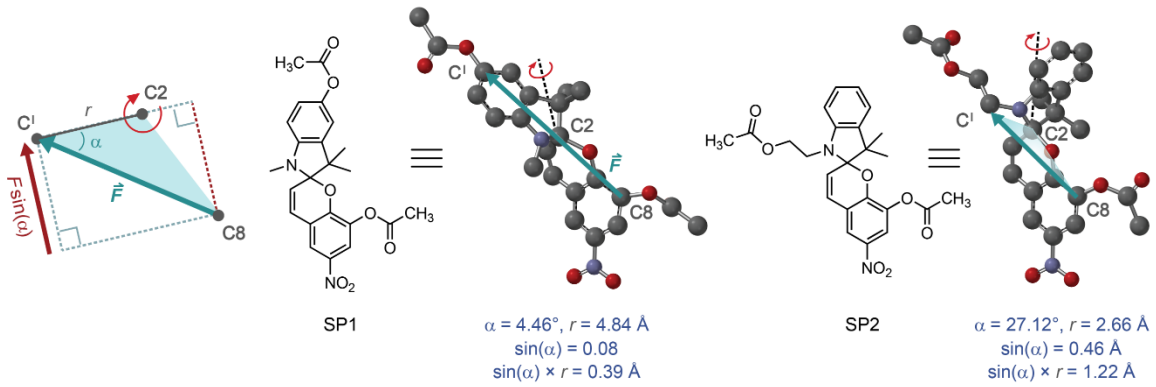

Figure S3.16. Geometric analysis performed on spiropyran models SP1 and SP2 to determine the angle between the external force vector and the indoline unit (α), and lever arm length (r). Structures correspond to the step immediately prior to C–O bond rupture from CoGEF calculations. SP1 and SP2 are predicted to undergo pyran bond cleavage at 4.4 and 2.7 nN, respectively.[52]

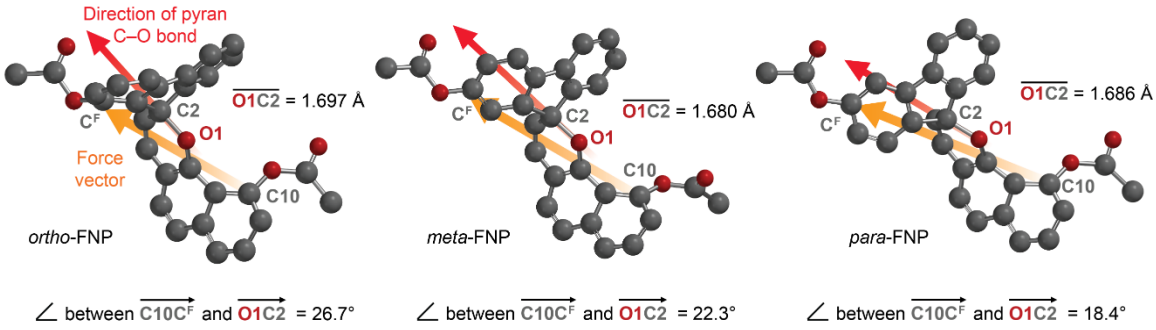

Figure S3.17. Vector alignment analysis performed on *ortho*-FNP, *meta*-FNP, and *para*-FNP models according to previously reported methods.[27] The atomic coordinates were obtained from CoGEF calculations (structures immediately prior to C–O bond cleavage) and used to calculate representative vectors for the force vector between terminal carbon atoms C10 and C^F (in yellow) and the direction of the pyran C–O bond (atoms O1 and C2, vector in red). The highest degree of alignment between the force vector and the C–O pyran bond is observed for the *para*-FNP model as indicated by the smallest angle, while the alignment is poorest for the *ortho*-FNP model. See Section III for additional details.

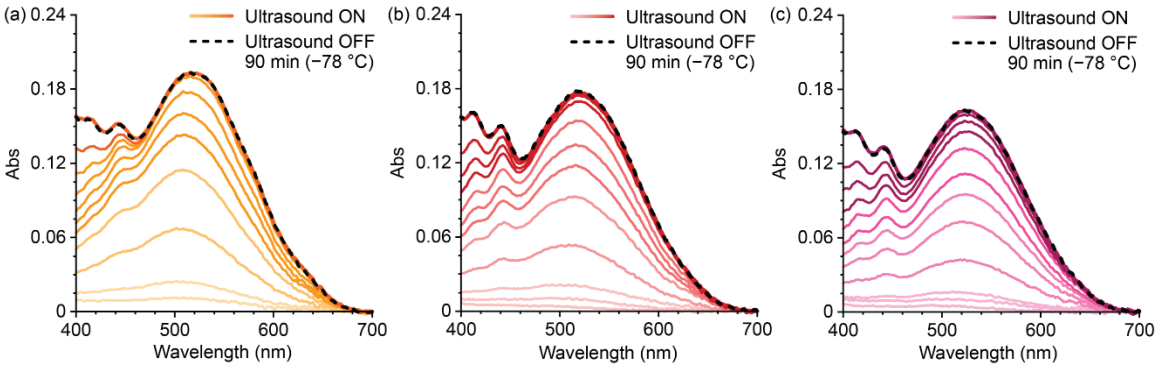

Figure S3.18. UV-vis absorption spectra acquired during and after the sonication of (a) ***ortho*-FNP**, (b) ***meta*-FNP**, and (c) ***para*-FNP** polymers. For each analogue, the absorption spectra of the mechanochemical reaction products remains unchanged at −78 °C in the dark for 90 min after sonication is turned off, confirming that no merocyanine reversion occurs.

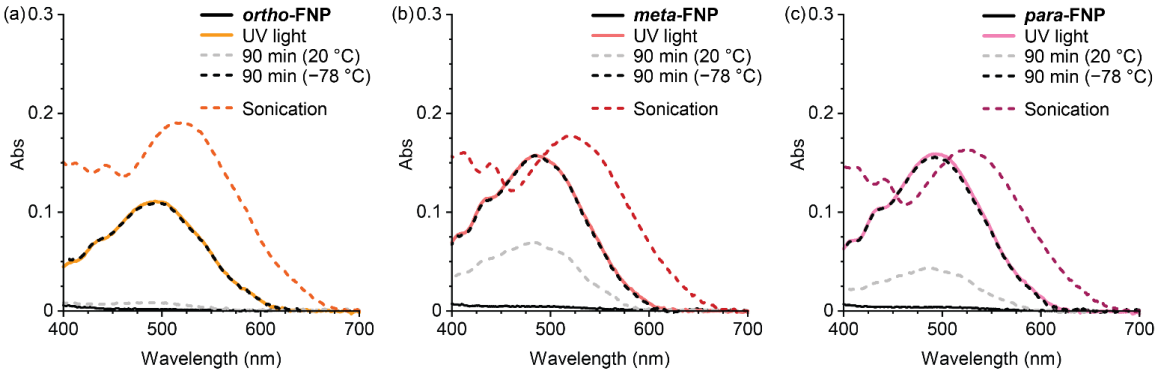

Figure S3.19. UV-vis absorption spectra of (a) ***ortho*-FNP**, (b) ***meta*-FNP**, and (c) ***para*-FNP** (2 mg/mL in THF with 30 mM BHT) before and after photoirradiation with UV light (365 nm, 2 min, −78 °C). Significant thermal reversion occurs upon warming to 20 °C, while reversion at −78 °C is negligible. The photogenerated merocyanine products, which maintain an intact ester group, exhibit absorption spectra that are hypsochromically shifted from the mechanochemically-generated products. See section VI for additional details.

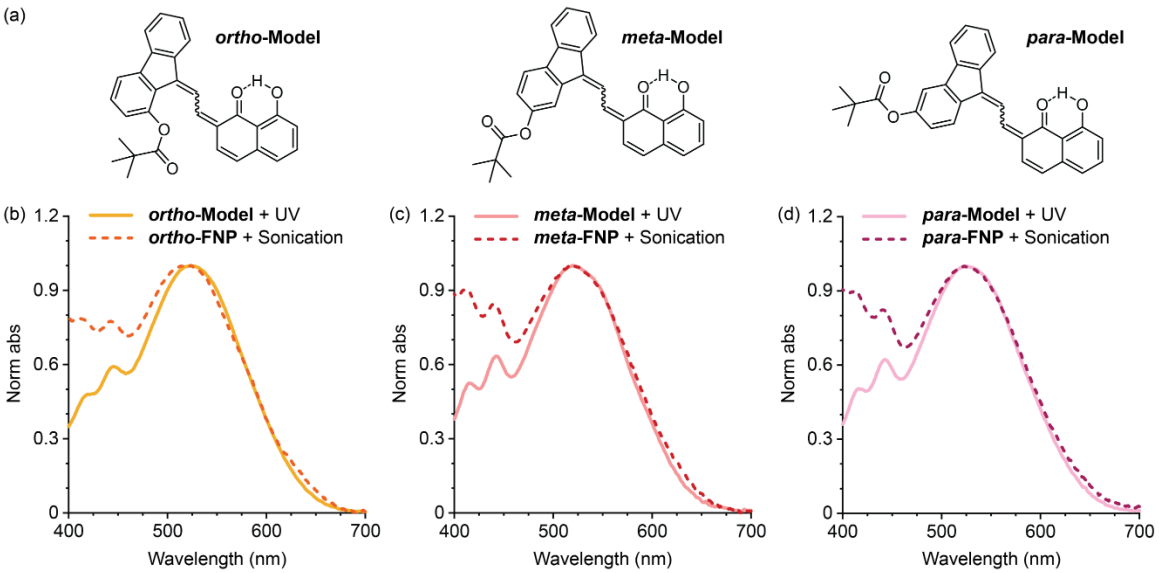

Figure S3.20. Structures and absorption spectra of small molecule model compounds. (a) Structures of merocyanine model compounds ***ortho*-Model**, ***meta*-Model**, and ***para*-Model**. UV-vis absorption spectra of the sonicated solutions of polymers (b) ***ortho*-FNP**, (c) ***meta*-FNP**, and (d) ***para*-FNP** compared to solutions of the analogous model compounds (10 mM in THF with 30 mM BHT). The model compound solutions were irradiated with UV light (365 nm, 5 minutes) in order to photoisomerize any exocyclic double bonds from *cis* to *trans* configuration. The merocyanine isomers with *trans* exocyclic alkenes are present in the product mixture from sonication due to *cis* to *trans* isomerization that occurs in the presence of ambient water, which is unique to the intramolecularly H-bonded merocyanines.[53]

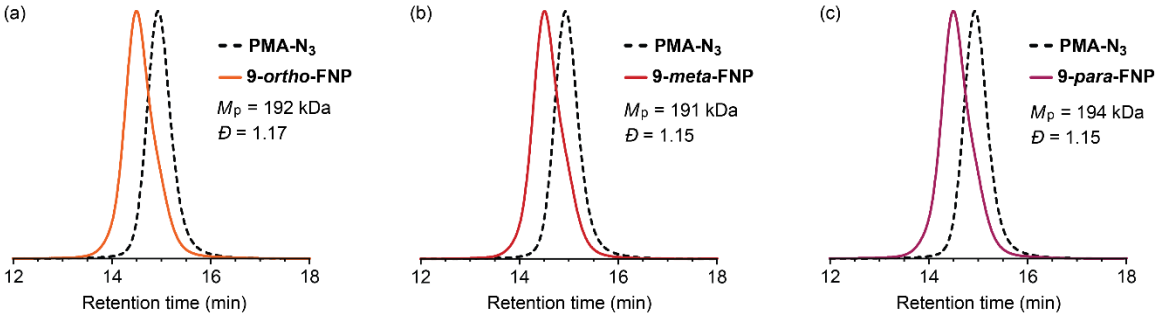

Figure S3.21. Characterization by GPC (refractive index response shown) confirms successful coupling reactions to generate mechanophore chain-centered polymers (a) **9-*ortho*-FNP**, (b) **9-*meta*-FNP**, and (c) **9-*para*-FNP** incorporating FNP mechanophores with polymer attachment at the 9-position of the naphthopyran.

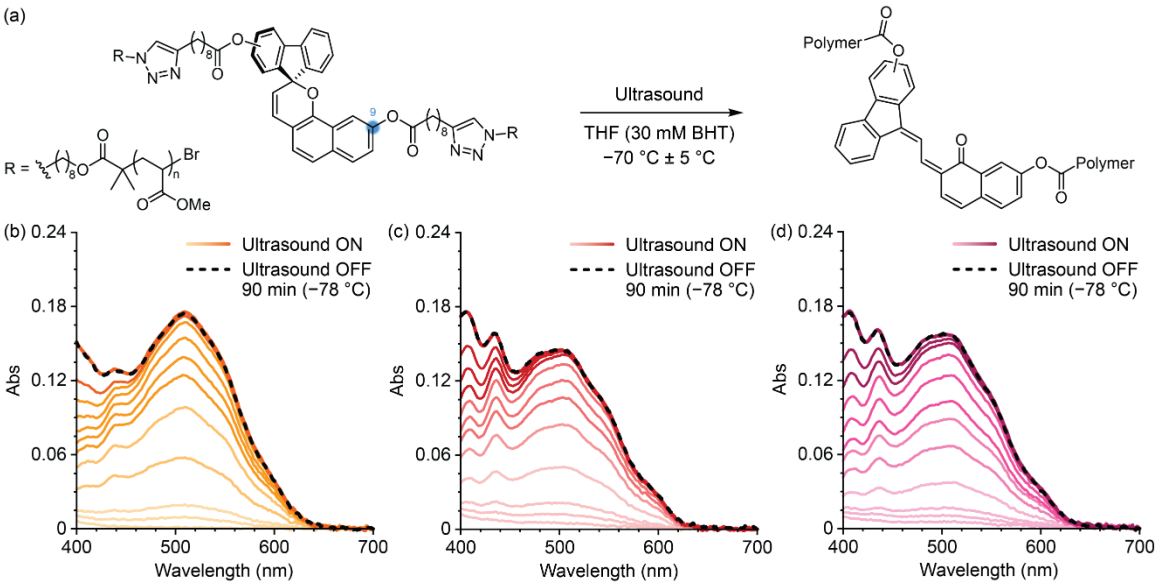

Figure S3.22. Ultrasonication experiments performed on **9-*ortho*-FNP**, **9-*meta*-FNP**, and **9-*para*-FNP**. (a) Ultrasound-induced mechanochemical activation of polymers functionalized with chain-centered 9-FNP mechanophores containing polymer attachment at the 9-position of the naphthopyran. UV-vis absorption spectra acquired during and after the sonication of (b) **9-*ortho*-FNP**, (c) **9-*meta*-FNP**, and (d) **9-*para*-FNP**. For all analogues, the absorption spectra of the mechanochemical reaction products remains unchanged at −78 °C in the dark for 90 min after sonication is turned off, confirming that no merocyanine reversion occurs.

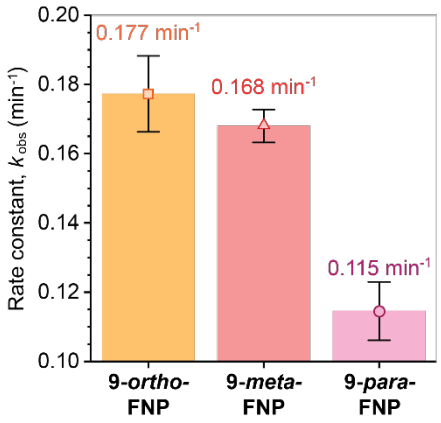

Figure S3.23. Rate constants (k_{obs}) for merocyanine formation from **9-*ortho*-FNP**, **9-*meta*-FNP**, and **9-*para*-FNP** determined from time-dependent absorption data acquired from sonication experiments (See Section VI for details). Data points and error bars represent average values and standard deviation from 4–5 replicate trials.

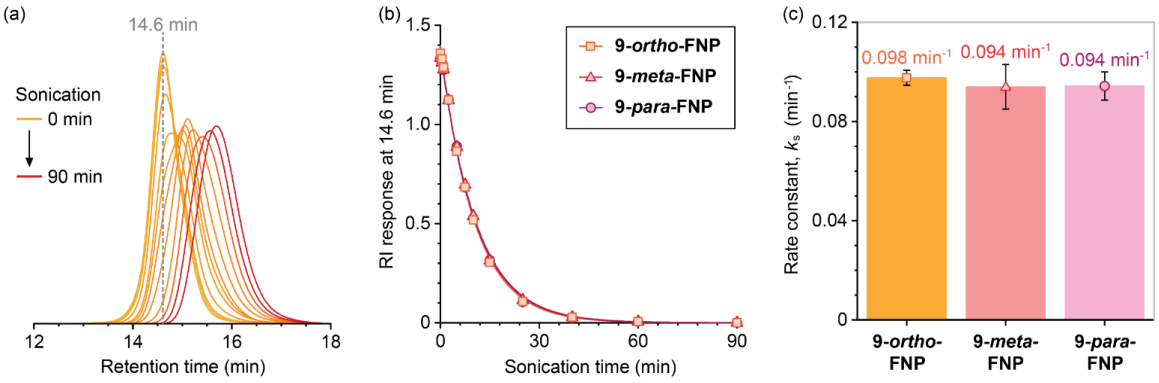

Figure S3.24. Ultrasound-induced polymer chain cleavage was monitored for **9-*ortho*-FNP**, **9-*meta*-FNP**, and **9-*para*-FNP**. (a) Representative time-dependent GPC traces (RI response) normalized by integrated peak area to determine the rate of nonspecific backbone scission during the ultrasound-induced mechanochemical activation of **9-*ortho*-FNP**. (b) RI response at t_R = 14.6 min (corresponding to the peak maximum of the unsonicated polymer) as a function of ultrasonication time for **9-*ortho*-FNP**, **9-*meta*-FNP**, and **9-*para*-FNP**, for which the full reaction profiles are fit to exponential decay (see Section VII for details). Data points represent average values from 3 replicate trials. (c) Rate constants (k_s) for polymer scission from the data in (b) illustrating that the rate of nonspecific backbone scission is invariant as a function of polymer attachment geometry.

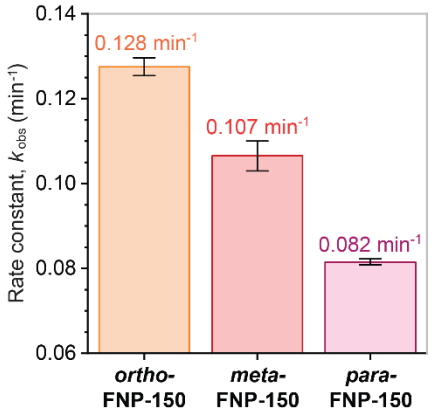

Figure S3.25. Rate constants (k_{obs}) for merocyanine accumulation from polymers ***ortho*-FNP-150**, ***meta*-FNP-150**, and ***para*-FNP-150** ($M_p \approx 150$ kDa) determined from time-dependent absorption data acquired from sonication experiments (See Section VI for additional details). Data points and error bars represent average values and standard deviation from duplicate trials.

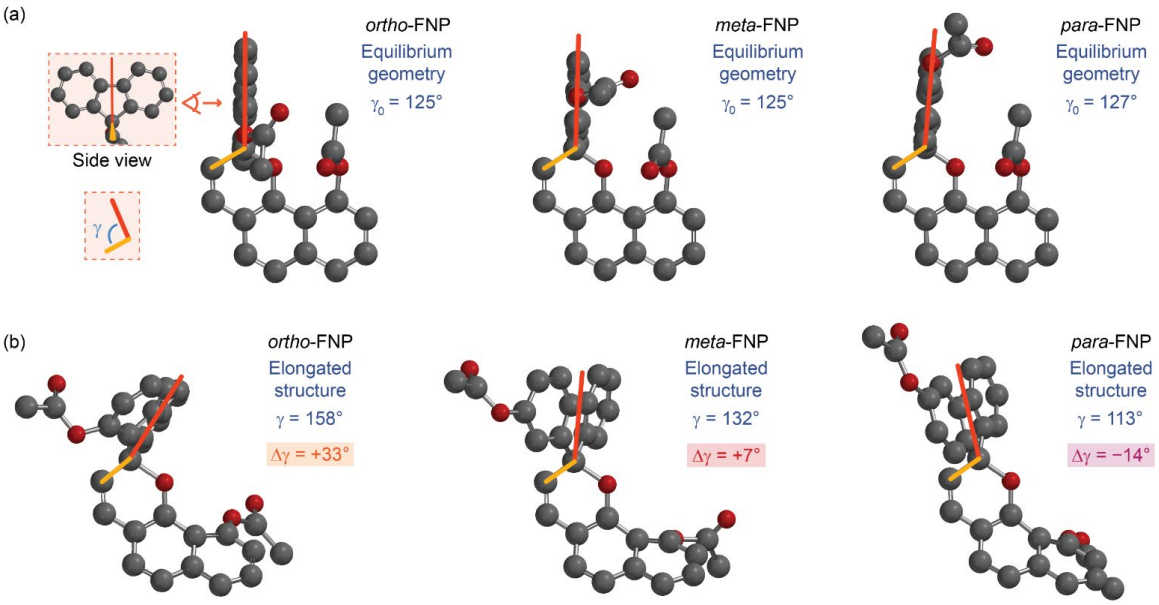

Figure S3.26. Truncated models of *ortho*-FNP, *meta*-FNP, and *para*-FNP from CoGEF calculations showing (a) the force-free equilibrium geometry, and (b) the structure immediately prior to C–O bond cleavage. The angle γ is defined by a line that vertically bisects the fluorene group and the C2–C3 bond of the pyran ring. See Section VIII for additional details.

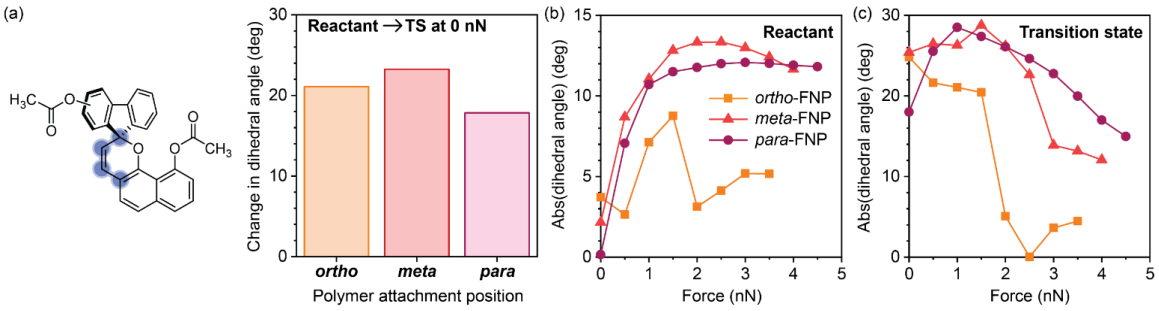

Figure S3.27. Evaluation of alternative molecular distortion involving the pyran ring. (a) The change in pyran dihedral angle (defined by the atoms highlighted in blue) for the force-free reaction going from reactant to transition state structures for *ortho*-FNP, *meta*-FNP, and *para*-FNP. Absolute pyran dihedral angle in the (b) reactant and (c) transition state structures as a function of external force from EFEI calculations (uB3LYP/def2-SVP). No correlation is observed between the reactivity of the FNP mechanophores and this pyran dihedral angle. See Section VIII for additional details.

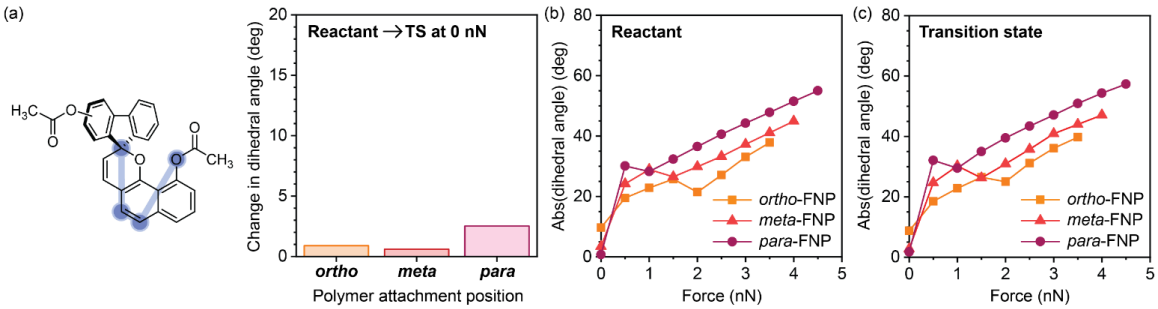

Figure S3.28. Evaluation of alternative molecular distortion involving the naphthopyran scaffold. (a) The change in naphthopyran dihedral angle (defined by the atoms highlighted in blue) for the force-free reaction going from reactant to transition state structures for *ortho*-FNP, *meta*-FNP, and *para*-FNP. Absolute dihedral angle in the (b) reactant and (c) transition state structures as a function of external force from EFEI calculations (uB3LYP/def2-SVP). No correlation is observed between the reactivity of the FNP mechanophores and this mode of dihedral angle. See Section VIII for additional details.

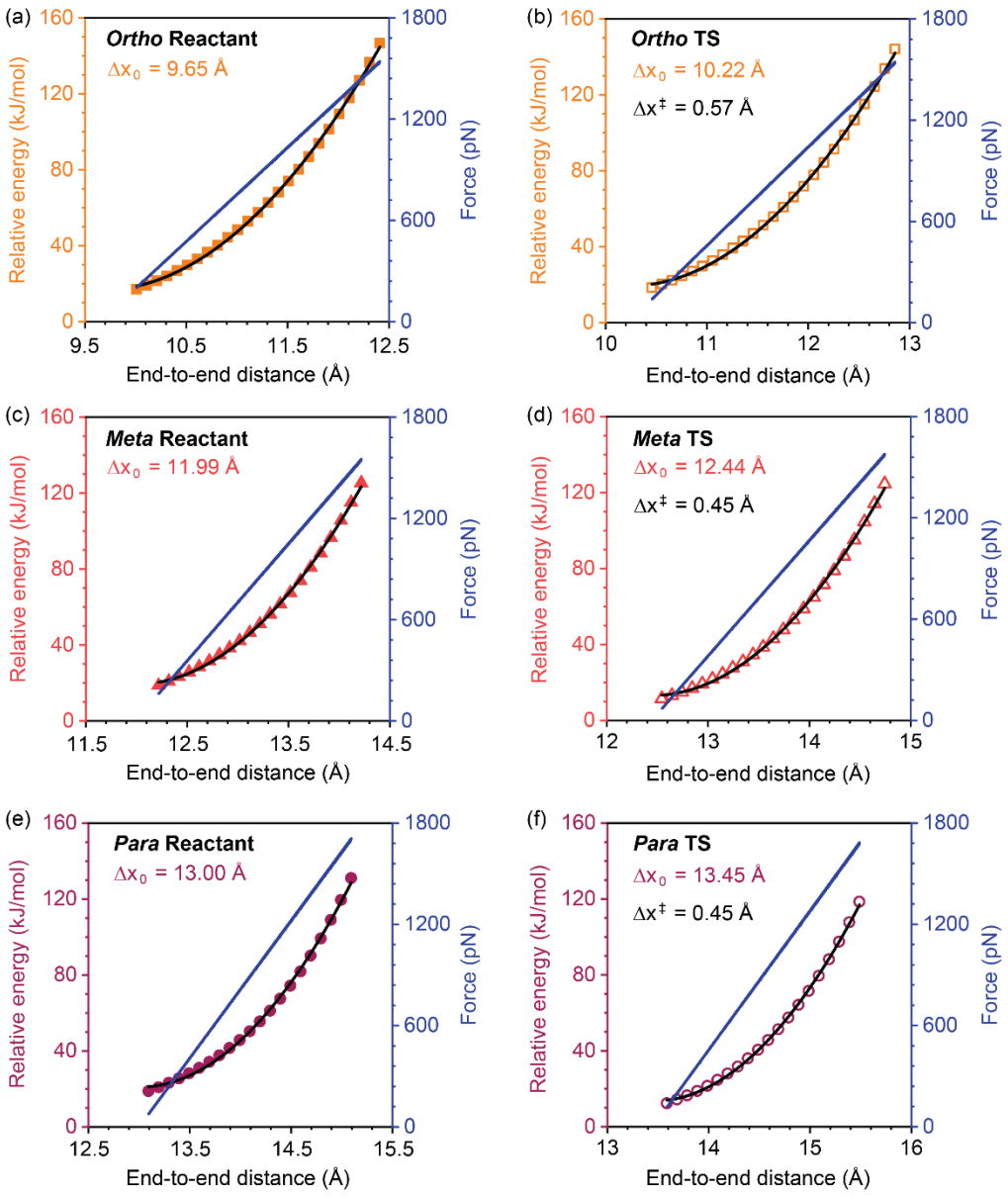

Figure S3.29. Calculation of activation lengths for (a, b) *ortho*-FNP, (c, d) *meta*-FNP, and (e, f) *para*-FNP. Data from CoGEF calculations performed on reactant and transition state structures was fit to a quadratic equation and the first derivative of the quadratic expression was calculated to obtain a linear function of force vs end-to-end distance. Structures were obtained from EFEI calculations at 2 nN of applied force. The force-free end-to-end distance is determined by extrapolating the line to zero force. See Section VIII for additional details.

III. Geometric Analyses on FNP Mechanophores

The structures of the FNP congeners from CoGEF calculations were analyzed to determine the value of sin(α) and sin(α) × *r* (Figures S3.30 and S3.31). Carbon atoms (labeled C^F and C10 or C9) were chosen as end points to approximate the external force vector to minimize the number of degrees of freedom following a previously published procedure.[27] The lever arm is defined by the ester-substituted fluorene unit, and is represented by the line connecting atoms C2 and C^F. The fluorene group rotates in the plane defined by atoms C^F, C2, and C10 or C9. Using this geometric model, the component of the force vector that is perpendicular to the fluorene group is equal to *F*sin(α). Using the structures from CoGEF calculations immediately prior to bond rupture, we also examined how the effective torsional force as represented by sin(α) changes as a function of polymer attachment position for 9-*ortho*-FNP, 9-*meta*-FNP, and 9-*para*-FNP. The trend in sin(α) is consistent with predicted reactivity, exhibiting an inverse relationship with values of F_{max} (Figure S3.32).

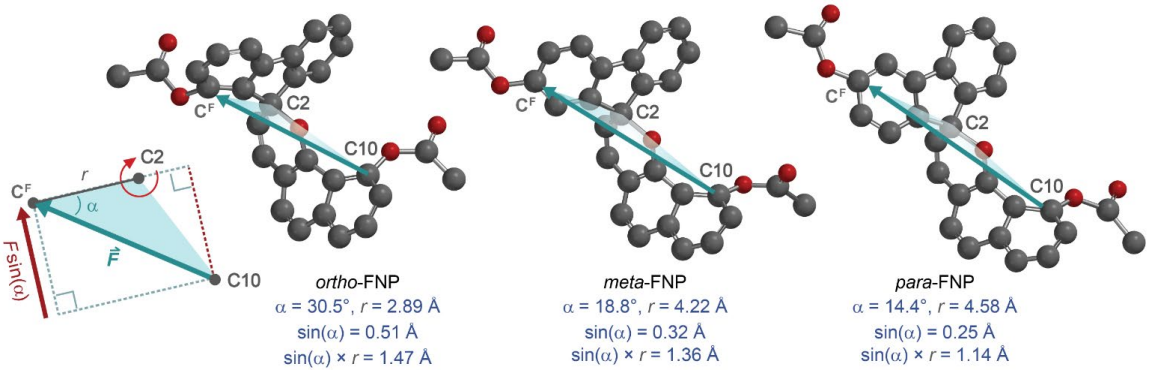

Figure S3.30. Geometric analysis performed on models *ortho*-FNP, *meta*-FNP and *para*-FNP to determine the angle between the external force vector and the fluorene unit. Structures correspond to the step immediately prior to C–O bond rupture from CoGEF calculations.

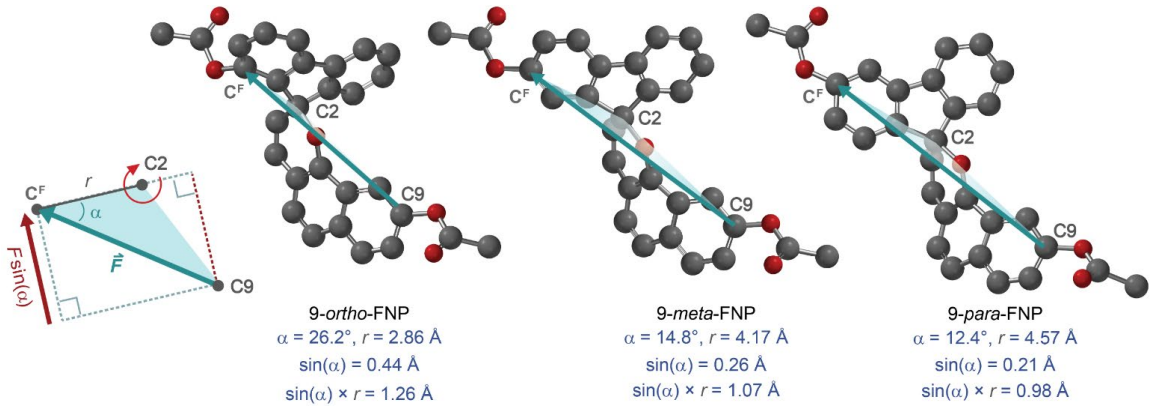

Figure S3.31. Geometric analysis performed on models 9-*ortho*-FNP, 9-*meta*-FNP and 9-*para*-FNP with attachment at the 9-position of the naphthopyran to determine the angle between the external force vector and the fluorene unit. Structures correspond to the step immediately prior to C–O bond rupture from CoGEF calculations.

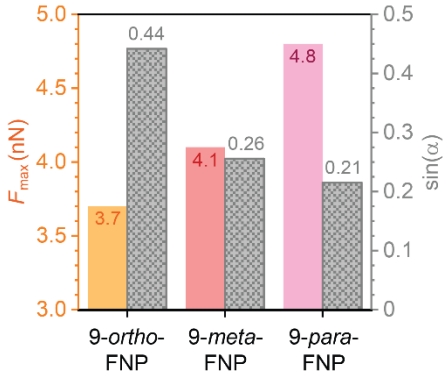

Figure S3.32. Relationship between the computed rupture force (F_{max}) for the 9-FNP mechanophore models and the effective torsional force as represented by the magnitude of sin(α).

The structures of the FNP congeners from CoGEF calculations were also analyzed to determine angle γ, which is defined as the angle between the line that originates at C2 and vertically bisects the fluorene group, and the pyran C2–C3 bond (Figures S3.26 and S3.33).

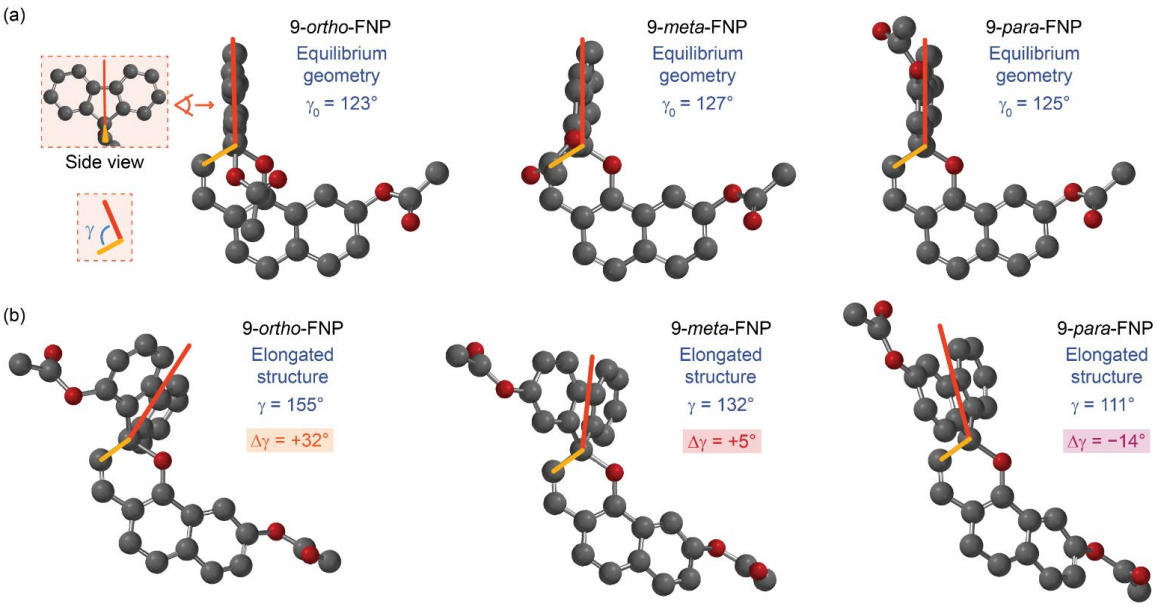

Figure S3.33. Truncated models of 9-*ortho*-FNP, 9-*meta*-FNP, and 9-*para*-FNP from CoGEF calculations showing (a) the force-free equilibrium geometry, and (b) the structure immediately prior to C–O bond cleavage. The angle γ is defined by a line that vertically bisects the fluorene group and the C2–C3 bond of the pyran ring. See Section VIII for additional details.

The structures of the FNP congeners from CoGEF calculations were also analyzed to evaluate the alignment between the external force vector and the C–O pyran bond, according to a previously reported procedure (Figures S3.17 and S3.34).[27] As discussed above, carbon atoms (labeled C^F and C9 or C10) were selected as end points to approximate the external force vector. A smaller angle indicates a higher degree of alignment between the external force vector and the C–O pyran bond. For both the series of models with attachment at the 10-position and the 9-position, the alignment between the external force vector and the C–O pyran bond follows the order *para* > *meta* > *ortho*, which is in direct contrast to the trend in reactivity as indicated by the predicted values of F_{max}. We note that the same trends are observed when the oxygen atoms (labeled O2 and O3) are used as end points to approximate the external force vector (Figure S3.35 and S3.36).

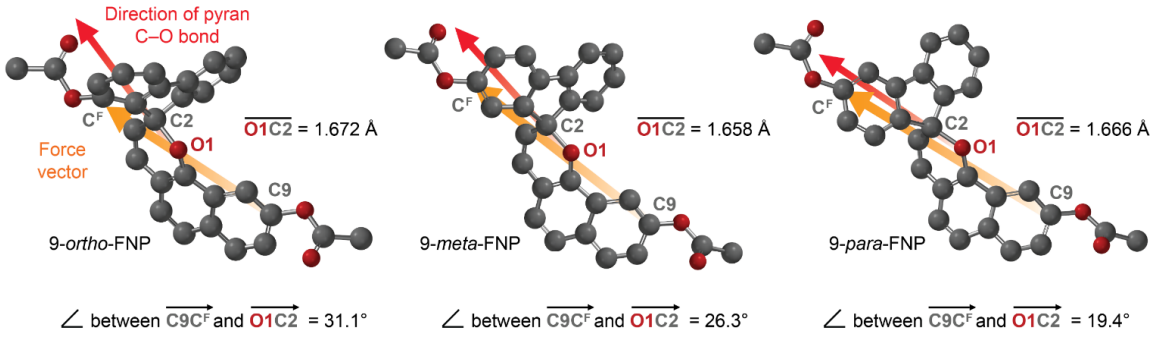

Figure S3.34. Vector alignment analysis performed on 9-*ortho*-FNP, 9-*meta*-FNP, and 9-*para*-FNP models with attachment at the 9-position of the naphthopyran according to previously reported methods.[27] The atomic coordinates were obtained from CoGEF calculations (structures immediately prior to C–O bond cleavage) and used to calculate representative vectors for the force vector between terminal carbon atoms C^F and C9 (in yellow) and the direction of the pyran C–O bond (atoms O1 and C2, vector in red). The highest degree of alignment between the force vector and the C–O pyran bond is observed for the 9-*para*-FNP model as indicated by the smallest angle, while the alignment is poorest for the 9-*ortho*-FNP model.

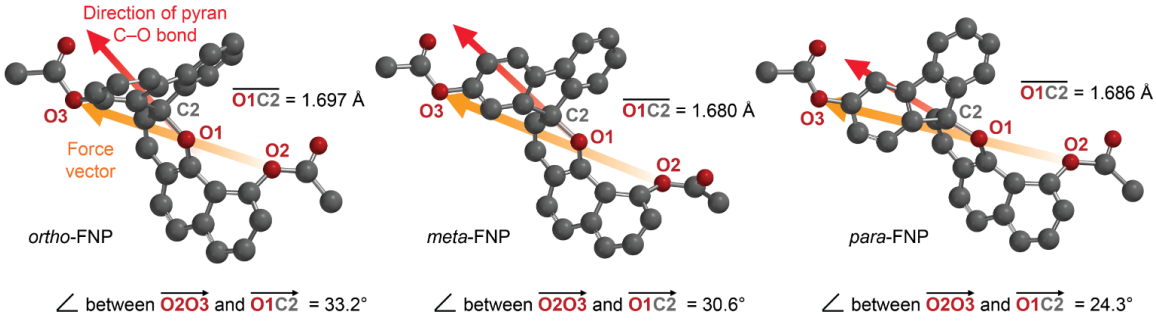

Figure S3.35. Vector alignment analysis performed on *ortho*-FNP, *meta*-FNP, and *para*-FNP models with attachment at the 10-position of the naphthopyran according to previously reported methods.[27] The atomic coordinates were obtained from CoGEF calculations (structures immediately prior to C–O bond cleavage) and used to calculate representative vectors for the force vector between terminal oxygen atoms O2 and O3 (in yellow) and the direction of the pyran C–O bond (atoms O1 and C2, vector in red). The highest degree of alignment between the force vector and the C–O pyran bond is observed for the *para*-FNP model as indicated by the smallest angle, while the alignment is poorest for the *ortho*-FNP model.

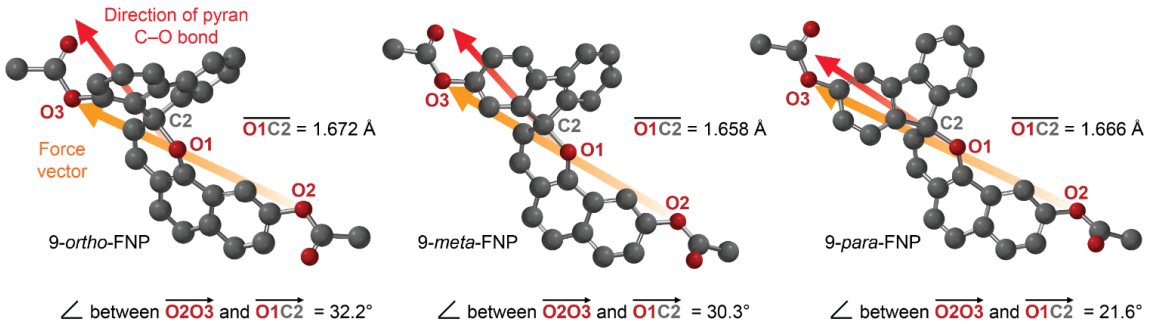

Figure S3.36. Vector alignment analysis performed on 9-*ortho*-FNP, 9-*meta*-FNP, and 9-*para*-FNP models with attachment at the 9-position of the naphthopyran according to previously reported methods.[27] The atomic coordinates were obtained from CoGEF calculations (structures immediately prior to C–O bond cleavage) and used to calculate representative vectors for the force vector between terminal oxygen atoms O2 and O3 (in yellow) and the direction of the pyran C–O bond (atoms O1 and C2, vector in red). The highest degree of alignment between the force vector and the C–O pyran bond is observed for the 9-*para*-FNP model as indicated by the smallest angle, while the alignment is poorest for the 9-*ortho*-FNP model.

Using the structures from CoGEF calculations immediately prior to bond rupture, we also examined how the perpendicular component of the force vector incident on the fluorene lever arm, $F_{max}\sin(\alpha)$, changes as a function of polymer attachment position. The trend in $F_{max}\sin(\alpha)$ is consistent with predicted reactivity, exhibiting an inverse relationship with values of F_{max} (Figure S3.37). To demonstrate how angle α evolves during the mechanochemical reaction, we analyzed the changes in angle α and sin(α) as a function of molecular elongation (Figure S3.38) as well as pyran C–O bond length (Figure S3.39) in the structures from CoGEF calculations. Additional analysis was performed using FNP reactant geometries under varying amounts of applied force from EFEI calculations (see Section VIII for additional details). Changes in angle α and sin(α) were evaluated as a function of force for *ortho*-FNP, *meta*-FNP, and *para*-FNP to further understand how the effective torsional force evolves with increasing force (Figure S3.40).

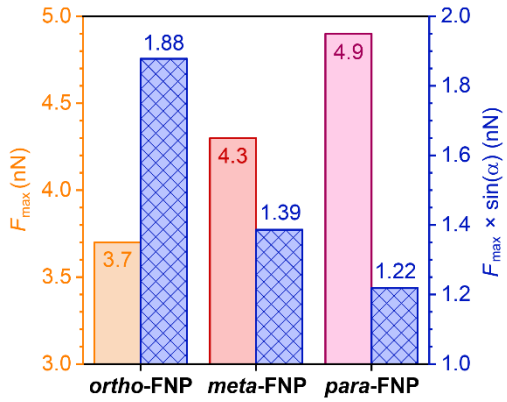

Figure S3.37. Relationship between predicted values of F_{max} and the quantity $F_{max}\sin(\alpha)$ for *ortho*-FNP, *meta*-FNP, and *para*-FNP. The quantity $F_{max}\sin(\alpha)$ represents the perpendicular component of the incident force vector on the fluorene lever arm in the plane of rotation. See Section III for additional details.

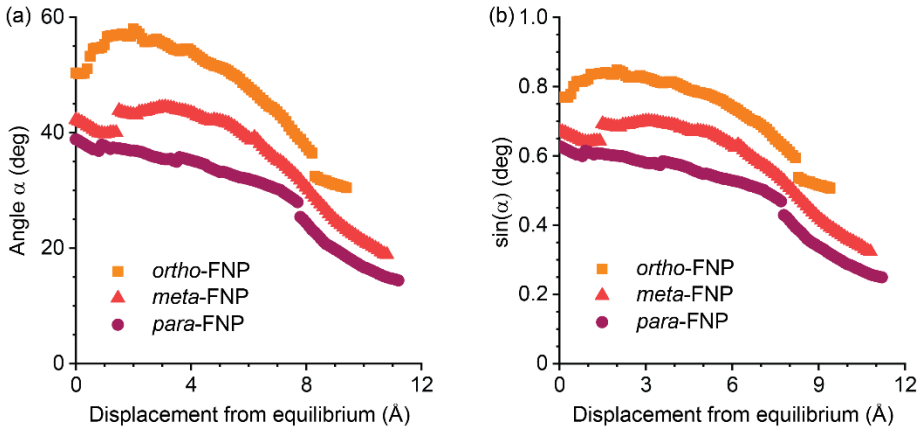

Figure S3.38. Geometric analysis from CoGEF calculations. (a) Angle α and (b) sin(α) as a function of displacement from equilibrium from CoGEF calculations.

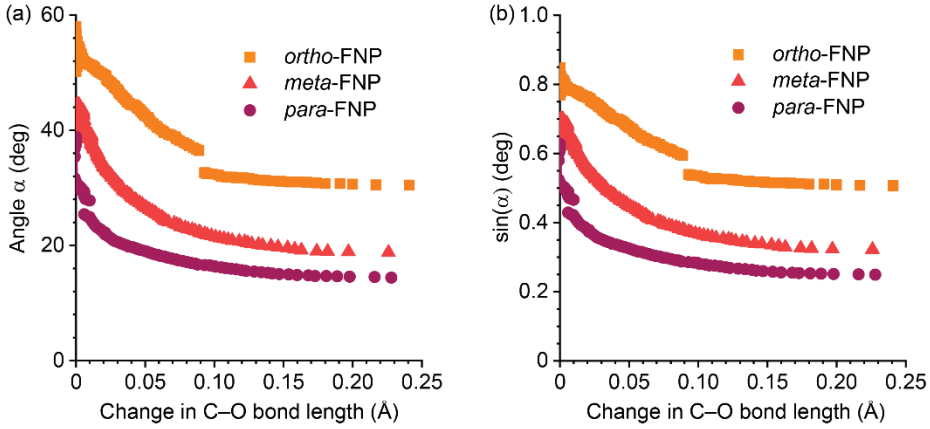

Figure S3.39. Geometric analysis from CoGEF calculations. (a) Angle α and (b) sin(α) as a function of change in pyran C–O bond length from CoGEF calculations.

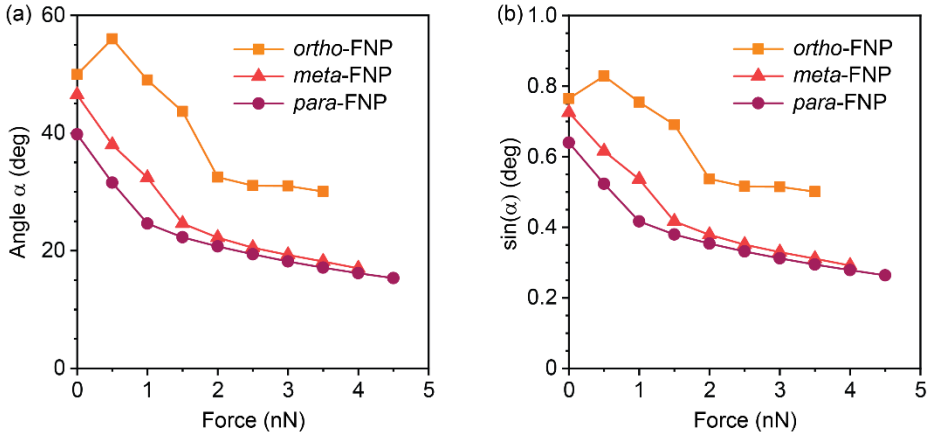

Figure S3.40. Geometric analysis from CoGEF calculations. (a) Angle α and (b) sin(α) as a function of external force from EFEI calculations. See Section VIII for additional details.

IV. Synthetic Details

Scheme S3.1. Synthesis of compounds used in this study.

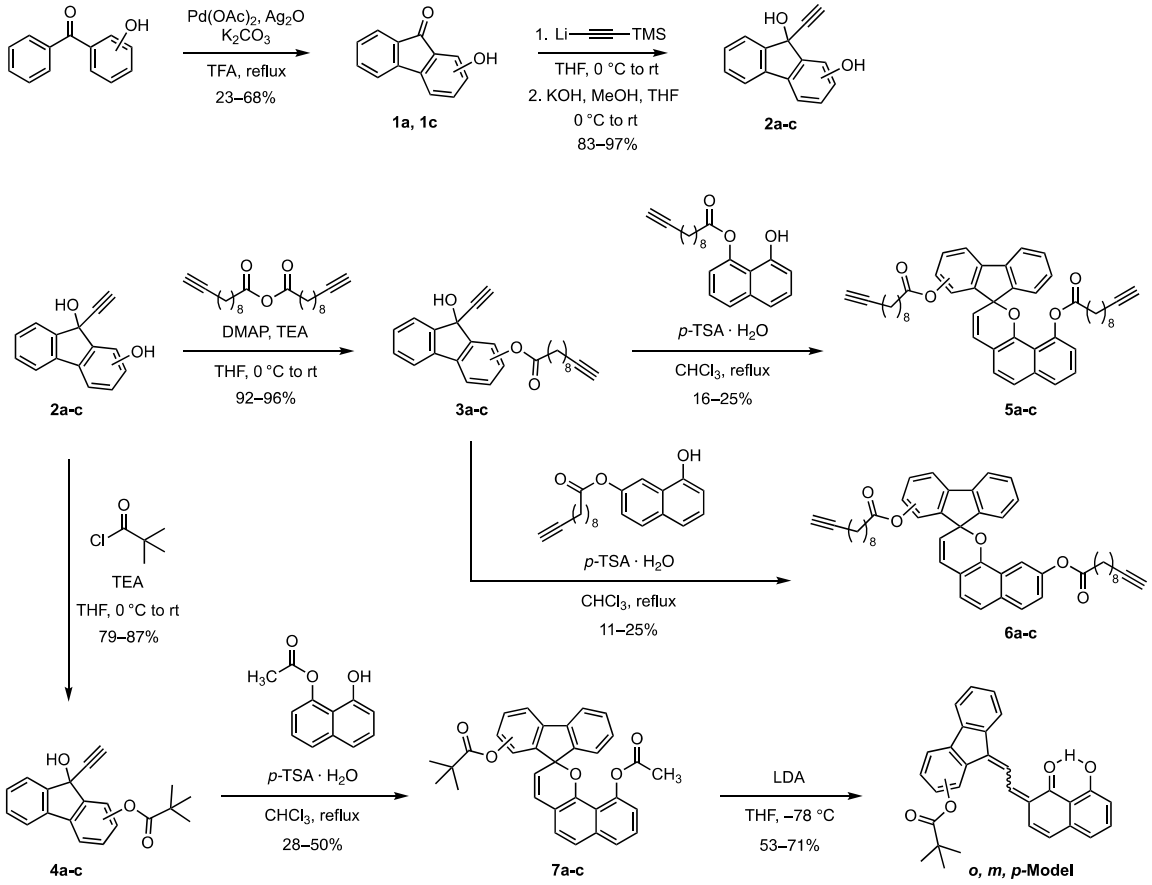

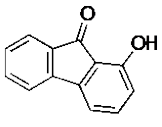

1a

1-hydroxy-9*H*-fluoren-9-one (1a). A flame-dried 100 mL two-neck round bottom flask equipped with a reflux condenser and stir bar was charged with 2-hydroxybenzophenone (1.50 g, 7.57 mmol), silver(I) oxide (2.63 g, 11.3 mmol), palladium acetate (170 mg, 0.757 mmol), and potassium carbonate (5.20 g, 37.6 mmol). The flask was evacuated and backfilled with N_2 (3×), and then cooled to 0 °C in an ice bath. A separate flame-dried 100 mL two-neck round bottom flask was charged with trifluoroacetic acid (20 mL) and the liquid was sparged with N_2 for 30 min. The

trifluoroacetic acid was added to the reaction flask slowly via syringe, which was subsequently stirred for 5 min. The reaction mixture was heated to reflux for 40 h, at which point the flask was cooled to 65 °C, hot ethyl acetate was added (250 mL), and the resulting suspension was filtered through celite. Toluene (500 mL) was added to the filtrate as a drying agent and the mixture was concentrated under reduced pressure (3×). The crude reaction mixture was dissolved in ethyl acetate (500 mL) and the solution was washed consecutively with saturated aqueous $NaHCO_3$ (3 × 150 mL) and brine (150 mL). The organic layer was dried over Na_2SO_4, filtered, and concentrated under reduced pressure. The crude material was purified by column chromatography on silica gel (0–20% EtOAc/hexanes) to provide the title compound as a yellow crystalline solid (342 mg, 23%).

^{1}H NMR (400 MHz, acetone-d_6) δ: 7.74 (dd, J = 7.4, 0.9 Hz, 1H), 7.61 (d, J = 7.3 Hz, 1H), 7.59 (td, J = 7.4, 1.1 Hz, 1H),7.47 (dd, J = 8.5, 7.2 Hz, 1H), 7.40 (td, J = 7.5, 1.0 Hz, 1H), 7.25 (dd, J = 7.2, 0.8 Hz, 1H), 6.81 (dt, J = 8.4, 0.6 Hz, 1H).

^{13}C{^{1}H} NMR (101 MHz, acetone-d_6) δ: 195.4, 157.8, 145.2, 144.8, 138.4, 135.6, 135.0, 130.1, 124.3, 122.1, 119.3, 118.2, 113.8.

TLC (25% EtOAc/hexanes): R_f = 0.42

HRMS (ESI m/z): calcd for $[C_{13}H_7O_2]^-$ $(M-H)^-$, 195.0452; found 195.0451.

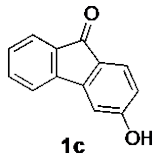

1c

3-hydroxy-9*H*-fluoren-9-one (1c). A flame-dried 100 mL two-neck round bottom flask equipped with a reflux condenser and stir bar was charged with 4-hydroxybenzophenone (1.00 g, 5.04 mmol), silver(I) oxide (1.75 g, 7.55 mmol), palladium acetate (113 mg, 0.503 mmol), and potassium carbonate (3.49 g, 25.3 mmol). The flask was evacuated and backfilled with N_2 (3×), and then cooled to 0 °C in an

ice bath. A separate flame-dried 100 mL two-neck round bottom flask was charged with trifluoroacetic acid (10 mL) and the liquid was sparged with N_2 for 30 min. The trifluoroacetic acid was added to the reaction flask slowly via syringe, which was subsequently stirred for 5 min. The reaction mixture was heated to reflux for 72 h, at which point the flask was cooled to 65 °C, hot ethyl acetate (100 mL) and toluene (100 mL) were added, and the suspension was concentrated under reduced pressure. The mixture was taken up into minimal ethyl acetate (20 mL) and purified on a silica plug (30% EtOAc/hexanes). The resulting solid was suspended in hot toluene and filtered, and the filtrate was collected to obtain the title compound as a tan crystalline solid (672 mg, 68%).

^{1}H NMR (400 MHz, acetone-d_6) δ: 7.66 (d, J = 7.3 Hz, 1H), 7.58 – 7.51 (m, 2H), 7.50 (d, J = 8.1 Hz, 1H), 7.36 (td, J = 7.4, 1.0 Hz, 1H), 7.18 (d, J = 2.1 Hz, 1H), 6.79 (dd, J = 8.1, 2.1 Hz, 1H).

^{13}C NMR (101 MHz, acetone-d_6) δ: 192.2, 164.9, 148.2, 144.2, 136.1, 135.1, 130.2, 126.9, 126.8, 124.0, 121.4, 116.0, 109.2.

TLC (25% EtOAc/hexanes): R_f = 0.33

HRMS (ESI m/z): calcd for $[C_{13}H_7O_2]^-$ $(M-H)^-$, 195.0452; found 195.0453.

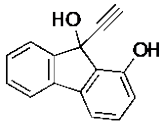

2a

9-ethynyl-9*H*-fluorene-1,9-diol (2a). A flame-dried 250 mL two-neck round bottom flask equipped with a stir bar was evacuated and backfilled with N_2 (3×) and charged with anhydrous THF (30 mL) and ethynyltrimethylsilane (1.60 mL, 11.5 mmol). The flask was cooled to 0 °C in an ice bath and n-butyllithium (2.5 M in hexanes, 4.10 mL, 10.3 mmol) was added dropwise via syringe. The reaction was stirred at 0 °C for 90 min. Compound **1a** (785 mg, 4.00 mmol) was added to the reaction in portions

under a flow of N_2. The reaction was stirred at 0 °C for 10 min, and then allowed to warm to room temperature. After stirring for 20 h, the solution was cooled to 0 °C in an ice bath and a solution of KOH (1.15 g, 20.5 mmol) in methanol (12 mL) was added to the reaction mixture. The reaction was warmed to room temperature and stirred for 4 h. The reaction mixture was cooled to 0 °C in an ice bath, neutralized by the slow addition of 1 M aqueous HCl, and extracted into EtOAc (250 mL). The organic layer was washed with saturated aqueous NH_4Cl (2 × 150 mL), saturated aqueous $NaHCO_3$ (150 mL), and brine (150 mL). The organic layer was dried over Na_2SO_4, filtered, and concentrated under reduced pressure. The crude material was purified by column chromatography on silica gel (5–50% EtOAc/hexanes) to give the title compound as a tan solid (862 mg, 97%).

^{1}H NMR (400 MHz, acetone-d_6) δ: 7.72 – 7.66 (m, 2H), 7.44 – 7.33 (m, 2H), 7.30 – 7.23 (m, 2H), 6.83 (dd, J = 6.1, 2.8 Hz, 1H), 2.89 (s, 1H).

^{13}C NMR (101 MHz, acetone-d_6) δ: 155.0, 148.8, 141.7, 140.1, 132.3, 131.8, 130.0, 129.1, 125.0, 121.0, 116.9, 112.6, 85.1, 74.2, 71.5.

TLC (50% EtOAc/hexanes): R_f = 0.62

HRMS (ESI *m*/*z*): calcd for $[C_{15}H_9O]^+$ $(M\text{-}OH)^+$, 205.0648; found 205.0649.

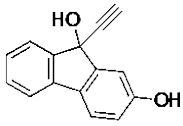

2b

9-ethynyl-9*H*-fluorene-2,9-diol (2b). A flame-dried 250 mL two-neck round bottom flask equipped with a stir bar was evacuated and backfilled with N_2 (3×) and charged with anhydrous THF (30 mL) and ethynyltrimethylsilane (2.00 mL, 14.4 mmol). The flask was cooled to 0 °C in an ice bath and n-butyllithium (2.5 M in hexanes, 5.10 mL, 12.8 mmol) was added dropwise via syringe. The reaction was stirred at 0 °C for 90 min. 2-hydroxy-9*H*-fluoren-9-one (1.00 g, 5.10 mmol)

in anhydrous THF (20 mL) was added to the reaction mixture via syringe under N_2. The reaction was stirred at 0 °C for 10 min, and then allowed to warm to room temperature. After stirring for 18 h, the solution was cooled to 0 °C in an ice bath and a solution of KOH (1.43 g, 25.5 mmol) in methanol (15 mL) was added to the reaction mixture. The reaction was warmed to room temperature and stirred for 6 h. The reaction mixture was cooled to 0 °C in an ice bath, neutralized by the slow addition of 1 M aqueous HCl, and extracted into EtOAc (400 mL). The organic layer was washed with deionized water (200 mL), saturated aqueous NH_4Cl (2 × 250 mL), saturated aqueous $NaHCO_3$ (200 mL), and brine (150 mL). The organic layer was dried over Na_2SO_4, filtered, and concentrated under reduced pressure. The crude material was purified by column chromatography on silica gel (5–50% EtOAc/hexanes) to give the title compound as a tan solid (938 mg, 83%).

^{1}H NMR (400 MHz, acetone-d_6) δ: 8.63 (br s, 1H), 7.63 (dd, J = 7.4, 1.2 Hz, 1H), 7.59 (d, J = 7.6 Hz, 1H), 7.55 (d, J = 8.2 Hz, 1H), 7.34 (ddd, J = 7.5, 7.5, 1.2 Hz, 1H), 7.25 (ddd, J = 7.4, 7.4, 1.0 Hz, 1H), 7.21 (d, J = 2.3 Hz, 1H), 6.88 (dd, J = 8.3, 2.4 Hz, 1H), 5.42 (br s, 1H), 2.91 (s, 1H).

^{13}C NMR (101 MHz, acetone-d_6) δ: 159.0, 150.8, 148.4, 140.4, 131.5, 130.0, 127.5, 125.0, 121.9, 119.8, 116.9, 112.5, 86.3, 74.8, 71.9.

TLC (50% EtOAc/hexanes): R_f = 0.64

HRMS (ESI m/z): calcd for $[C_{15}H_9O]^+$ $(M\text{-}OH)^+$, 205.0648; found 205.0646.

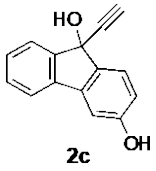

2c

9-ethynyl-9*H*-fluorene-3,9-diol (2c). A flame-dried 250 mL two-neck round bottom flask equipped with a stir bar was evacuated and backfilled with N_2 (3×) and charged with anhydrous THF (30 mL) and ethynyltrimethylsilane

(1.00 mL, 7.22 mmol). The flask was cooled to 0 °C in an ice bath and n-butyllithium (2.5 M in hexanes, 2.50 mL, 6.25 mmol) was added dropwise via syringe. The reaction was stirred at 0 °C for 2 h 30 min. Compound **1c** (484 mg, 2.47 mmol) in anhydrous THF (10 mL) was added to the reaction mixture via syringe under N_2. The reaction was stirred at 0 °C for 10 min, and then allowed to warm to room temperature. After stirring for 18 h, the solution was cooled to 0 °C in an ice bath and a solution of KOH (760 mg, 13.5 mmol) in methanol (12 mL) was added to the reaction mixture. The reaction was warmed to room temperature and stirred for 7 h. The reaction mixture was cooled to 0 °C in an ice bath, neutralized by the slow addition of 1 M aqueous HCl, and extracted into EtOAc (300 mL). The organic layer was washed with deionized water (100 mL), saturated aqueous NH_4Cl (2 × 200 mL), saturated aqueous $NaHCO_3$ (200 mL), and brine (150 mL). The organic layer was dried over Na_2SO_4, filtered, and concentrated under reduced pressure. The crude material was purified by column chromatography on silica gel (5–50% EtOAc/hexanes) to give the title compound as a tan solid (460 mg, 84%).

^{1}H NMR (400 MHz, acetone-d_6) δ: 8.63 (br s, 1H), 7.70 – 7.62 (m, 2H), 7.51 (d, J = 8.2 Hz, 1H), 7.38 (ddd, J = 7.4, 7.4, 1.5 Hz, 1H), 7.34 (ddd, J = 7.3, 7.3, 1.4 Hz, 1H), 7.17 (d, J = 2.2 Hz, 1H), 6.83 (dd, J = 8.2, 2.3 Hz, 1H), 5.33 (br s, 1H), 2.88 (s, 1H).

^{13}C NMR (101 MHz, acetone-d_6) δ: 159.6, 149.8, 141.6, 139.94, 139.89, 129.9, 129.0, 126.2, 125.1, 120.7, 115.9, 107.6, 86.5, 74.4, 71.4.

TLC (50% EtOAc/hexanes): R_f = 0.67

HRMS (ESI m/z): calcd for $[C_{15}H_9O]^+$ $(M\text{-}OH)^+$, 205.0648; found 205.0646.

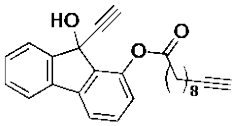

3a

9-ethynyl-9-hydroxy-9*H*-fluoren-1-yl undec-10-ynoate (3a). A flame-dried 50 mL two-neck round bottom flask equipped with a stir bar was charged with compound **2a** (294 mg, 1.32 mmol) and 4-dimethylaminopyridine (10.0 mg, 0.082 mmol). The flask was evacuated and backfilled with N_2 (3×), and anhydrous THF (10 mL) was added. Triethylamine (0.25 mL, 1.8 mmol) was added via syringe, and then the solution was cooled to 0 °C in an ice bath. A solution of 10-undecynoic anhydride (458 mg, 1.32 mmol) in anhydrous THF (10 mL) was added dropwise over 10 minutes under N_2. The reaction was warmed to room temperature and stirred for 16 h. The reaction was diluted with EtOAc (200 mL) and the organic layer was washed with saturated aqueous NH_4Cl (3 × 150 mL), saturated aqueous $NaHCO_3$ (150 mL), and brine (150 mL). The organic layer was dried over Na_2SO_4, filtered, and concentrated under reduced pressure. The crude material was purified by column chromatography on silica gel (0–30% EtOAc/hexanes) to give the product as a pale yellow oil (486 mg, 95%).

^{1}H NMR (400 MHz, $CDCl_3$) δ: 7.71 – 7.68 (m, 1H), 7.63 – 7.59 (m, 1H), 7.51 (dd, *J* = 7.5, 1.0 Hz, 1H), 7.46 – 7.34 (m, 3H), 7.03 (dd, *J* = 8.0, 1.0 Hz, 1H), 3.20 (br s, 1H), 2.694 (t, *J* = 7.6, 1H), 2.689 (t, *J* = 7.5, 1H), 2.44 (s, 1H), 2.20 (td, *J* = 7.0, 2.6 Hz, 2H), 1.95 (t, *J* = 2.7 Hz, 1H), 1.88 – 1.77 (m, 2H), 1.58 – 1.50 (m, 2H), 1.50 – 1.32 (m, 8H).

^{13}C NMR (101 MHz, $CDCl_3$) δ: 172.8, 147.5, 146.6, 141.8, 138.5, 136.7, 131.4, 130.0, 129.2, 124.4, 122.6, 120.6, 118.2, 84.9, 82.8, 73.3, 71.1, 68.3, 34.4, 29.23, 29.20, 29.0, 28.8, 28.5, 24.9, 18.5.

TLC (25% EtOAc/hexanes): R_f = 0.63

HRMS (ESI *m*/*z*): calcd for $[C_{26}H_{26}O_3Na]^+$ $(M+Na)^+$, 409.1774; found 409.1779.

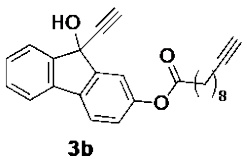

3b

9-ethynyl-9-hydroxy-9*H*-fluoren-2-yl undec-10-ynoate (3b). A flame-dried 100 mL two-neck round bottom flask equipped with a stir bar was charged with compound **2b** (500 mg, 2.25 mmol) and 4-dimethylaminopyridine (14.0 mg, 0.115 mmol). The flask was evacuated and backfilled with N_2 (3×), and anhydrous THF (25 mL) was added. Triethylamine (0.40 mL, 2.9 mmol) was added via syringe, and then the solution was cooled to 0 °C in an ice bath. A solution of 10-undecynoic anhydride (818 mg, 2.36 mmol) in anhydrous THF (15 mL) was added dropwise over 10 minutes under N_2. The reaction was warmed to room temperature and stirred for 18 h. The reaction was diluted with EtOAc (300 mL) and the organic layer was washed with saturated aqueous NH_4Cl (3 × 150 mL), saturated aqueous $NaHCO_3$ (150 mL), and brine (150 mL). The organic layer was dried over Na_2SO_4, filtered, and concentrated under reduced pressure. The crude material was purified by column chromatography on silica gel (0–30% EtOAc/hexanes) to give the product as a pale tan oil (837 mg, 96%).

^{1}H NMR (400 MHz, $CDCl_3$) δ: 7.68 (dd, *J* = 7.4, 1.3 Hz, 1H), 7.58 (d, J = 8.2 Hz, 1H), 7.57 (dd, J = 7.5, 1.2 Hz, 1H),7.43 (d, *J* = 2.2 Hz, 1H), 7.39 (ddd, *J* = 7.5, 7.5, 1.3 Hz, 1H), 7.33 (ddd, *J* = 7.4, 7.4, 1.2 Hz, 1H), 7.11 (dd, *J* = 8.2, 2.2 Hz, 1H), 2.82 (br s, 1H), 2.57 (t, *J* = 7.5 Hz, 2H), 2.47 (s, 1H), 2.19 (td, *J* = 7.0, 2.7 Hz, 2H), 1.95 (t, *J* = 2.7 Hz, 1H), 1.76 (p, *J* = 7.4 Hz, 2H), 1.58 – 1.50 (m, 2H), 1.47 – 1.33 (m, 8H).

^{13}C NMR (101 MHz, $CDCl_3$) δ: 172.4, 151.1, 148.1, 146.9, 138.5, 136.7, 130.1, 128.6, 124.4, 123.2, 120.9, 120.2, 118.2, 84.9, 83.5, 74.4, 71.8, 68.3, 34.5, 29.22, 29.15, 29.0, 28.8, 28.5, 25.0, 18.5.

TLC (25% EtOAc/hexanes): R_f = 0.57

HRMS (ESI *m*/*z*): calcd for $[C_{26}H_{26}O_3Na]^+$ $(M+Na)^+$, 409.1774; found 409.1773.

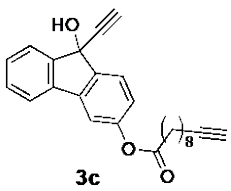

3c

9-ethynyl-9-hydroxy-9*H*-fluoren-3-yl undec-10-ynoate (3c). A flame-dried 50 mL two-neck round bottom flask equipped with a stir bar was charged with compound **2c** (217 mg, 0.98 mmol) and 4-dimethylaminopyridine (6.0 mg, 0.049 mmol). The flask was evacuated and backfilled with N_2 (3×), and anhydrous THF (10 mL) was added. Triethylamine (0.18 mL, 1.3 mmol) was added via syringe, and then the solution was cooled to 0 °C in an ice bath. A solution of 10-undecynoic anhydride (356 mg, 1.03 mmol) in anhydrous THF (5 mL) was added dropwise over 10 minutes under N_2. The reaction was warmed to room temperature and stirred for 18 h. The reaction was diluted with EtOAc (200 mL) and the organic layer was washed with saturated aqueous NH_4Cl (3 × 150 mL), saturated aqueous $NaHCO_3$ (150 mL), and brine (150 mL). The organic layer was dried over Na_2SO_4, filtered, and concentrated under reduced pressure. The crude material was purified by column chromatography on silica gel (0–30% EtOAc/hexanes) to give the product as a pale tan oil (346 mg, 92%).

^{1}H NMR (400 MHz, $CDCl_3$) δ: 7.70 – 7.67 (m, 1H), 7.68 (d, *J* = 8.1 Hz, 1H), 7.59 – 7.52 (m, 1H), 7.40 (ddd, *J* = 7.5, 7.5, 1.4 Hz, 1H), 7.36 (ddd, *J* = 7.4, 7.4, 1.4 Hz, 1H), 7.32 (d, *J* = 2.1 Hz, 1H), 7.02 (dd, *J* = 8.2, 2.1 Hz, 1H), 2.69 (br s, 1H), 2.58 (t, *J* = 7.5 Hz, 2H), 2.47 (s, 1H), 2.19 (td, *J* = 7.0, 2.7 Hz, 2H), 1.95 (t, *J* = 2.6 Hz, 1H), 1.77 (p, *J* = 7.6 Hz, 2H), 1.58 – 1.50 (m, 2H), 1.47 – 1.31 (m, 8H).

^{13}C NMR (101 MHz, $CDCl_3$) δ: 172.4, 152.3, 147.3, 144.0, 140.9, 138.4, 130.0, 129.2, 125.3, 124.4, 121.7, 120.6, 113.9, 84.8, 83.7, 74.2, 71.6, 68.3, 34.5, 29.22, 29.16, 29.0, 28.8, 28.5, 25.0, 18.5.

TLC (25% EtOAc/hexanes): R_f = 0.48

HRMS (ESI *m*/*z*): calcd for $[C_{26}H_{26}O_3Na]^+$ $(M+Na)^+$, 409.1774; found 409.1772.

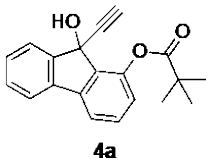

4a

9-ethynyl-9-hydroxy-9*H*-fluoren-1-yl pivalate (4a). A flame-dried 100 mL two-neck round bottom flask equipped with a stir bar was charged with compound **2a** (225 mg, 1.01 mmol). The flask was evacuated and backfilled with N_2 (3×), and anhydrous THF (30 mL) was added. Triethylamine (0.18 mL, 1.3 mmol) was added via syringe, and then the solution was cooled to 0 °C in an ice bath. Trimethylacetyl chloride (0.13 mL, 1.06 mmol) was added dropwise over 10 minutes under N_2. The reaction was warmed to room temperature and stirred for 20 h. The reaction was diluted with EtOAc (200 mL) and the organic layer was washed with saturated aqueous NH_4Cl (3 × 150 mL), saturated aqueous $NaHCO_3$ (150 mL), and brine (150 mL). The organic layer was dried over Na_2SO_4, filtered, and concentrated under reduced pressure. The crude material was purified by column chromatography on silica gel (0–30% EtOAc/hexanes) to give the product as a pale tan oil (256 mg, 82%).

^{1}H NMR (400 MHz, $CDCl_3$) δ: 7.72 – 7.67 (m, 1H), 7.64 – 7.59 (m, 1H), 7.51 (d, J = 7.6 Hz, 1H), 7.47 – 7.34 (m, 3H), 7.00 (d, J = 8.0 Hz, 1H), 2.43 (s, 1H), 1.46 (s, 9H).

^{13}C NMR (101 MHz, $CDCl_3$) δ: 177.8, 147.9, 146.8, 141.8, 138.4, 136.8, 131.5, 130.0, 129.3, 124.4, 122.5, 120.6, 118.1, 83.1, 73.4, 71.2, 39.5, 27.5.

TLC (25% EtOAc/hexanes): R_f = 0.70

HRMS (ESI *m*/*z*): calcd for $[C_{20}H_{17}O_2]^+$ $(M\text{-}OH)^+$, 289.1223; found 289.1222.

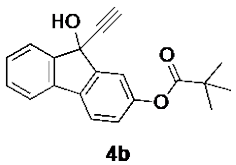

4b

9-ethynyl-9-hydroxy-9*H*-fluoren-2-yl pivalate (4b). A flame-dried 100 mL two-neck round bottom flask equipped with a stir bar was charged with compound **2b** (387 mg, 1.74 mmol). The flask was evacuated and backfilled with N_2 (3×), and anhydrous THF (30 mL) was added.

Triethylamine (0.32 mL, 2.3 mmol) was added via syringe, and then the solution was cooled to 0 °C in an ice bath. Trimethylacetyl chloride (0.23 mL, 1.9 mmol) was added dropwise over 10 minutes under N_2. The reaction was warmed to room temperature and stirred for 20 h. The reaction was diluted with EtOAc (200 mL) and the organic layer was washed with saturated aqueous NH_4Cl (3 × 150 mL), saturated aqueous $NaHCO_3$ (150 mL), and brine (150 mL). The organic layer was dried over Na_2SO_4, filtered, and concentrated under reduced pressure. The crude material was purified by column chromatography on silica gel (0–30% EtOAc/hexanes) to give the product as a pale tan oil (466 mg, 87%).

^{1}H NMR (400 MHz, $CDCl_3$) δ: 7.69 (d, *J* = 7.3 Hz, 1H), 7.59 (d, *J* = 8.2 Hz, 1H), 7.58 (d, J = 7.3 Hz, 1H), 7.42 (d, *J* = 2.1 Hz, 1H), 7.40 (ddd, *J* = 7.4, 7.4, 1.3 Hz, 1H), 7.34 (ddd, *J* = 7.4, 7.4, 1.2 Hz, 1H), 7.09 (dd, *J* = 8.2, 2.2 Hz, 1H), 2.48 (s, 1H), 1.38 (s, 9H).

^{13}C NMR (101 MHz, $CDCl_3$) δ: 177.2, 151.6, 148.1, 146.9, 138.5, 136.6, 130.1, 128.6, 124.5, 123.2, 121.0, 120.3, 118.1, 83.5, 74.5, 71.9, 39.3, 27.3.

TLC (25% EtOAc/hexanes): R_f = 0.65

HRMS (ESI *m*/*z*): calcd for $[C_{20}H_{17}O_2]^+$ $(M\text{-}OH)^+$, 289.1223; found 289.1221.

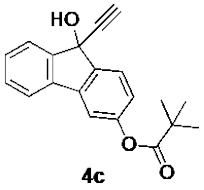

4c

9-ethynyl-9-hydroxy-9*H*-fluoren-3-yl pivalate (4c). A flame-dried 100 mL two-neck round bottom flask equipped with a stir bar was charged with compound **2c** (327 mg, 1.47 mmol). The flask was evacuated and backfilled with N_2 (3×), and anhydrous THF (15 mL) was added. Triethylamine (0.27 mL, 1.9 mmol) was added via syringe, and then the solution was cooled to 0 °C in an ice bath. Trimethylacetyl chloride (0.19 mL, 1.5 mmol) was added dropwise over 10 minutes under N_2. The reaction was warmed to room temperature and stirred for 20 h. The reaction was

diluted with EtOAc (200 mL) and the organic layer was washed with saturated aqueous NH_4Cl (3 × 150 mL), saturated aqueous $NaHCO_3$ (150 mL), and brine (150 mL). The organic layer was dried over Na_2SO_4, filtered, and concentrated under reduced pressure. The crude material was purified by column chromatography on silica gel (0–30% EtOAc/hexanes) to give the product as a pale tan oil (358 mg, 79%).

^{1}H NMR (400 MHz, $CDCl_3$) δ: 7.72 – 7.68 (m, 1H), 7.69 (d, *J* = 8.1 Hz, 1H) 7.59 – 7.55 (m, 1H), 7.4 (ddd, *J* = 7.5, 7.5, 1.4 Hz, 1H), 7.36 (ddd, *J* = 7.4, 7.4, 1.3 Hz, 1H), 7.30 (d, *J* = 2.2 Hz, 1H), 7.01 (dd, *J* = 8.1, 2.1 Hz, 1H), 2.59 (br s, 1H), 2.47 (s, 1H), 1.39 (s, 9H).

^{13}C NMR (101 MHz, $CDCl_3$) δ: 177.2, 152.8, 147.3, 143.9, 140.9, 138.4, 130.1, 129.2, 125.3, 124.4, 121.6, 120.6, 113.9, 83.7, 74.3, 71.6, 39.3, 27.3.

TLC (25% EtOAc/hexanes): R_f = 0.50

HRMS (ESI *m*/*z*): calcd for $[C_{20}H_{17}O_2]^+$ $(M\text{-}OH)^+$, 289.1223; found 289.1226.

General Procedure A for the Synthesis of Fluorenyl Naphthopyrans. To a flame-dried two-neck round bottom flask equipped with a stir bar and reflux condenser was added the naphthol and a catalytic amount of *p*-toluenesulfonic acid monohydrate (*p*TSA·H_2O). The flask was evacuated and backfilled with N_2 (3×) followed by the addition of a solution of propargyl alcohol in chloroform via syringe under N_2. The reaction was heated to reflux and stirred for the indicated amount of time. Upon completion, the reaction was cooled to room temperature and diluted with dichloromethane (50 mL) and the organic layer was washed consecutively with deionized water (3 × 25 mL) and brine (25 mL). The organic layer was dried over Na_2SO_4, filtered, and concentrated under reduced pressure.

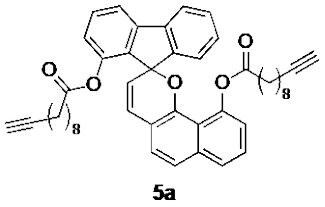

5a

Spiro[benzo[*h*]chromene-2,9'-fluorene]-1',10-diyl bis(undec-10-ynoate) (5a). Synthesized according to General Procedure A with 8-hydroxynaphthalen-1-yl undec-10-ynoate (115 mg, 0.354 mmol), *p*-toluenesulfonic acid monohydrate (17 mg, 0.09 mmol), compound **3a** (164 mg, 0.424 mmol), and chloroform (3 mL). The reaction was stirred at reflux for 1 h 45 min. The crude material was purified by column chromatography on silica gel (0–20% EtOAc/hexanes) followed by a reverse-phase chromatographic separation on a C18 column (80–100% acetonitrile/H_2O). A final chromatographic separation on silica gel (0–15% Et_2O/CH_2Cl_2:hexanes (1:1)) afforded the title compound as a red oil (53 mg, 22%).

^{1}H NMR (400 MHz, acetone-d_6) δ: 7.86 (d, J = 7.4 Hz, 1H), 7.74 (dd, J = 7.6, 0.8 Hz, 1H), 7.71 (dd, J = 8.3, 1.2 Hz, 1H), 7.57 – 7.48 (m, 4H), 7.42 – 7.33 (m, 3H), 7.13 (dd, J = 8.2, 0.8 Hz, 1H), 6.90 (dd, J = 7.5, 1.2 Hz, 1H), 6.86 (d, J = 9.9 Hz, 1H), 5.42 (d, J = 9.9 Hz, 1H), 2.35 (t, J = 2.6 Hz, 1H), 2.34 (t, J = 2.7 Hz, 1H), 2.20 (td, J = 7.0, 2.7 Hz, 2H), 2.17 (td, J = 7.1, 2.6 Hz, 2H), 1.96 (ddd, J = 16.6, 8.8, 6.3 Hz, 1H), 1.83 – 1.63 (m, 2H), 1.59 – 0.90 (m, 25H).

^{13}C NMR (101 MHz, acetone-d_6) δ: 172.3, 171.6, 150.8, 150.0, 149.4, 147.9, 141.9, 139.0, 138.7, 137.9, 132.0, 131.0, 129.8, 126.90, 126.86, 126.6, 126.3, 124.8, 124.0, 123.7, 121.6, 121.3, 120.7, 119.6, 118.3, 115.9, 87.2, 85.1, 69.9, 69.8, 34.2, 33.9, 29.9, 29.8, 29.7, 29.52, 29.50, 29.40, 29.35, 29.3, 25.0, 24.6, 18.8, 18.7.

TLC (25% EtOAc/hexanes): R_f = 0.77

HRMS (ESI *m*/*z*): calcd for $[C_{47}H_{49}O_5]^+$ $(M+H)^+$, 693.3575; found 693.3593.

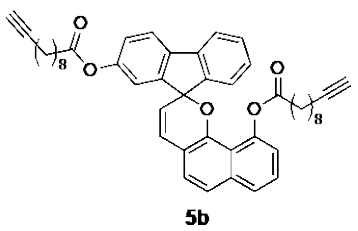

5b

Spiro[benzo[*h*]chromene-2,9'-fluorene]-2',10-diyl bis(undec-10-ynoate) (5b). Synthesized according to General Procedure A with 8-hydroxynaphthalen-1-yl undec-10-ynoate (133 mg, 0.410 mmol), *p*-toluenesulfonic acid monohydrate (12 mg, 0.06 mmol), compound **3b** (205 mg, 0.530 mmol), and chloroform (3 mL). The reaction was stirred at reflux 1 h 45 min. The crude material was purified by column chromatography on silica gel (0–20% EtOAc/hexanes) followed by a reverse-phase chromatographic separation on a C18 column (80–100% acetonitrile/H_2O). A final chromatographic separation on silica gel (0–15% Et_2O/CH_2Cl_2:hexanes (1:1)) afforded the title compound as a red oil (45 mg, 16%).

^{1}H NMR (400 MHz, acetone-d_6) δ: 7.87 (d, J = 8.1 Hz, 1H), 7.83 (d, J = 7.6 Hz, 1H), 7.71 (d, J = 8.3 Hz, 1H), 7.55 (d, J = 8.3 Hz, 1H), 7.53 – 7.46 (m, 2H), 7.43 – 7.35 (m, 2H), 7.32 – 7.23 (m, 3H), 6.95 (d, J = 9.7 Hz, 1H), 6.90 (d, J = 7.4 Hz, 1H), 5.64 (d, J = 9.7 Hz, 1H), 2.55 (t, J = 7.4 Hz, 2H), 2.35 (t, J = 2.7 Hz, 1H), 2.29 (t, J = 2.8 Hz, 1H), 2.20 (td, J = 7.0, 2.6 Hz, 2H), 2.16 (td, 7.0, 2.6 Hz, 2H), 1.73 – 0.95 (m, 26H).

^{13}C NMR (101 MHz, acetone-d_6) δ: 172.42, 172.37, 152.3, 149.73, 149.72, 148.6, 147.7, 139.0, 137.9, 137.1, 131.1, 129.2, 127.00, 126.97, 126.5, 126.1, 125.8, 125.3, 124.7, 122.1, 121.7, 121.1, 120.8, 120.0, 119.9, 117.0, 86.9, 85.1, 85.0, 69.9, 69.8, 34.6, 33.9, 29.9, 29.73, 29.70, 29.4, 29.3, 25.5, 24.8, 18.8, 18.7.

TLC (25% EtOAc/hexanes): R_f = 0.74

HRMS (ESI *m*/*z*): calcd for $[C_{47}H_{49}O_5]^+$ $(M+H)^+$, 693.3575; found 693.3577.

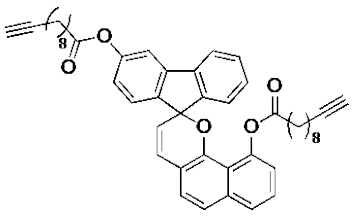

5c

Spiro[benzo[*h*]chromene-2,9'-fluorene]-3',10-diyl bis(undec-10-ynoate) (5c). Synthesized according to General Procedure A with 8-hydroxynaphthalen-1-yl undec-10-ynoate (115 mg, 0.354 mmol), *p*-toluenesulfonic acid monohydrate (15 mg, 0.08 mmol), compound **3c** (164 mg, 0.424 mmol) and chloroform (3 mL). The reaction was stirred at reflux for 1 h 45 min. The crude material was purified by column chromatography on silica gel (0–20% EtOAc/hexanes) followed by a reverse-phase chromatographic separation on a C18 column (80–100% acetonitrile/H_2O). A final chromatographic separation on silica gel (0–15% Et_2O/CH_2Cl_2:hexanes (1:1)) afforded the title compound as a red oil (62 mg, 25%).

^{1}H NMR (400 MHz, acetone-d_6) δ: 7.85 (dt, J = 7.6, 0.9 Hz, 1H), 7.71 (dd, J = 8.3, 1.2 Hz, 1H), 7.60 (d, J = 2.1 Hz, 1H), 7.58 – 7.47 (m, 4H), 7.42 (d, J = 8.3 Hz, 1H), 7.40 – 7.30 (m, 2H), 7.04 (dd, J = 8.2, 2.1 Hz, 1H), 6.96 (d, J = 9.8 Hz, 1H), 6.90 (dd, J = 7.5, 1.2 Hz, 1H), 5.66 (d, J = 9.8 Hz, 1H), 2.64 (t, J = 7.4 Hz, 2H), 2.34 (t, J = 2.7 Hz, 1H), 2.31 (t, J = 2.7 Hz, 1H), 2.20 (td, J = 7.0, 2.7 Hz, 2H), 2.18 (td, J = 7.0, 2.7 Hz, 2H), 1.76 (p, J = 7.4 Hz, 2H), 1.63 – 1.57 (m, 2H), 1.56 – 1.35 (m, 14H), 1.32 – 1.24 (m, 2H), 1.22 – 1.12 (m, 2H), 1.11 – 0.96 (m, 4H).

^{13}C NMR (101 MHz, acetone-d_6) δ: 172.42, 172.36, 153.8, 149.8, 149.0, 147.7, 145.5, 141.3, 138.9, 137.8, 131.1, 129.8, 127.0, 126.93, 126.90, 126.5, 126.2, 125.7, 125.5, 122.6, 122.0, 121.4, 120.7, 120.0, 117.2, 114.9, 86.6, 85.1, 85.0, 69.9, 69.8, 34.7, 33.9, 30.0, 29.9, 29.8, 29.7, 29.39, 29.38, 29.3, 25.6, 24.8, 18.8, 18.7.

TLC (25% EtOAc/hexanes): R_f = 0.79

HRMS (ESI *m*/*z*): calcd for $[C_{47}H_{49}O_5]^+$ $(M+H)^+$, 693.3575; found 693.3578.

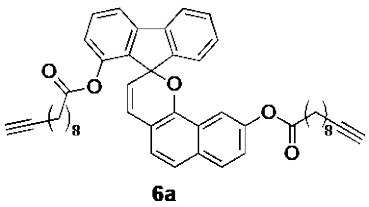

6a

Spiro[benzo[*h*]chromene-2,9'-fluorene]-1',9-diyl bis(undec-10-ynoate) (6a). Synthesized according to General Procedure A with 8-hydroxynaphthalen-2-yl undec-10-ynoate (117 mg, 0.361 mmol), *p*-toluenesulfonic acid monohydrate (10 mg, 0.053 mmol), compound **3a** (167 mg, 0.432 mmol), and chloroform (3 mL). The reaction was stirred at reflux for 1 h 45 min. The crude material was purified by column chromatography on silica gel (0–20% EtOAc/hexanes) followed by a reverse-phase chromatographic separation on a C18 column (80–100% acetonitrile/H_2O). A final chromatographic separation on silica gel (0–15% Et_2O/CH_2Cl_2:hexanes (1:1)) afforded the title compound as a red oil (60 mg, 24%).

^{1}H NMR (400 MHz, acetone-d_6) δ: 7.87 (d, J = 8.7 Hz, 1H), 7.87 – 7.83 (m, 1H), 7.73 (dd, J = 7.6, 0.9 Hz, 1H), 7.56 – 7.45 (m, 5H), 7.39 (d, J = 8.3 Hz, 1H), 7.33 (td, J = 7.5, 1.1 Hz, 1H), 7.21 (dd, J = 8.9, 2.4 Hz, 1H), 7.06 (dd, J = 8.1, 0.8 Hz, 1H), 6.91 (d, J = 9.9 Hz, 1H), 5.48 (d, J = 9.9 Hz, 1H), 2.53 (t, J = 7.5 Hz, 2H), 2.34 (t, J = 2.7 Hz, 1H), 2.29 (t, J = 2.7 Hz, 1H), 2.17 (td, J = 7.1, 2.7 Hz, 2H), 2.14 (td, J = 7.1, 2.7 Hz, 2H), 2.01 – 1.91 (m, 1H), 1.72 – 1.60 (m, 3H), 1.52 – 1.42 (m, 4H), 1.41 – 1.24 (m, 10H), 1.23 – 1.09 (m, 3H), 1.09 – 0.95 (m, 5H).

^{13}C NMR (101 MHz, acetone-d_6) δ: 172.5, 171.7, 150.6, 149.6, 149.5, 142.1, 139.4, 138.8, 133.4, 132.1, 131.0, 129.88, 129.85, 126.0, 125.6, 125.2, 124.6, 124.18, 124.16, 123.1, 121.4, 121.0, 118.6, 115.1, 113.6, 87.2, 85.1, 85.0, 69.83, 69.76, 34.5, 34.0, 29.7, 29.6, 29.5, 29.44, 29.35, 29.32, 29.25, 25.4, 24.9, 18.74, 18.68.

TLC (25% EtOAc/hexanes): R_f = 0.82

HRMS (ESI *m*/*z*): calcd for $[C_{47}H_{49}O_5]^+$ $(M+H)^+$, 693.3575; found 693.3579.

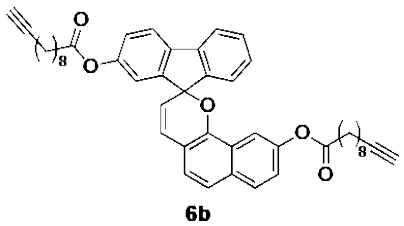

6b

Spiro[benzo[*h*]chromene-2,9'-fluorene]-2',9-diyl bis(undec-10-ynoate) (6b). Synthesized according to General Procedure A with 8-hydroxynaphthalen-2-yl undec-10-ynoate (133 mg, 0.410 mmol), *p*-toluenesulfonic acid monohydrate (12 mg, 0.06 mmol), compound **3b** (207 mg, 0.536 mmol) and chloroform (3 mL). The reaction was stirred at reflux for 1 h 20 min. The crude material was purified by column chromatography on silica gel (0–20% EtOAc/hexanes) followed by a reverse-phase chromatographic separation on a C18 column (80–100% acetonitrile/H_2O). A final chromatographic separation on silica gel (0–15% Et_2O/CH_2Cl_2:hexanes (1:1)) afforded the title compound as a red oil (30 mg, 11%).

^{1}H NMR (400 MHz, acetone-d_6) δ: 7.87 (d, J = 8.9 Hz, 1H), 7.85 (d, J = 8.2 Hz, 1H), 7.82 (d, J = 7.6 Hz, 1H), 7.56 – 7.44 (m, 4H), 7.40 (d, J = 8.3 Hz, 1H), 7.30 (d, J = 2.2 Hz, 1H), 7.28 (ddd, J = 7.5, 7.5, 1.1 Hz, 1H), 7.24 – 7.18 (m, 2H), 6.99 (d, J = 9.8 Hz, 1H), 5.68 (d, J = 9.8 Hz, 1H), 2.530 (t, J = 7.5 Hz, 2H), 2.528 (t, J = 7.5 Hz, 2H), 2.293 (t, J = 2.7 Hz, 1H), 2.289 (d, J = 2.7 Hz, 1H), 2.15 (td, J = 7.1, 2.6 Hz, 2H), 2.14 (td, J = 7.1, 2.6 Hz, 2H), 1.71 – 1.59 (m, 4H), 1.53 – 1.43 (m, 4H), 1.42 – 1.25 (m, 16H).

^{13}C NMR (101 MHz, acetone-d_6) δ: 172.6, 172.4, 152.3, 149.9, 149.7, 149.4, 148.8, 139.1, 137.3, 133.4, 131.1, 130.0, 129.2, 125.9, 125.7, 125.58, 125.57, 125.48, 124.7, 123.1, 121.9, 121.5, 121.2, 119.7, 116.1, 113.5, 87.0, 85.0, 69.78, 69.77, 34.52, 34.48, 29.61, 29.58, 29.33, 29.32, 25.4, 25.3, 18.7.

TLC (25% EtOAc/hexanes): R_f = 0.79

HRMS (ESI *m*/*z*): calcd for $[C_{47}H_{49}O_5]^+$ $(M+H)^+$, 693.3575; found 693.3578.

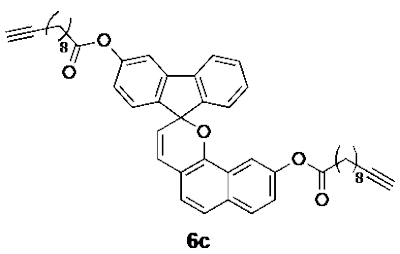

6c

Spiro[benzo[*h*]chromene-2,9'-fluorene]-3',9-diyl bis(undec-10-ynoate) (6c). Synthesized according to General Procedure A with 8-hydroxynaphthalen-2-yl undec-10-ynoate (117 mg, 0.361 mmol), *p*-toluenesulfonic acid monohydrate (10 mg, 0.054 mmol), compound **3c** (167 mg, 0.432 mmol) and chloroform (3 mL). The reaction was stirred at reflux for 1 h 30 min. The crude material was purified by column chromatography on silica gel (0–20% EtOAc/hexanes) followed by a reverse-phase chromatographic separation on a C18 column (80–100% acetonitrile/H_2O). A final chromatographic separation on silica gel (0–15% Et_2O/CH_2Cl_2:hexanes (1:1)) afforded the title compound as a red oil (63 mg, 25%).

^{1}H NMR (400 MHz, acetone-d_6) δ: 7.86 (d, J = 8.9 Hz, 1H), 7.83 (dt, J = 7.6, 1.0 Hz, 1H), 7.59 (d, J = 2.1 Hz, 1H), 7.57 – 7.52 (m, 3H), 7.49 (d, J = 2.4 Hz, 1H), 7.47 (ddd, J = 7.6, 7.6, 1.2 Hz, 1H), 7.41 (d, J = 8.3 Hz, 1H), 7.31 (ddd, J = 7.5, 7.5, 1.1 Hz, 1H), 7.20 (dd, J = 8.8, 2.4 Hz, 1H), 7.02 (dd, J = 8.2, 2.1 Hz, 1H), 6.99 (d, J = 9.9 Hz, 1H), 5.69 (d, J = 9.8 Hz, 1H), 2.62 (t, J = 7.4 Hz, 2H), 2.53 (t, J = 7.5 Hz, 2H), 2.31 (t, J = 2.7 Hz, 1H), 2.29 (t, J = 2.7 Hz, 1H), 2.17 (td, J = 7.0, 2.7 Hz, 2H), 2.14 (td, J = 7.0, 2.6 Hz, 2H), 1.79 – 1.70 (m, 2H), 1.68 – 1.58 (m, 2H), 1.56 – 1.26 (m, 20H).

^{13}C NMR (101 MHz, acetone-d_6) δ: 172.6, 172.5, 153.8, 149.7, 149.5, 149.1, 145.7, 141.5, 139.0, 133.4, 131.1, 130.0, 129.8, 126.7, 125.94, 125.87, 125.7, 125.6, 125.5, 123.1, 122.6, 121.5, 121.4, 116.3, 115.1, 113.5, 86.7, 85.0, 69.81, 69.77, 34.6, 34.5, 29.9, 29.7, 29.6, 29.4, 29.32, 29.29, 25.6, 25.3, 18.71, 18.69.

TLC (25% EtOAc/hexanes): R_f = 0.79

HRMS (ESI m/z): calcd for $[C_{47}H_{49}O_5]^+$ $(M+H)^+$, 693.3575; found 693.3572.

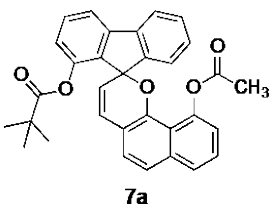

7a

10-acetoxyspiro[benzo[*h*]chromene-2,9'-fluoren]-1'-yl pivalate (7a). Synthesized according to General Procedure A with 8-hydroxynaphthalen-1-yl acetate (146 mg, 0.722 mmol), *p*-toluenesulfonic acid monohydrate (21 mg, 0.11 mmol), compound **4a** (265 mg, 0.865 mmol) and chloroform (3 mL). The reaction was stirred at reflux for 1 h 30 min. The crude material was purified by column chromatography on silica gel (0–20% EtOAc/hexanes) followed by a second chromatographic separation on silica gel (0–15% Et_2O/CH_2Cl_2:hexanes (1:1)) afforded the title compound as a red oil (177 mg, 50%).

^{1}H NMR (400 MHz, $CDCl_3$) δ: 7.65 (dt, *J* = 7.6, 0.9 Hz, 1H), 7.60 (dd, *J* = 8.3, 1.2 Hz, 1H), 7.56 (dd, *J* = 7.6, 1.0 Hz, 1H), 7.51 – 7.40 (m, 3H), 7.39 (ddd, *J* = 7.6, 7.6, 1.1 Hz, 1H), 7.31 (dd, *J* = 8.3, 7.4 Hz, 1H), 7.23 (d, *J* = 8.3 Hz, 1H), 7.17 (ddd, *J* = 7.5, 7.5, 1.1 Hz, 1H), 7.06 (dd, *J* = 8.1, 1.0 Hz, 1H), 6.88 (dd, *J* = 7.5, 1.2 Hz, 1H), 6.73 (d, *J* = 9.8 Hz, 1H), 5.62 (d, *J* = 9.8 Hz, 1H), 1.40 (s, 3H), 1.08 (s, 9H).

^{13}C NMR (101 MHz, $CDCl_3$) δ: 176.8, 170.1, 149.8, 149.3, 146.9, 146.7, 142.3, 138.0, 137.1, 136.9, 131.5, 130.3, 129.1, 126.4, 126.1, 125.4, 125.2, 124.5, 124.2, 122.8, 121.1, 120.2, 119.8, 119.0, 117.4, 116.0, 85.9, 39.3, 27.0, 19.7.

TLC (25% EtOAc/hexanes): R_f = 0.64

HRMS (ESI *m*/*z*): calcd for $[C_{32}H_{27}O_5]^+$ $(M+H)^+$, 491.1853; found 491.1855.

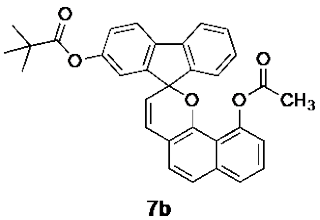

7b

10-acetoxyspiro[benzo[*h*]chromene-2,9'-fluoren]-2'-yl pivalate (7b). Synthesized according to General Procedure A with 8-hydroxynaphthalen-1-yl acetate (130 mg, 0.643 mmol), *p*-toluenesulfonic acid monohydrate (18 mg, 0.09 mmol),

compound **4b** (237 mg, 0.774 mmol) and chloroform (3 mL). The reaction was stirred at reflux for 1 h 20 min. The crude material was purified by column chromatography on silica gel (0–20% EtOAc/hexanes) followed by a second chromatographic separation on silica gel (0–15% Et_2O/CH_2Cl_2:hexanes (1:1)) afforded the title compound as a red oil (88 mg, 28%).

^{1}H NMR (400 MHz, acetone-d_6) δ: 7.86 (d, J = 8.2 Hz, 1H), 7.82 (dt, J = 7.5, 0.9 Hz, 1H), 7.70 (dd, J = 8.4, 1.2 Hz, 1H), 7.54 (d, J = 8.3 Hz, 1H), 7.50 – 7.44 (m, 2H), 7.41 (d, J = 8.3 Hz, 1H), 7.37 (dd, J = 8.3, 7.4 Hz, 1H), 7.31 (d, J = 2.2 Hz, 1H), 7.27 (ddd, J = 7.5, 7.5, 1.1 Hz, 1H), 7.22 (dd, J = 8.2, 2.2 Hz, 1H), 6.97 (d, J = 9.8 Hz, 1H), 6.90 (dd, J = 7.4, 1.2 Hz, 1H), 5.68 (d, J = 9.8 Hz, 1H), 1.32 (s, 3H), 1.30 (s, 9H).

^{13}C NMR (101 MHz, acetone-d_6) δ: 177.1, 169.8, 152.6, 149.8, 149.6, 148.3, 147.6, 139.0, 137.8, 137.5, 131.2, 129.2, 127.03, 126.96, 126.5, 126.1, 125.9, 125.0, 124.6, 122.0, 121.7, 121.0, 120.6, 120.0, 119.9, 117.0, 86.8, 39.6, 27.3, 19.7.

TLC (25% EtOAc/hexanes): R_f = 0.70

HRMS (ESI m/z): calcd for $[C_{32}H_{27}O_5]^+$ $(M+H)^+$, 491.1853; found 491.1862.

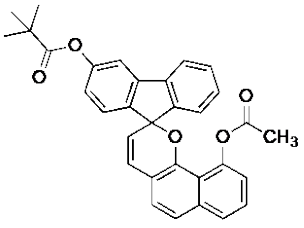

7c

10-acetoxyspiro[benzo[*h*]chromene-2,9'-fluoren]-3'-yl pivalate (7c). Synthesized according to General Procedure A with 8-hydroxynaphthalen-1-yl acetate (146 mg, 0.722 mmol), *p*-toluenesulfonic acid monohydrate (21 mg, 0.11 mmol), compound **4c** (265 mg, 0.865 mmol) and chloroform (3 mL). The reaction was stirred at reflux for 1 h 45 min. The crude material was purified by column chromatography on silica gel (0–20% EtOAc/hexanes) followed by a second chromatographic separation on silica gel (0–15% Et_2O/CH_2Cl_2:hexanes (1:1)) afforded the title compound as a red oil (135 mg, 38%).

^{1}H NMR (400 MHz, $CDCl_3$) δ: 7.62 (dt, J = 7.1, 0.9 Hz, 1H), 7.61 (dd, J = 8.4, 1.2 Hz, 1H), 7.58 (dt, J = 7.5, 1.0 Hz, 1H), 7.57 (d, J = 8.1 Hz, 1H), 7.44 (d, J = 8.4 Hz, 1H), 7.42 (ddd, J = 7.5, 7.5, 1.2 Hz, 1H), 7.37 (d, *J* = 2.1 Hz, 1H), 7.34 – 7.26 (m, 3H), 6.93 (dd, *J* = 8.1, 2.1 Hz, 1H), 6.87 (dd, *J* = 7.4, 1.2 Hz, 1H), 6.80 (d, *J* = 9.8 Hz, 1H), 5.58 (d, *J* = 9.8 Hz, 1H), 1.40 (s, 9H), 1.35 (s, 3H).

^{13}C NMR (101 MHz, $CDCl_3$) δ: 177.2, 170.3, 152.9, 149.0, 148.2, 146.6, 144.8, 140.6, 138.1, 137.0, 130.2, 129.1, 126.54, 126.49, 126.1, 125.7, 125.6, 125.0, 124.4, 121.5, 121.2, 120.2, 119.7, 119.0, 116.1, 113.6, 85.8, 39.3, 27.3, 19.8.

TLC (25% EtOAc/hexanes): R_f = 0.74

HRMS (ESI *m/z*): calcd for $[C_{32}H_{27}O_5]^+$ $(M+H)^+$, 491.1853; found 491.1854.

General Procedure B for Synthesis of Model Compounds. Model compounds were synthesized following the literature procedure.[40] Lithium diisopropylamide (LDA) was freshly prepared in a flame-dried 25 mL Schlenk flask. Anhydrous THF and diisopropylamine were added via syringe under N_2. The flask was cooled to −78 °C and n-butyllithium (2.5 M in hexanes) was added via syringe under N_2. The reaction was stirred for the indicated amount of time. A separate flame dried 25 mL Schlenk flask equipped with a stir bar was charged with the naphthopyran and the vessel was evacuated and backfilled with N_2 (3×). Anhydrous THF was added via syringe under N_2, the solution was cooled to −78 °C, and the LDA solution was added dropwise via syringe in 0.5–1.0 mL portions over the indicated amount of time. After complete addition, the reaction was removed from the cooling bath and immediately diluted with ethyl acetate (50 mL) and saturated aqueous NH_4Cl solution (50 mL). The organic layer was washed with saturated aqueous NH_4Cl

solution (2 × 50 mL) and then brine (50 mL), dried over Na_2SO_4, filtered, and concentrated under reduced pressure.

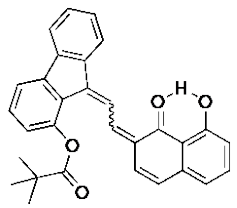

***ortho*-Model**

9-(2-(8-hydroxy-1-oxonaphthalen-2(1*H*)-ylidene)ethylidene)-9*H*-fluoren-1-yl pivalate (*ortho*-Model). Synthesized using General Procedure B with diisopropylamine (0.29 mL, 2.07 mmol) and n-butyllithium (2.5 M in hexanes, 0.82 mL, 2.05 mmol) in THF (9 mL). An aliquot of the LDA solution (1.50 mL, 0.308 mmol) was added to a solution of compound **7a** (100 mg, 0.204 mmol) in THF (5 ml) and the reaction was stirred at −78 °C for 1 h. Additional LDA (0.5 mL, 0.103 mmol) was added and the reaction was stirred at −78 °C for 2 h, and then the reaction was quenched. Purification by column chromatography on silica gel (0–25% EtOAc/hexanes) afforded the title compound as a dark purple solid (52 mg, 57%). The product is a mixture of merocyanine stereoisomers that readily interconvert.

^{1}H NMR (400 MHz, CD_2Cl_2) δ: 13.37 (s, 0.1H), 13.27 (s, 0.8H), 8.91 (d, J = 12.3 Hz, 0.1H), 8.80 (d, J = 13.0 Hz, 0.9H), 8.11 – 8.07 (m, 0.9H), 8.02 (d, J = 13.2 Hz, 1H), 7.96 (d, J = 7.8 Hz, 0.1H), 7.77 – 6.73 (m, 11H) 1.52 (s, 8.1H), 1.50 (s, 0.9H).

^{13}C NMR (101 MHz, CD_2Cl_2) δ: 189.9, 177.2, 164.8, 149.6, 145.9, 143.3, 141.8, 138.8, 137.3, 137.2, 136.8, 133.6, 131.1, 130.5, 129.9, 128.8, 127.7, 127.4, 124.5, 122.9, 122.8, 121.0, 120.1, 117.91, 117.87, 116.1, 40.0, 30.3, 27.7, 27.6.

TLC (25% EtOAc/hexanes): R_f = 0.74

HRMS (ESI *m*/*z*): calcd for $[C_{30}H_{25}O_4]^+$ $(M+H)^+$, 449.1747; found 449.1747.

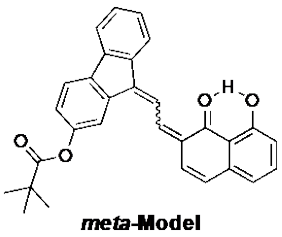

***meta*-Model**

9-(2-(8-hydroxy-1-oxonaphthalen-2(1*H*)-ylidene)ethylidene)-9*H*-fluoren-2-yl pivalate (*meta*-Model). Synthesized using General Procedure B with diisopropylamine (0.16 mL, 1.14 mmol) and n-butyllithium (2.5 M in hexanes, 0.46 mL, 1.15 mmol) in THF (9.4 mL). An aliquot of the LDA solution (1.00 mL, 0.114 mmol) was added to a solution of compound **7b** (56 mg, 0.114 mmol) in THF (3 ml) and the reaction was stirred at −78 °C for 3 h. Additional LDA (1.0 mL, 0.114 mmol) was added and the reaction was stirred at −78 °C for 1 h, and then the reaction was quenched. Purification by column chromatography on silica gel (0–25% EtOAc/hexanes) afforded the title compound as a dark purple solid (27 mg, 53%). The product is a mixture of merocyanine stereoisomers that readily interconvert.

^{1}H NMR (400 MHz, CD_2Cl_2) δ: 13.45 (s, 0.03H, -O*H*), 13.44 (s, 0.04H, -O*H*), 13.25 (s, 0.3H, -O*H*), 13.23 (s, 0.6H, -O*H*), 8.92 (d, *J* = 13.0 Hz, 0.03H), 8.80 (d, *J* = 12.8 Hz, 0.05H), 8.66 (d, *J* = 13.4 Hz, 0.6H), 8.55 (d, *J* = 13.5 Hz, 0.3H), 8.04 (d, *J* = 7.9 Hz, 0.6H), 7.98 – 6.62 (m, 12.4H), 1.44 (s, 2.7H), 1.42 (s, 0.9H), 1.41 (s, 5.4H).

^{13}C NMR (101 MHz, CD_2Cl_2) δ: 189.8, 189.7, 177.9, 177.7, 164.80, 164.77, 151.5, 151.4, 145.6, 145.5, 142.0, 140.8, 140.2, 140.0, 139.6, 138.8, 138.7, 138.3, 138.0, 137.21, 137.16, 135.3, 135.0, 133.8, 133.7, 130.8, 130.7, 128.2, 127.9, 127.6, 127.5, 127.4, 123.81, 123.75, 122.7, 122.6, 122.0, 121.2, 121.1, 120.84, 120.78, 120.5, 120.12, 120.10, 117.8, 116.0, 115.6, 39.7, 39.6, 30.3, 27.5.

TLC (25% EtOAc/hexanes): R_f = 0.84

HRMS (ESI *m*/*z*): calcd for $[C_{30}H_{25}O_4]^+$ $(M+H)^+$, 449.1747; found 449.1750.

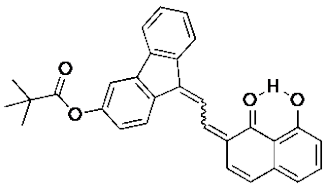

para-Model

9-(2-(8-hydroxy-1-oxonaphthalen-2(1*H*)-ylidene)ethylidene)-9*H*-fluoren-3-yl pivalate (*para*-Model). Synthesized using General Procedure B with diisopropylamine (0.26 mL, 1.86 mmol) and n-butyllithium (2.5 M in hexanes, 0.73 mL, 1.83 mmol) in THF (9 mL). An aliquot of the LDA solution (1.20 mL, 0.220 mmol) was added to a solution of compound **7c** (90 mg, 0.183 mmol) in THF (5 ml) and the reaction was stirred at −78 °C for 1 h. Additional LDA (0.60 mL, 0.110 mmol) was added and the reaction was stirred at −78 °C for 1 h, and then the reaction was quenched. Purification by column chromatography on silica gel (0–25% EtOAc/hexanes) afforded the title compound as a dark purple solid (59 mg, 71%). The product is a mixture of merocyanine stereoisomers that readily interconvert.

^{1}H NMR (400 MHz, CD_2Cl_2) δ: 13.47 (s, 0.3H, -O*H*), 13.25 (s, 0.7H, -O*H*), 8.82 (dd, *J* = 13.0, 11.4 Hz, 0.3H), 8.61 (d, *J* = 13.7 Hz, 0.4H), 8.56 (d, *J* = 13.7 Hz, 0.3H), 8.08 – 6.64 (m, 13H), 1.41 (s, 4.4H), 1.40 (s, 4.6H).

^{13}C NMR (101 MHz, CD_2Cl_2) δ: 191.6, 191.5, 189.7, 177.5, 177.4, 165.0, 164.8, 153.69, 153.66, 153.42, 153.37, 146.8, 146.7, 145.51, 145.47, 144.21, 144.17, 142.5, 142.4, 142.2, 142.0, 141.62, 141.58, 140.6, 140.0, 139.8, 138.8, 138.6, 137.4, 137.2, 137.1, 137.0, 136.7, 135.5, 135.4, 134.2, 134.1, 133.43, 133.38, 132.6, 132.5, 131.4, 130.7, 130.59, 130.56, 130.52, 128.7, 128.5, 128.40, 128.35, 128.1, 127.6, 127.4, 127.3, 127.2, 127.0, 126.47, 126.45, 125.1, 124.8, 123.5, 122.8, 122.7, 122.6, 122.0, 121.2, 121.11, 121.05, 120.9, 120.8, 120.7, 120.0, 119.9, 119.6, 119.4, 117.6, 117.4, 116.7, 116.0, 114.5, 114.1, 39.7, 39.6, 27.5.

TLC (25% EtOAc/hexanes): R_f = 0.81

HRMS (ESI *m*/*z*): calcd for $[C_{30}H_{25}O_4]^+$ $(M+H)^+$, 449.1747; found 449.1751.

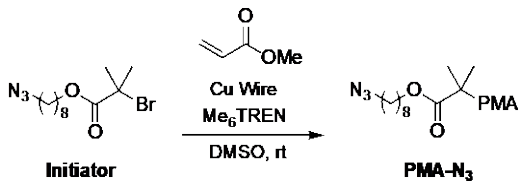

PMA-N_3. Synthesized by controlled radical polymerization following the procedure by Nguyen *et. al.*[54] A flame-dried 50 mL Schlenk flask equipped with a stir bar was charged with freshly cut 20 G copper wire (2 cm), **Initiator** (21.2 mg, 0.066 mmol), DMSO (9.5 mL), and methyl acrylate (9.50 mL, 106 mmol). The flask was sealed and the solution was degassed via three freeze-pump-thaw cycles, then backfilled with N_2 and warmed to room temperature. Tris[2-(dimethylamino)ethyl]amine (Me_6TREN) (21 mL, 0.078 mmol) was added via microsyringe and the reaction was stirred at room temperature for 1 h. Upon completion of polymerization, the flask was opened to atmosphere and diluted with a minimal amount of CH_2Cl_2. The polymer was precipitated (3×) into methanol cooled with dry ice and then dried under vacuum to provide the title polymer as a tacky colorless solid (5.1 g, 56%). M_n = 89.3 kg/mol, M_p = 98.0 kDa, $Đ$ = 1.08.

PMA-N_3-79. Synthesized by controlled radical polymerization following the procedure by Nguyen *et. al.*[54] A flame-dried 50 mL Schlenk flask equipped with a stir bar was charged with freshly cut 20 G copper wire (2 cm), **Initiator** (31.0 mg, 0.097 mmol), DMSO (10 mL), and methyl acrylate (10.0 mL, 111 mmol). The flask was sealed and the solution was degassed via three freeze-pump-thaw cycles, then backfilled with N_2 and warmed to room temperature. Tris[2-(dimethylamino)ethyl]amine (Me_6TREN) (31 mL, 0.116 mmol) was added via microsyringe and the reaction was stirred at room temperature for 1 h. Upon

completion of polymerization, the flask was opened to atmosphere and diluted with a minimal amount of CH_2Cl_2. The polymer was precipitated (3×) into methanol cooled with dry ice and then dried under vacuum to provide the title polymer as a tacky colorless solid (6.3 g, 66%). M_n = 75.4 kg/mol, M_p = 79.1 kDa, $Đ$ = 1.11.

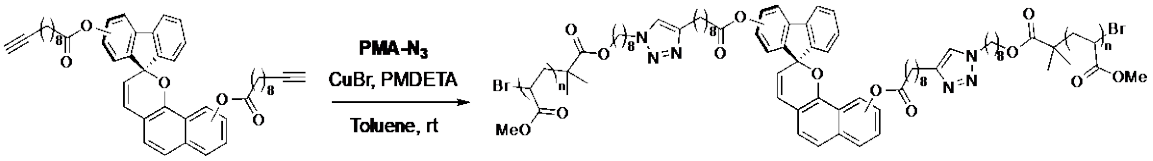

General Procedure C for the Synthesis of Polymers Incorporating a Chain-Centered Fluorenyl Naphthopyran. Polymers were synthesized by a Cu(I)-catalyzed azide-alkyne cycloaddition (CuAAC) reaction based on a procedure adapted from the literature.[18] A flame dried Schlenk flask equipped with a stir bar was charged with **PMA-N$_3$** and pentamethyldiethylenetriamine (PMDETA). The flask was evacuated and backfilled with N_2 (3×) and brought into a glovebox. A solution of the bis-alkyne functionalized fluorenyl naphthopyran in anhydrous toluene was added to the flask, followed by copper(I) bromide. Additional toluene was introduced to achieve a final polymer concentration of approximately 50 mg/mL. The flask was sealed and the solution was stirred at room temperature in the glovebox for 24 h. After removal from the glovebox, the solution was filtered through a plug of basic alumina, the filtrate was concentrated under reduced pressure, and the residue was dissolved in a minimal amount of CH_2Cl_2. The polymer was precipitated (3×) into methanol cooled with dry ice and then dried under vacuum.

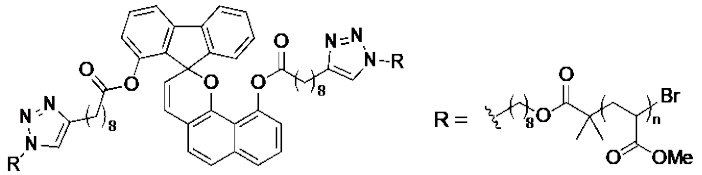

***ortho*-FNP.** Synthesized using General Procedure C with **PMA-N$_3$** (809 mg, 0.00906 mmol), PMDETA (10 mL, 0.049 mmol), **5a** (3.0 mg, 0.0043 mmol), copper(I) bromide (4 mg, 0.028 mmol), and toluene (16 mL). The title polymer was isolated as a tacky pale peach solid (670 mg, 83%). M_n = 159 kg/mol, M_p = 189 kDa, $Đ$ = 1.13.

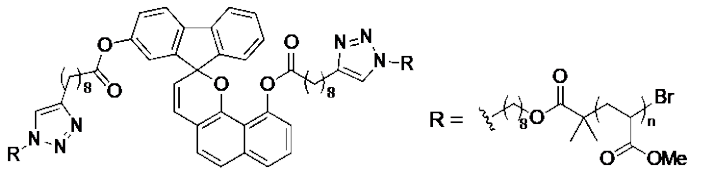

***meta*-FNP.** Synthesized using General Procedure C with **PMA-N$_3$** (809 mg, 0.00906 mmol), PMDETA (10 mL, 0.049 mmol), **5b** (3.0 mg, 0.0043 mmol), copper(I) bromide (4 mg, 0.028 mmol), and toluene (16 mL). The title polymer was isolated as a tacky pale peach solid (659 mg, 81%). M_n = 164 kg/mol, M_p = 191 kDa, $Đ$ = 1.16.

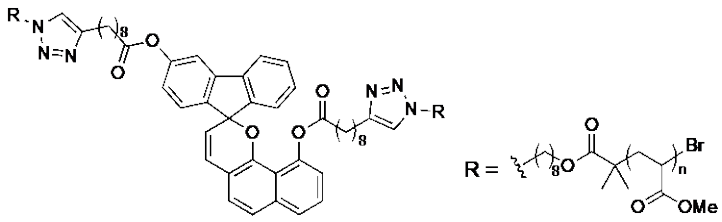

***para*-FNP.** Synthesized using General Procedure C with **PMA-N$_3$** (809 mg, 0.00906 mmol), PMDETA (10 mL, 0.049 mmol), **5c** (3.0 mg, 0.0043 mmol), copper(I) bromide (4 mg, 0.028 mmol), and toluene (16 mL). The title polymer was isolated as a tacky pale peach solid (655 mg, 81%). M_n = 167 kg/mol, M_p = 192 kDa, $Đ$ = 1.17.

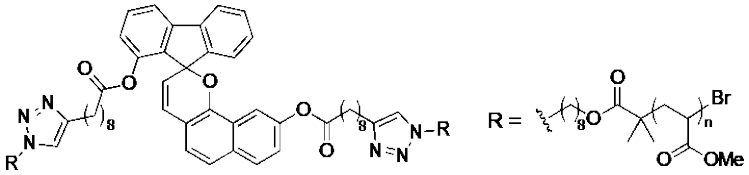

9-*ortho*-FNP. Synthesized using General Procedure C with **PMA-N$_3$** (809 mg, 0.00906 mmol), PMDETA (10 mL, 0.049 mmol), **6a** (3.0 mg, 0.0043 mmol), copper(I) bromide (4 mg, 0.028 mmol), and toluene (16 mL). The title polymer was isolated as a tacky pale peach solid (665 mg, 82%). M_n = 162 kg/mol, M_p = 192 kDa, $Đ$ = 1.17.

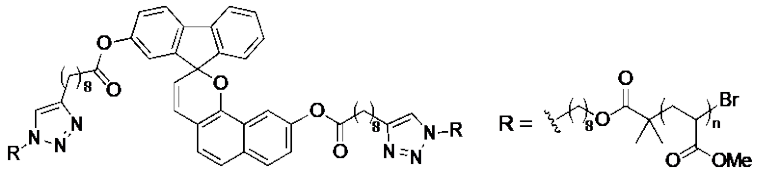

9-*meta*-FNP. Synthesized using General Procedure C with **PMA-N$_3$** (764 mg, 0.00856 mmol), PMDETA (10 mL, 0.049 mmol), **6b** (2.8 mg, 0.0040 mmol), copper(I) bromide (4 mg, 0.028 mmol), and toluene (16 mL). The title polymer was isolated as a tacky pale peach solid (625 mg, 82%). M_n = 164 kg/mol, M_p = 191 kDa, $Đ$ = 1.15.

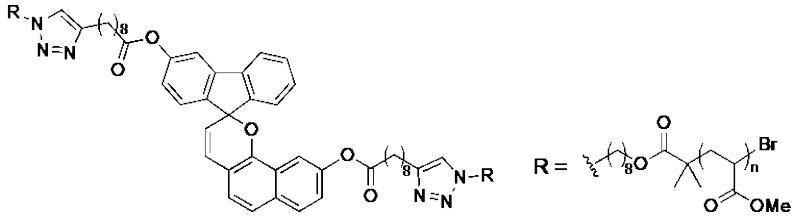

9-*para*-FNP. Synthesized using General Procedure C with **PMA-N$_3$** (809 mg, 0.00906 mmol), PMDETA (10 mL, 0.049 mmol), **6a** (3.0 mg, 0.0043 mmol), copper(I) bromide (4 mg, 0.028 mmol), and toluene (16 mL). The title polymer was isolated as a tacky pale peach solid (664 mg, 82%). M_n = 168 kg/mol, M_p = 194 kDa, $Đ$ = 1.15.

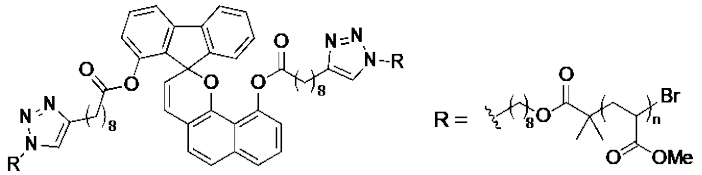

***ortho*-FNP-150.** Synthesized using General Procedure C with **PMA-N$_3$-79** (643 mg, mmol), PMDETA (10 mL, 0.049 mmol), **5a** (3.0 mg, 0.0043 mmol), copper(I) bromide (4.0 mg, 0.026 mmol), and toluene (13 mL). The title polymer was isolated as a tacky pale peach solid (466 mg, 72%). M_n = 125 kg/mol, M_p = 151 kDa, $Đ$ = 1.16.

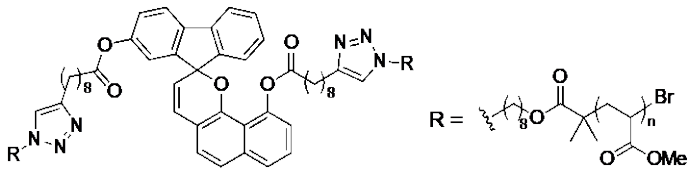

***meta*-FNP-150.** Synthesized using General Procedure C with **PMA-N$_3$-79** (815 mg, mmol), PMDETA (11 mL, 0.053 mmol), **5b** (3.8 mg, 0.0055 mmol), copper(I) bromide (5.0 mg, 0.035 mmol), and toluene (16 mL). The title polymer was isolated as a tacky pale peach solid (700 mg, 85%). M_n = 129 kg/mol, M_p = 155 kDa, $Đ$ = 1.20.

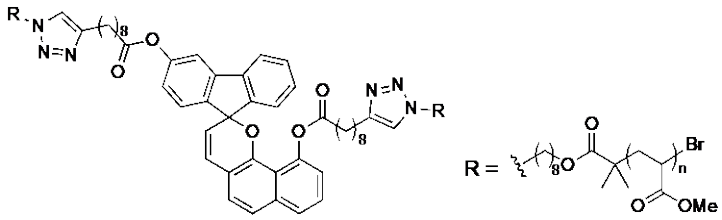

***para*-FNP-150.** Synthesized using General Procedure C with **PMA-N$_3$-79** (643 mg, mmol), PMDETA (10 mL, 0.049 mmol), **5c** (3.0 mg, 0.0043 mmol), copper(I) bromide (4.0 mg, 0.026 mmol), and toluene (13 mL). The title polymer was isolated as a tacky pale peach solid (510 mg, 79%). M_n = 138 kg/mol, M_p = 155 kDa, $Đ$ = 1.23.

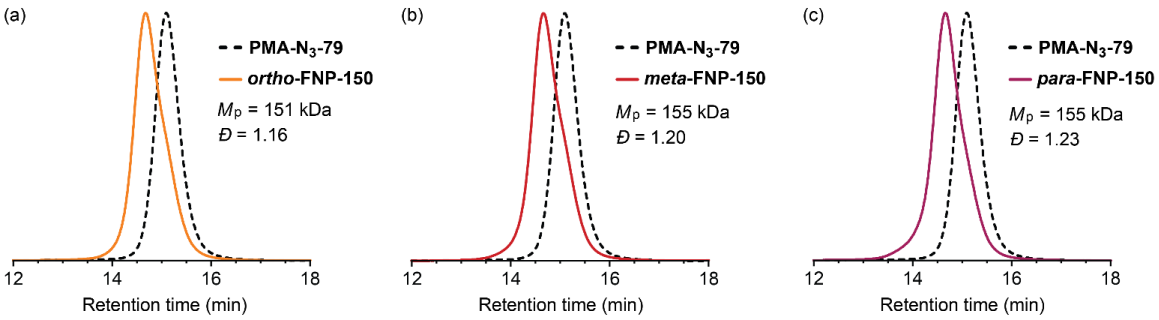

Figure S3.41. Characterization by GPC (refractive index response shown) confirms successful coupling reactions to generate mechanophore chain-centered polymers (a) ***ortho*-FNP-150**, (b) ***meta*-FNP-150**, and (c) ***para*-FNP-150** with $M_p \approx 150$ kDa incorporating FNP mechanophores with polymer attachment at the 10-position of the naphthopyran.

V. Characterization of PMA Polymers by NMR Spectroscopy

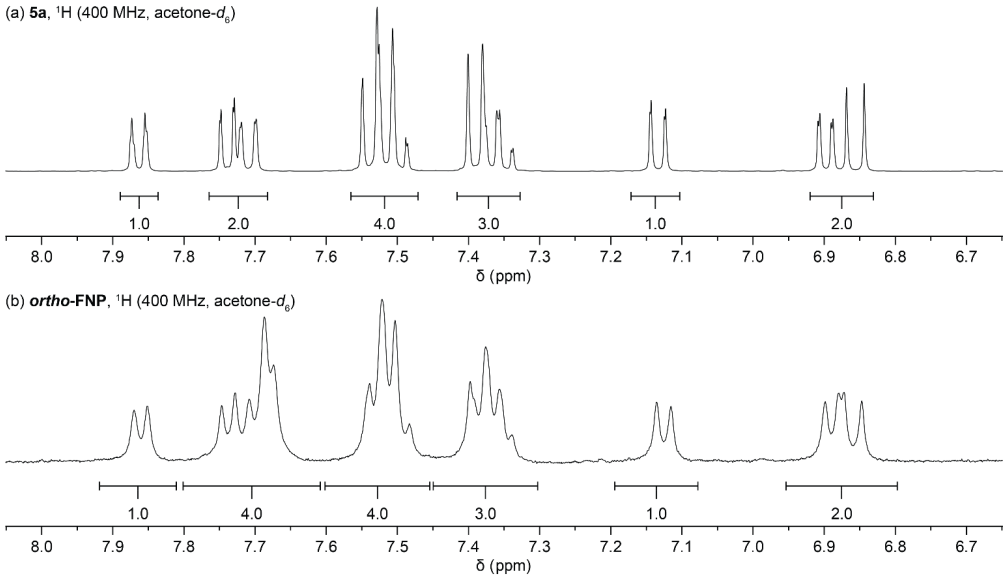

Figure S3.42. Partial ^{1}H spectra (400 MHz, acetone-d_6) of (a) small molecule bis-alkyne **5a**, and (b) polymer ***ortho*-FNP** demonstrating successful click coupling. The appearance of new resonances corresponding to two new protons in the region 7.6 – 7.7 ppm is attributed to the formation of two equivalents of triazole in the CuAAC reaction.

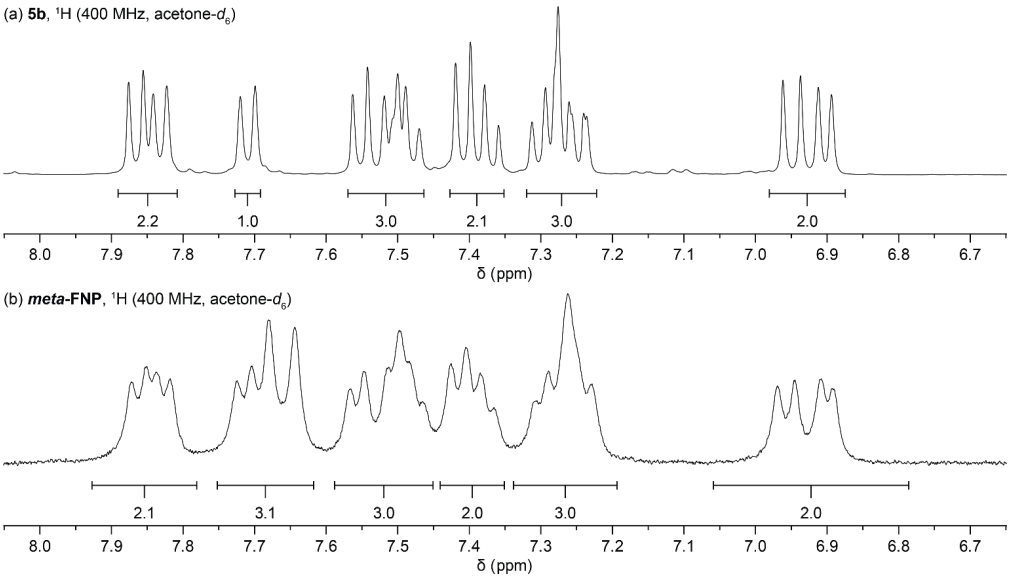

Figure S3.43. Partial ^{1}H spectra (400 MHz, acetone-d_6) of (a) small molecule bis-alkyne **5b**, and (b) polymer ***meta*-FNP** demonstrating successful click coupling. The appearance of new resonances corresponding to two new protons at 7.64 and 7.68 ppm is attributed to the formation of two equivalents of triazole in the CuAAC reaction.

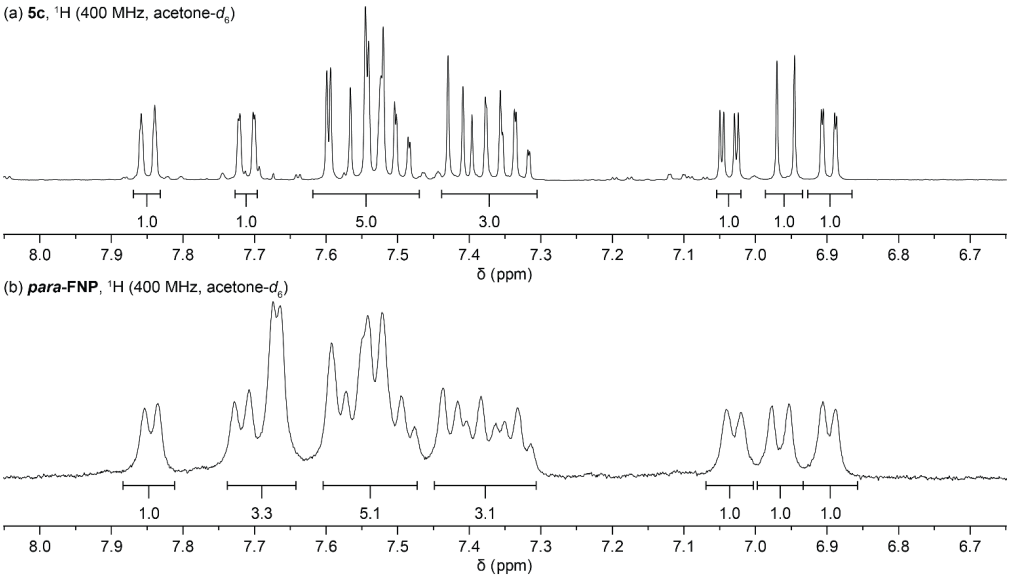

Figure S3.44. Partial ^{1}H spectra (400 MHz, acetone-d_6) of (a) small molecule bis-alkyne **5c**, and (b) polymer ***para*-FNP** demonstrating successful click coupling. The appearance of new resonances corresponding to two new protons at 7.66 and 7.67 ppm is attributed to the formation of two equivalents of triazole in the CuAAC reaction.

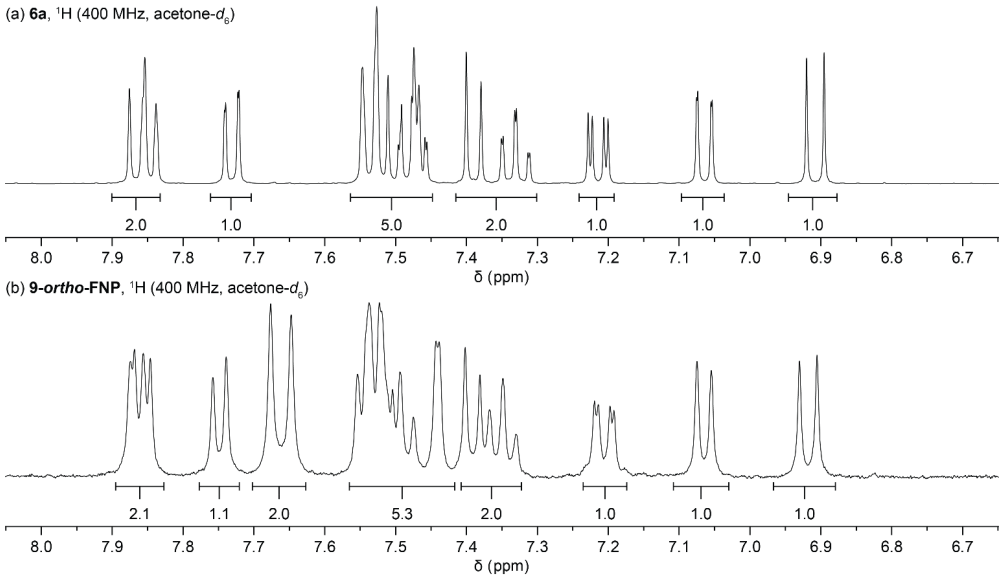

Figure S3.45. Partial ^{1}H spectra (400 MHz, acetone-d_6) of (a) small molecule bis-alkyne **6a**, and (b) polymer **9-*ortho*-FNP** demonstrating successful click coupling. The appearance of new resonances corresponding to two new protons at 7.65 and 7.68 ppm is attributed to the formation of two equivalents of triazole in the CuAAC reaction.

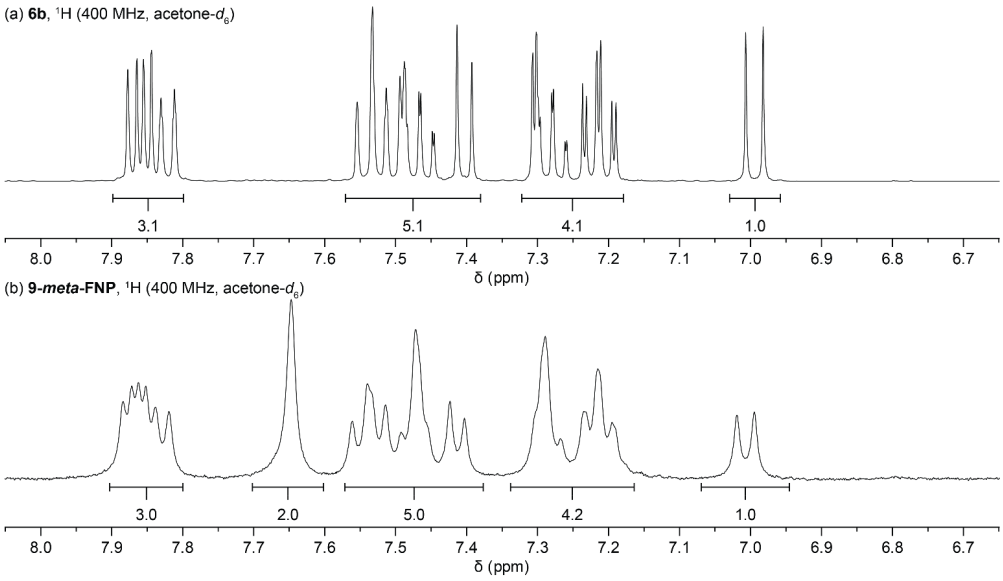

Figure S3.46. Partial ^{1}H spectra (400 MHz, acetone-d_6) of (a) small molecule bis-alkyne **6b**, and (b) polymer **9-*meta*-FNP** demonstrating successful click coupling. The appearance of new resonances corresponding to two new protons at 7.65 ppm is attributed to the formation of two equivalents of triazole in the CuAAC reaction.

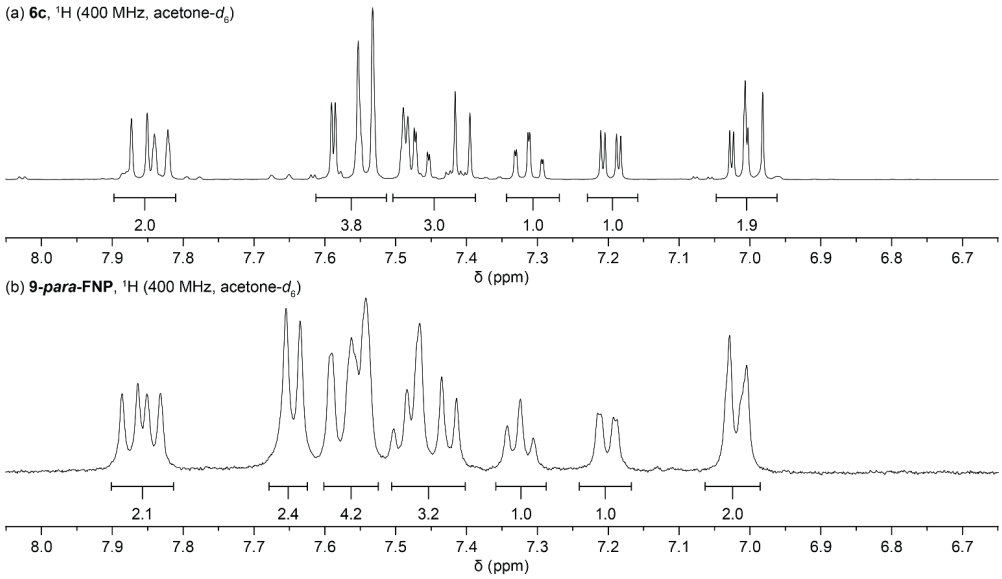

Figure S3.47. Partial ^{1}H spectra (400 MHz, acetone-d_6) of (a) small molecule bis-alkyne **6c**, and (b) polymer **9-*para*-FNP** demonstrating successful click coupling. The appearance of new resonances corresponding to two new protons at 7.63 and 7.65 ppm is attributed to the formation of two equivalents of triazole in the CuAAC reaction.

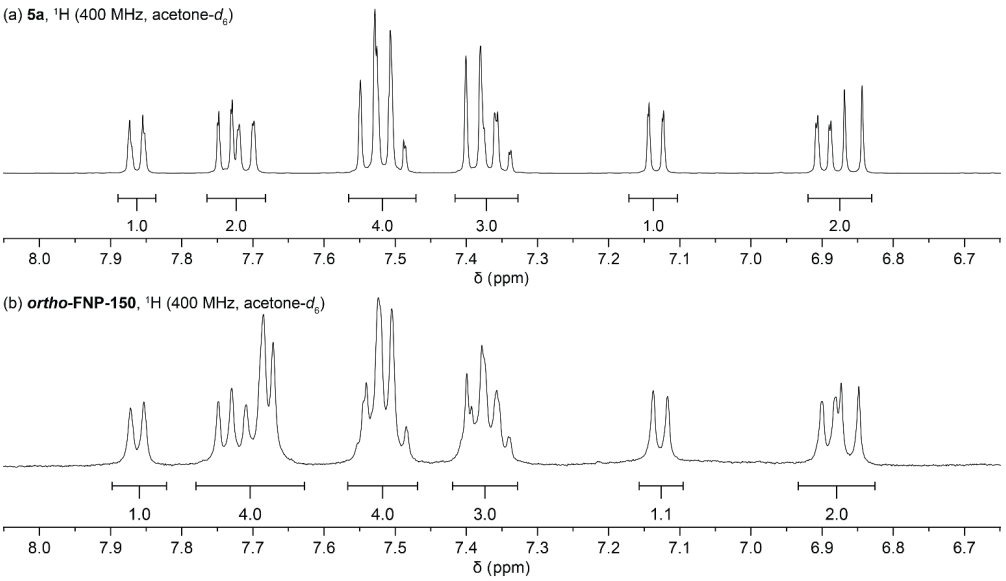

Figure S3.48. Partial ^{1}H spectra (400 MHz, acetone-d_6) of (a) small molecule bis-alkyne **5a**, and (b) polymer ***ortho*-FNP-150** demonstrating successful click coupling. The appearance of new resonances corresponding to two new protons from 7.65 to 7.71 ppm is attributed to the formation of two equivalents of triazole in the CuAAC reaction.

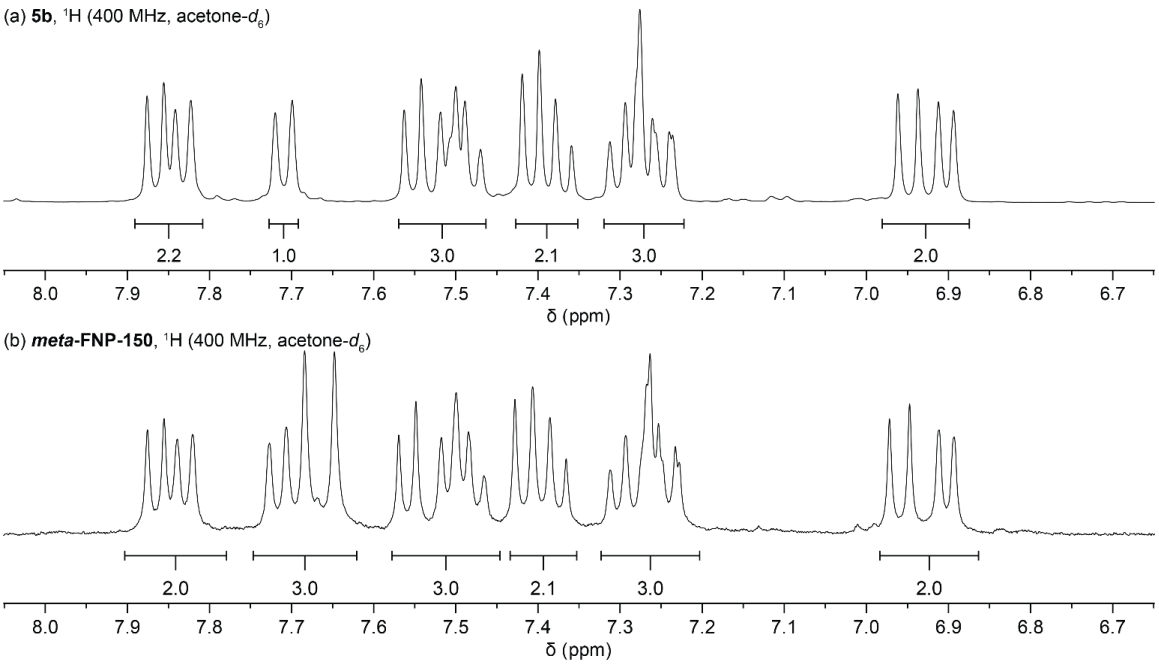

Figure S3.49. Partial ^{1}H spectra (400 MHz, acetone-d_6) of (a) small molecule bis-alkyne **5b**, and (b) polymer ***meta*-FNP-150** demonstrating successful click coupling. The appearance of new resonances corresponding to two new protons at 7.65 and 7.68 ppm is attributed to the formation of two equivalents of triazole in the CuAAC reaction.

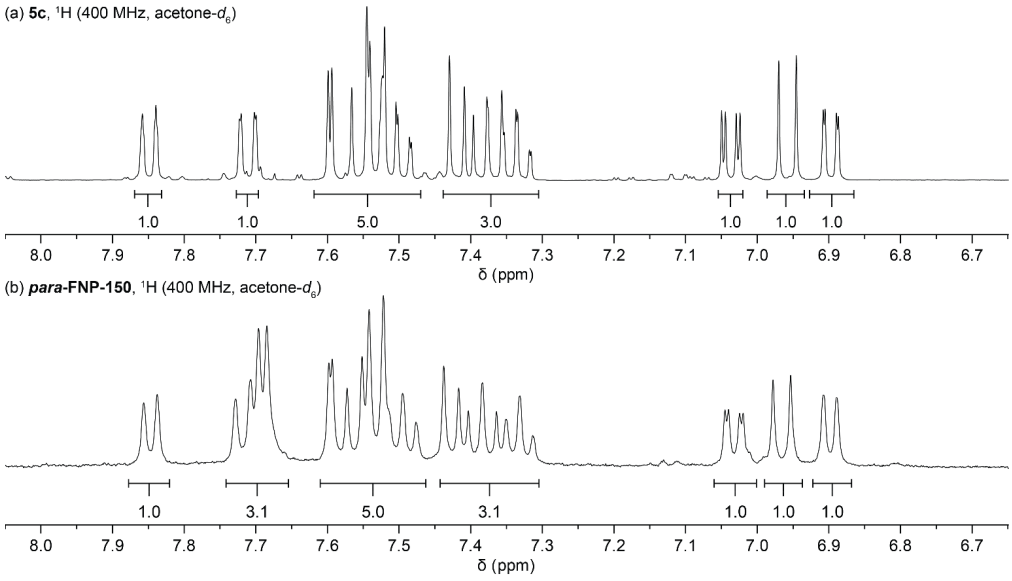

Figure S3.50. Partial ^{1}H spectra (400 MHz, acetone-d_6) of (a) small molecule bis-alkyne **5c**, and (b) polymer ***para*-FNP-150** demonstrating successful click coupling. The appearance of new resonances corresponding to two new protons at 7.68 and 7.70 ppm is attributed to the formation of two equivalents of triazole in the CuAAC reaction.

VI. Details for Sonication and Photoirradiation Experiments

General Procedure for Sonication Experiments. A dry reaction vessel was fitted with rubber septa, placed onto the sonication probe, and allowed to cool under a stream of dry argon. The vessel was charged with a solution of the polymer in THF (2 mg/mL, 20 mL) containing 30 mM BHT to avoid decomposition side reactions resulting from free radicals generated during sonication.[55,56] The sonication vessel was submerged in a well-packed dry ice/acetone bath and the solution was sparged with argon for 30 min. After sparging, the gas inlet line was removed from solution and placed in the headspace of the reaction vessel to maintain an inert atmosphere for the duration of sonication. Pulsed sonication (1 s on / 3 s off) at 20 kHz (6.5 ± 0.1 W/cm^2) was then initiated. The temperature inside the reaction vessel equilibrated to −70 ± 5 °C, as measured by a thermocouple inserted into the solution (Digi-Sense EW-91428-02 thermometer with Digi-Sense probe EW-08466-83). Sonication intensity was calibrated via the literature method.[57] The entire system was kept in the dark for the duration of the experiment. Aliquots (0.4 mL) were removed at 0, 0.5, 1, 2.5, 5, 7.5, 10, 15, 25, 40, 60, and 90 min (sonication "on" time). The aliquots were quickly passed through a 0.45 μm PTFE syringe filter directly into a quartz cuvette inside the UV-vis spectrophotometer, and the collection of absorption spectra (800–300 nm) was immediately initiated. The absorbance values measured at 700 nm were subtracted at each time point to account for drift during the experiments. The instrument was baseline corrected using a 30 mM solution of BHT in THF.

General Procedure for Photoirradiation Experiments. A dry reaction vessel was fitted with rubber septa, placed onto the sonication probe, and allowed to cool under a stream of dry argon. The vessel was charged with a solution of the polymer in THF (2 mg/mL, 10 mL)

containing 30 mM BHT. The sonication vessel was submerged in a well-packed dry ice/acetone bath at −78 °C and the solution was sparged with argon for 30 min. The solution was then irradiated with 365 nm UV light for 2 min, and then the gas inlet line was removed from solution and placed in the headspace of the reaction vessel to maintain an inert atmosphere for the duration of irradiation experiment. Aliquots (0.4 mL) of the solution were removed after 20 min and 90 min, and quickly passed through a 0.45 μm PTFE syringe filter directly into a quartz cuvette positioned inside the UV-vis spectrophotometer, and an absorption spectrum (800–300 nm) was immediately acquired. For one of the aliquots, a second absorption spectrum was collected after 90 min at 20 °C to monitor the extent of merocyanine reversion at room temperature.

Mechanochemical activation of 2*H*-naphthopyran compounds with polymer attachment *via* an ester linkage at the 10-position undergo mechanically-mediated scission of the C(O)–O ester bond to generate thermally persistent merocyanines.[40,53] These merocyanine species with an intramolecular hydrogen-bond typically have absorption maxima that are bathochromically shifted from that of the photochemically generated merocyanine species, which maintain intact ester groups. Consistent with these observations, UV photoirradiation of ***ortho*-FNP**, ***meta*-FNP**, and ***para*-FNP** generates thermally transient products with absorption maxima that are hypsochromically shifted by approximately 20–30 nm compared to the products generated under ultrasonication conditions (see Figure S3.19). The color that remains after 90 min at 20 °C can be attributed to merocyanine isomers with *trans* configuration of the exocyclic alkene that are generated photochemically.[58]

Mechanical activation of 2*H*-naphthopyrans with polymer attachment *via* an ester linkage at the 9-position does not result in the formation of thermally persistent merocyanine

isomers, and the absorption spectra of merocyanine isomers generated under force are typically consistent with those generated under UV light irradiation.[40,53] Photoirradiation of **9-*ortho*-FNP**, **9-*meta*-FNP**, and **9-*para*-FNP** generates thermally transient merocyanine products with absorption spectra that closely match the spectra of the products generated by ultrasonication (Figure S3.51). The color that remains after 90 min at 20 °C can be attributed to merocyanine isomers with *trans* configuration of the exocyclic alkene that are generated photochemically.[58]

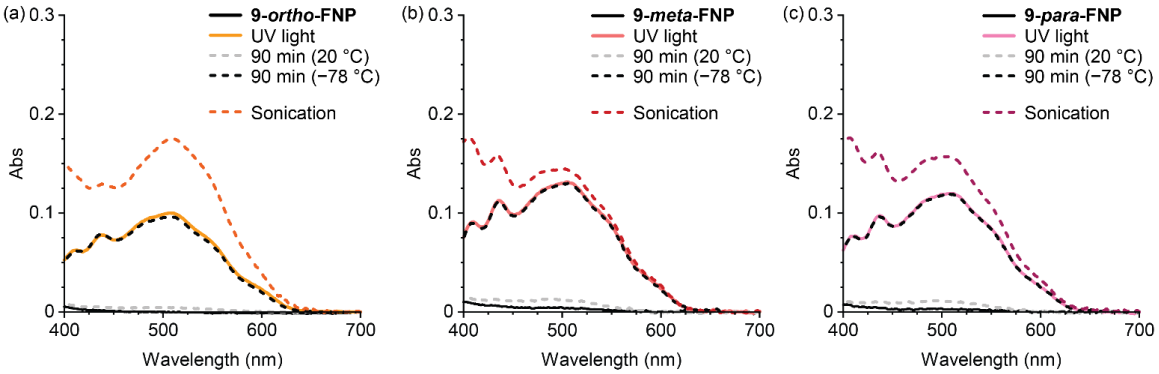

Figure S3.51. Absorption spectra of (a) **9-*ortho*-FNP**, (b) **9-*meta*-FNP**, and (c) **9-*para*-FNP** (2 mg/mL in THF with 30 mM BHT) following irradiation with UV light (365 nm, 2 min) at −78 °C (solid colored lines). Reversion at 20 °C is significant (dashed grey lines), while reversion at −78 °C is negligible (dashed black lines). The products from photochemical activation exhibit absorption spectra with absorption maxima that match those of the mechanochemically-generated products (dashed colored lines).

VII. Determination of Reaction Rate Constants

Determination of k_{obs} from time-dependent UV-vis absorption measurements. The kinetics of mechanochemical product formation were determined from time-dependent absorption profiles during sonication at the observed λ_{max} of each FNP mechanophore.[59]

Time-dependent absorption profiles were fit to the integrated rate law for product formation using simple first-order kinetics, given by eq. S3.1:

$$Abs_t = A \cdot (1 - e^{-k_{obs} \cdot t}) + Abs_0 \qquad \text{(S3.1)}$$

where Abs_t and Abs_0 are the absorbance at λ_{max} at time t and $t = 0$, respectively; the pre-exponential factor A corresponds to the maximum absorbance attained upon extended sonication; and k_{obs} is the observed rate constant of product accumulation determined from fitting the spectroscopic data to the integrated rate law. Abs_0, A, and k_{obs} are fit-determined quantities. Note that a small amount of merocyanine dye (with naphthyl ester intact) exists in the sample initially due to thermal equilibration.[40] Including the term Abs_0 accounts for this initial signal and improves fitting characteristics. Data and values of k_{obs} are summarized in Figures S3.52–S3.54.

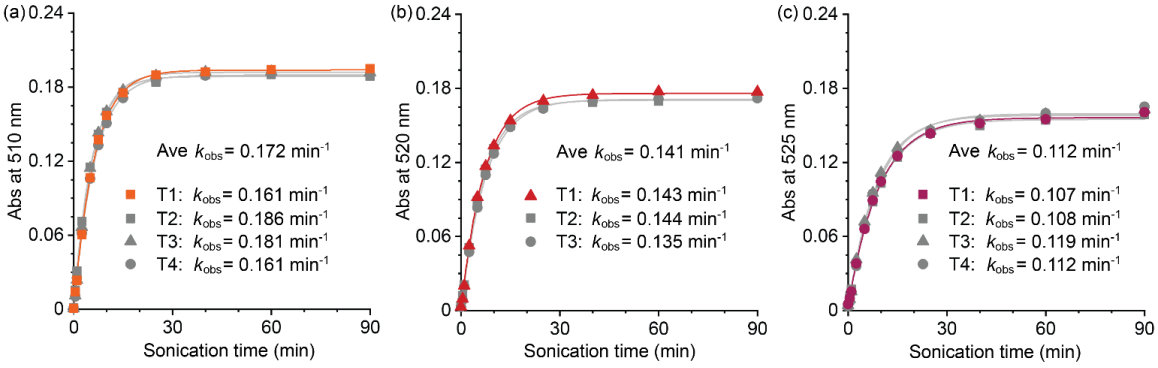

Figure S3.52. Absorbance monitored at λ_{max} as a function of sonication time for (a) ***ortho*-FNP** (510 nm), (b) ***meta*-FNP** (520 nm), and (c) ***para*-FNP** (525 nm). Data points are averages from 3–4 replicate trials (T1–T4). Rate constants (k_{obs}) for merocyanine accumulation are determined by fitting the data to eq. S3.1.

Consistent with computational predictions of reactivity (Figures S3.9–S3.11), the average observed rate constant (k_{obs}) of merocyanine formation for **9-*meta*-FNP** is intermediate between that of **9-*ortho*-FNP** and **9-*para*-FNP** (Figure S3.23); however the reaction rate for **9-*meta*-FNP** (0.168 min^{-1}) is more similar to the reaction rate of **9-*ortho*-**

FNP (0.177 min^{-1}) than might be expected from their relative predicted F_{max} values (4.1 and 3.7 nN, respectively). Notably, for all five sonication trials performed on **9-*meta*-FNP**, the 90 min timepoint displays slightly lower absorbance at λ_{max} than the 60 min timepoint (Figure S3.53). Furthermore, although exact merocyanine concentrations are unable to be determined due to uncertainty in the merocyanine extinction coefficients, we also note that sonications of **9-*meta*-FNP** generate solutions with lower final absorbance at λ_{max} compared to sonications of **9-*para*-FNP**. These observations may suggest that the merocyanine species derived from **9-*meta*-FNP** exhibits a small amount of degradation under the sonication conditions, which would artificially inflate the measured rate constant for that mechanophore. Notably, previous reports have suggested that the relative rates of photo-induced degradation of merocyanines derived from fluorenyl naphthopyrans are sensitive to substitution pattern.[60]

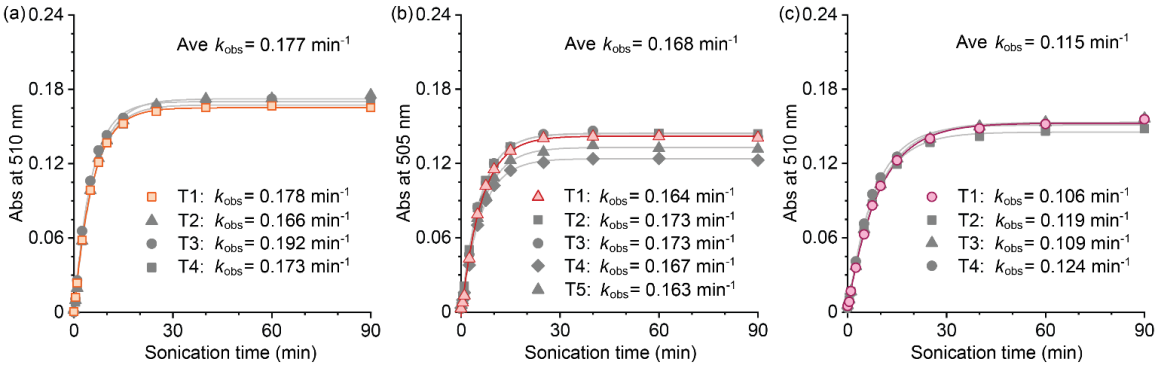

Figure S3.53. Absorbance monitored at λ_{max} as a function of sonication time for (a) **9-*ortho*-FNP** (510 nm), (b) **9-*meta*-FNP** (505 nm), and (c) **9-*para*-FNP** (510 nm). Data points are averages from 4–5 replicate trials (T1–T5). Rate constants (k_{obs}) for merocyanine accumulation are determined by fitting the data to eq. S3.1.

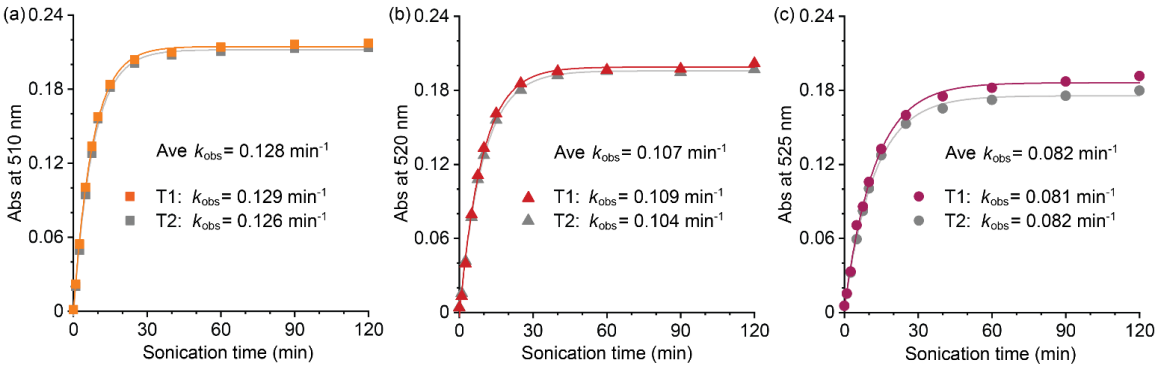

Figure S3.54. Absorbance monitored at λ_{max} as a function of sonication time for (a) ***ortho*-FNP-150** (510 nm), (b) ***meta*-FNP-150** (520 nm), and (c) ***para*-FNP-150** (525 nm). Data points are averages from duplicate trials. Rate constants (k_{obs}) for merocyanine accumulation are determined by fitting the data to eq. S3.1.

Determination of backbone scission rates from time-dependent GPC-RI measurements. The rate of polymer chain scission for **9-*ortho*-FNP**, **9-*meta*-FNP**, and **9-*para*-FNP** was determined according to the literature method by monitoring the attenuation of the refractive index (RI) signal from GPC measurements at the retention time corresponding to the starting material polymer exposed to varying duration of ultrasonication.[42,56] GPC-RI curves were normalized to peak area for each sonication timepoint. Attenuation of the normalized GPC-RI response at the retention time corresponding to the peak maximum for the initial polymer was plotted as a function of sonication time and fit to eq. S3.2:

$$RI_t = A \cdot (e^{-k_s \cdot t}) \qquad \text{(S3.2)}$$

where RIt is the normalized GPC-RI signal at time t, A corresponds to the experimental RI amplitude at $t = 0$, and k_s is the rate constant for polymer scission determined from fitting to the integrated rate law. A and k_s are fit-determined quantities. Data and values of k_s are summarized in Figure S3.55.

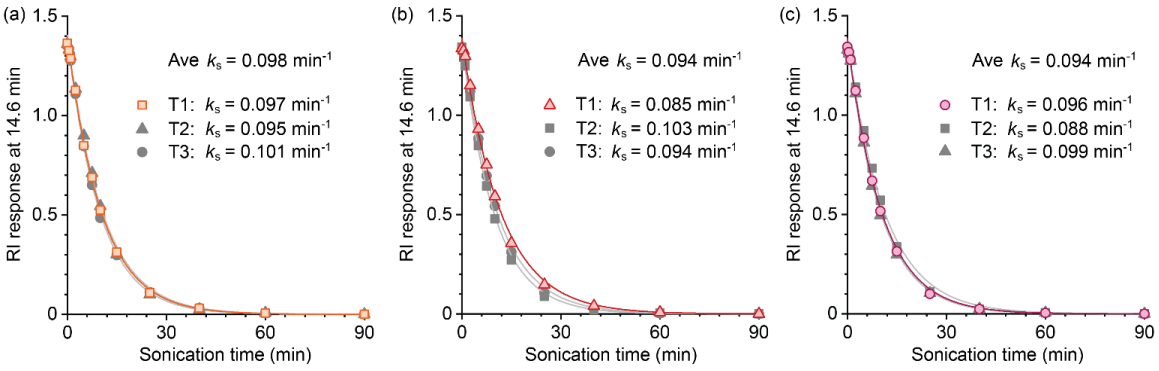

Figure S3.55. GPC refractive index response at retention time t_R = 14.6 min (corresponding to the peak maximum of the unsonicated polymer) as a function of ultrasonication time for (a) **9-*ortho*-FNP**, (b) **9-*meta*-FNP**, and (c) **9-*para*-FNP**. Data points are averages from 3 replicate trials (T1–T3). Rate constants (k_s) for polymer scission are determined by fitting the data to eq. S3.2.

VIII. DFT Calculations

CoGEF Calculations. CoGEF calculations were performed using Spartan ′24 Parallel Suite according to previously reported methods.[23,36] Ground state energies were calculated using DFT at the B3LYP/6-31G* level of theory. Truncated models of each mechanophore with terminal acetoxy groups were used in the calculations. For each structure, the equilibrium conformations of the unconstrained molecule were initially calculated using molecular mechanics (MMFF) followed by optimization of the equilibrium geometries using DFT (B3LYP/6-31G*). Starting from the equilibrium geometry of the unconstrained molecules (energy = 0 kJ/mol), the distance between the terminal methyl groups of the truncated structures was increased in increments of 0.05 Å and the energy was minimized at each step. The maximum force associated with the mechanochemical reaction was calculated from the slope of the curve immediately prior to bond cleavage using the final two contiguous data points. The optimized geometry coordinates are provided below for the equilibrium

geometries and the structures immediately prior to C–O bond cleavage for each FNP regioisomer model.

To understand potential solvent effects on the predicted values of F_{max} for naphthopyran ring opening and force-mediated geometric changes, we performed CoGEF calculations using the Conductor-Like Polarizable Continuum Model (CPCM). To simulate THF and DMF solvent environments a dielectric constant of 7.43 and 37.22 was used, respectively. Using a solvation model does not significantly impact the predicted values of F_{max} (Table 3.1) or the torsional analysis performed on structures immediately prior to bond rupture (Table 3.2–3.3). For CoGEF calculations performed on *para*-FNP using the THF or DMF solvation models, the naphthyl ester O–C(O) bond was predicted to break prior to pyran C–O bond cleavage. To obtain the values listed below, CoGEF calculations were performed using a truncated model of *para*-FNP with the ester O–C(O) bond constrained (Figures S3.56 and S3.57).

Table 3.1. Values of F_{max} in various simulated environments.

Molecule	Gas[a]	THF[b]	DMF[c]
Ortho-FNP	3.7 nN	3.5 nN	3.5 nN
Meta-FNP	4.3 nN	4.1 nN	4.0 nN
Para-FNP	4.9 nN	4.7 nN	4.6 nN

[a]Calculation performed on an isolated molecule. [b]Calculation performed using the conductor-like polarizable continuum model (CPCM) with a dielectric constant of 7.43. [c]Calculation performed using CPCM with a dielectric constant of 37.22.

Table 3.2. Values of sin(α) in various simulated environments.

Molecule	Gas[a]	THF[b]	DMF[c]
Ortho-FNP	0.51	0.50	0.50
Meta-FNP	0.32	0.33	0.30
Para-FNP	0.25	0.26	0.25

[a]Calculation performed on an isolated molecule. [b]Calculation performed using the conductor-like polarizable continuum model (CPCM) with a dielectric constant of 7.43. [c]Calculation performed using CPCM with a dielectric constant of 37.22.

Table 3.3. Angle γ in various simulated environments.

Molecule	Gas[a]	THF[b]	DMF[c]
Ortho-FNP	158°	156°	157°
Meta-FNP	132°	133°	133°
Para-FNP	113°	113°	116°

[a]Calculation performed on an isolated molecule. [b]Calculation performed using the conductor-like polarizable continuum model (CPCM) with a dielectric constant of 7.43. [c]Calculation performed using CPCM with a dielectric constant of 37.22.

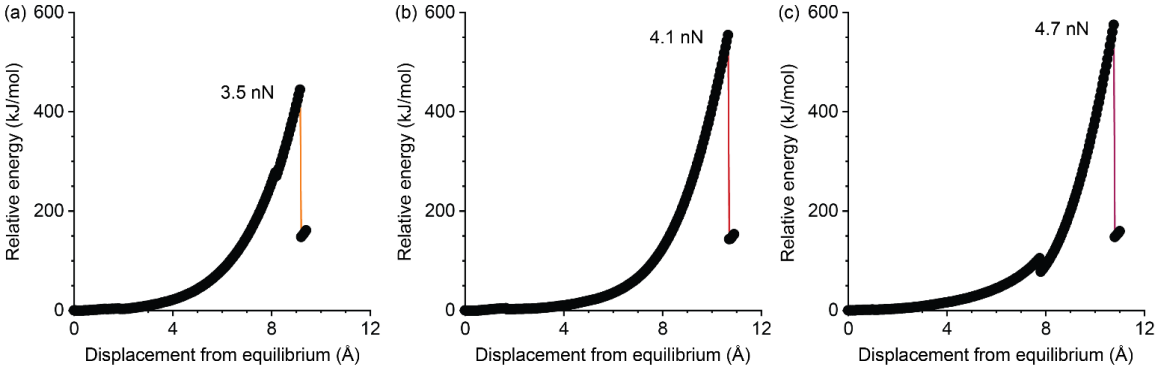

Figure S3.56. Density functional theory (DFT) calculations using the constrained geometries simulate external force (CoGEF) method and a Polarizable Continuum Model with a 7.43 dielectric constant performed on a truncated models of (a) *ortho*-FNP, (b) *meta*-FNP, and (c) *para*-FNP. The ring-opening reaction is predicted to occur at a maximum force of 3.5 nN, 4.1 nN, and 4.7 nN, respectively. Calculations were performed at the B3LYP/6-31G* level.

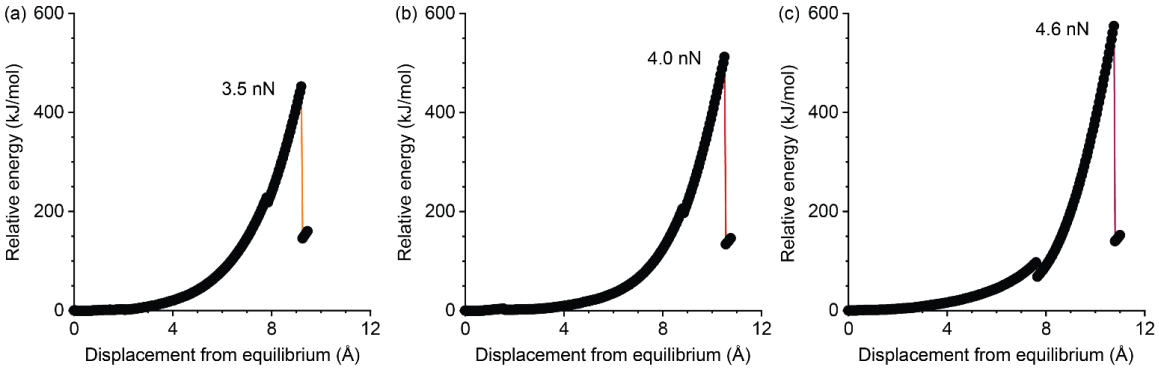

Figure S3.57. Density functional theory (DFT) calculations using the constrained geometries simulate external force (CoGEF) method and a Polarizable Continuum Model with a 37.22 dielectric constant performed on a truncated models of (a) *ortho*-FNP, (b) *meta*-FNP, and (c) *para*-FNP. The ring-opening reaction is predicted to occur at a maximum force of 3.5 nN, 4.0 nN, and 4.6 nN, respectively. Calculations were performed at the B3LYP/6-31G* level.

Determination of Activation Length Using the CoGEF Method. Activation length was modeled using Spartan ′24 Parallel Suite according to previously reported methods.[61] Truncated models of each mechanophore with terminal acetoxy groups were used in the calculations. Elongated reactant and transition state structures were obtained from EFEI calculations with an external force of 2 nN (see below). Starting from these elongated molecules, the distance between the terminal methyl groups of the truncated structures was decreased in increments of 0.1 Å and the energy was minimized at each step using the semi-empirical AM1 level of theory. The energy data from approximately 20 to 140 kJ/mol was fit to a quadratic function, and the first derivative of the quadratic fit yields force as a function of end-to-end distance. This line was extrapolated to zero force to obtain the force-free contour length.

Force-Free Transition State Calculation on Unsubstituted Fluorenyl Naphthopyran

The equilibrium geometry was calculated at the B3LYP/6-31G* level of theory using Spartan ′24 Parallel Suite. The transition state geometry was approximated using an initial energy profile at the HF/6-31+G* level of theory by lengthening the C–O bond involved in the desired ring-opening reaction. The energy maximum from this energy profile was then chosen as the starting point for a transition state geometry optimization, which was conducted at the HF/6-31+G* level of theory. Subsequent geometry optimization was performed at the B3LYP/6-31G* level of theory and the optimized structure was subjected to a final energy and frequency calculation at the B3LYP/6-31G* level of theory using a fine integration grid (99,590). The calculation returned a single imaginary vibrational frequency corresponding to the expected bond-breaking mode.

Force-Free Transition State Calculations on Fluorenyl Naphthopyrans. DFT calculations were performed using ORCA v. 5.0.3.[62] Truncated models of each mechanophore with terminal acetoxy groups were used in the calculations. All calculations were performed at the uB3LYP[63–65]/def2-SVP level of theory with the DFT-D3(BJ)[66] dispersion correction. The equilibrium geometries of the fluorenyl naphthopyrans were found via a geometry optimization calculation and confirmed with a frequency calculation, ensuring no negative vibrational frequencies were observed. The transition state geometry was first approximated with a relaxed surface scan lengthening the C–O bond involved in the naphthopyran ring-opening reaction by increments of 0.1 Å. The structure corresponding to the maximum point on this energy profile was then chosen as the input for a transition state geometry optimization. The transition state was confirmed by a frequency calculation yielding a single imaginary vibrational frequency corresponding to the expected bond-breaking mode.

EFEI Calculations. DFT calculations were performed using ORCA v. 5.0.3 according to previously reported methods.[67] Force-modified potential energy surfaces (FMPES) were constructed using the external force is explicitly included (EFEI) method,[68] where external force was applied in the range of 0 – 4.5 nN in 0.5 nN increments. All calculations were performed at the uB3LYP/def2-SVP level of theory with the DFT-D3(BJ) dispersion correction unless specified otherwise. Reactant and transition state geometry optimizations at low forces (0.5 – 2 nN) were carried out over three steps. First, reactant geometries were optimized using the force-free equilibrium geometry as the input structure. Then a relaxed surface scan lengthening the C–O pyran bond was performed in increments of 0.1 Å. The highest energy structure was then used as input for the transition state geometry optimization.

For all three calculations the force was kept constant and defined in the geometry block of the ORCA input file. To obtain reactant and transition state geometries at higher forces, calculations were performed sequentially starting at 2.5 nN where the 2 nN reactant and transition state geometries were used as inputs for the 2.5 nN geometry and transition state optimizations, respectively. In turn, the resulting optimized geometries at 2.5 nN were used as the input structures for the 3.0 nN calculations, and so on. All reactant geometries were confirmed with a frequency calculation to ensure no negative vibrational frequencies were observed. Frequency calculations performed on the transition state geometries confirm the presence of a single imaginary vibrational frequency corresponding to the desired bond-breaking vibrational mode. Single-point energy calculations were performed at the uB3LYP-D3(BJ)/def2-TZVPP level of theory on all optimized geometries, where the sum of the calculated external potential and single point energy terms is the total electronic energy (E) for a molecule. The difference in E between the reactant and transition state structures at a given force is defined as $\Delta E^{\ddagger}$. The optimized geometry coordinates of the reactant and transition state structures are provided in the DFT structures supplemental zip file. Representative ORCA input files are shown below in Figures S3.58 – 3.61.

```
! UKS B3LYP D3BJ def2-SVP OPT RIJCOSX freq

%geom
POTENTIALS
 { C a b F }
# Force F (nN) applied to atoms a and b
end
end

*xyz 0 1
#xyz coordinates of input structure go here
*
```

Figure S3.58. Representative ORCA input for EFEI geometry optimization at the uB3LYP-D3BJ/def2-SVP level of theory.

```
! UKS B3LYP D3BJ def2-SVP OPT RIJCOSX

%geom Scan
B c d = Di, Df, s
# Scanning distance between atoms c and d from
# distance (angstroms) Di to Df, in s steps
end
POTENTIALS
 { C a b F }
# Force F (nN) applied to atoms a and b
end
end

*xyz 0 1
#xyz coordinates of input structure go here
*
```

Figure S3.59. Representative ORCA input for EFEI relaxed surface scan at the uB3LYP-D3BJ/def2-SVP level of theory.

```
! UKS B3LYP D3BJ def2-SVP OptTS RIJCOSX freq

%geom
Calc_Hess true
Recalc_Hess 10
POTENTIALS
 { C a b F }
# Force F (nN) applied to atoms a and b
end
end

*xyz 0 1
#xyz coordinates of input structure go here
*
```

Figure S3.60. Representative ORCA input for EFEI transition state optimization at the uB3LYP-D3BJ/def2-SVP level of theory.

```
! UKS B3LYP D3BJ def2-TZVPP RIJCOSX

%geom
POTENTIALS
 { C a b F }
# Force F (nN) applied to atoms a and b
end
end

*xyz 0 1
#xyz coordinates of input structure go here
*
```

Figure S3.61. Representative ORCA input for EFEI single point energy calculation at the uB3LYP-D3BJ/def2-TZVPP level of theory.

As mentioned above, the geometry optimization procedure was segmented into regions of higher and lower force due to a rotation of the ester group on the naphthopyran that occurs below 2 nN for all three FNP species. The rotation of the ester group results in subtle discontinuities on the FMPES that are observed between 0.5 – 1 nN for *para*-FNP, 1 – 1.5 nN for *meta*-FNP, and 1.5 – 2 nN for *ortho*-FNP (Figure S3.62). Once the ester has undergone this rotation and force is increased, the ester group does not rotate back to the original conformation.

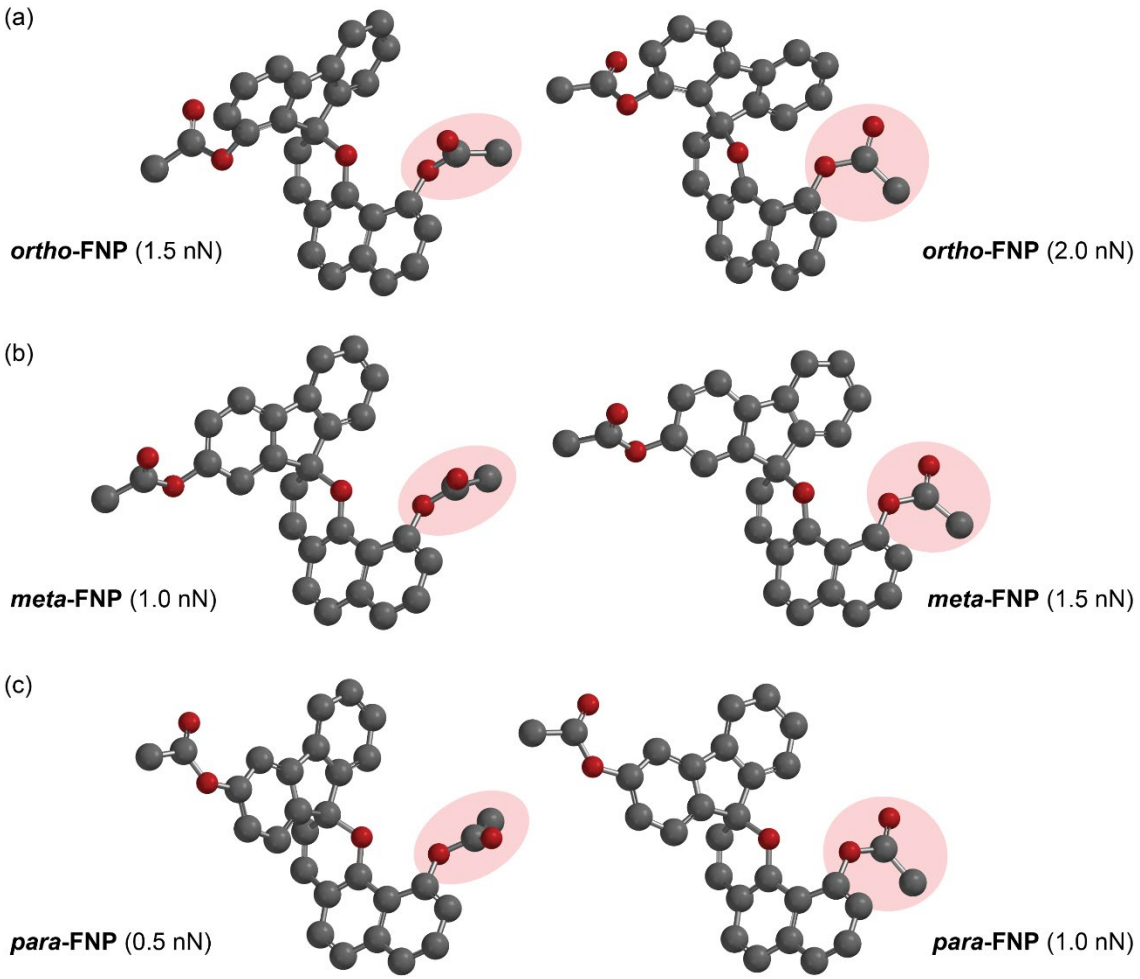

Figure S3.62. Structures of (a) *ortho*-FNP, (b) *meta*-FNP, and (c) *para*-FNP before (left) and after (right) the naphthyl ester flips, which causes subtle discontinuities in the FMPES due to the abrupt change in geometry.

^{1}H and ^{13}C NMR Spectra

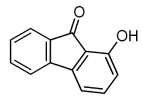

1a

^{1}H (400 MHz, acetone-d_6)

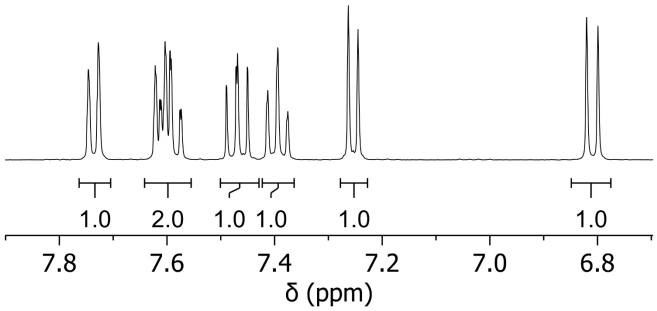

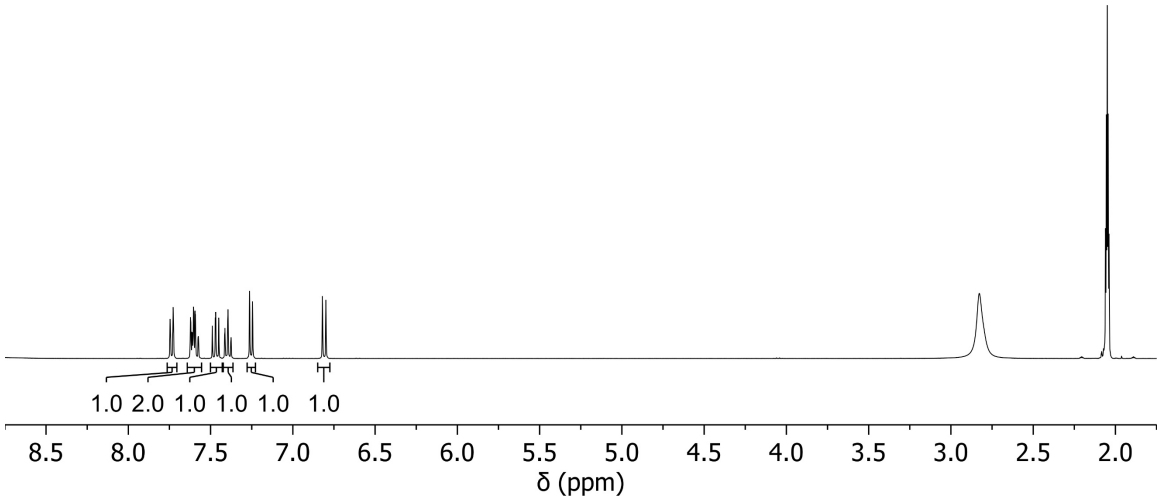

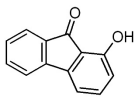

1a

^{13}C (101 MHz, acetone-d_6)

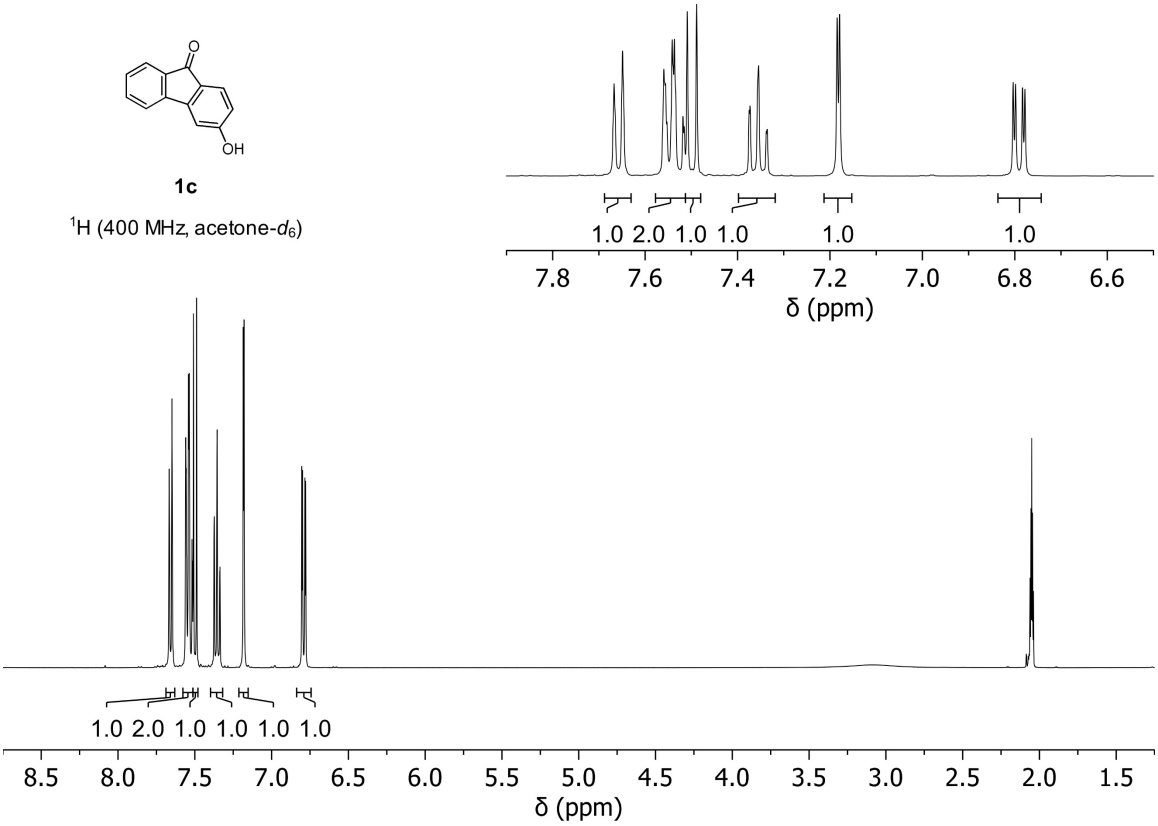
O
OH
1c
1H (400 MHz, acetone-d6)
1.0 2.0 1.0 1.0 1.0 1.0
8.5 8.0 7.5 7.0 6.5 6.0 5.5 5.0 4.5 4.0 3.5 3.0 2.5 2.0 1.5
δ (ppm)
1.0 2.0 1.0 1.0 1.0 1.0
7.8 7.6 7.4 7.2 7.0 6.8 6.6
δ (ppm)

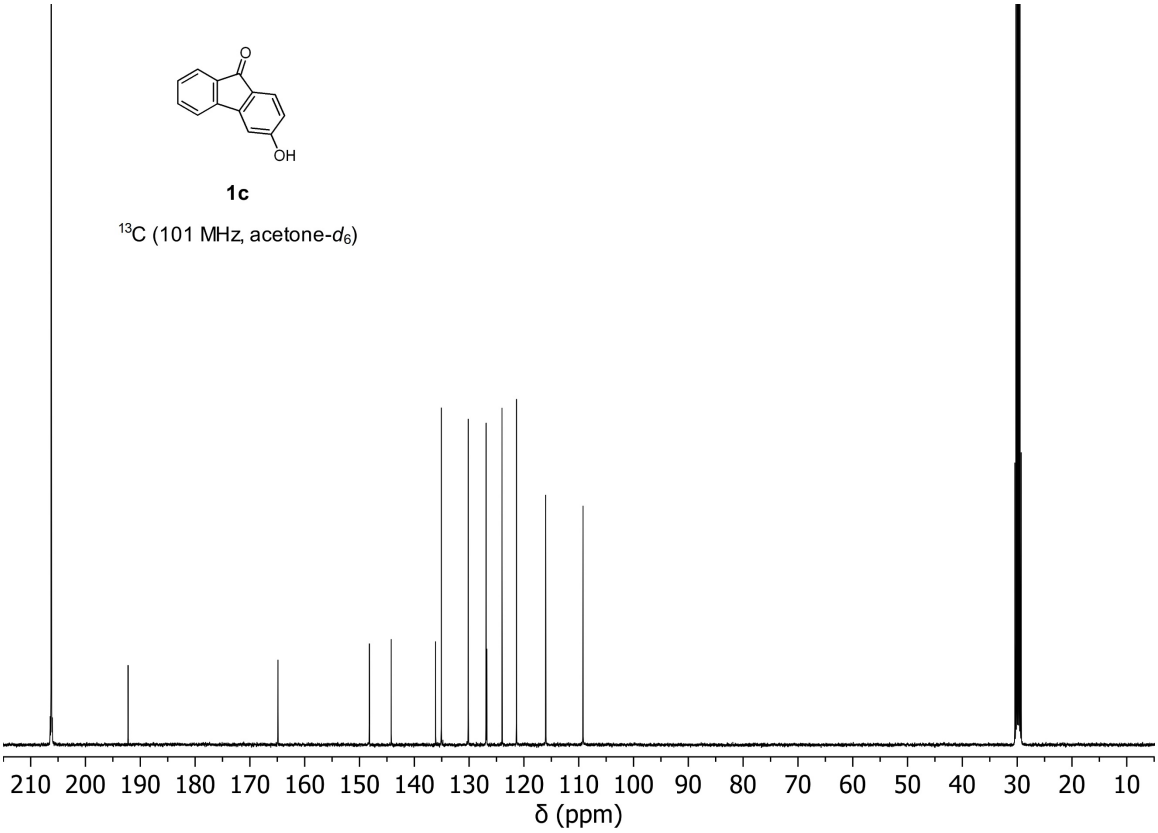
O
OH
1c
13C (101 MHz, acetone-d6)
210 200 190 180 170 160 150 140 130 120 110 100 90 80 70 60 50 40 30 20 10
δ (ppm)

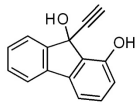

2a

^{1}H (400 MHz, acetone-d_6)

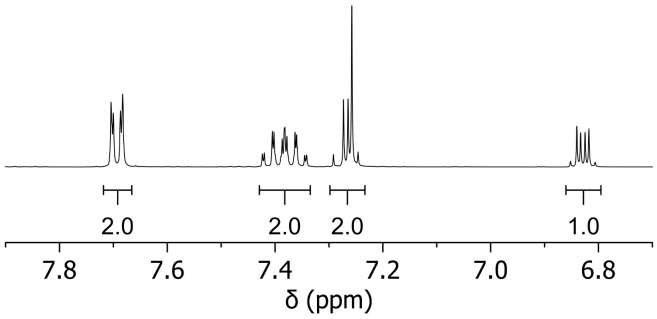

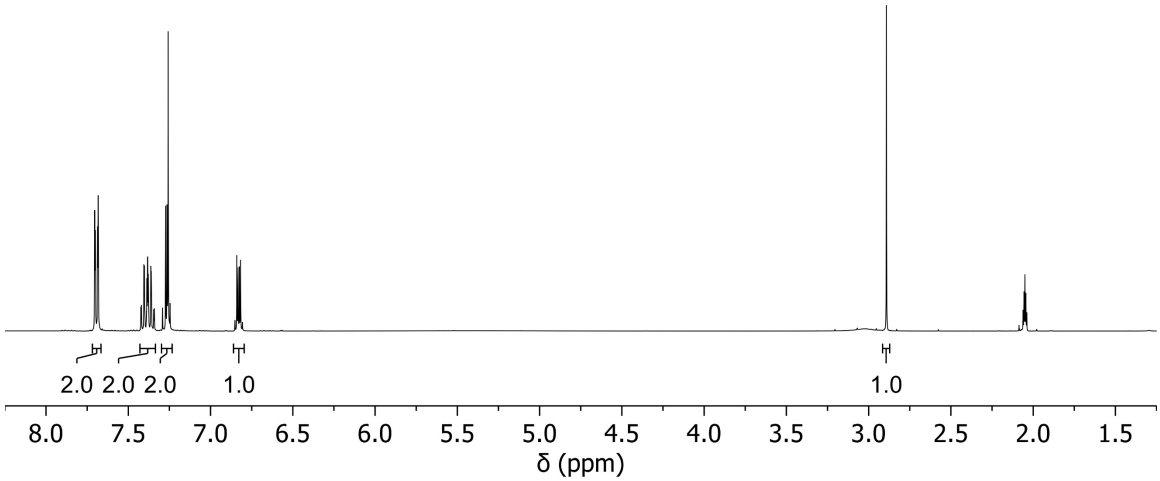

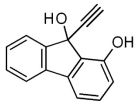

2a

^{13}C (101 MHz, acetone-d_6)

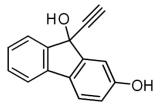

2b

^{1}H (400 MHz, acetone-d_6)

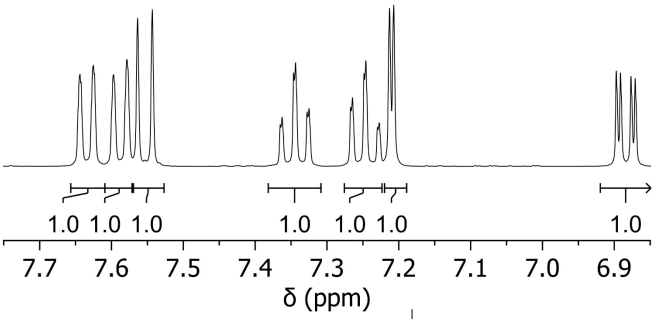

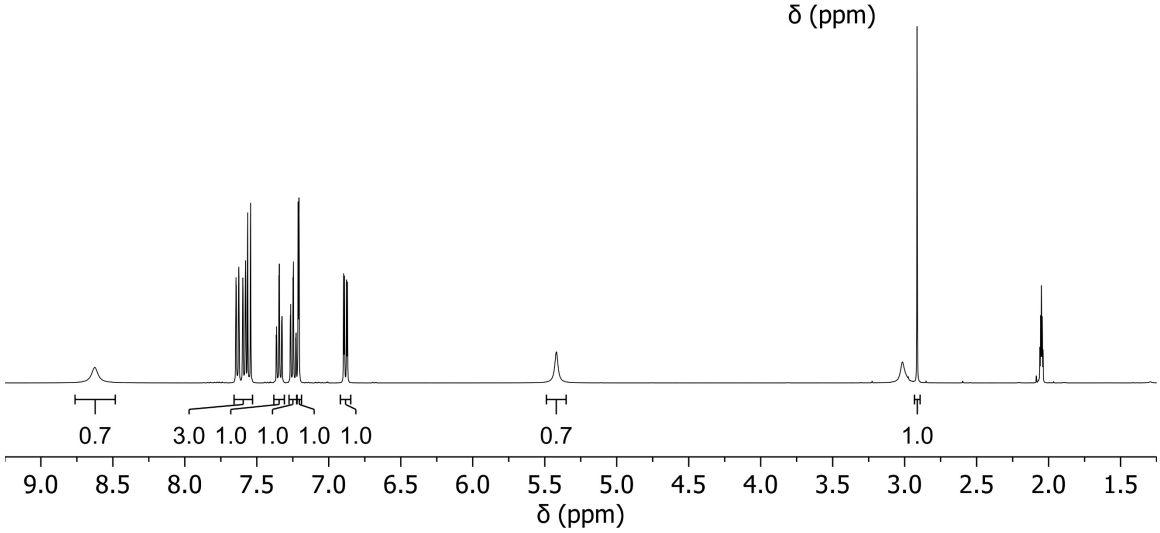

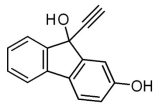

2b

^{13}C (101 MHz, acetone-d_6)

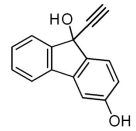

2c

^{1}H (400 MHz, acetone-d_6)

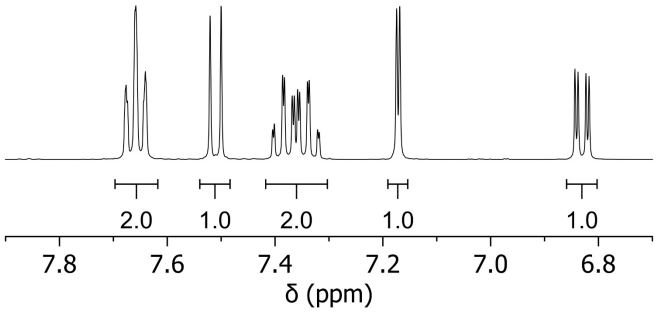

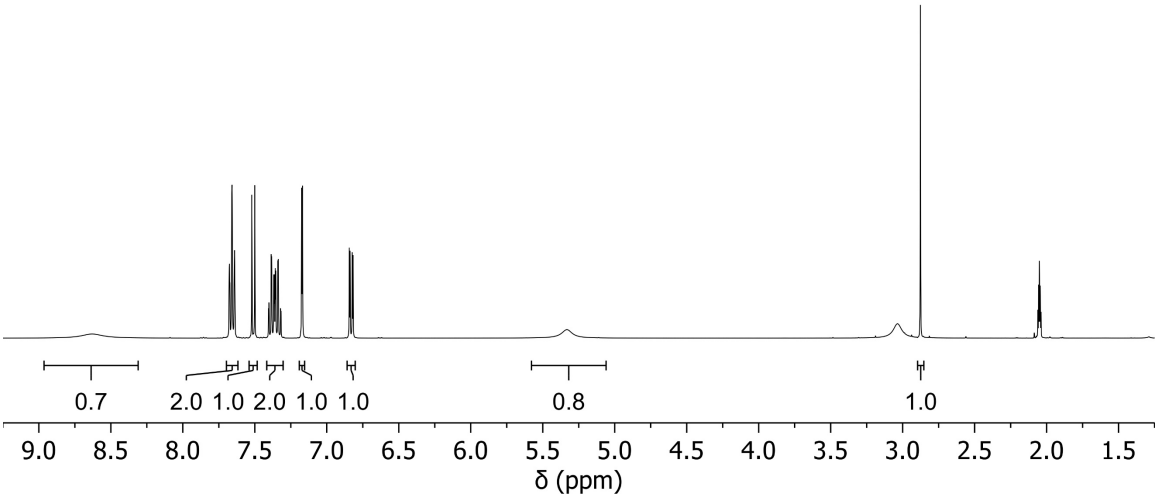

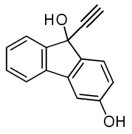

2c

^{13}C (101 MHz, acetone-d_6)

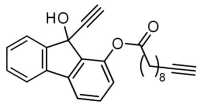

3a

^{1}H (400 MHz, $CDCl_3$)

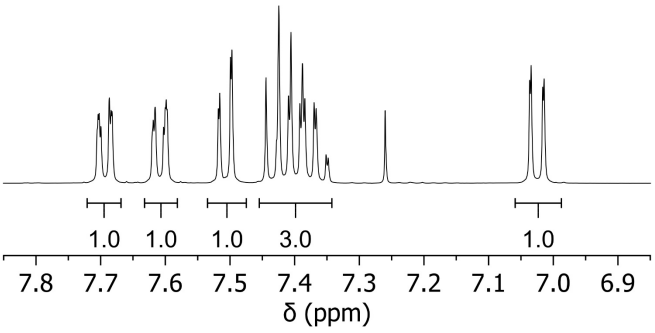

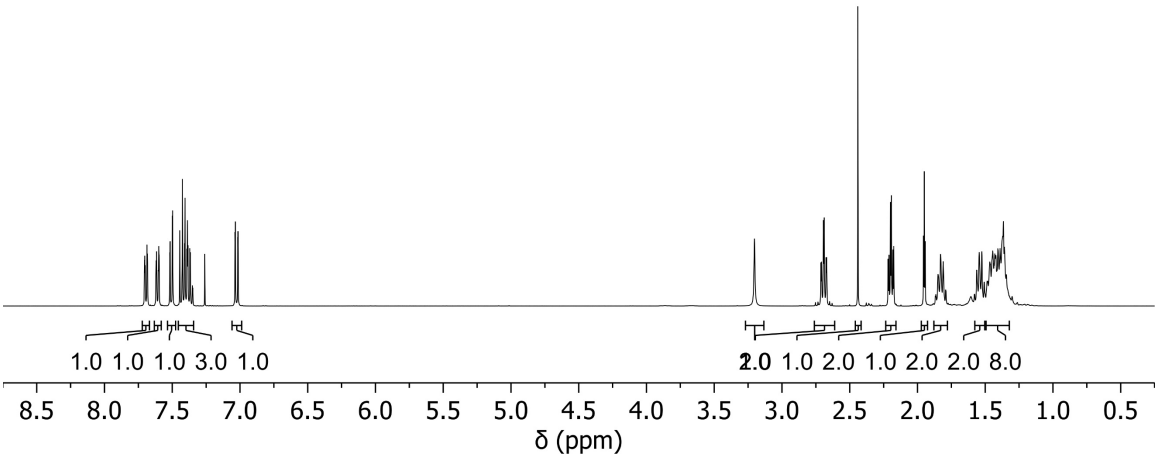

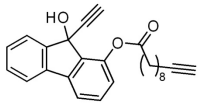

3a

^{13}C (101 MHz, $CDCl_3$)

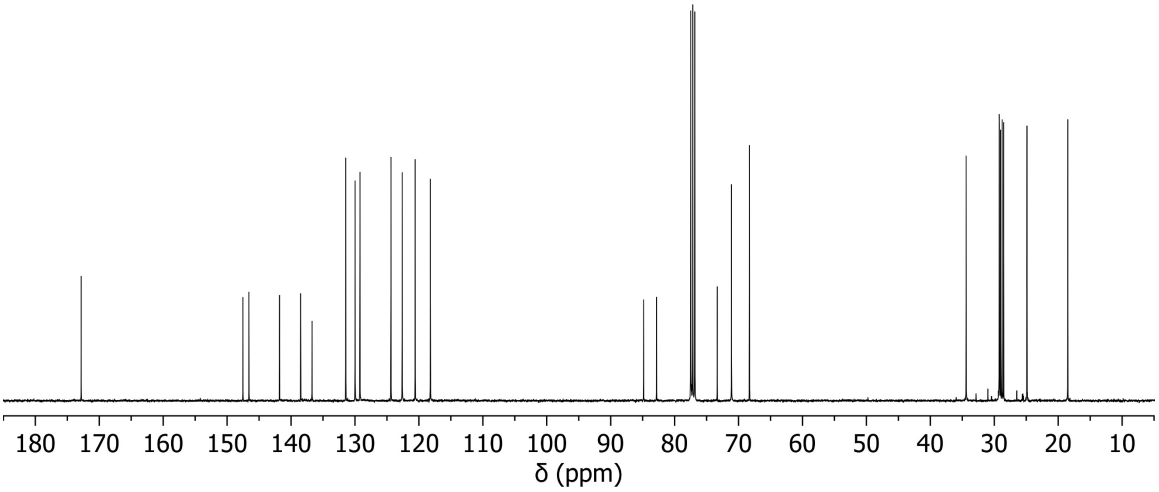

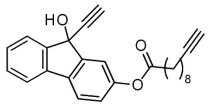

3b

^{1}H (400 MHz, $CDCl_3$)

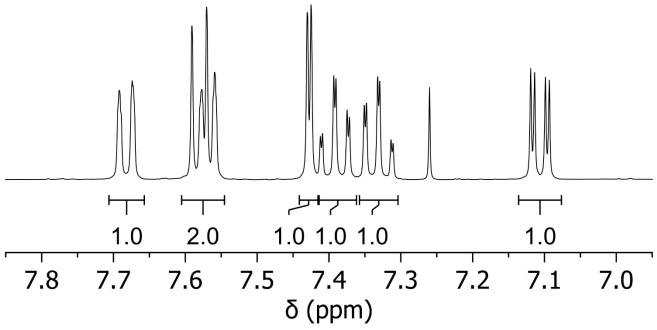

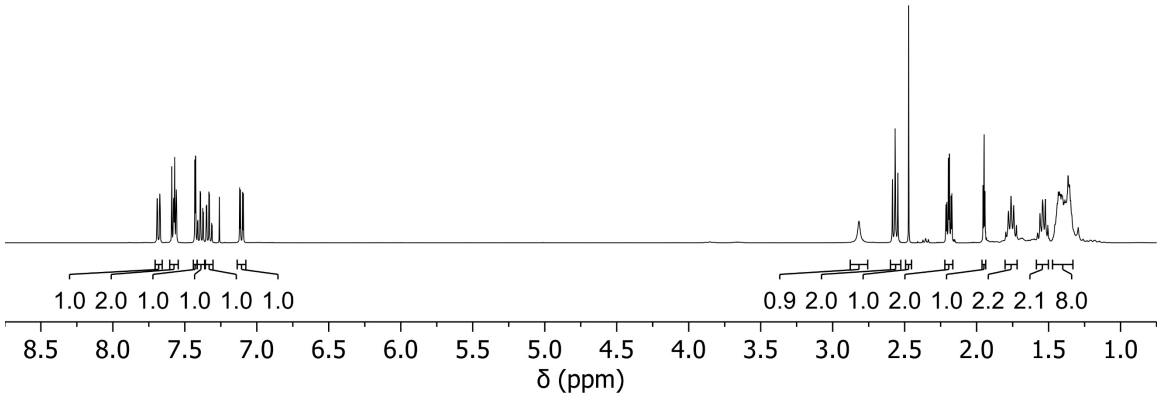

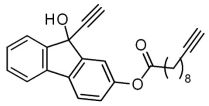

3b

^{13}C (101 MHz, $CDCl_3$)

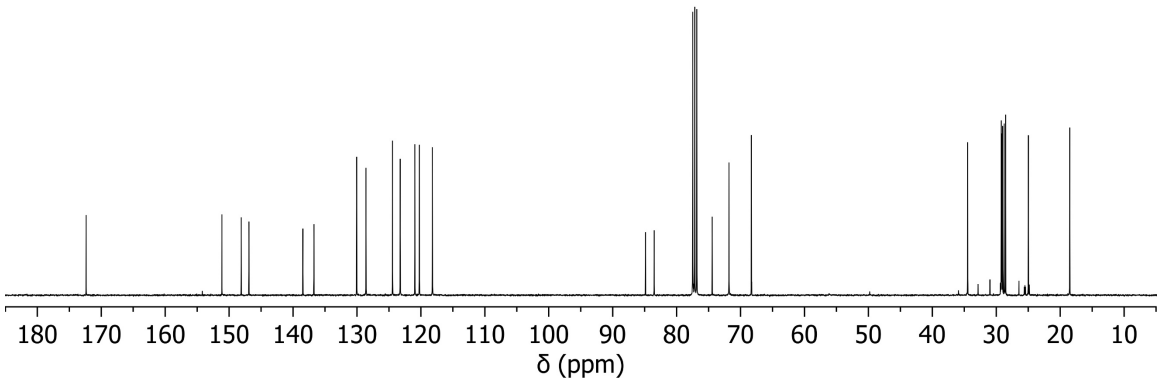

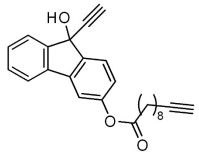

3c

^{1}H (400 MHz, $CDCl_3$)

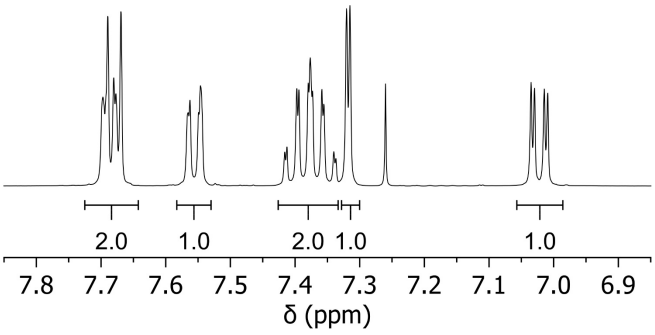

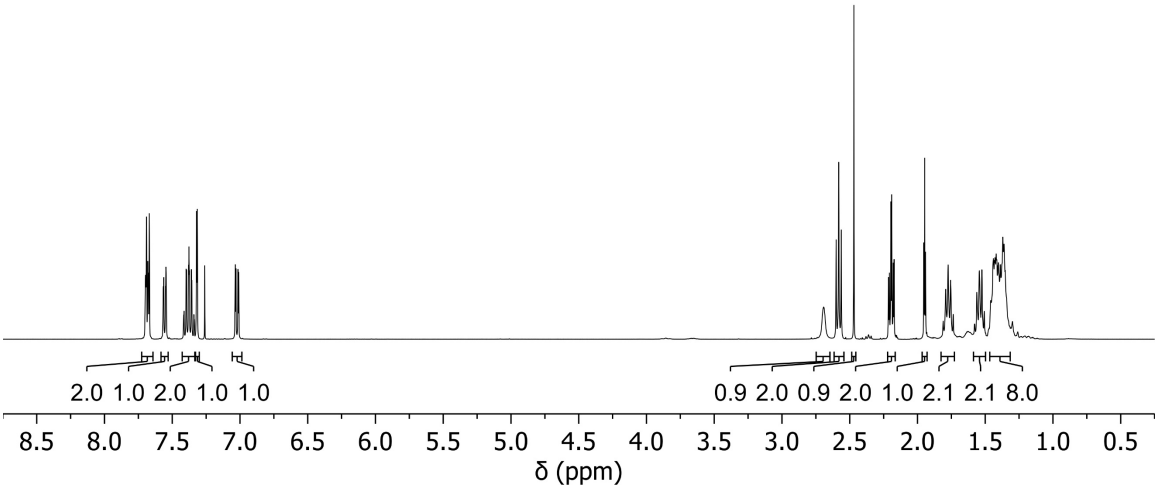

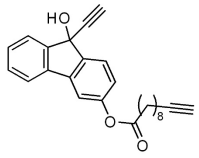

3c

^{13}C (101 MHz, $CDCl_3$)

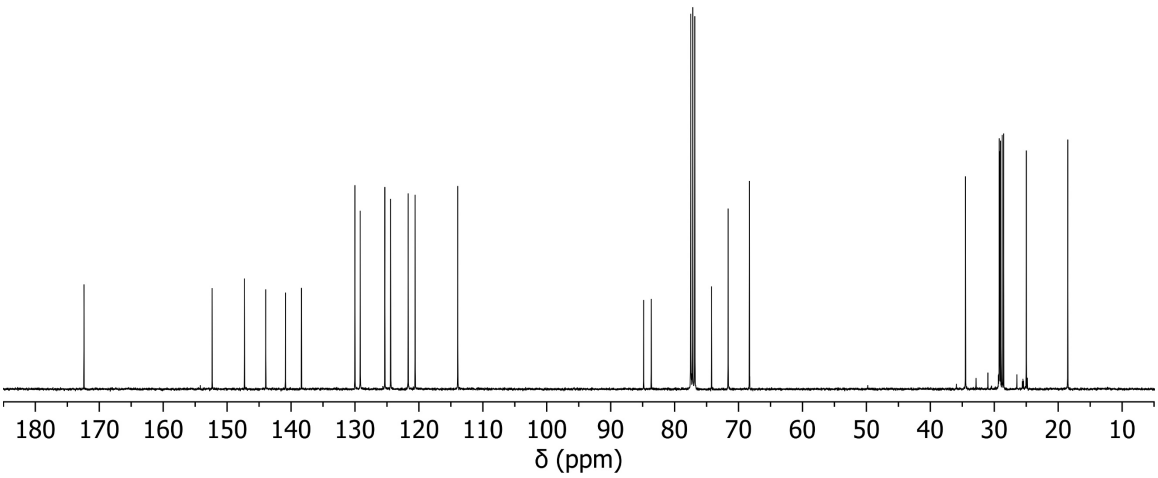

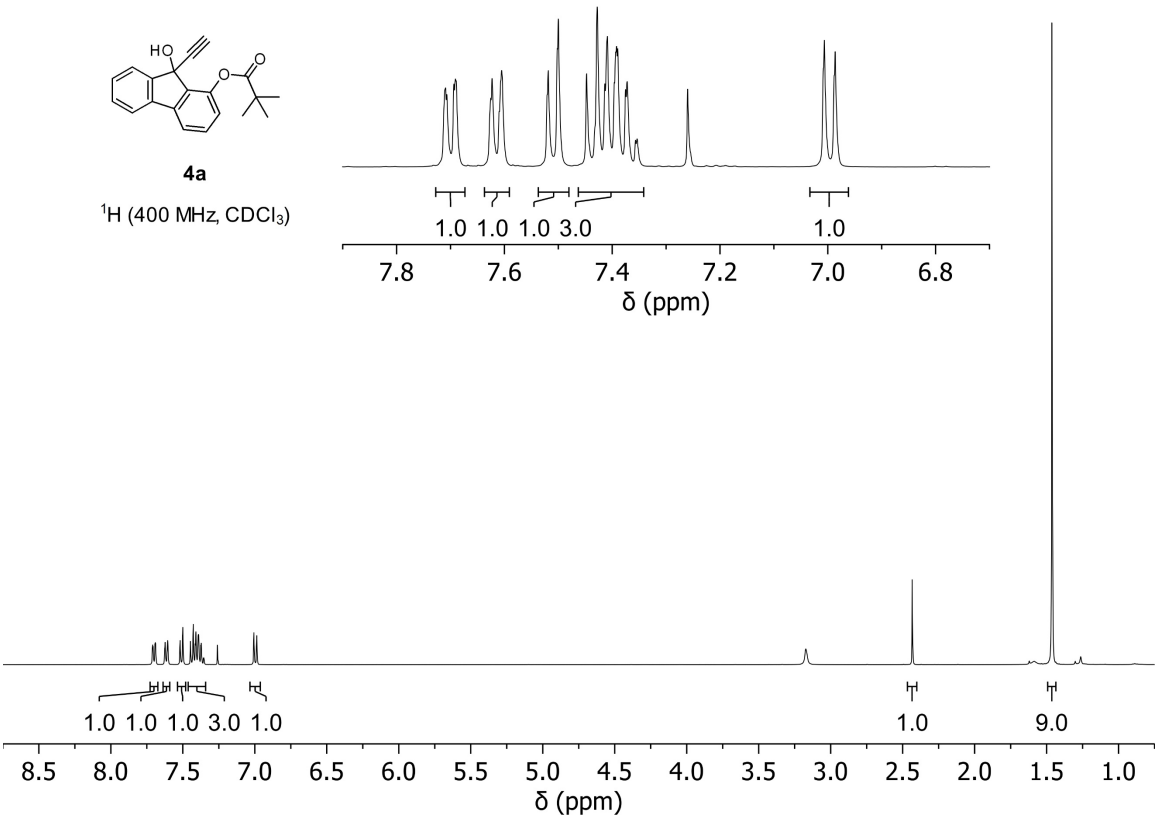

4a

^{1}H (400 MHz, $CDCl_3$)

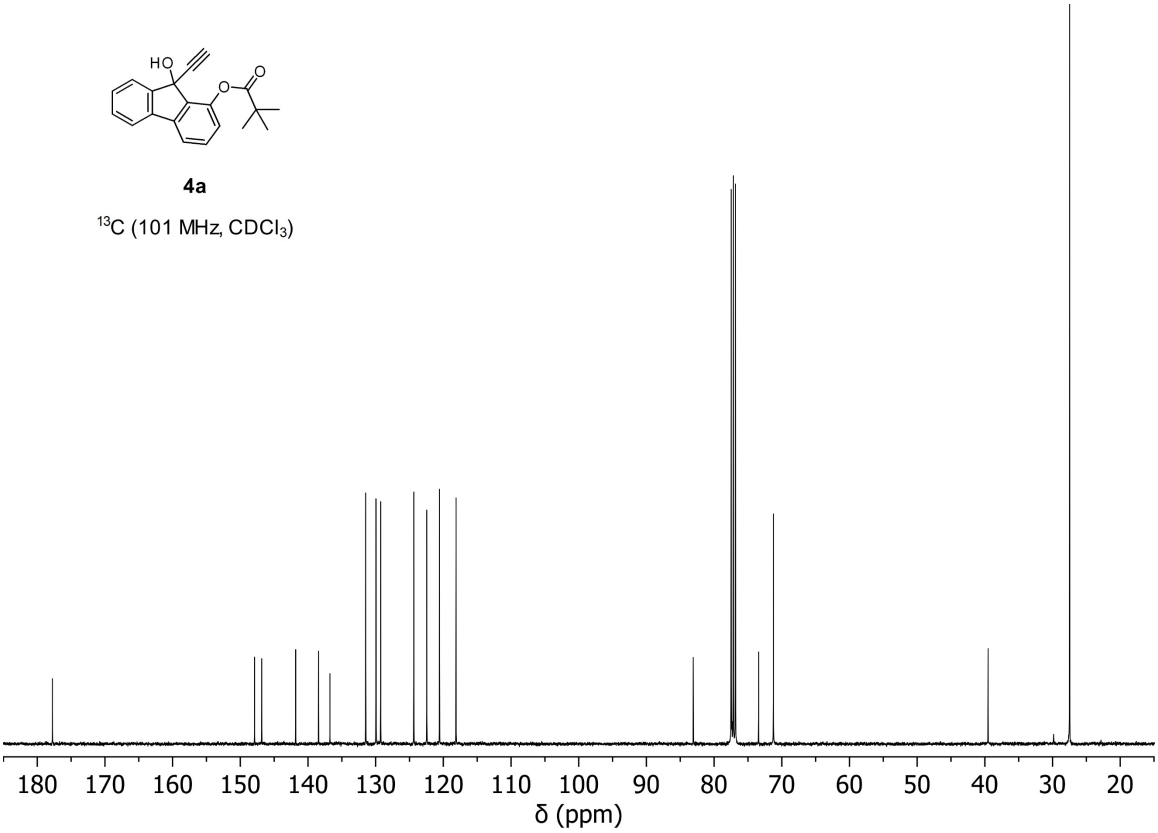

4a

^{13}C (101 MHz, $CDCl_3$)

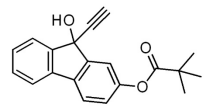

4b

^{1}H (400 MHz, $CDCl_3$)

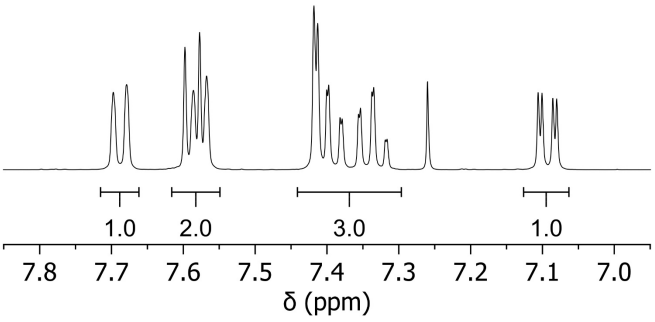

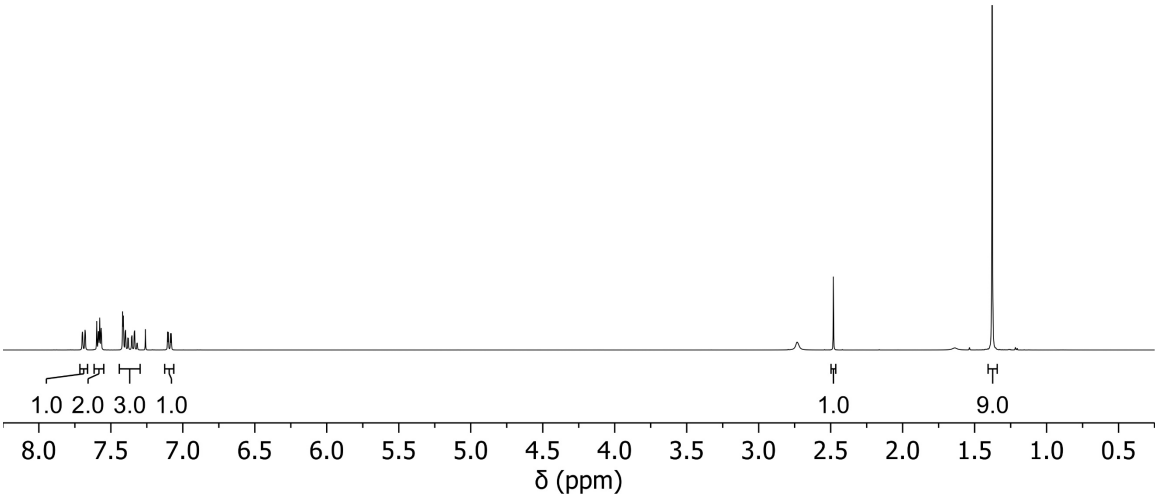

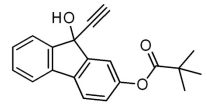

4b

^{13}C (101 MHz, $CDCl_3$)

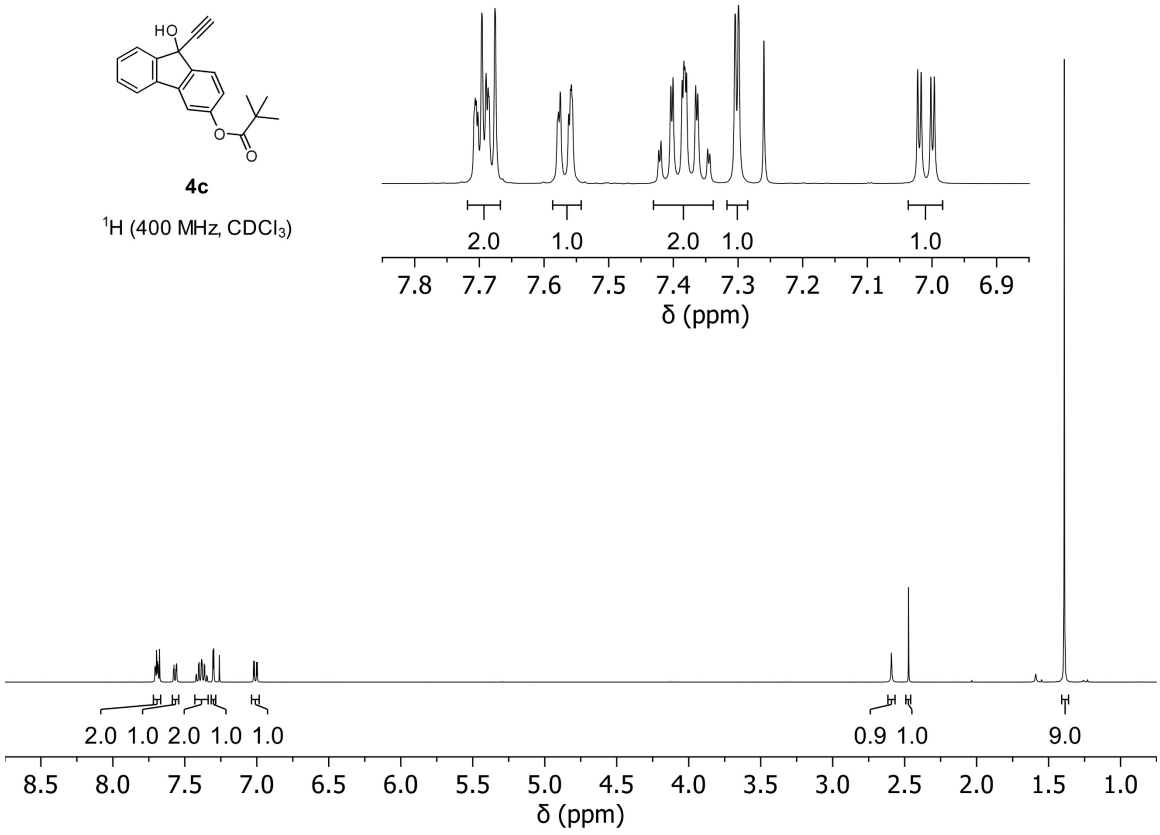

4c

^{1}H (400 MHz, $CDCl_3$)

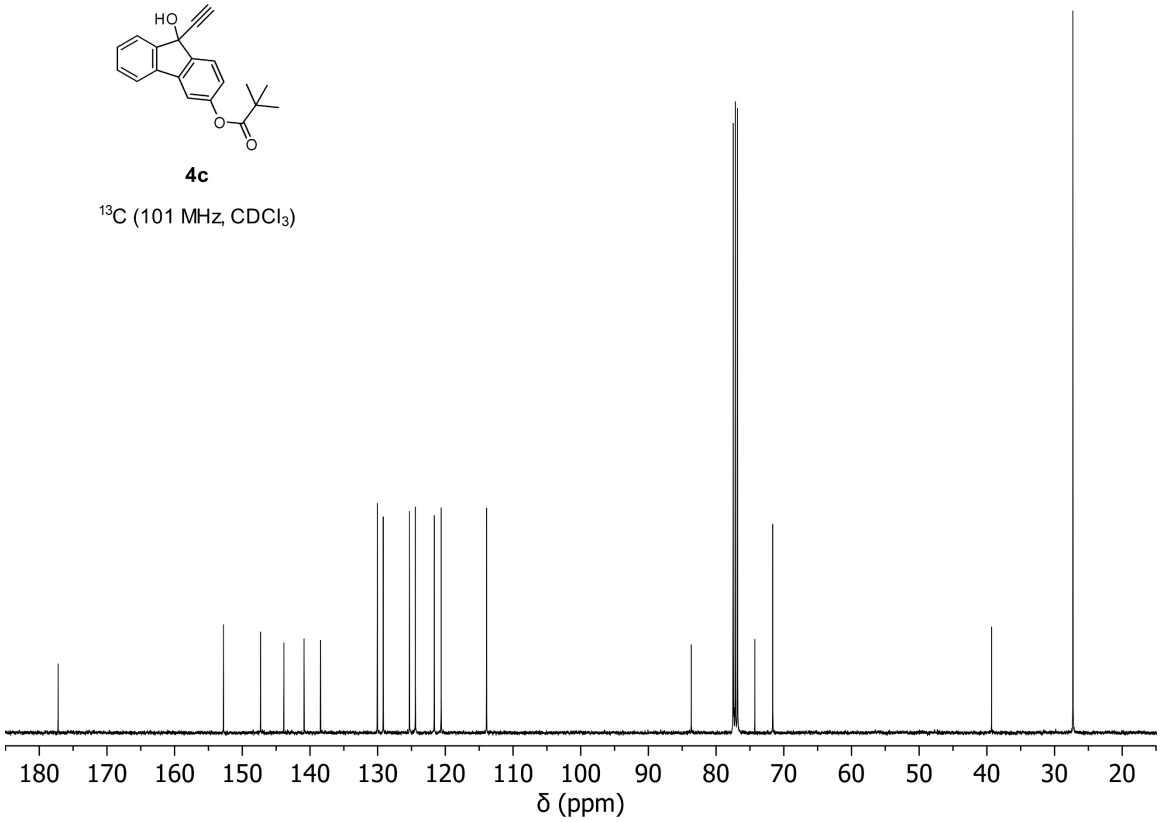

4c

^{13}C (101 MHz, $CDCl_3$)

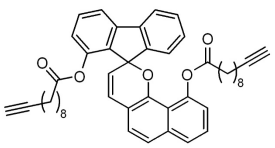

5a

^{1}H (400 MHz, acetone-d_6)

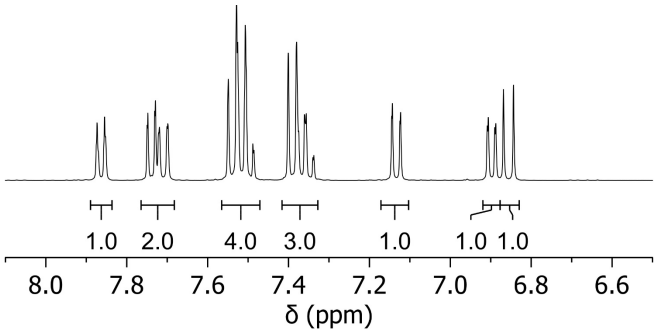

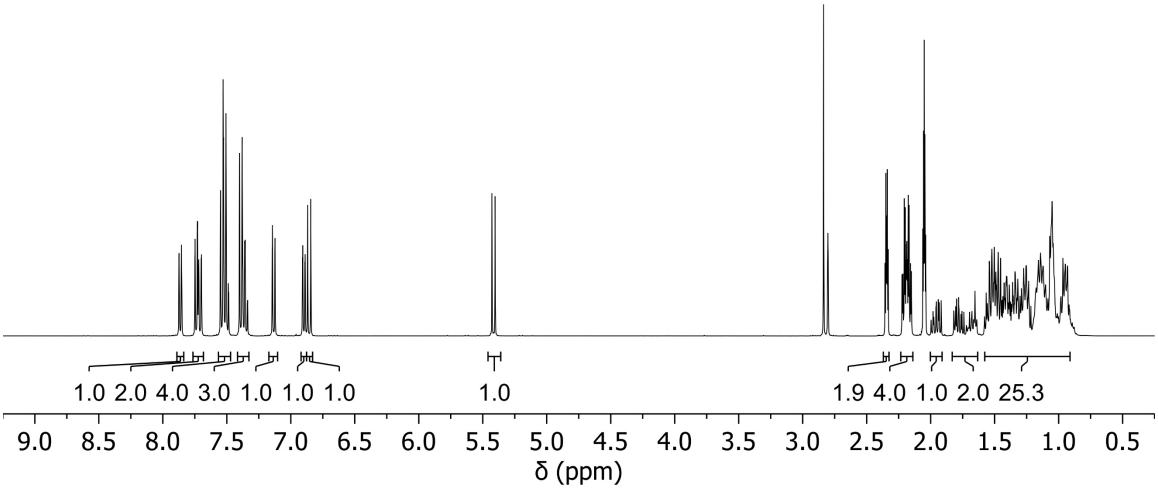

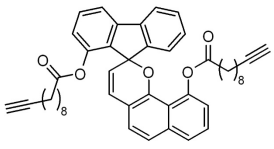

5a

^{13}C (101 MHz, acetone-d_6)

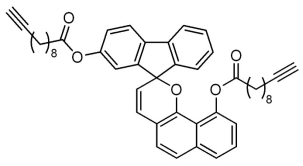

5b

^{1}H (400 MHz, acetone-d_6)

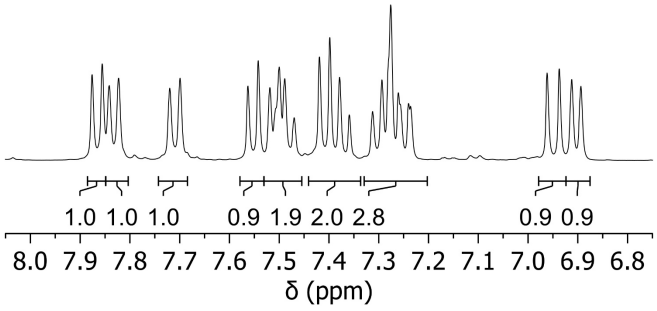

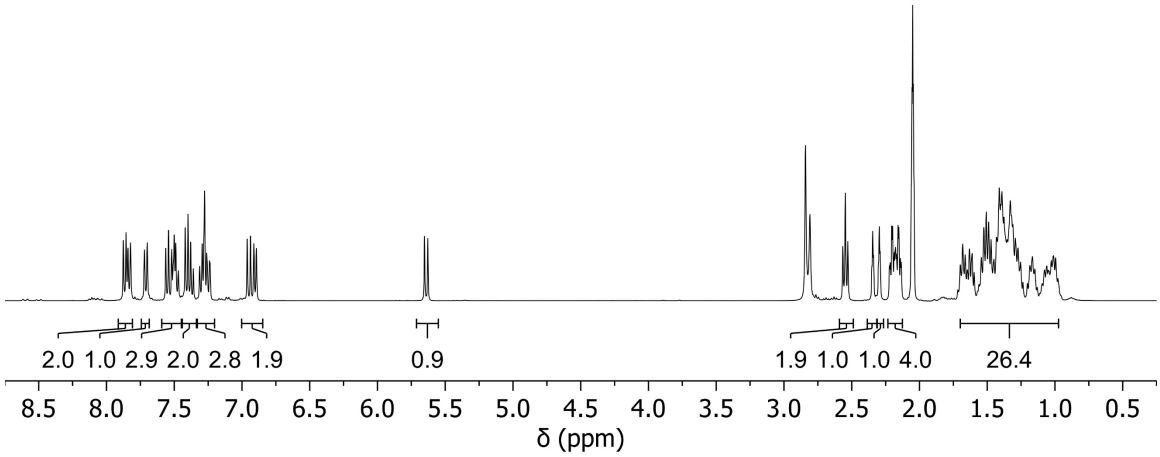

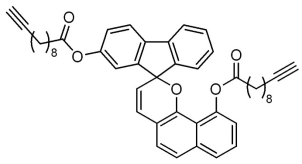

5b

^{13}C (101 MHz, acetone-d_6)

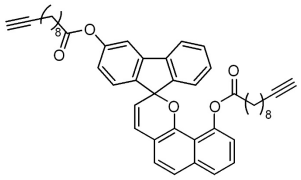

5c

^{1}H (400 MHz, acetone-d_6)

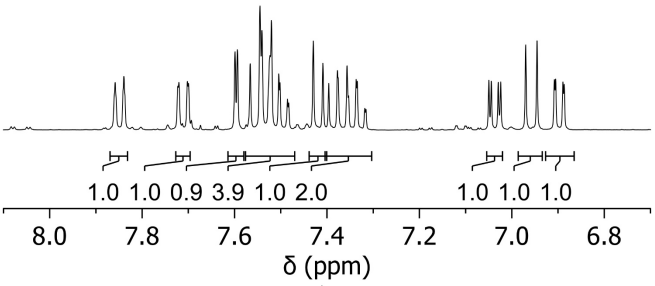

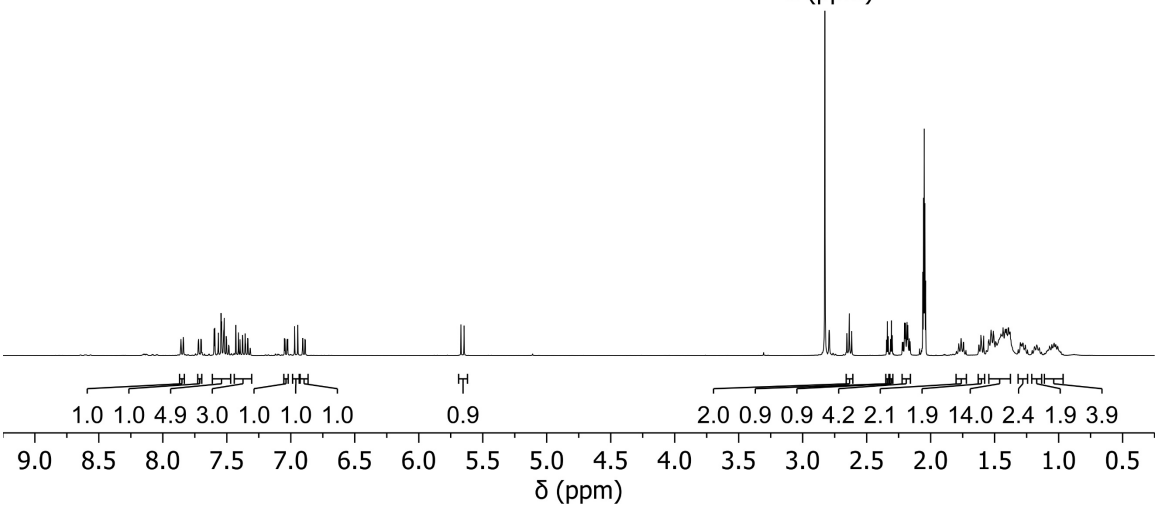

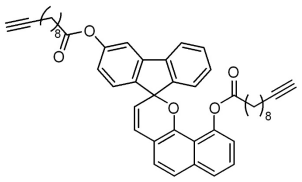

5c

^{13}C (101 MHz, acetone-d_6)

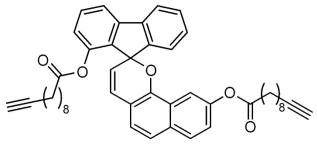

6a

^{1}H (400 MHz, acetone-d_6)

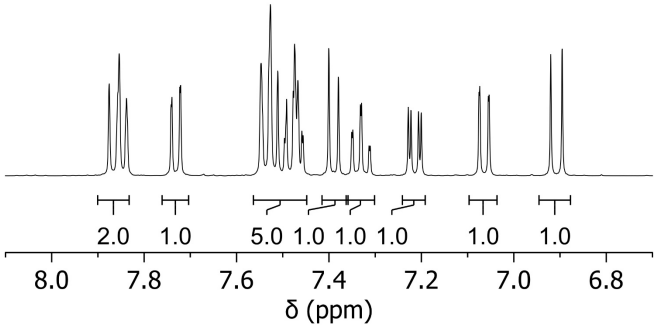

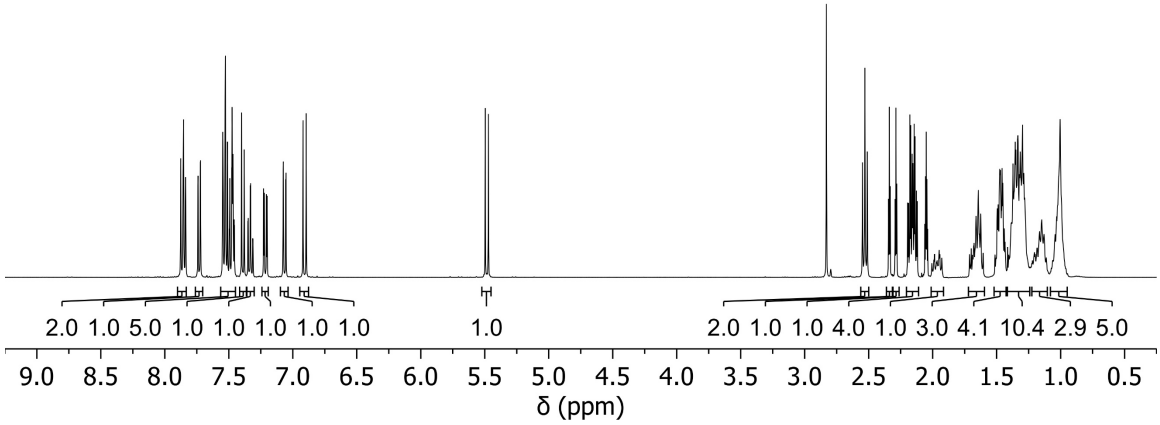

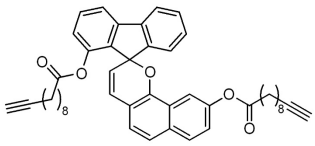

6a

^{13}C (101 MHz, acetone-d_6)

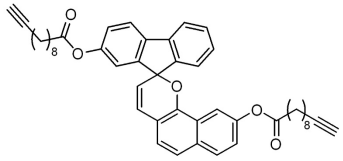

6b

^{1}H (400 MHz, acetone-d_6)

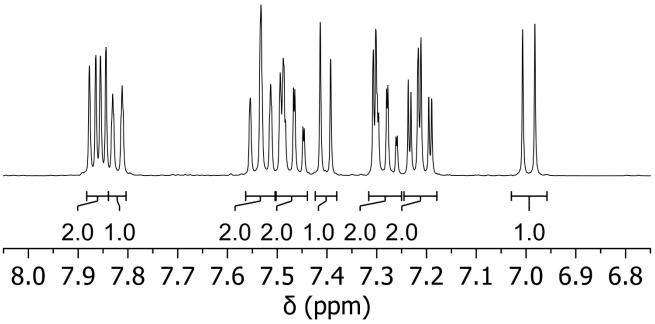

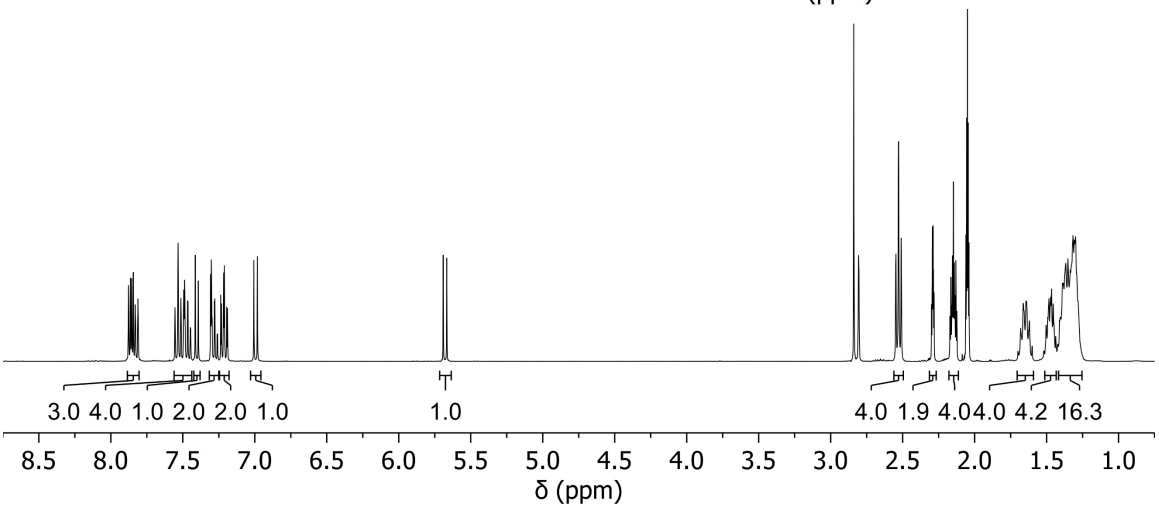

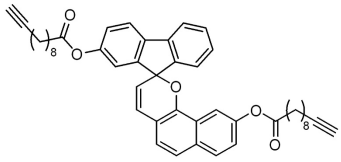

6b

^{13}C (101 MHz, acetone-d_6)

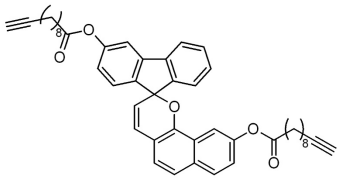

6c

^{1}H (400 MHz, acetone-d_6)

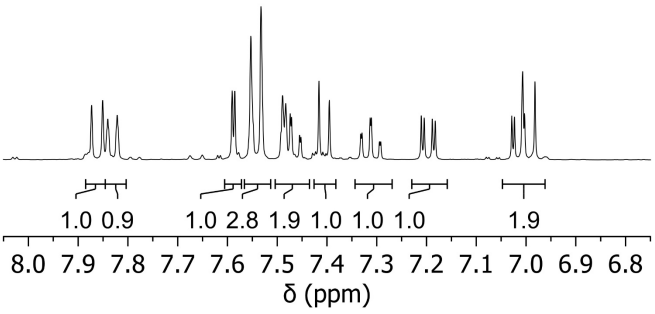

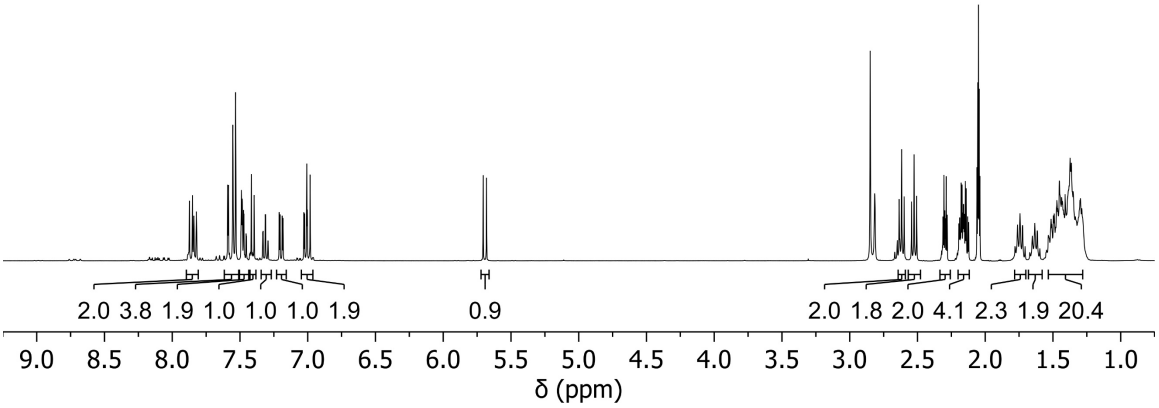

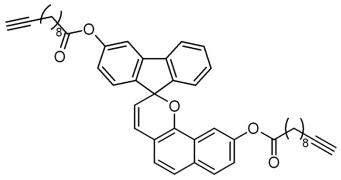

6c

^{13}C (101 MHz, acetone-d_6)

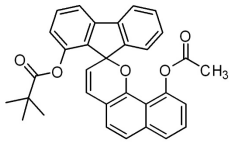

7a

^{1}H (400 MHz, $CDCl_3$)

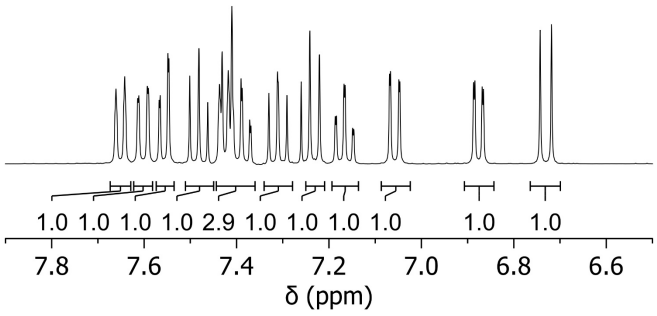

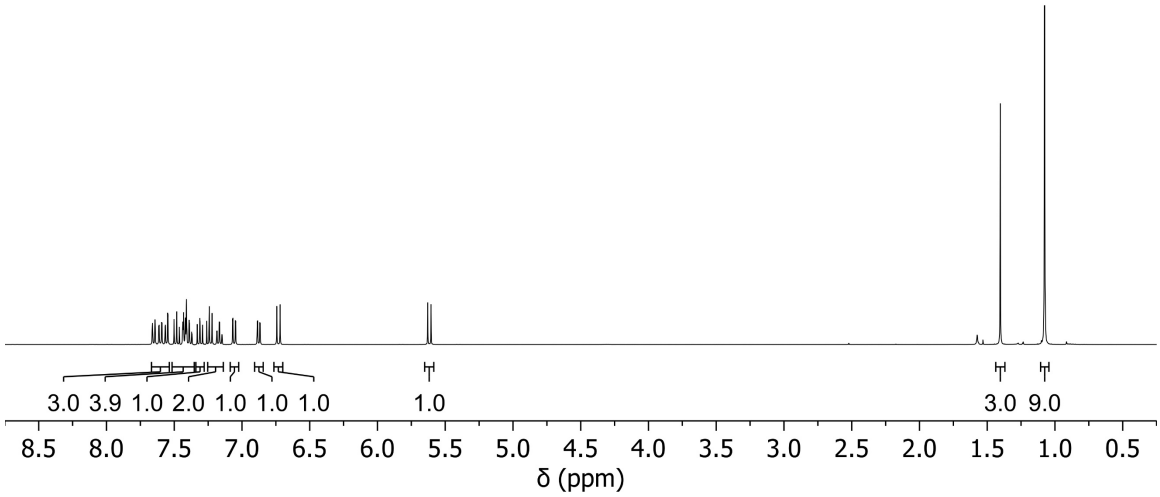

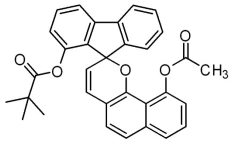

7a

^{13}C (101 MHz, $CDCl_3$)

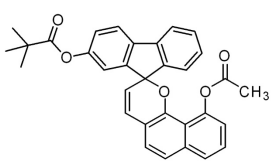

7b

^{1}H (400 MHz, acetone-d_6)

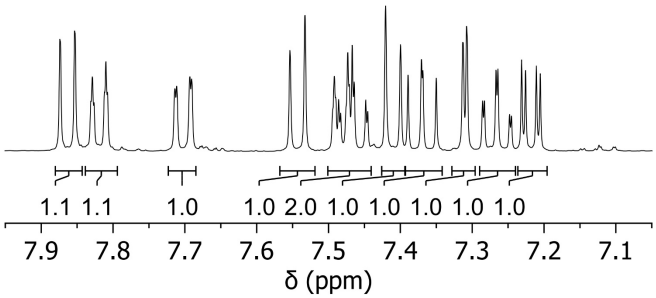

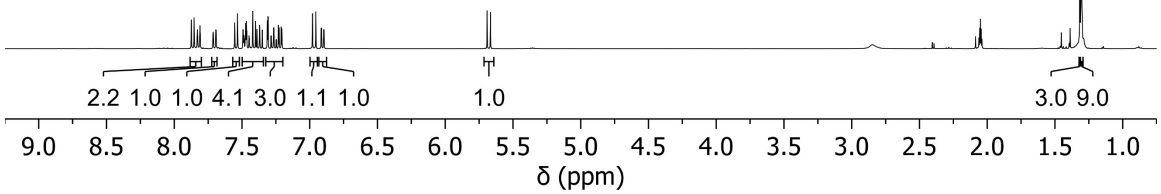

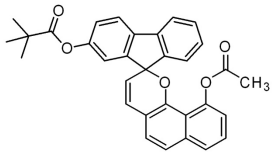

7b

^{13}C (101 MHz, acetone-d_6)

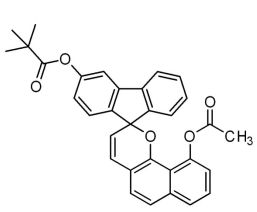

7c

^{1}H (400 MHz, $CDCl_3$)

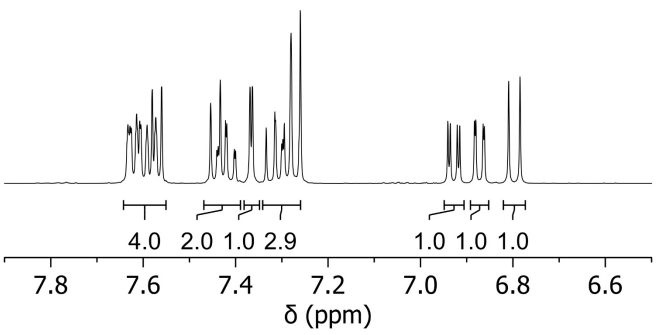

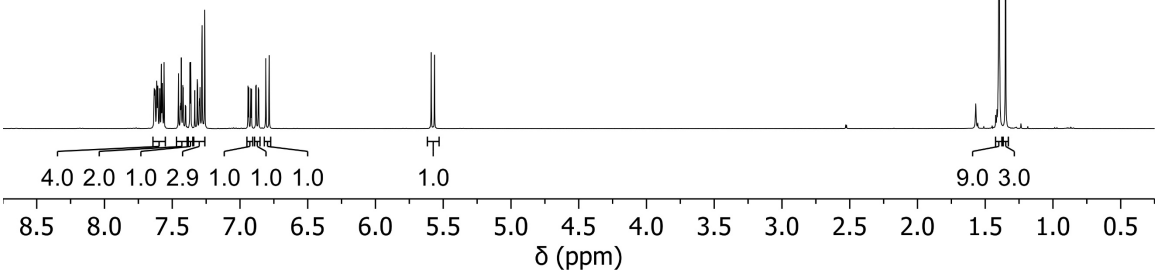

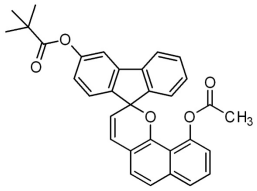

7c

^{13}C (101 MHz, $CDCl_3$)

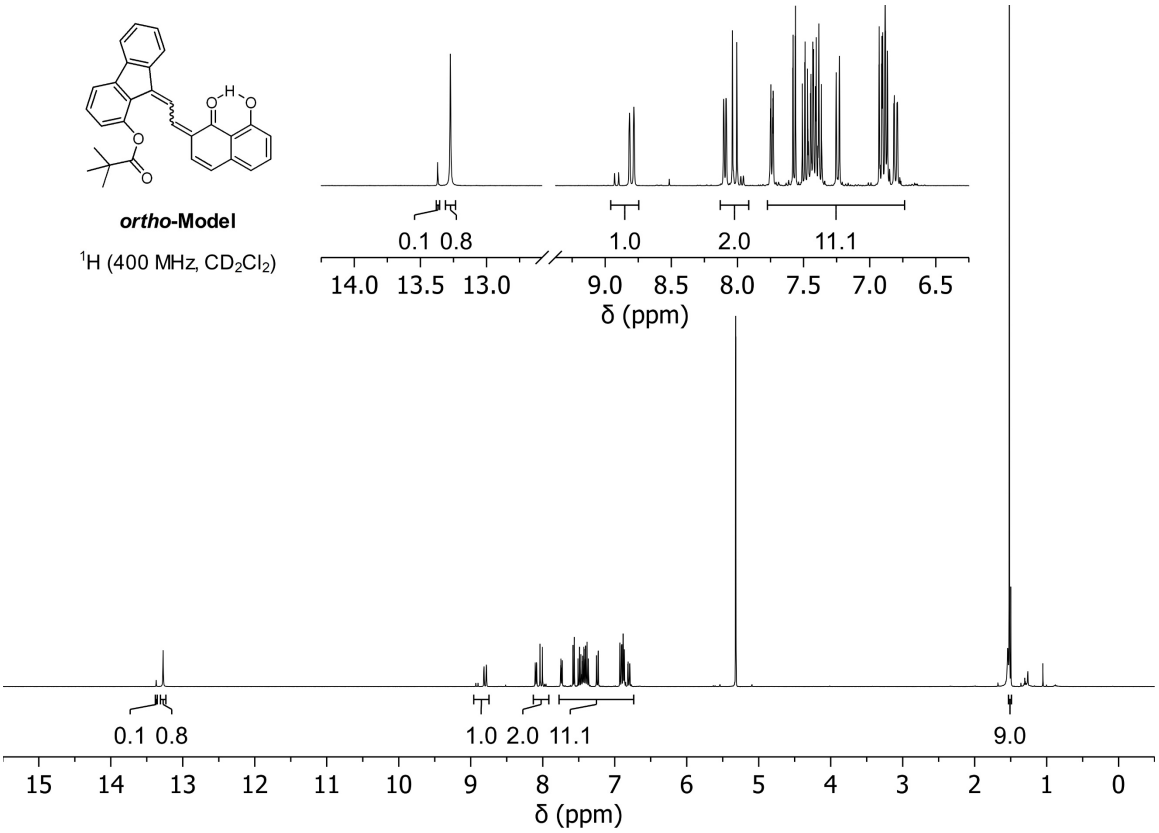

***ortho*-Model**

^{1}H (400 MHz, CD_2Cl_2)

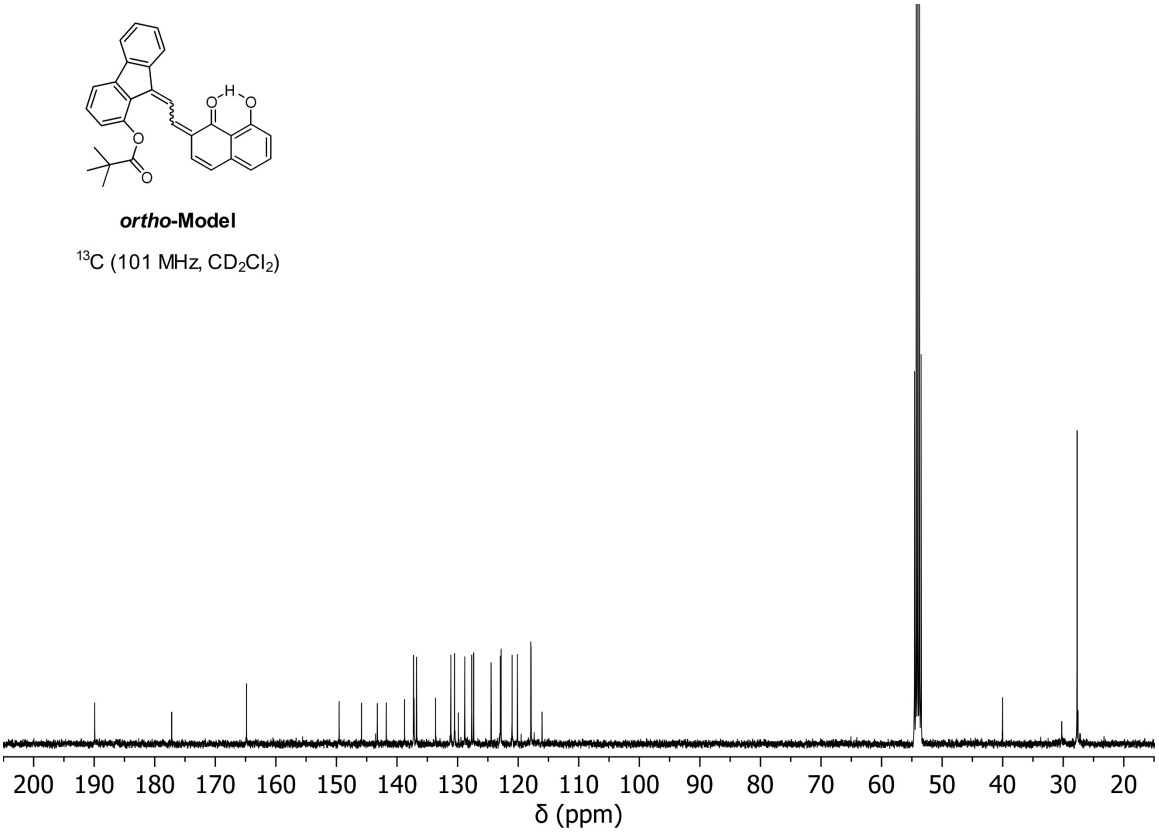

***ortho*-Model**

^{13}C (101 MHz, CD_2Cl_2)

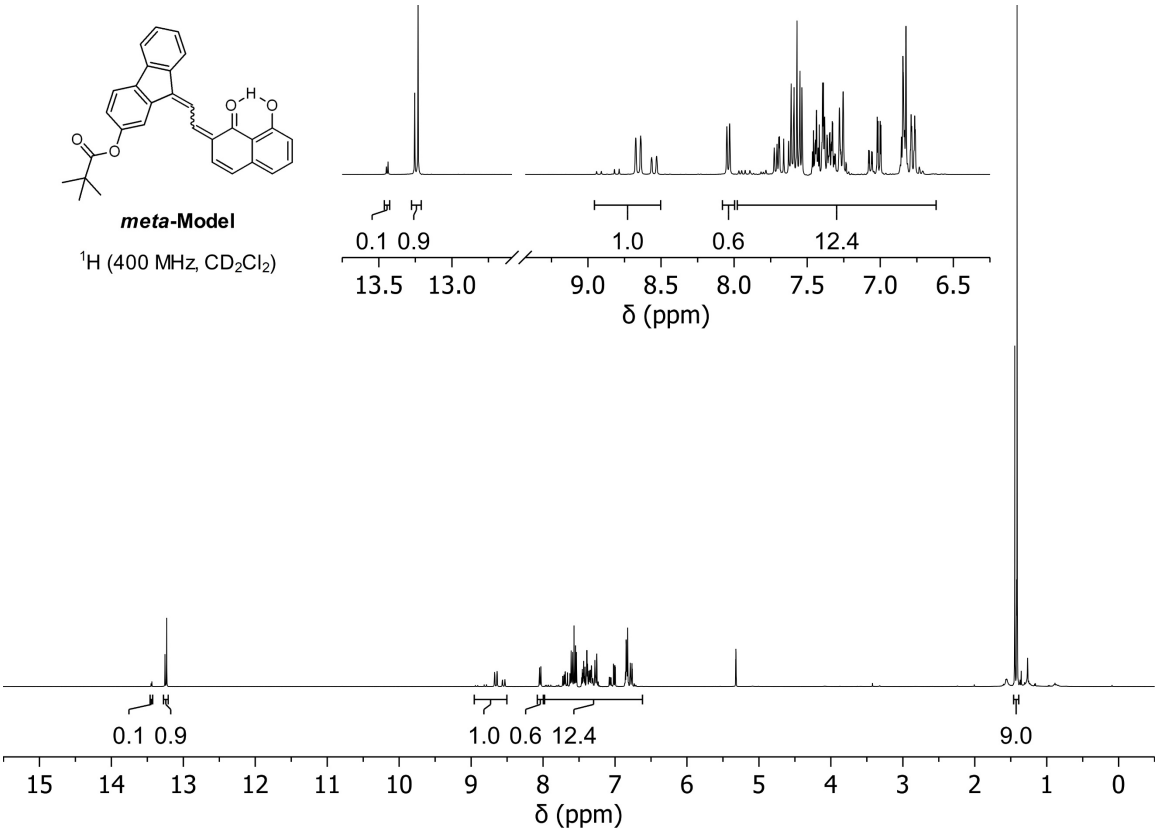
meta-Model
1H (400 MHz, CD2Cl2)
0.1 0.9
1.0
0.6
12.4
13.5 13.0
9.0 8.5 8.0 7.5 7.0 6.5
δ (ppm)
0.1 0.9
1.0 0.6 12.4
9.0
15 14 13 12 11 10 9 8 7 6 5 4 3 2 1 0
δ (ppm)

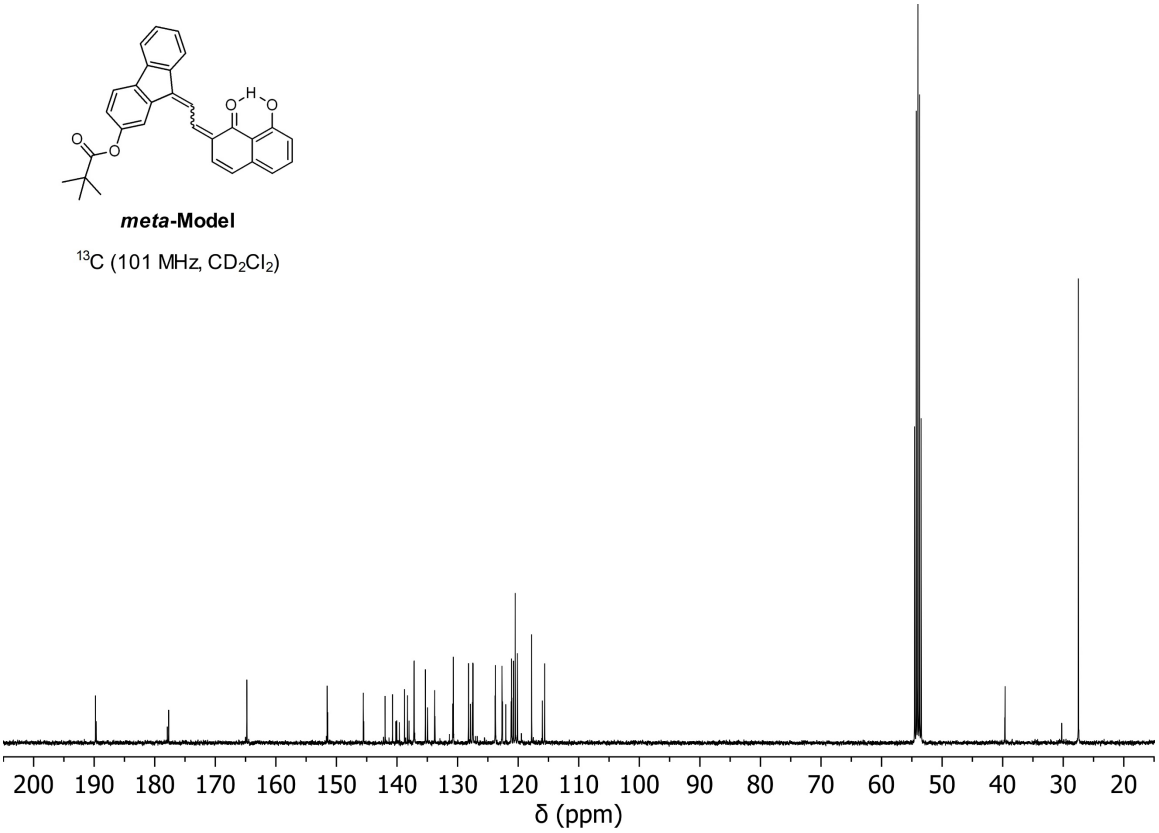
meta-Model
13C (101 MHz, CD2Cl2)
200 190 180 170 160 150 140 130 120 110 100 90 80 70 60 50 40 30 20
δ (ppm)

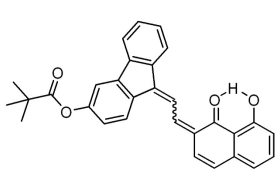

***para*-Model**

^{1}H (400 MHz, CD_2Cl_2)

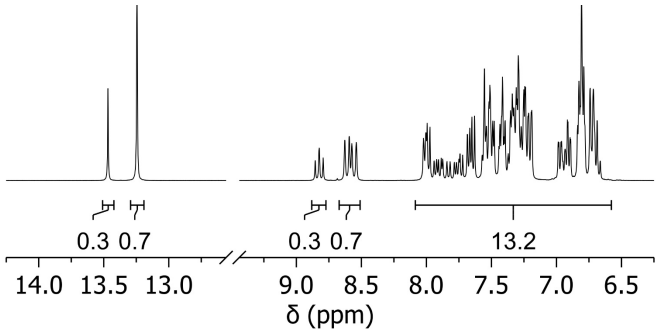

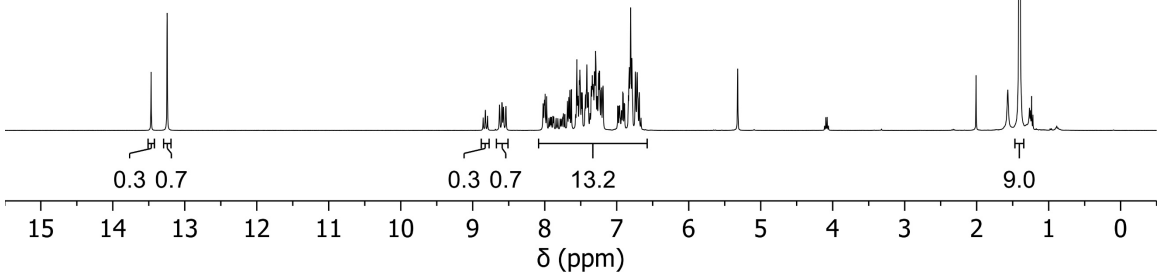

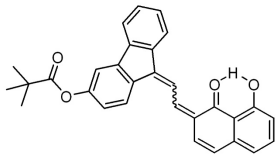

***para*-Model**

^{13}C (101 MHz, CD_2Cl_2)

References

(1) Li, J.; Nagamani, C.; Moore, J. S. Polymer Mechanochemistry: From Destructive to Productive. *Acc. Chem. Res.* **2015**, *48*, 2181–2190.

(2) Beyer, M. K.; Clausen-Schaumann, H. Mechanochemistry: The Mechanical Activation of Covalent Bonds. *Chem. Rev.* **2005**, *105*, 2921–2948.

(3) Caruso, M. M.; Davis, D. A.; Shen, Q.; Odom, S. A.; Sottos, N. R.; White, S. R.; Moore, J. S. Mechanically-Induced Chemical Changes in Polymeric Materials. *Chem. Rev.* **2009**, *109*, 5755–5798.

(4) Davis, D. A.; Hamilton, A.; Yang, J.; Cremar, L. D.; Van Gough, D.; Potisek, S. L.; Ong, M. T.; Braun, P. V.; Martínez, T. J.; White, S. R.; Moore, J. S.; Sottos, N. R. Force-Induced Activation of Covalent Bonds in Mechanoresponsive Polymeric Materials. *Nature* **2009**, *459*, 68–72.

(5) Göstl, R.; Sijbesma, R. P. π-Extended Anthracenes as Sensitive Probes for Mechanical Stress. *Chem. Sci.* **2016**, *7*, 370–375.

(6) Chen, Y.; Spiering, A. J. H.; Karthikeyan, S.; Peters, G. W. M.; Meijer, E. W.; Sijbesma, R. P. Mechanically Induced Chemiluminescence from Polymers Incorporating a 1,2-Dioxetane Unit in the Main Chain. *Nat. Chem.* **2012**, *4*, 559–562.

(7) Liu, P.; Tseng, Y.-L.; Ge, L.; Zeng, T.; Shabat, D.; Robb, M. J. Mechanically Triggered Bright Chemiluminescence from Polymers by Exploiting a Synergy between Masked 2-Furylcarbinol Mechanophores and 1,2-Dioxetane Chemiluminophores. *J. Am. Chem. Soc.* **2024**, *146*, 22151–22156.

(8) Diesendruck, C. E.; Steinberg, B. D.; Sugai, N.; Silberstein, M. N.; Sottos, N. R.; White, S. R.; Braun, P. V.; Moore, J. S. Proton-Coupled Mechanochemical Transduction: A Mechanogenerated Acid. *J. Am. Chem. Soc.* **2012**, *134*, 12446–12449.

(9) Larsen, M. B.; Boydston, A. J. "Flex-Activated" Mechanophores: Using Polymer Mechanochemistry To Direct Bond Bending Activation. *J. Am. Chem. Soc.* **2013**, *135*, 8189–8192.

(10) Hu, X.; Zeng, T.; Husic, C. C.; Robb, M. J. Mechanically Triggered Small Molecule Release from a Masked Furfuryl Carbonate. *J. Am. Chem. Soc.* **2019**, *141*, 15018–15023.

(11) Shi, Z.; Song, Q.; Göstl, R.; Herrmann, A. Mechanochemical Activation of Disulfide-Based Multifunctional Ppolymers for Theranostic Drug Release. *Chem. Sci.* **2021**, *12*, 1668–1674.

(12) Sun, Y.; Neary, W. J.; Burke, Z. P.; Qian, H.; Zhu, L.; Moore, J. S. Mechanically Triggered Carbon Monoxide Release with Turn-On Aggregation-Induced Emission. *J. Am. Chem. Soc.* **2022**, *144*, 1125–1129.

(13) Zeng, T.; Ordner, L. A.; Liu, P.; Robb, M. J. Multimechanophore Polymers for Mechanically Triggered Small Molecule Release with Ultrahigh Payload Capacity. *J. Am. Chem. Soc.* **2024**, *146*, 95–100.

(14) Chen, Z.; Mercer, J. A. M.; Zhu, X.; Romaniuk, J. A. H.; Pfattner, R.; Cegelski, L.; Martinez, T. J.; Burns, N. Z.; Xia, Y. Mechanochemical Unzipping of Insulating Polyladderene to Semiconducting Polyacetylene. *Science* **2017**, *357*, 475–479.

(15) Boswell, B. R.; Mansson, C. M. F.; Cox, J. M.; Jin, Z.; Romaniuk, J. A. H.; Lindquist, K. P.; Cegelski, L.; Xia, Y.; Lopez, S. A.; Burns, N. Z. Mechanochemical Synthesis of an Elusive Fluorinated Polyacetylene. *Nat. Chem.* **2021**, *13*, 41–46.
(16) Piermattei, A.; Karthikeyan, S.; Sijbesma, R. P. Activating Catalysts with Mechanical Force. *Nat. Chem.* **2009**, *1*, 133–137.
(17) Michael, P.; Binder, W. H. A Mechanochemically Triggered "Click" Catalyst. *Angew. Chem. Int. Ed.* **2015**, *54*, 13918–13922.
(18) Nixon, R.; De Bo, G. Three Concomitant C–C Dissociation Pathways During the Mechanical Activation of an N-Heterocyclic Carbene Precursor. *Nat. Chem.* **2020**, *12*, 826–831.
(19) McFadden, M. E.; Barber, R. W.; Overholts, A. C.; Robb, M. J. Naphthopyran Molecular Switches and Their Emergent Mechanochemical Reactivity. *Chem. Sci.* **2023**, *14*, 10041–10067.
(20) Liu, Y.; Holm, S.; Meisner, J.; Jia, Y.; Wu, Q.; Woods, T. J.; Martinez, T. J.; Moore, J. S. Flyby Reaction Trajectories: Chemical Dynamics Under Extrinsic Force. *Science* **2021**, *373*, 208–212.
(21) Hickenboth, C. R.; Moore, J. S.; White, S. R.; Sottos, N. R.; Baudry, J.; Wilson, S. R. Biasing Reaction Pathways with Mechanical Force. *Nature* **2007**, *446*, 423–427.
(22) Wang, J.; Kouznetsova, T. B.; Niu, Z.; Ong, M. T.; Klukovich, H. M.; Rheingold, A. L.; Martinez, T. J.; Craig, S. L. Inducing and Quantifying Forbidden Reactivity with Single-Molecule Polymer Mechanochemistry. *Nat. Chem.* **2015**, *7*, 323–327.
(23) Klein, I. M.; Husic, C. C.; Kovács, D. P.; Choquette, N. J.; Robb, M. J. Validation of the CoGEF Method as a Predictive Tool for Polymer Mechanochemistry. *J. Am. Chem. Soc.* **2020**, *142*, 16364–16381.
(24) Brown, C. L.; Craig, S. L. Molecular Engineering of Mechanophore Activity for Stress-Responsive Polymeric Materials. *Chem. Sci.* **2015**, *6*, 2158–2165.
(25) Konda, S. S. M.; Brantley, J. N.; Varghese, B. T.; Wiggins, K. M.; Bielawski, C. W.; Makarov, D. E. Molecular Catch Bonds and the Anti-Hammond Effect in Polymer Mechanochemistry. *J. Am. Chem. Soc.* **2013**, *135*, 12722–12729.
(26) Gossweiler, G. R.; Kouznetsova, T. B.; Craig, S. L. Force-Rate Characterization of Two Spiropyran-Based Molecular Force Probes. *J. Am. Chem. Soc.* **2015**, *137*, 6148–6151.
(27) Robb, M. J.; Kim, T. A.; Halmes, A. J.; White, S. R.; Sottos, N. R.; Moore, J. S. Regioisomer-Specific Mechanochromism of Naphthopyran in Polymeric Materials. *J. Am. Chem. Soc.* **2016**, *138*, 12328–12331.
(28) Stevenson, R.; De Bo, G. Controlling Reactivity by Geometry in Retro-Diels–Alder Reactions under Tension. *J. Am. Chem. Soc.* **2017**, *139*, 16768–16771.
(29) Wang, L.; Zheng, X.; Kouznetsova, T. B.; Yen, T.; Ouchi, T.; Brown, C. L.; Craig, S. L. Mechanochemistry of Cubane. *J. Am. Chem. Soc.* **2022**, *144*, 22865–22869.
(30) Ding, S.; Wang, W.; Germann, A.; Wei, Y.; Du, T.; Meisner, J.; Zhu, R.; Liu, Y. Bicyclo[2.2.0]hexene: A Multicyclic Mechanophore with Reactivity Diversified by External Forces. *J. Am. Chem. Soc.* **2024**, *146*, 6104–6113.
(31) Kryger, M. J.; Munaretto, A. M.; Moore, J. S. Structure–Mechanochemical Activity Relationships for Cyclobutane Mechanophores. *J. Am. Chem. Soc.* **2011**, *133*, 18992–18998.

(32) Flear, E. J.; Horst, M.; Yang, J.; Xia, Y. Force Transduction Through Distant Force-Bearing Regioisomeric Linkages Affects the Mechanochemical Reactivity of Cyclobutane. *Angew. Chem. Int. Ed.* **2024**, *63*, e202406103.
(33) Klukovich, H. M.; Kouznetsova, T. B.; Kean, Z. S.; Lenhardt, J. M.; Craig, S. L. A Backbone Lever-Arm Effect Enhances Polymer Mechanochemistry. *Nat. Chem.* **2013**, *5*, 110–114.
(34) Wang, J.; Kouznetsova, T. B.; Kean, Z. S.; Fan, L.; Mar, B. D.; Martínez, T. J.; Craig, S. L. A Remote Stereochemical Lever Arm Effect in Polymer Mechanochemistry. *J. Am. Chem. Soc.* **2014**, *136*, 15162–15165.
(35) Huang, W.; Zhu, Z.; Wen, J.; Wang, X.; Qin, M.; Cao, Y.; Ma, H.; Wang, W. Single Molecule Study of Force-Induced Rotation of Carbon–Carbon Double Bonds in Polymers. *ACS Nano* **2017**, *11*, 194–203.
(36) Beyer, M. K. The Mechanical Strength of a Covalent Bond Calculated by Density Functional Theory. *J. Chem. Phys.* **2000**, *112*, 7307–7312.
(37) Young, H. D.; Zemansky, M. W.; Sears, F. W.; Freedman, R. A.; Ford, A. L. Sears & Zemansky's University Physics with Modern Physics. Fifteenth edition, extended edition. Always learning; Pearson: Harlow, Essex, 2020.
(38) May, P. A.; Moore, J. S. Polymer Mechanochemistry: Techniques to Generate Molecular Force via Elongational Flows. *Chem. Soc. Rev.* **2013**, *42*, 7497.
(39) Lenhardt, J. M.; Black Ramirez, A. L.; Lee, B.; Kouznetsova, T. B.; Craig, S. L. Mechanistic Insights into the Sonochemical Activation of Multimechanophore Cyclopropanated Polybutadiene Polymers. *Macromolecules* **2015**, *48*, 6396–6403.
(40) McFadden, M. E.; Robb, M. J. Generation of an Elusive Permanent Merocyanine via a Unique Mechanochemical Reaction Pathway. *J. Am. Chem. Soc.* **2021**, *143*, 7925–7929.
(41) Osler, S. K.; McFadden, M. E.; Zeng, T.; Robb, M. J. Mechanochemical Reactivity of a Multimodal 2*H*-Bis-Naphthopyran Mechanophore. *Polym. Chem.* **2023**, *14*, 2717–2723.
(42) McFadden, M. E.; Overholts, A. C.; Osler, S. K.; Robb, M. J. Validation of an Accurate and Expedient Initial Rates Method for Characterizing Mechanophore Reactivity. *ACS Macro Lett.* **2023**, *12*, 440–445.
(43) Overholts, A. C.; Robb, M. J. Examining the Impact of Relative Mechanophore Activity on the Selectivity of Ultrasound-Induced Mechanochemical Chain Scission. *ACS Macro Lett.* **2022**, *11*, 733–738.
(44) Lee, B.; Niu, Z.; Wang, J.; Slebodnick, C.; Craig, S. L. Relative Mechanical Strengths of Weak Bonds in Sonochemical Polymer Mechanochemistry. *J. Am. Chem. Soc.* **2015**, *137*, 10826–10832.
(45) Kucharski, T. J.; Huang, Z.; Yang, Q.; Tian, Y.; Rubin, N. C.; Concepcion, C. D.; Boulatov, R. Kinetics of Thiol/Disulfide Exchange Correlate Weakly with the Restoring Force in the Disulfide Moiety. *Angew. Chem. Int. Ed.* **2009**, *48*, 7040–7043.
(46) Groote, R.; Szyja, B. M.; Leibfarth, F. A.; Hawker, C. J.; Doltsinis, N. L.; Sijbesma, R. P. Strain-Induced Strengthening of the Weakest Link: The Importance of Intermediate Geometry for the Outcome of Mechanochemical Reactions. *Macromolecules* **2014**, *47*, 1187–1192.
(47) Ribas-Arino, J.; Shiga, M.; Marx, D. Understanding Covalent Mechanochemistry. *Angew. Chem. Int. Ed.* **2009**, *48*, 4190–4193.

(48) Sun, Y.; Kevlishvili, I.; Kouznetsova, T. B.; Burke, Z. P.; Craig, S. L.; Kulik, H. J.; Moore, J. S. The Tension-Activated Carbon–Carbon Bond. *Chem.* **2024**, *10*, 3055–3066.
(49) O'Neill, R. T.; Boulatov, R. Experimental Quantitation of Molecular Conditions Responsible for Flow-Induced Polymer Mechanochemistry. *Nat. Chem.* **2023**, *15*, 1214–1223.
(50) Wang, J.; Kouznetsova, T. B.; Niu, Z.; Rheingold, A. L.; Craig, S. L. Accelerating a Mechanically Driven *anti* -Woodward–Hoffmann Ring Opening with a Polymer Lever Arm Effect. *J. Org. Chem.* **2015**, *80*, 11895–11898.
(51) Wang, Z.; Craig, S. L. Stereochemical Effects on the Mechanochemical Scission of Furan–Maleimide Diels–Alder Adducts. *Chem. Commun.* **2019**, *55*, 12263–12266.
(52) Klein, I. M.; Husic, C. C.; Kovács, D. P.; Choquette, N. J.; Robb, M. J. Validation of the CoGEF Method as a Predictive Tool for Polymer Mechanochemistry. *J. Am. Chem. Soc.* **2020**, *142*, 16364–16381.
(53) Osler, S. K.; McFadden, M. E.; Zeng, T.; Robb, M. J. Mechanochemical Reactivity of a Multimodal 2*H*-Bis-Naphthopyran Mechanophore. *Polym. Chem.* **2023**, *14*, 2717–2723.
(54) Nguyen, N. H.; Rosen, B. M.; Lligadas, G.; Percec, V. Surface-Dependent Kinetics of Cu(0)-Wire-Catalyzed Single-Electron Transfer Living Radical Polymerization of Methyl Acrylate in DMSO at 25 °C. *Macromolecules* **2009**, *42*, 2379–2386.
(55) Yang, J.; Horst, M.; Werby, S. H.; Cegelski, L.; Burns, N. Z.; Xia, Y. Bicyclohexene-peri-naphthalenes: Scalable Synthesis, Diverse Functionalization, Efficient Polymerization, and Facile Mechanoactivation of Their Polymers. *J. Am. Chem. Soc.* **2020**, *142*, 14619–14626.
(56) Overholts, A. C.; McFadden, M. E.; Robb, M. J. Quantifying Activation Rates of Scissile Mechanophores and the Influence of Dispersity. *Macromolecules* **2022**, *55*, 276–283.
(57) Berkowski, K. L.; Potisek, S. L.; Hickenboth, C. R.; Moore, J. S. Ultrasound-Induced Site-Specific Cleavage of Azo-Functionalized Poly(ethylene glycol). *Macromolecules* **2005**, *38*, 8975–8978.
(58) Aiken, S.; Booth, K.; Gabbutt, C. D.; Mark Heron, B.; Rice, C. R.; Charaf-Eddin, A.; Jacquemin, D. The First Structural and Spectroscopic Characterisation of a Ring-Opened Form of a 2*H*-Naphtho[1,2-b]pyran: A Novel Photomerocyanine. *Chem. Commun.* **2014**, *50*, 7900.
(59) McFadden, M. E.; Osler, S. K.; Sun, Y.; Robb, M. J. Mechanical Force Enables an Anomalous Dual Ring-Opening Reaction of Naphthodipyran. *J. Am. Chem. Soc.* **2022**, *144*, 22391–22396.
(60) Demadrille, R.; Rabourdin, A.; Campredon, M.; Giusti, G. Spectroscopic Characterisation and Photodegradation Studies of Photochromic Spiro[fluorene-9,3′-[3′H]-naphtho[2,1-b]pyrans]. *J. Photochem. Photobiol. A* **2004**, *168*, 143–152.
(61) Klukovich, H. M.; Kouznetsova, T. B.; Kean, Z. S.; Lenhardt, J. M.; Craig, S. L. A Backbone Lever-Arm Effect Enhances Polymer Mechanochemistry. *Nat. Chem.* **2013**, *5*, 110–114.
(62) Neese, F. Software update: The ORCA program system—Version 5.0. *WIREs Comput Mol Sci* **2022**, *12*, e1606.

(63) Becke, A. D. Density-Functional Thermochemistry. I. The Effect of the Exchange-Only Gradient Correction. *J. Chem. Phys.* **1992**, *96*, 2155–2160.
(64) Stephens, P. J.; Devlin, F. J.; Chabalowski, C. F.; Frisch, M. J. Ab Initio Calculation of Vibrational Absorption and Circular Dichroism Spectra Using Density Functional Force Fields. *J. Phys. Chem.* **1994**, *98*, 11623–11627.
(65) Lee, C.; Yang, W.; Parr, R. G. Development of the Colle-Salvetti Correlation-Energy Formula into a Functional of the Electron Density. *Phys. Rev. B* **1988**, *37*, 785–789.
(66) Grimme, S.; Antony, J.; Ehrlich, S.; Krieg, H. A Consistent and Accurate *Ab Initio* Parametrization of Density Functional Dispersion Correction (DFT-D) for the 94 Elements H-Pu. *J. Chem. Phys.* **2010**, *132*, 154104.
(67) Sun, Y.; Kevlishvili, I.; Kouznetsova, T. B.; Burke, Z. P.; Craig, S. L.; Kulik, H. J.; Moore, J. S. The Tension-Activated Carbon–Carbon Bond. *Chem.* **2024**, *10*, 3055–3066.
(68) Ribas-Arino, J.; Shiga, M.; Marx, D. Understanding Covalent Mechanochemistry. *Angew. Chem. Int. Ed.* **2009**, *48*, 4190–4193.

Chapter 4

Strain-Dependent Multicolor Mechanochromism of 3*H*-Bis-Naphthopyran in Solid Polymeric Materials

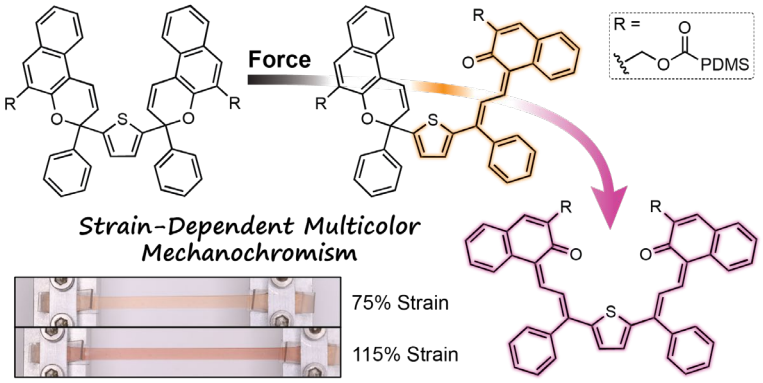

This chapter has been adapted with permission from Osler, S. K.; Conner, A.V.; McFadden, M. E.; Robb, M. J. Strain-Dependent Multicolor Mechanochromism of 3*H*-Bis-Naphthopyran in Solid Polymeric Materials. *Chem. Sci*. **2025**, DOI: 10.1039/D5SC05757D.

Abstract

Multimodal mechanophores are important targets for the design of complex stress-sensing materials due to their multicolor mechanochromic properties, which potentially enable discrete visual outputs under varying levels of stress and/or strain. We have developed a novel 3H-bis-naphthopyran mechanophore that imbues solid polymeric materials with force-dependent colorimetric sensing capabilities. Polydimethylsiloxane (PDMS) elastomers incorporating a 3*H*-bis-naphthopyran crosslinker were synthesized and deformed under uniaxial tension. The relative distribution of two distinctly colored merocyanine dyes is systematically biased under varying levels of applied stress and/or

strain, resulting in the appearance of distinct coloration, which is characterized by pronounced changes in visible absorption spectra. This work demonstrates that judiciously designed bis-naphthopyran mechanophores can function as force sensors that visually report on the magnitude of applied force in elastomeric materials.

Introduction

Mechanophores are stress-sensitive molecules that undergo specific and productive chemical transformations in response to mechanical force.[1] Force is transduced to mechanophores by covalently attached polymer chains.[2,3] Mechanochromic mechanophores couple a colorimetric output, i.e., a visible color change, with force-induced chemical reactions to function as molecular force probes. Mechanochromic mechanophores that undergo reversible color changes in response to mechanical activation enable the detection of stress and/or strain in polymeric materials and have potential applications in patterning, data storage, and damage sensing. A rich library of mechanochromic mechanophores have been developed with applications in bulk materials for stress detection including derivatives of naphthopyran,[4] spiropyran,[5] spirothiopyran,[6] oxazine,[7] diarylbibenzofuranone,[8,9] and rhodamine.[10,11] Our group has dedicated significant effort to the development of naphthopyran force probes, which we have identified as a privileged class of mechanochromic mechanophores due to their synthetic accessibility and structural and functional modularity.[12]

Naphthopyran mechanophores undergo a ring-opening reaction to generate highly colored merocyanine dyes in response to mechanical force.[12] Mechanochemical activation of naphthopyran derivatives has been achieved using ultrasonication in solution,[13–16] and in bulk materials under tensile and compressive stress.[4,13–15,17] We have been particularly

interested in multimodal naphthopyran mechanophores that contain multiple pyran reactive sites, as these molecules provide access to distinct states that are coupled to unique absorption properties, and therefore visual signals.[18] Multimodal bis-naphthopyran[19,20] and naphthodipyran[21] mechanophores exhibit multicolor mechanochromism in solution-phase ultrasonication experiments, displaying varying coloration as a function of force or ultrasound exposure, respectively. However, multicolor mechanochromism from naphthopyran mechanophores has not been achieved to date in bulk materials. In a few examples, stress and/or strain-dependent multicolor mechanochromism has been demonstrated in bulk materials that incorporate two distinct mechanophores.[22–25] These dual mechanophore systems typically capitalize on either the unique mechanical properties within different regions of multi-material networks or polymer blends, and/or the distinct reversion behavior of the mechanophores to achieve a multicolor response. Significantly, demonstrations of gradient multicolor mechanochromism from a single mechanophore in bulk materials are so far limited to non-covalent systems. Sommer and coworkers reported the torsional spring mechanophore, which exhibits subtle but well-defined changes in absorption wavelength as a function of applied stress.[26,27] Mechanophores that display stress-dependent changes in fluorescence emission have also been described, however, they require irradiation with UV light for detection and are not easily observable by the naked eye.[28–30] Polymeric materials that incorporate multimodal naphthopyrans are theoretically capable of distinguishing between varying mechanical loads through discreet visual signals and remain a highly desirable research target in the field of polymer mechanochemistry.

We previously reported a 3*H*-bis-naphthopyran mechanophore that combines two naphthopyran subunits linked to a central thiophene ring (Scheme 4.1).[19] Photochemical or

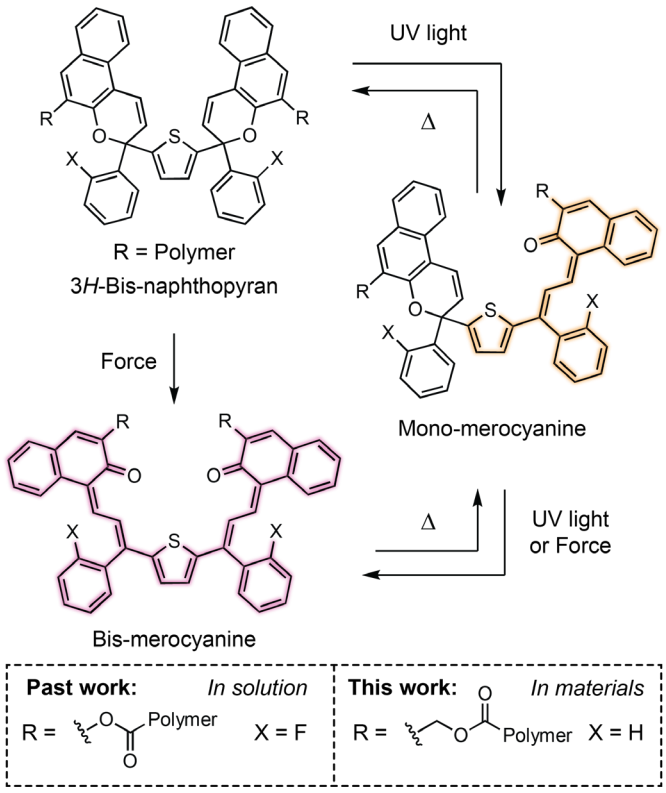

Scheme 4.1. Mechanochemical and photochemical reactivity of 3*H*-bis-naphthopyran mechanophores.

mechanochemical activation of this 3*H*-naphthopyran compound generates interconverting mono- and bis-merocyanine isomers that display yellow and purple coloration, respectively. Whereas photochemical activation with UV light promotes sequential ring-opening reactions to generate mono-merocyanine and then bis-merocyanine dyes,[31–33] ultrasound-induced mechanochemical activation results in the generation of the purple-colored bis-merocyanine dye directly from the fully ring-closed bis-naphthopyran.[19] Under these conditions, the yellow-colored mono-merocyanine product is generated exclusively from the thermal cycloreversion of the bis-merocyanine. Force-dependent multicolor mechanochromism in solution is achieved via a dynamic equilibrium that is established by the relative rates of force-induced ring-opening and thermal cycloreversion; the position of this equilibrium depends on the magnitude of force applied to the mechanophore, which is dictated by the length of the attached polymer chain.[19,34] Unfortunately, incorporating this particular bis-naphthopyran mechanophore into bulk materials results in significant background coloration and has impeded research toward successful solid-state applications in our laboratory.

Results and Discussion

Here, we report a novel 3*H*-bis-naphthopyran mechanophore that achieves force-dependent multicolor mechanochromism in crosslinked polydimethylsiloxane (PDMS) elastomers subjected to varying loads under uniaxial tension. Key to this advance is the judicious incorporation of structural features on the 3*H*-bis-napthopyran scaffold that increase the force-free rate of cycloreversion from the merocyanine states. In direct contrast, our previously studied bis-naphthopyran mechanophore incorporated substituents, including *ortho*-fluoro groups and aryl ester linkages, designed to increase the lifetime of the merocyanine species and enhance their accumulation in solution.[19,32,35] Eliminating the *ortho*-fluoro substituents and incorporating a methylene spacer at the polymer attachment position on the naphthopyran core significantly reduces undesired background coloration in PDMS materials (see Scheme 4.1).[17] Enabled by these structural modifications, we hypothesized that increasing tension applied to a polymer network incorporating 3*H*-bis-naphthopyran crosslinks would systematically bias the mechanostationary state[36] comprising different concentrations of the two uniquely colored merocyanine products. While individual strands in bulk networks experience a distribution of forces due to network inhomogeneity,[37] the fraction of strands experiencing greater force is anticipated to increase as a function of increasing tensile load. Therefore, for an elastomer that incorporates 3*H*-bis-napthopyran crosslinkers, we expect to observe a product distribution that favors the yellow-colored mono-merocyanine product at low strain values and the purple-colored bis-merocyanine species as applied tension is increased, resulting in an overall graded change in appearance from yellow to purple.

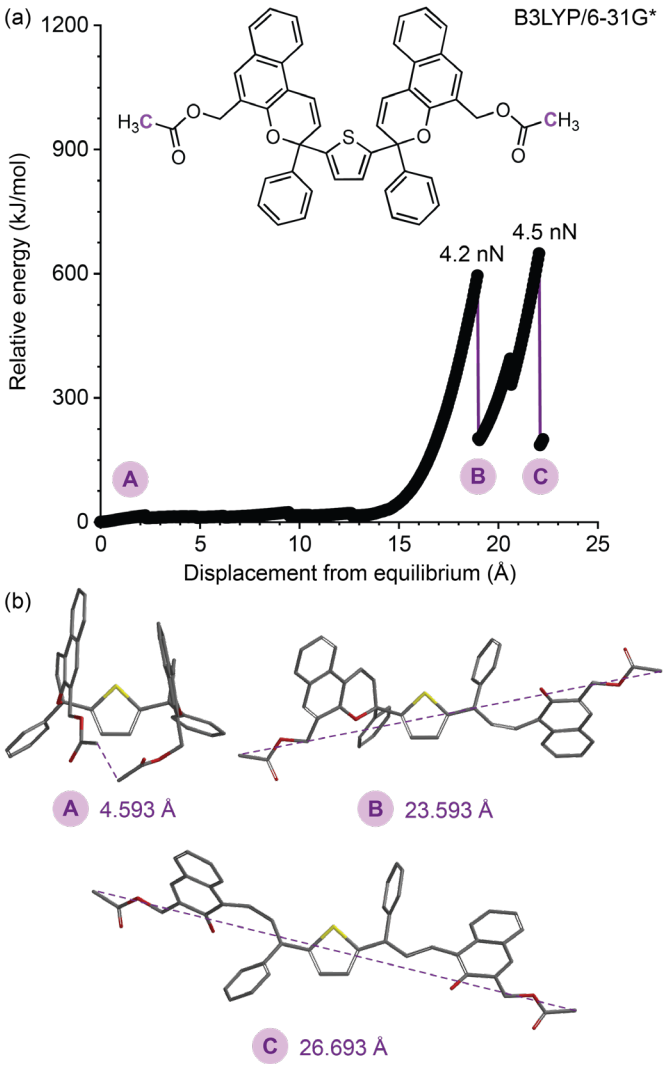

Figure 4.1. CoGEF calculations performed on 3*H*-bis-naphthopyran. (a) Density functional theory (DFT) calculations using the constrained geometries simulate external force (CoGEF) method performed on a truncated model of the 3*H*-bis-naphthopyran mechanophore predict the expected ring-opening reactions to generate mono-merocyanine and bis-merocyanine products. Calculations were performed at the B3LYP/6-31G* level of theory. (b) The corresponding computed structures of the truncated molecule at various points of elongation are shown along with the associated constraint distance between the terminal carbon atoms. Data for the (R,S) diastereomer is included in the Experimental Details section.

To assess the mechanochemical reactivity of the novel 3*H*-bis-naphthopyran, we performed preliminary density functional theory (DFT) calculations using the constrained geometries simulate external force (CoGEF) method[38,39] on a truncated model at the B3LYP/6-31G* level of theory (Figure 4.1). The 3*H*-bis-naphthopyran molecule is predicted to undergo a single ring-opening reaction to generate mono-merocyanine at a maximum rupture force (F_{max}) of 4.2 nN. Further mechanical elongation is predicted to facilitate the second ring-opening reaction at a rupture force of 4.5 nN to generate the bis-merocyanine product. While data for the (R,S) diastereomer are shown in Figure 4.1, the (S,S) diastereomer is also predicted to undergo similar

sequential ring-opening reactions (Figure S4.5). The calculated F_{max} values, which provide a relative measure of the force sensitivity of a mechanophore,[38] are comparable to the F_{max} values calculated for the previously studied 3*H*-bis-naphthopyran mechanophore.[19]

We initially performed solution phase photoirradiation experiments to understand the absorption changes that accompany the ring-opening reactions of the novel 3*H*-bis-naphthopyran mechanophore. With the ultimate goal of incorporating the mechanophore into PDMS elastomers via standard hydrosilylation chemistry (*vide infra*), we synthesized small molecule 3*H*-bis-naphthopyran crosslinker **BNP** functionalized with terminal vinyl groups (Figure 4.2a). A solution of **BNP** (8 μg/mL in THF, 30 mM BHT) was irradiated with UV light (λ = 311 nm) for 15 min at −78 °C and ultraviolet–visible (UV–vis) absorption spectra were acquired using a spectrometer equipped with a cryostat to characterize merocyanine accumulation (Figure 4.2b, see the Experimental Details section). The results are consistent with previous studies that demonstrate sequential ring-opening reactions under UV light for bis-naphthopyran derivatives.[19,31–33] At

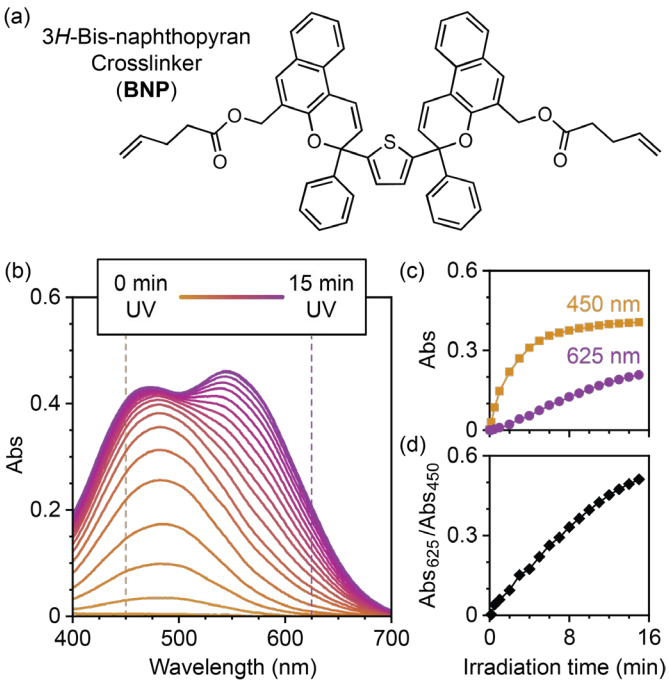

Figure 4.2. Photoirradiation of a 3*H*-bis-naphthopyran small molecule in solution. (a) Structure of the 3*H*-bis-naphthopyran crosslinker (**BNP**) used in this study. (b) UV-vis absorption spectra acquired during the photoirradiation (311 nm, 15 min) of a solution of **BNP** in THF (8 μg/mL, 30 mM BHT, −78 °C). (c) Absorbance at 450 nm and 625 nm as a function of photoirradiation time. (d) Ratio of the absorbance at 625 nm and 450 nm as a function of irradiation time.

early irradiation times, the absorption spectrum is dominated by a feature with an absorption maximum at ~480 nm, consistent with the initial generation of the yellow-colored mono-merocyanine species. Extended photoirradiation causes the accumulated mono-merocyanine to undergo a second ring-opening reaction to generate the bis-merocyanine product, which is accompanied by a bathochromic shift in the absorption spectrum and the emergence of an optical feature with an absorption maximum at ~560 nm, consistent with the extended conjugation of the bis-merocyanine dye. To provide additional insight into the relative rates of mono- and bis-merocyanine formation, the absorbance at characteristic wavelengths of 450 nm and 625 nm were monitored over the course of the photoirradiation experiment (Figure 4.2c). Monitoring at 625 nm allows for the selective detection of the bis-merocyanine species. The absorbance at 450 nm increases rapidly at early irradiation times and approaches a plateau, while the absorbance at 625 nm increases slowly early in the experiment and then steadily increases during prolonged exposure to UV light. Importantly, the ratio of absorbance values at 625 nm and 450 nm increases over the duration of the photoirradiation experiment, reflecting the changing distribution of mono- and bis-merocyanine products (Figure 4.2d). We note that the photochemically generated mono-merocyanine and bis-merocyanine dyes are stable at −78 °C in solution; however, thermal reversion is observed at 20 °C (Figure S4.6). Photoirradiation of **BNP** at 20 °C does not result in the accumulation of any significant amount of the bis-merocyanine dye, presumably due to rapid thermal reversion at elevated temperatures (Figure S4.7).[32]

To investigate the mechanochemical reactivity of the 3*H*-bis-naphthopyran mechanophore in bulk materials, we incorporated **BNP** (~0.8 wt% loading) into PDMS elastomers via Pt-catalyzed hydrosilylation[40] to yield **BNP-PDMS**. Uniaxial tension was

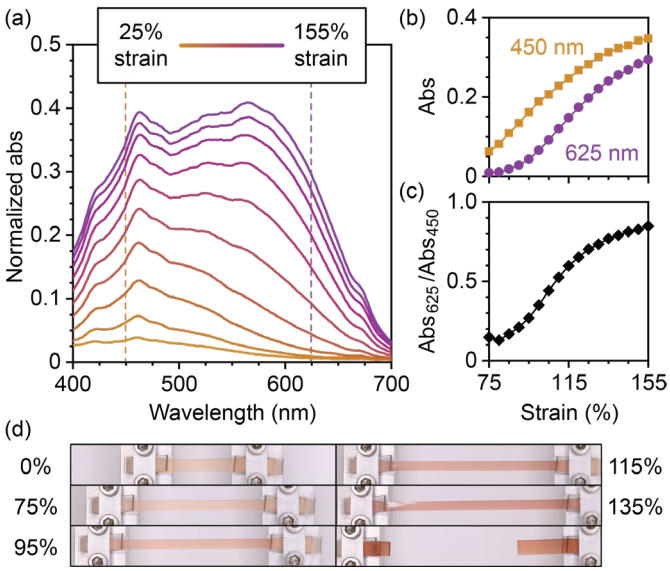

Figure 4.3. Tensile experiments performed on samples of **BNP-PDMS**. (a) Normalized UV-vis absorption spectra acquired during uniaxial tensile loading of **BNP-PDMS**. (b) Absorbance at 450 nm and 625 nm as a function of strain. (c) Ratio of the absorbance at 625 nm versus 450 nm as a function of strain. (d) Photographs of a different sample of **BNP-PDMS** at various strain values. The sample failed between 135 and 140% strain.

applied to samples of **BNP-PDMS** using a load frame while in-line UV–vis absorption measurements were recorded to monitor the strain-dependent changes in absorption (Figure 4.3a**,** see Experimental Details section). The absorbance values at 450 nm and 625 nm were monitored during tensile experiments to investigate how the relative populations of mono-merocyanine and bis-merocyanine products vary as a function of mechanical loading (Figure 4.3b). At low strain values, the absorption spectrum is dominated by shorter wavelength features (400–550 nm), consistent with a merocyanine population that is enriched in the yellow-colored mono-merocyanine species. As the strain is increased, absorption at longer wavelengths (>550 nm) increases monotonically, indicating that the bis-merocyanine species is accumulating at increasing concentrations with higher mechanical loading. The relative population of merocyanine species is increasingly biased toward the bis-merocyanine product at higher strain values, which is reflected in the ratio of the absorbance values at 625 nm and 450 nm over the course of the tensile loading experiment (Figure 4.3c). Photographs of a separate sample of **BNP-PDMS** that was subjected to identical uniaxial tensile loading illustrate the force-dependent variation in color that results

from the varying composition of merocyanine species at discrete strain values (Figure 4.3d and Figure S4.8). We note that these results do not necessarily distinguish between two potential activation pathways whereby the bis-merocyanine species is generated either directly from the bis-naphthopyran mechanophore, or by the mechanochemical activation of intermediate mono-merocyanine species in a stepwise process. Ongoing work in our group is focused on understanding the mechanism of activation of multimodal naphthopyran mechanophores.

The reproducibility of the strain-dependent multicolor mechanochromic response of PDMS elastomers incorporating the 3*H*-bis-naphthopyran mechanophore was investigated by performing similar tensile loading experiments on three separate samples of **BNP-PDMS** (Figure S4.9). In each case, increasing strain is accompanied by a bathochromic expansion in the overall absorption spectrum. Accumulation of the yellow-colored mono-merocyanine product is consistently favored at low strain, whereas increasing concentration of the purple-colored merocyanine dye is observed with increasing tensile loading. We also performed replicate tensile loading experiments on a single sample to investigate the repeatability of the force-sensing performance. A specimen of **BNP-PDMS** was subjected to uniaxial tension to a strain of 120% and then allowed to relax in the dark for 1 h. The sample was then subjected to a second tensile loading, which revealed nearly identical changes in absorption as a function of strain (Figure S4.9). Together, these results demonstrate that elastomers incorporating the 3*H*-bis-naphthopyran molecular force sensor exhibit reproducible and repeatable changes in color in response to varying mechanical loads. To confirm the mechanical origin of the observed behavior, a control PDMS network (**Control-PDMS**) incorporating a 3*H*-bis-naphthopyran mechanophore functionalized with a single terminal

alkene group (~0.8 wt % loading) was synthesized and subjected to uniaxial tension (see Experimental Details section). As expected, deformation of **Control-PDMS** under uniaxial tension does not result in any strain-dependent changes in color; critically, the ratio of absorbance at 625 nm and 450 nm remains constant over the course of the tensile loading experiment (Figures S4.10 and S4.11). This result demonstrates that the generation of mono- and bis-merocyanine dyes observed upon tensile loading **BNP-PDMS** requires force to be transduced across the 3*H*-bis-naphthopyran crosslinkers.

To further interrogate the multicolor mechanochromic behavior of the bis-naphthopyran mechanophore, a sample of **BNP-PDMS** was loaded to a constant strain and absorption spectra were recorded continuously to characterize the time-dependent changes in merocyanine distribution (Figure S4.12). The specimen was first loaded to 90% strain and held in tension for 1 h. An increase in the overall visible absorption is observed during this period at constant strain; the ratio of the absorbance at 625 and 450 nm increases asymptotically to approach a constant value, consistent with an increase in the relative population of the bis-merocyanine species. Upon further increasing the strain of the sample to 120%, a similar increase in absorption is observed with the ratio of the absorbance at 625 and 450 nm again increasing to achieve a new plateau value, suggesting another shift in the equilibrium to favor additional accumulation of the bis-merocyanine species. Merocyanine reversion is not observed to any significant extent while the specimen is maintained in tension, even upon photoirradiation with white light, which is routinely used to facilitate the reversion of naphthopyran-derived merocyanine dyes (Figure S4.13).[12] The mechanochemical activation of bis-naphthopyran in bulk materials therefore contrasts the previously observed solution-phase behavior, wherein ultrasound-induced mechanical

activation of bis-naphthopyran rapidly establishes a dynamic equilibrium between mono- and bis-merocyanine products that results from competing rates of bis-merocyanine formation and thermal reversion.[19] Notably, attenuation of the absorption spectrum occurs rapidly after a sample of **BNP-PDMS** maintained at 90% strain is relaxed to its original length, reflecting the transience of the merocyanine products in the absence of an applied force of tension (Figure S4.14).

Similar to the solution-phase results presented earlier, the differences between the photochemical and mechanochemical reactivity of the 3*H*-bis-naphthopyran mechanophore are readily apparent in PDMS materials. A sample of **BNP-PDMS** was irradiated with UV light (λ = 311 nm) for 300 s at room temperature and absorption spectra were acquired to monitor merocyanine accumulation (Figure 4.4a). The absorption spectrum is dominated by a peak with a maximum at ~480 nm that increases in intensity with longer exposure to UV light, indicating that the distribution of photochemically generated merocyanine species strongly favors the mono-merocyanine product. Photoirradiation does not result in any significant accumulation of the bis-merocyanine product due to fast thermal reversion at room temperature, even in the solid state.[19,32] We note that

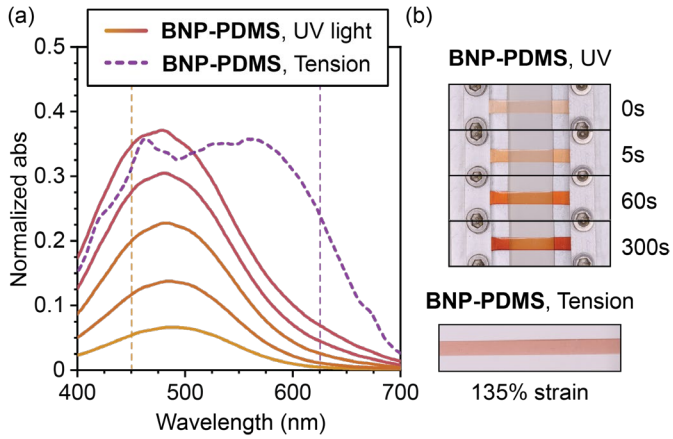

Figure 4.4. Photoirradiation vs. mechanical activation of **BNP-PDMS**. (a) Absorption spectra of **BNP-PDMS** after 5 s, 30 s, 60 s, 120 s, and 300 s of photoirradiation with 311 nm UV light compared to a sample of **BNP-PDMS** at 135% strain. (b) Photographs of **BNP-PDMS** after 0 s, 5 s, 60 s, and 300 s of photoirradiation with UV light compared to a sample of **BNP-PDMS** at 135% strain.

photodegradation and an overall decrease in visible absorption was observed upon extended UV photoirradiation (Figure S4.15). The photochromic behavior of **BNP-PDMS** contrasts strongly with the mechanochromic properties of the material, which exhibits significant absorption at wavelengths up to ~700 nm upon mechanical loading to 135% strain. These differences in the merocyanine dye composition generated with either UV light or mechanical loading are readily observable by the naked eye (Figure 4.4b). Samples of **BNP-PDMS** appear red-orange in color after exposure to UV light, whereas **BNP-PDMS** samples loaded in tension appear purple-red, consistent with the longer wavelength absorption observed spectroscopically that accompanies bis-merocyanine formation.

Conclusions

In summary, we have developed a novel multimodal 3*H*-bis-naphthopyran mechanophore that displays force-dependent multicolor mechanochromic behavior in bulk polymeric materials. Polydimethylsiloxane (PDMS) elastomers incorporating a judiciously designed 3*H*-bis-naphthopyran mechanophore as a crosslinker were subjected to uniaxial tensile loading and the mechanochromic properties were characterized by UV-vis absorption spectroscopy as a function of strain. A significant bathochromic shift in the overall absorption is observed upon increasing strain applied to the materials as a result of force-dependent variation in the accumulative distribution of distinctly colored merocyanine products. At low strain, the product distribution is dominated by the yellow-colored mono-merocyanine species, while higher strains increasingly bias the population toward the purple-colored bis-merocyanine species. The strain-dependent changes in color are clearly observed in the gauge region of the PDMS elastomers at varying levels of mechanical loading. This study introduces a bis-naphthopyran mechanophore that functions as a molecular force

sensor that is capable of distinguishing between different magnitudes of force through discreet colorimetric signals in solid polymeric materials.

Acknowledgements

Financial support from an NSF CAREER Award (CHE-2145791) is gratefully acknowledged. We thank the Center for Catalysis and Chemical Synthesis of the Beckman Institute at Caltech for access to equipment. We thank the Peters laboratory at Caltech for use of their UV-vis spectrometer. M.J.R. gratefully acknowledges the Alfred P. Sloan Foundation for a Sloan Research Fellowship and the Camille and Henry Dreyfus Foundation for a Camille Dreyfus Teacher-Scholar Award.

Experimental Details

I. General Experimental Details

Reagents from commercial sources were used without further purification unless otherwise stated. Dry THF was obtained from a Pure Process Technology solvent purification system. All reactions were performed under a N_2 or argon atmosphere unless specified otherwise. Column chromatography was performed on a Biotage Isolera system using SiliCycle SiliaSep HP flash cartridges.

NMR spectra were recorded using a 400 MHz Bruker Avance III HD with Prodigy Cryoprobe. All ^{1}H NMR spectra are reported in δ units, parts per million (ppm), and were measured relative to the signals for residual acetone (2.05 ppm) or chloroform (7.26 ppm) in deuterated solvent. All ^{13}C NMR spectra were measured in deuterated solvents and are reported in ppm relative to the signals for acetone (206.26 ppm) or chloroform (77.16 ppm).

Multiplicity and qualifier abbreviations are as follows: s = singlet, d = doublet, t = triplet, q = quartet, m = multiplet, br = broad, app = apparent.

High resolution mass spectra (HRMS) were obtained via either by direct injection on an Agilent 1260 Infinity II Series HPLC coupled to a 6230 LC/TOF system in electrospray ionization (ESI+) mode or a JEOL JMS-T2000GC AccuTOF GC Alpha operating in field desorption mode. UV-vis absorption spectra were recorded on either a Thermo Scientific Evolution 220 spectrometer or a Cary 60 spectrometer equipped with an Unisoku cryostat. Tensile experiments were performed using a manually operated Velmex load frame (left-right screw drive model). Digital photographs of PDMS materials were acquired using a Canon Rebel SL3 digital camera with a 100 mm macro lens and are uncorrected. Photoirradiation with UV light was performed using a Philips PL-S 9W/01/2P UVB bulb with a narrow emission of 305–315 nm and a peak at 311 nm under ambient conditions unless indicated otherwise. Photoirradiation with white light was carried out using a 13 W broadband fluorescent lamp (Bayco Model BA-506) filtered through a 425 nm bandpass filter.

Reagents 3-(hydroxymethyl)naphthalen-2-ol[17] and 1,1′-(thiophene-2,5-diyl)bis(1-phenylprop-2-yn-1-ol)[20] were synthesized as previously reported.

II. Supplementary Figures

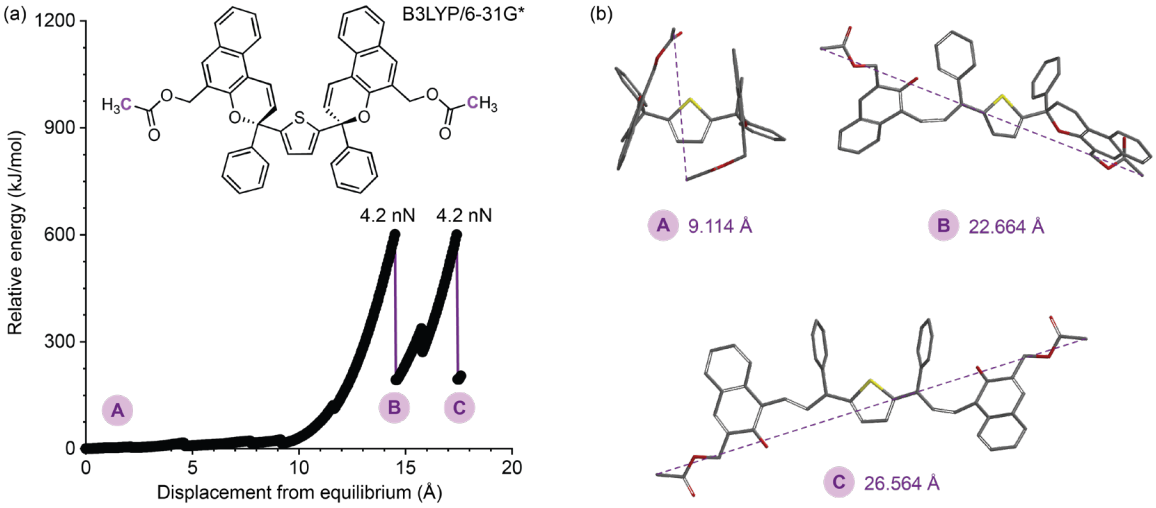

Figure S4.5. CoGEF calculations performed on 3*H*-bis-naphthopyran. (a) Density functional theory (DFT) calculations using the constrained geometries simulate external force (CoGEF) method performed on a truncated model of (S,S)-3*H*-bis-naphthopyran predict the expected ring-opening reactions to generate mono-merocyanine and bis-merocyanine products. (b) The corresponding computed structures of the truncated molecule at various points of elongation are shown along with the associated constraint distance between the terminal carbon atoms. See Section V for details.

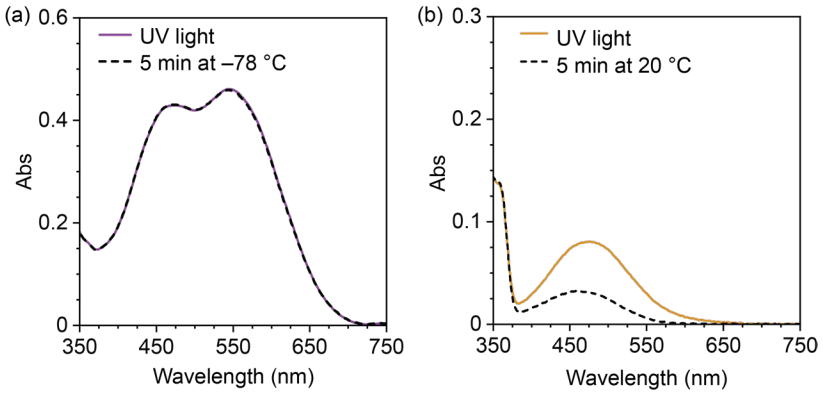

Figure S4.6. Absorption spectra of **BNP** (8 μg/mL in THF with 30 mM BHT) acquired immediately following irradiation with UV light (311 nm) at either (a) −78 °C or (b) 20 °C (solid colored traces). No reversion is observed at −78 °C, while reversion at 20 °C is significant (dashed black traces). See Section VII for details.

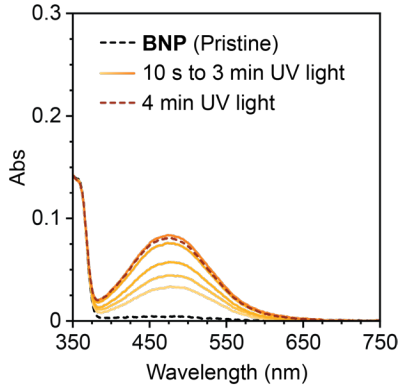

Figure S4.7. Absorption spectra of **BNP** (8 μg/mL in THF with 30 mM BHT) acquired after varying exposure to UV light (311 nm) at 20 °C. See Section VII for details.

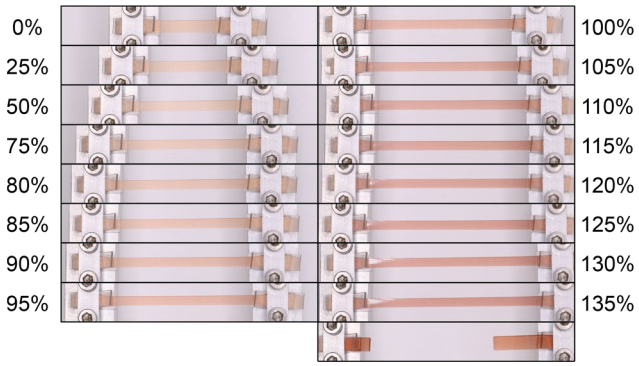

Figure S4.8. Photographs of a sample of **BNP-PDMS** at various strain values. Sample failure occurred between 135% and 140% strain.

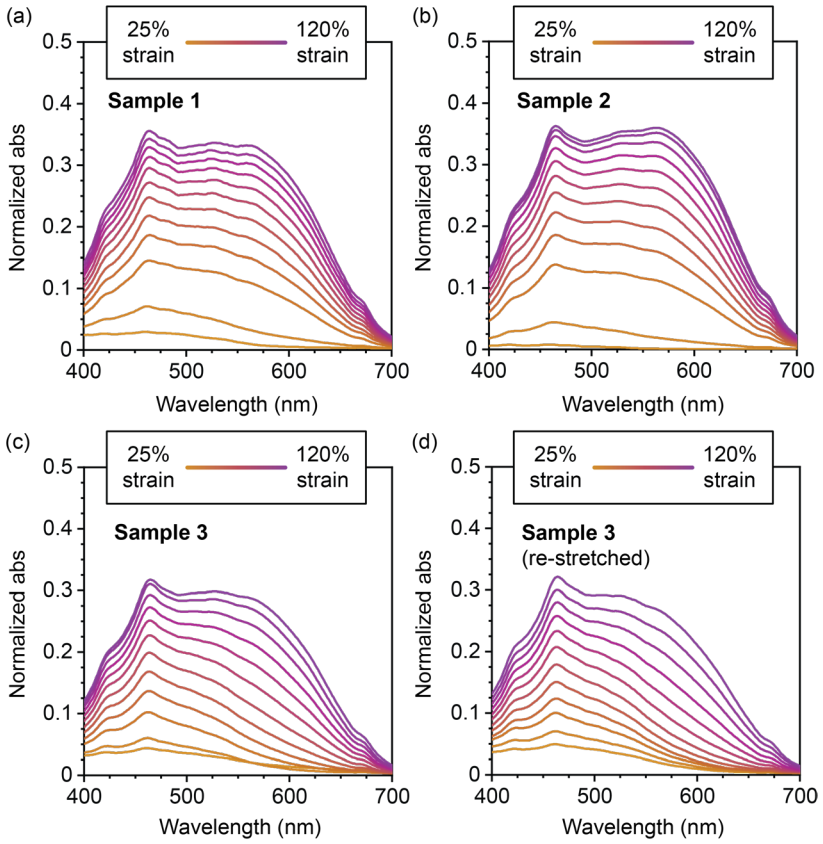

Figure S4.9. Individual samples (**Samples 1**–**3**) of **BNP-PDMS** were loaded to approximately 120% strain under uniaxial tension. (a–c) UV–vis absorption spectra were acquired to monitor changes in merocyanine distribution. (d) **Sample 3** was allowed to relax for 1 h following the initial loading experiment (panel c), and was subsequently loaded again to 120% strain. See Section VI for details.

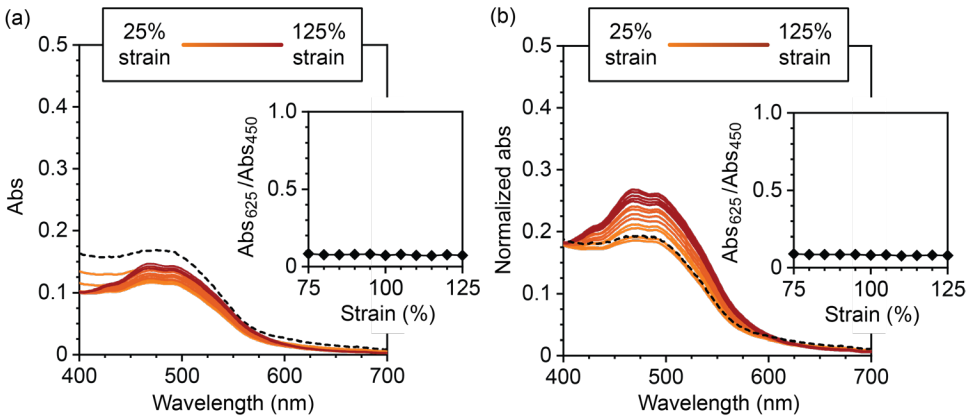

Figure S4.10. UV–vis absorption spectra collected during tensile loading of a sample of **Control-PDMS**. Spectra are shown after (a) baseline correction using the absorbance at 790 nm, and then (b) after normalization from 300 nm to 800 nm. Significantly, the ratio of absorbance at 625 nm and 450 nm is invariant as a function of strain. Spectra at 0% strain are shown with a dashed black line.

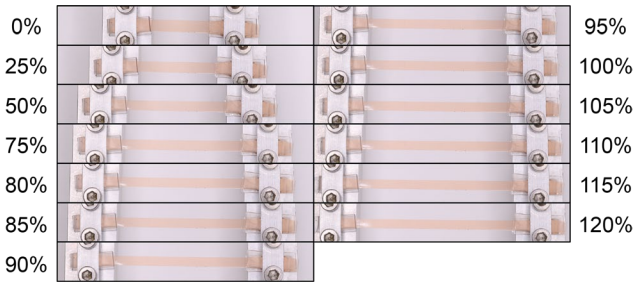

Figure S4.11. Photographs of a sample of **Control-PDMS** at various strain values.

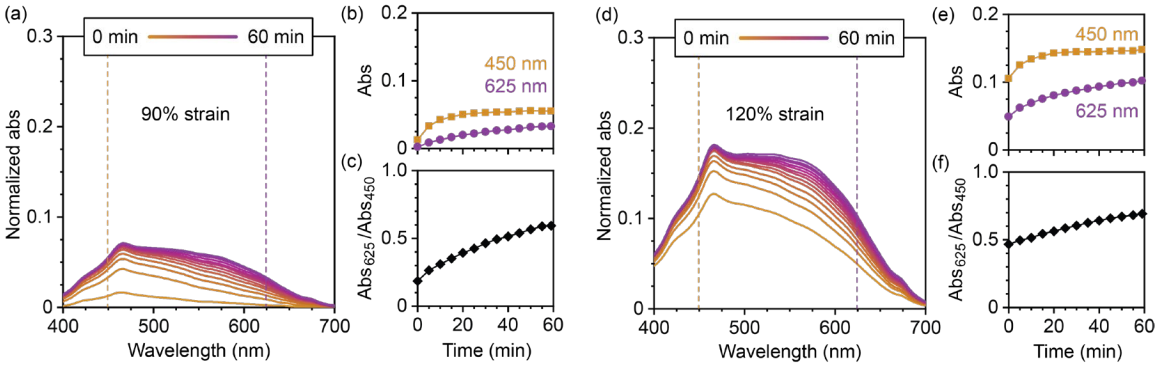

Figure S4.12. UV-vis absorption spectra recorded over time for a sample of **BNP-PDMS** maintained at a constant strain of (a) 90%, and (d) 120%. The sample was loaded to 90% strain and held in tension for 1 h. Subsequently, the sample was extended to 120% strain and held in tension for an additional 1 h. UV–vis absorption spectra were acquired to monitor time-dependent changes in merocyanine distribution. Absorbance at 450 nm and 625 nm was monitored as a function of time at (b) 90% strain and (e) 120% strain. The ratio of the absorbance at 625 nm versus 450 nm was monitored as a function of time at (c) 90% strain and (f) 120% strain.

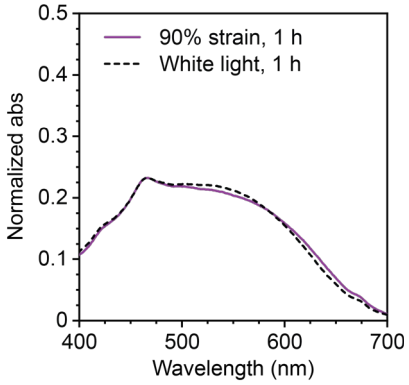

Figure S4.13. UV-vis absorption spectra acquired from a sample of **BNP-PDMS** after being held at 90% strain for 1 h, and the same film maintained at 90% strain after photoirradiation with white light for 1 h.

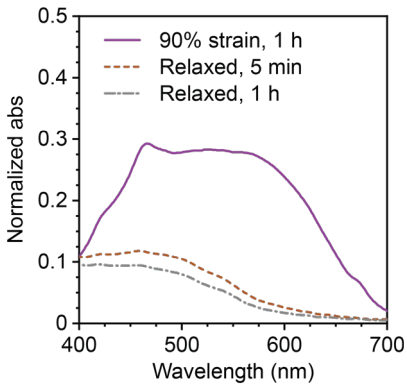

Figure S4.14. UV-vis absorption spectra acquired from a sample of **BNP-PDMS** after being held at 90% strain for 1 h, and then following stress relaxation (after 5 min and 1 h).

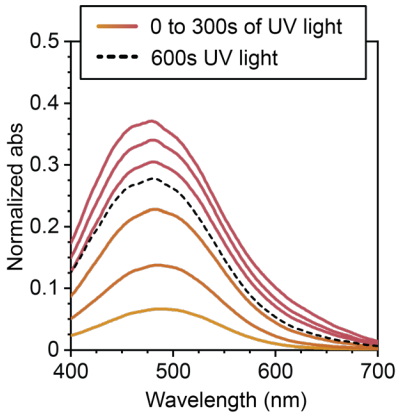

Figure S4.15. Absorption spectra of **BNP-PDMS** acquired during irradiation with UV light (311 nm, 300 s) (solid colored lines). Extended irradiation (311 nm, 600 s) causes photodegradation that is accompanied by an overall decrease in visible absorption (dashed black line).

III. Synthetic Details

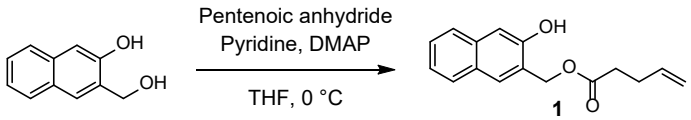

3-hydroxynaphthalen-2-yl methyl pent-4-enoate (1). To a flame dried 2-neck 100 mL RBF equipped with a stir bar was added 3-(hydroxymethyl)naphthalen-2-ol (665 mg, 3.82 mmol) and catalytic N,N-dimethylaminopyridine (46 mg, 0.38 mmol). The flask was evacuated and backfilled with N_2 three times. Anhydrous THF (23 mL) and pyridine (0.31 mL, 3.8 mmol) were added sequentially via syringe under N_2. The solution was cooled to 0 °C in an ice bath. A solution of pentenoic anhydride (0.70 mL, 3.83 mmol) in anhydrous THF (7 mL) was added dropwise via syringe over 10 min at 0 °C. After stirring for 16 h, the reaction was diluted with EtOAc (200 mL) and washed sequentially with saturated aqueous NH_4Cl (200 mL), saturated aqueous $NaHCO_3$ (150 mL), and brine (150 mL). The organic layer was dried over $MgSO_4$, filtered, and concentrated. The crude material was purified by column chromatography on silica gel (0–35% EtOAc/hexanes) to provide the title compound as a white solid (546 mg, 56%).

^{1}H NMR (400 MHz, $CDCl_3$) δ: 7.81 (s, 1H), 7.76 (dd, J = 8.3, 1.2 Hz, 1H), 7.68 (dd, J = 8.4, 1.2 Hz, 1H), 7.43 (ddd, J = 8.2, 6.8, 1.3 Hz, 1H), 7.39 (s, 1H), 7.33 (ddd, J = 8.1, 6.8, 1.2 Hz, 1H), 7.29 (s, 1H), 5.79 (ddt, J = 16.7, 10.3, 6.4 Hz, 1H), 5.33 (s, 2H), 5.03 (dq, J = 17.1, 1.6 Hz, 1H), 4.98 (dq, J = 10.2, 1.3 Hz, 1H), 2.53 – 2.45 (m, 2H), 2.43 – 2.34 (m, 2H).

^{13}C NMR (101 MHz, $CDCl_3$) δ: 175.3, 152.8, 136.3, 135.4, 131.9, 128.6, 127.9, 127.1, 126.4, 124.2, 124.0, 116.0, 112.2, 63.4, 33.6, 28.8.

TLC (25% EtOAc/hexanes): R_f = 0.45

HRMS (FD, *m/z*): calcd for $[C_{16}H_{16}O_3]^+$ $(M)^+$, 256.10940, found 256.11004.

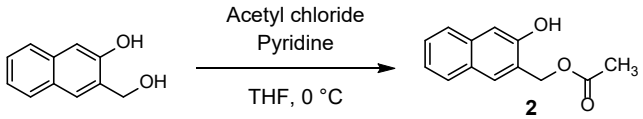

2

3-hydroxynaphthalen-2-yl methyl acetate (2). To a flame dried 2-neck 100 mL RBF equipped with a stir bar was added 3-(hydroxymethyl)naphthalen-2-ol (498 mg, 2.86 mmol). The flask was evacuated and backfilled with N_2 three times. Anhydrous THF (15 mL) and pyridine (0.23 mL, 2.9 mmol) were added sequentially via syringe under N_2. The solution was cooled to 0 °C in an ice bath. Acetyl chloride (0.20 mL, 2.8 mmol) was added dropwise via syringe over 10 min at 0 °C. After stirring for 18 h, the reaction was diluted with EtOAc (200 mL) and washed sequentially with saturated aqueous NH_4Cl (150 mL), saturated aqueous $NaHCO_3$ (150 mL), and brine (150 mL). The organic layer was dried over $MgSO_4$, filtered, and concentrated. The crude material was purified by column chromatography on silica gel (5–40% EtOAc/hexanes) to provide the title compound as a white solid (357 mg, 58%).

^{1}H NMR (400 MHz, $CDCl_3$) δ: 7.81 (s, 1H), 7.76 (d, J = 8.2 Hz, 1H), 7.68 (d, J = 8.3 Hz, 1H), 7.47 – 7.40 (m, 2H), 7.33 (ddd, J = 8.1, 6.9, 1.2 Hz, 1H), 7.28 (s, 1H), 5.32 (s, 2H), 2.14 (s, 3H).

^{13}C NMR (101 MHz, $CDCl_3$) δ: 173.3, 152.8, 135.4, 131.9, 128.6, 127.9, 127.1, 126.4, 124.2, 124.0, 112.1, 63.4, 21.1.

TLC (25% EtOAc/hexanes): R_f = 0.33

HRMS (FD, *m/z*): calcd for $[C_{13}H_{12}O_3]^+$ $(M)^+$, 216.07810, found 216.07843.

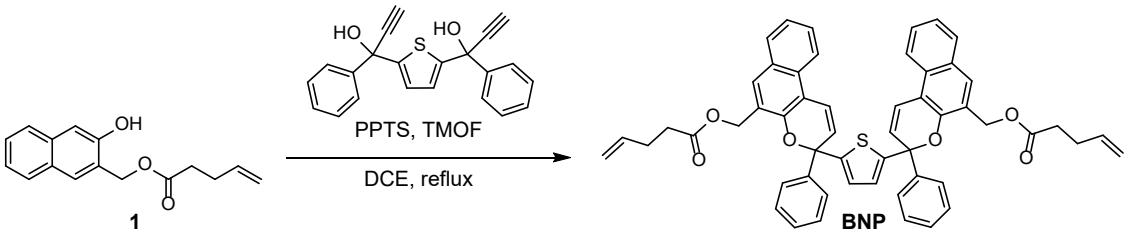

Thiophene-2,5-diylbis(3-phenyl-3H-benzo[f]chromene-3,5-diyl) bis(methylene) bis(pent-4-enoate) (BNP). Bis-naphthopyran **BNP** was synthesized according to the literature following the general procedure developed by Zhao and Carreira.[41] To a flame-dried two-neck round bottom flask was added naphthol **1** (393 mg, 1.53 mmol), 1,1'-(thiophene-2,5-diyl)bis(1-phenylprop-2-yn-1-ol) (230 mg, 0.67 mmol), and a catalytic amount of pyridinium *p*-toluenesulfonate (PPTS) (20 mg, 0.080 mmol). The flask was evacuated and backfilled with N_2 (3×) followed by the sequential addition of 1,2-dichloroethane (5 mL) and trimethyl orthoformate (0.33 mL, 3.02 mmol) via syringe. The reaction was heated to reflux and stirred for 2 h 15 min. The reaction was cooled to room temperature and concentrated with celite. Purification by column chromatography on silica gel (0–15% Et_2O/CH_2Cl_2:hexanes (1:1)) afforded the title compound (mixture of diastereomers) as a foamy red solid (512 mg, 93%).

^{1}H NMR (400 MHz, acetone-d_6) δ: 8.09 – 8.01 (m, 2H), 7.83 – 7.77 (m, 4H), 7.64 – 7.58 (m, 4H), 7.53 – 7.46 (m, 2H), 7.43 (app dd, J = 10.0, 5.4 Hz, 2H), 7.40 – 7.30 (m, 6H), 7.29 – 7.23 (m, 2H), 6.85 (s, 1H), 6.82 (s, 1H), 6.41 (d, J = 9.9 Hz, 2H), 5.80 (app ddtd, J = 16.6, 10.2, 6.5, 0.9 Hz, 2H), 5.36 (s, 2H), 5.31 (s, 2H), 5.03 (dq, J = 17.2, 1.7 Hz, 2H), 4.93 (ddt, J = 10.3, 2.1, 1.3 Hz, 2H), 2.48 – 2.40 (m, 4H), 2.35 – 2.27 (m, 4H).

^{13}C NMR (101 MHz, acetone-d_6) δ: 173.0, 172.9, 151.1, 149.13, 149.11, 145.12, 145.06, 138.0, 130.72, 130.65, 130.62, 129.9, 129.5, 129.18, 129.15, 128.9, 128.2, 128.1, 126.98,

126.96, 126.5, 126.4, 126.00, 125.97, 125.2, 122.3, 120.7, 120.6, 115.8, 114.9, 81.7, 81.6, 62.3, 62.2, 34.09, 34.06, 29.68, 29.67.

TLC (25% EtOAc/hexanes): $R_f = 0.58$

HRMS (ESI, *m/z*): calcd for $[C_{54}H_{45}O_6S]^+$ $(M+H)^+$, 821.2932, found 821.2922.

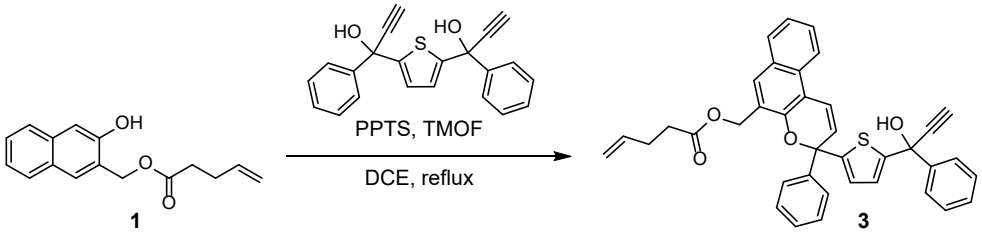

3-(5-(1-hydroxy-1-phenylprop-2-yn-1-yl)thiophen-2-yl 3-phenyl-3*H*-benzo[f]chromen-5-yl)methyl pent-4-enoate (3). To a flame-dried two-neck round bottom flask was added 1,1'-(thiophene-2,5-diyl)bis(1-phenylprop-2-yn-1-ol) (500 mg, 1.45 mmol) and a catalytic amount of pyridinium *p*-toluenesulfonate (PPTS) (18 mg, 0.072 mmol). The flask was evacuated and backfilled with N_2 (3×) followed by the sequential addition of 1,2-dichloroethane (10 mL) and trimethyl orthoformate (0.23 mL, 2.1 mmol) via syringe. The reaction was lowered into an oil bath at 106 °C and a solution of naphthol **1** (371 mg, 1.45 mmol) in 1,2-dichloroethane (6 mL) was added dropwise over 15 min. The reaction was refluxed and stirred for 5 h, and then the reaction was cooled to room temperature and concentrated. The residue was diluted into 200 mL EtOAc and washed sequentially with saturated aqueous $NaHCO_3$ (150 mL) and brine (150 mL). The organic layer was dried over Na_2SO_4, filtered, and concentrated. The crude material was purified by column chromatography on silica gel (20–100% DCM/hexanes) to provide the title compound (mixture of diastereomers) as a dark red foamy solid (389 mg, 46%).

^{1}H NMR (400 MHz, acetone-d_6) δ: 8.08 (d, J = 8.9 Hz, 1H), 7.84 (d, J = 3.0 Hz, 1H), 7.81 (d, J = 8.3 Hz, 1H), 7.69 – 7.71 (m, 4H), 7.51 (ddt, J = 8.6, 7.0, 1.7 Hz, 1H), 7.47 (dd, J = 10.0, 2.3 Hz, 1H), 7.41 – 7.23 (m, 7H), 6.90 – 6.82 (m, 2H), 6.45 (d, J = 9.9 Hz, 0.5H), 6.44 (d, J = 9.9 Hz, 0.5H), 6.02 (app d, J = 1.2 Hz, 1H), 5.88 (app ddtd, J = 16.7, 10.2, 6.4, 1.7 Hz, 1H), 5.39 (app d, J = 3.6 Hz, 2H), 5.08 (dp, J = 17.2, 1.6 Hz, 1H), 4.97 (dp, J = 10.3, 1.5 Hz, 1H), 3.35 (app d, J = 3.3 Hz, 1H), 2.55 – 2.48 (m, 2H), 2.43 – 2.34 (m, 2H).

^{13}C NMR (101 MHz, acetone-d_6) δ: 173.0, 153.02, 153.01, 150.04, 150.00, 149.12, 149.10, 145.84, 145.83, 145.3, 138.0, 130.63, 130.61, 130.60, 130.58, 129.9, 129.5, 129.1, 128.9, 128.7, 128.58, 128.56, 128.22, 128.19, 128.05, 126.9, 126.5, 126.2, 126.1, 126.0, 125.2, 125.03, 124.96, 122.3, 120.6, 115.8, 114.8, 87.18, 87.16, 81.59, 81.56, 76.0, 71.94, 71.92, 62.2, 34.1, 29.7.

TLC (25% EtOAc/hexanes): R_f = 0.43

HRMS (ESI, *m/z*): calcd for $[C_{38}H_{29}O_3S]^+$ $(M-OH)^+$, 565.1832, found 565.1825.

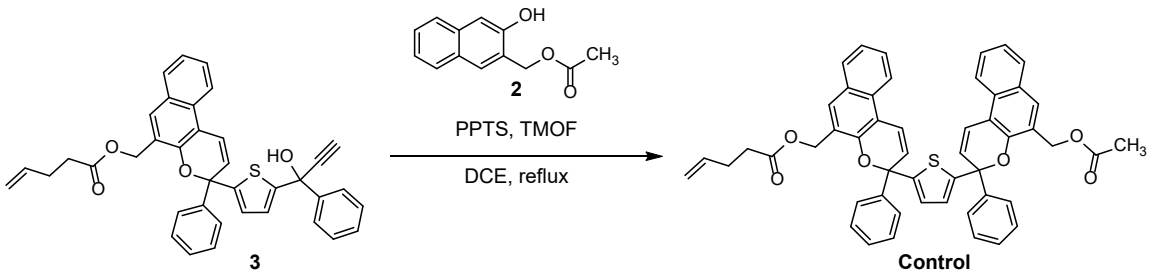

3-(5-(5-(acetoxymethyl)-3-phenyl-3*H*-benzo[f]chromen-3-yl)thiophen-2-yl-3-phenyl-3*H*-benzo[f]chromen-5-yl)methyl pent-4-enoate (Control). To a flame-dried two-neck round bottom flask was added naphthol **2** (67 mg, 0.31 mmol) and a catalytic amount of pyridinium *p*-toluenesulfonate (PPTS) (7 mg, 0.03 mmol). The flask was evacuated and backfilled with N_2 (3×) and a solution of **3** (180 mg, 0.31 mmol) in 1,2-dichloroethane (5 mL) was added via syringe. Trimethyl orthoformate (0.07 mL, 0.64 mmol) was added via

syringe. The reaction was heated to reflux and stirred for 2 h 10 min. The reaction was cooled to room temperature and concentrated with celite. Purification by column chromatography on silica gel (20–100% DCM/hexanes) afforded the title compound (mixture of diastereomers) as a foamy pink solid (210 mg, 87%).

^{1}H NMR (400 MHz, acetone-d_6) δ: 8.05 (t, J = 8.0 Hz, 2H), 7.83 – 7.76 (m, 4H), 7.65 – 7.57 (m, 4H), 7.53 – 7.40 (m, 4H), 7.40 – 7.30 (m, 6H), 7.30 – 7.23 (m, 2H), 6.89 – 6.77 (m, 2H), 6.41 (d, J = 9.9 Hz, 1H), 6.40 (d, J = 10.0 Hz, 1H), 5.80 (ddt, J = 16.8, 10.4, 6.4 Hz, 1H), 5.41 – 5.21 (m, 4H), 5.01 (dqd, J = 17.2, 1.7, 0.8 Hz, 1H), 4.91 (dddd, J = 10.3, 2.9, 2.0, 1.1 Hz, 1H), 2.49 – 2.39 (m, 2H), 2.35 – 2.27 (m, 2H), 2.00 (s, 1.5H), 1.97 (s, 1.5H).

^{13}C NMR (101 MHz, Acetone) δ: 173.0, 172.9, 170.87, 170.85, 151.2, 151.14, 151.12, 149.14, 149.11, 145.2, 145.10, 145.06, 138.0, 130.73, 130.69, 130.66, 130.63, 129.9, 129.5, 129.19, 129.17, 129.15, 128.9, 128.8, 128.21, 128.18, 128.09, 126.99, 126.96, 126.94, 126.50, 126.48, 126.42, 126.35, 126.00, 125.97, 125.2, 122.3, 120.7, 120.64, 120.59, 115.8, 114.9, 114.8, 81.72, 81.69, 81.63, 81.62, 62.31, 62.26, 62.23, 62.20, 34.09, 34.05, 29.7, 21.02, 20.99.

TLC (25% EtOAc/hexanes): R_f = 0.48

HRMS (ESI, *m/z*): calcd for $[C_{38}H_{29}O_3S]^+$ $(M+H)^+$, 781.2619, found 781.2609.

IV. Preparation of PDMS Materials

PDMS materials incorporating 3*H*-bis-naphthopyrans **BNP** and **Control** (~0.8 wt%) were prepared following previously reported procedures using the two-part Sylgard® 184 elastomer kit (Dow Corning).[4,40] PDMS films approximately 0.5 mm thick were cut into 5 mm strips for testing.

General Procedure A for the Preparation of PDMS Materials. The naphthopyran crosslinker was dissolved in a minimal amount of xylene in a 20 mL scintillation vial. Sylgard® 184 prepolymer base was added and the contents were thoroughly mixed in a vortex mixer with intermittent gentle heating to form a homogeneous dispersion. Sylgard® 184 curing agent was added and the contents were mixed thoroughly using a vortex mixer. The mixture was pipetted onto a clean 1.5 in x 1.5 in Delrin plate, which was placed inside a vacuum chamber and evacuated under high vacuum (~30 mTorr) for 2 h. The Delrin plate was then transferred to an oven and cured at 80 °C overnight. After curing, the plate was removed from the oven and the PDMS film was peeled off and cut into 5 mm strips.

BNP-PDMS (Specimen 1) was synthesized using General Procedure A with **BNP** (9.8 mg, 0.012 mmol), xylenes (0.15 mL), Sylgard® 184 prepolymer base (1.056 g), and Sylgard® 184 curing agent (0.1056 g).

BNP-PDMS (Specimen 2) was synthesized using General Procedure A with **BNP** (10.1 mg, 0.012 mmol), xylenes (0.15 mL), Sylgard® 184 prepolymer base (1.351 g), and Sylgard® 184 curing agent (0.1346 g).

BNP-PDMS (Specimen 3) was synthesized using General Procedure A with **BNP** (10.0 mg, 0.012 mmol), xylenes (0.15 mL), Sylgard® 184 prepolymer base (1.320 g), and Sylgard® 184 curing agent (0.1316 g).

Control-PDMS was synthesized using General Procedure A with **Control** (9.8 mg, 0.013 mmol), xylenes (0.15 mL), Sylgard® 184 prepolymer base (1.087 g), and Sylgard® 184 curing agent (0.1087 g).

V. DFT Calculations (CoGEF)

CoGEF calculations were performed using Spartan ′24 Parallel Suite according to previously reported methods.[38] Ground state energies were calculated using DFT at the B3LYP/6-31G* level of theory. Truncated models of each mechanophore with terminal acetoxy groups were used in the calculations. For each structure, the equilibrium conformations of the unconstrained molecule were initially calculated using molecular mechanics (MMFF) followed by optimization of the equilibrium geometries using DFT (B3LYP/6-31G*). Starting from the equilibrium geometry of the unconstrained molecules (energy = 0 kJ/mol), the distance between the terminal methyl groups of the truncated structures was increased in increments of 0.05 Å and the energy was minimized at each step. The maximum force associated with the mechanochemical reaction was calculated from the slope of the curve immediately prior to bond cleavage using the final two contiguous data points.

VI. In Situ Absorption Measurements and Data Processing

Visible absorption spectra were acquired for 5 mm-long PDMS specimens subjected to uniaxial tension using a custom Velmex load frame (manually-operated, left-right screw drive model). For experiments under increasing tension (Figures 4.3 and S4.9), the samples were uniaxially stretched to the specified strain and maintained in tension for the duration of the spectral acquisition time (60 s). For experiments under constant tension (Figures S4.12–S4.14), the samples were uniaxially stretched to the specified strain and maintained in tension for approximately 1 h. Absorption spectra (300–800 nm) were acquired using a Thermo Scientific Evolution 220 spectrometer. The load frame was placed inside of the spectrometer such that the beam passed through the center of the PDMS specimen.

For tensile and photoirradiation experiments performed on samples of **BNP-PDMS**, absorption spectra were corrected and normalized according to the following procedure. A representative example is highlighted in Figure S4.16. The absorbance values measured at 790 nm were subtracted from the full absorption spectra (Figure S4.16a). To account for specimen thinning that occurs during mechanical loading, the spectra were then normalized from 300 nm to 800 nm (Figure S4.16b). To observe the spectroscopic changes that accompany the application of mechanical tension or UV light, the spectrum of the pristine specimen (0% strain) was subtracted from all other absorption spectra (Figure S4.16c). The resulting spectra were then smoothed via the Savitzky-Golay method using a second order polynomial (Figure S4.16d). For all data sets, the ratio of absorbance at 625 nm and 450 nm increases as a function of applied strain or time under tension.

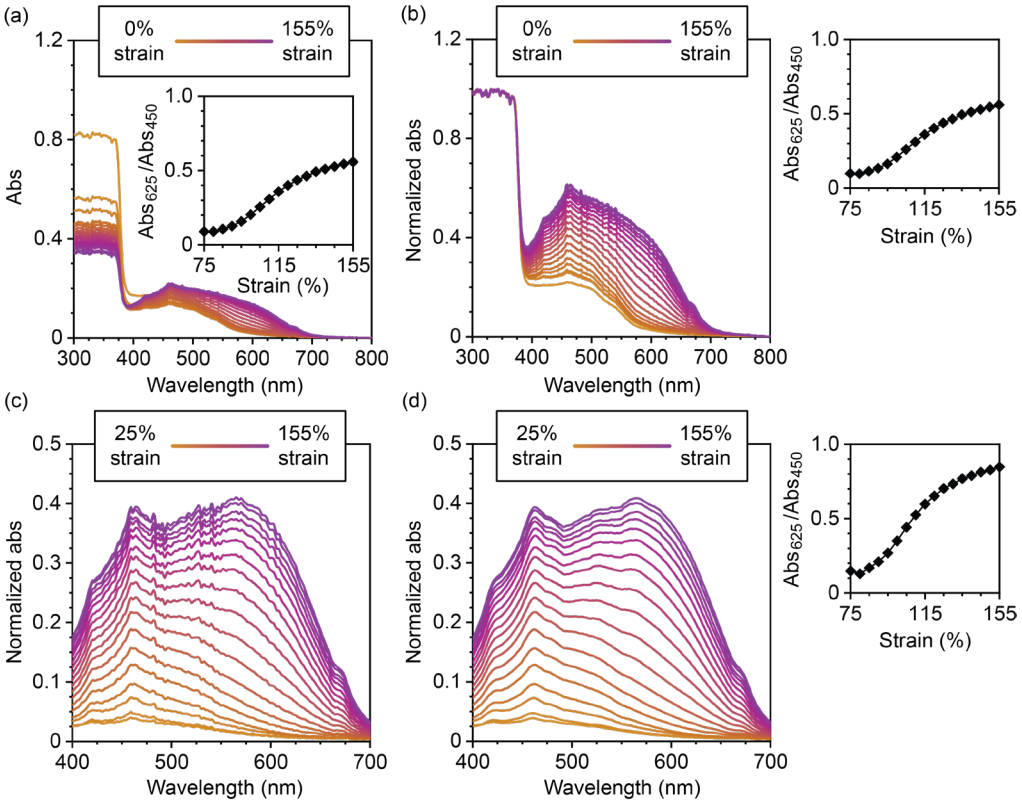

Figure S4.16. Representative data illustrating processing methods. UV–vis absorption spectra acquired during mechanical loading of a sample of **BNP-PDMS** under increasing uniaxial tension. The raw absorption spectra were (a) corrected to the absorbance value at 790 nm, and (b) normalized from 300 nm to 800 nm. (c) The absorption spectrum of the pristine sample (0% strain) was subtracted from the normalized spectra at higher strain values (25–155% strain). (d) The data were smoothed via the Savitzky-Golay method.

VII. Details for Photoirradiation Experiments

Photoirradiation of BNP at −78 °C. A quartz cuvette was charged with a solution of **BNP** (8 μg/mL in THF with 30 mM BHT) and placed inside of a Cary 60 spectrometer equipped with an Unisoku cryostat maintained at −78 °C. The cold solution was irradiated with UV light (311 nm) through a window in an orthogonal direction to the analytical light beam. The solution was irradiated with UV light for a total time of 10 s, 30 s, 1 min, 2 min, 3 min…15 min, and an absorption spectrum (300–900 nm) was collected for each time point. The UV light was turned off during spectrum collection. The absorbance values measured at 790 nm

were subtracted at each timepoint to account for drift during the experiment. To monitor thermal reversion of photochemically generated merocyanines at −78 °C, the final timepoint was maintained at −78 °C for 5 min and an addition absorption spectrum was collected (Figure S4.6a).

Photoirradiation of BNP at 20 °C. A two-sided quartz cuvette was charged with a solution of **BNP** (8 μg/mL in THF with 30 mM BHT). Absorption spectra of photochemically generated merocyanines were measured at room temperature (20 °C) by exposing the cuvette to a UV light source (311 nm) positioned 2 inches away from the cuvette. The cuvette was immediately placed inside a Thermo Scientific Evolution 220 spectrometer and the absorption spectrum (300–800 nm) was collected. Spectra were collected after 10 s, 30 s, 1 min, 2 min, 3 min, and 4 min of total irradiation time. The absorbance values measured at 790 nm were subtracted at each timepoint to account for drift during the experiment. To monitor thermal reversion of photochemically generated merocyanines at 20 °C, the final timepoint was maintained at 20 °C in the dark for 5 min and an additional absorption spectrum was collected (Figure S4.6b).

UV Photoirradiation of BNP-PDMS. Visible absorption spectra were acquired for a 5 mm strip of **BNP-PDMS** using a custom Velmex load frame (manually-operated, left-right screw drive model). The samples were maintained at 0% strain. Absorption spectra (300–800 nm) were acquired using a Thermo Scientific Evolution 220 spectrometer. The load frame was placed inside of the spectrometer such that the analytical light beam passed through the center of the PDMS specimen. During irradiation with UV light (311 nm), the light source was positioned inside the spectrometer ~1 inch from the PDMS sample. Spectra were collected

after 5 s, 30 s, 60 s, 120 s, 300 s, and 600 s of total irradiation time, and the UV light source was removed from the apparatus during spectrum collection (60 s). Absorption spectra were corrected and normalized as outlined in Section VI.

White light Photoirradiation of BNP-PDMS. Visible absorption spectra were acquired for a 5 mm strip of **BNP-PDMS** using a custom Velmex load frame (manually-operated, left-right screw drive model). The sample was maintained at 90% strain for approximately 1 h prior to white light irradiation. Absorption spectra (300–800 nm) were acquired using a Thermo Scientific Evolution 220 spectrometer. The load frame was placed inside of the spectrometer such that the analytical light beam passed through the center of the PDMS specimen. During irradiation with white light, the light source was positioned inside the spectrometer ~3 inch from the PDMS sample. A spectrum was collected after 1 h of total irradiation time, and the white light source was removed from the apparatus during spectrum collection (60 s). Absorption spectra were corrected and normalized as outlined in Section VI. The sample was irradiated with white light using a 13 W broadband fluorescent lamp (Bayco Model BA-506) filtered through a 425 nm bandpass filter.

^{1}H and ^{13}C NMR Spectra

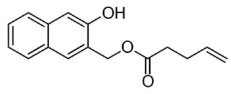

1

^{1}H (400 MHz, $CDCl_3$)

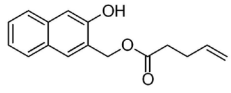

1

^{13}C (101 MHz, $CDCl_3$)

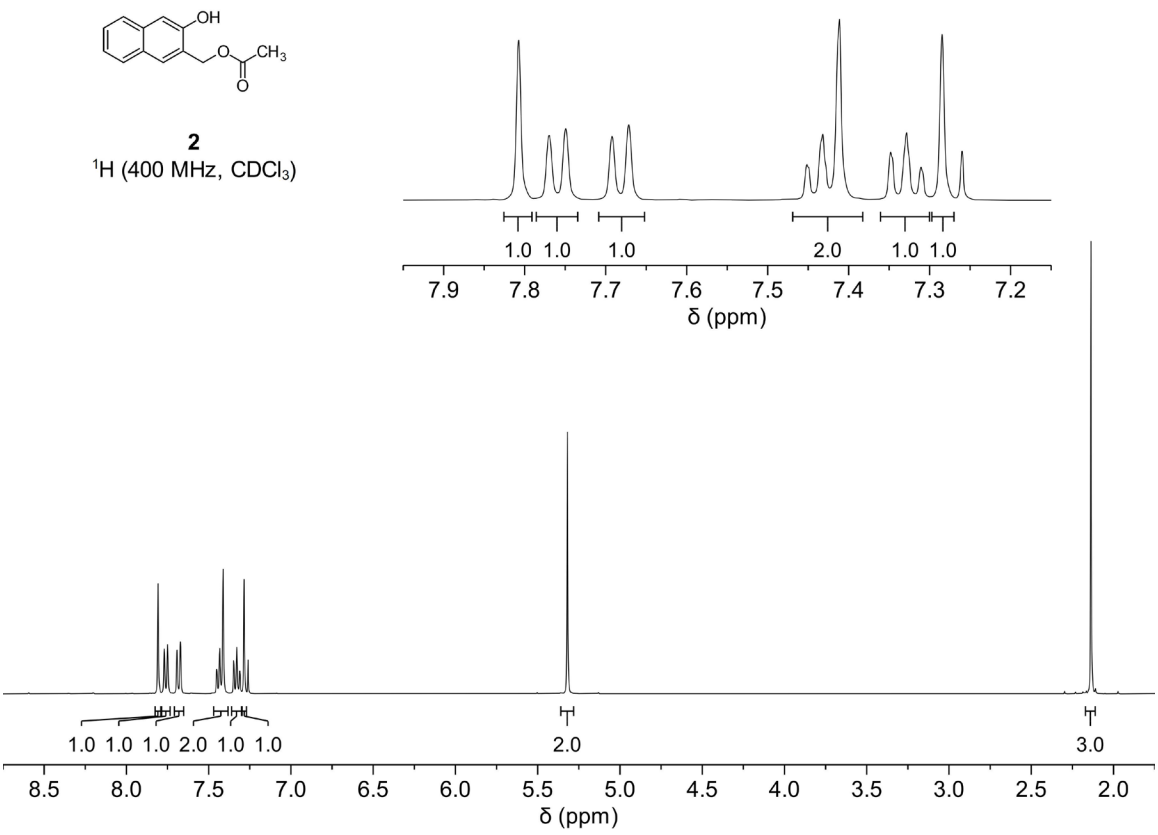
OH
O
CH3
O
2
1H (400 MHz, CDCl3)
1.0 1.0 1.0 2.0 1.0 1.0
2.0
3.0
8.5 8.0 7.5 7.0 6.5 6.0 5.5 5.0 4.5 4.0 3.5 3.0 2.5 2.0
δ (ppm)
1.0 1.0 1.0 2.0 1.0 1.0
7.9 7.8 7.7 7.6 7.5 7.4 7.3 7.2
δ (ppm)

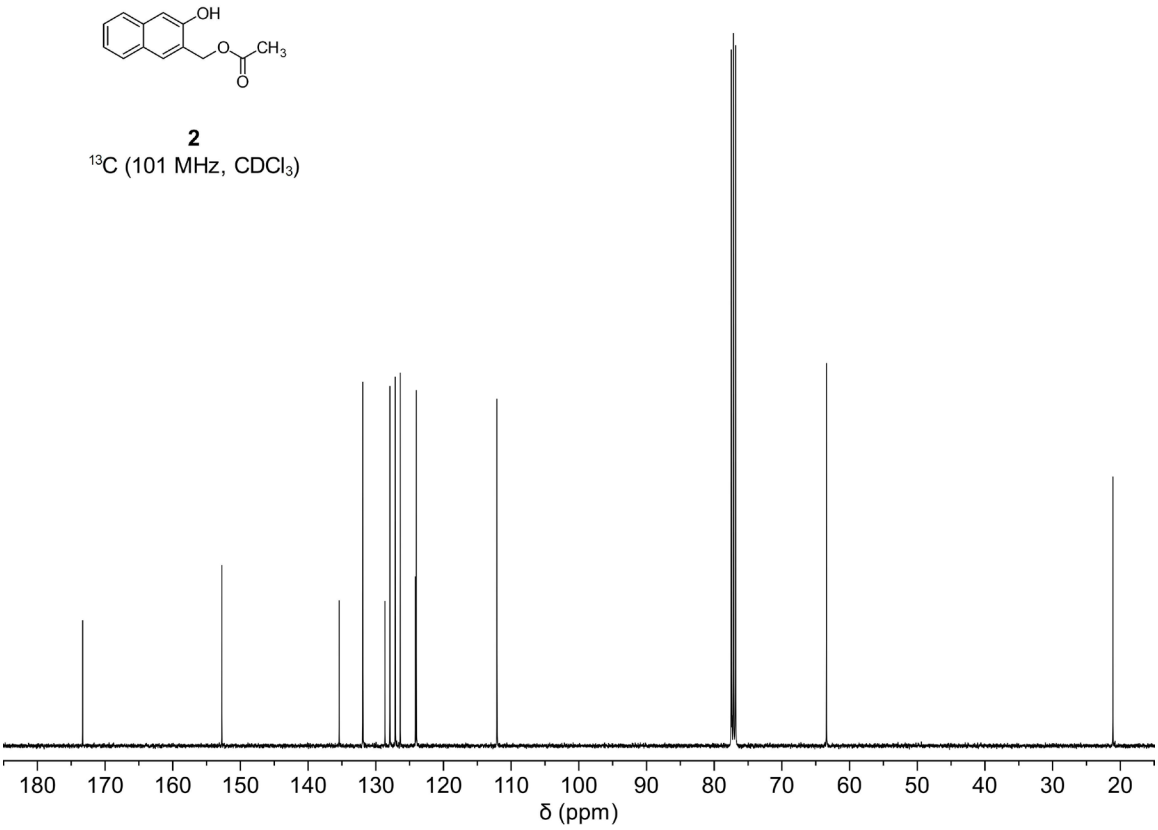
OH
O
CH3
O
2
13C (101 MHz, CDCl3)
180 170 160 150 140 130 120 110 100 90 80 70 60 50 40 30 20
δ (ppm)

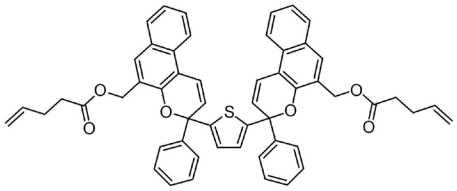

BNP

^{1}H (400 MHz,acetone-d_6)

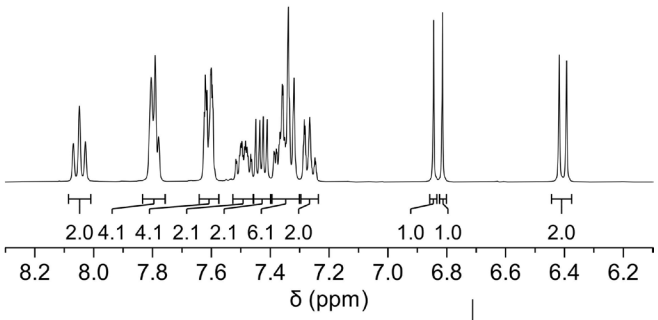

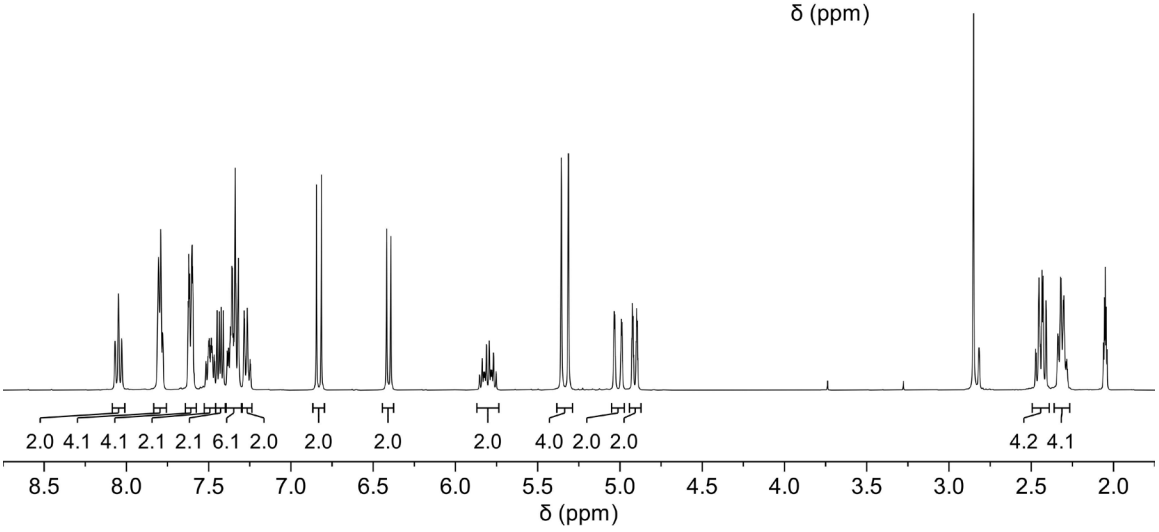

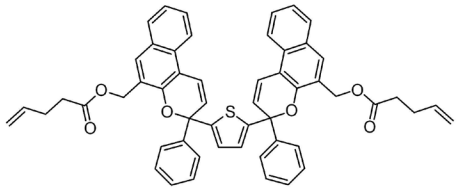

BNP

^{13}C (101 MHz,acetone-d_6)

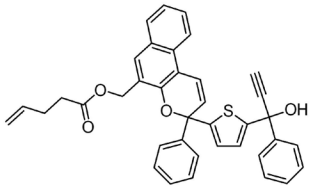

3

^{1}H (400 MHz,acetone-d_6)

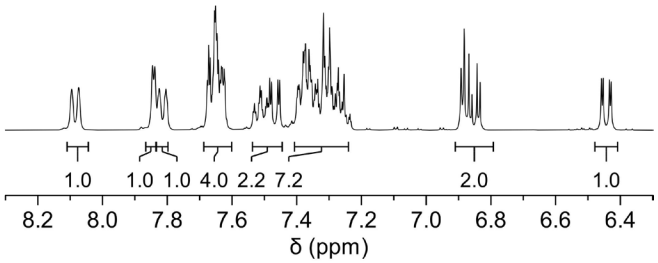

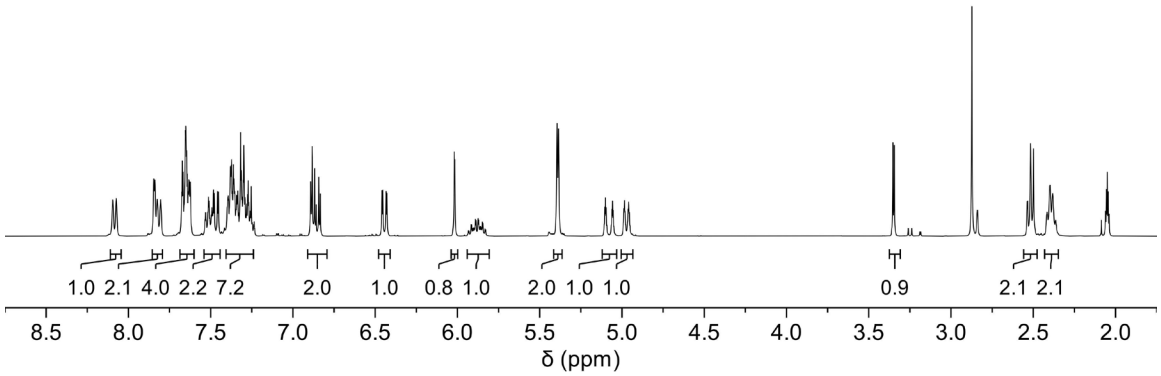

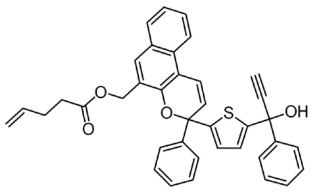

3

^{13}C (101 MHz,acetone-d_6)

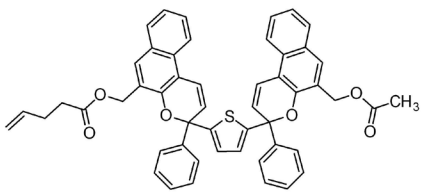

Control

^{1}H (400 MHz,acetone-d_6)

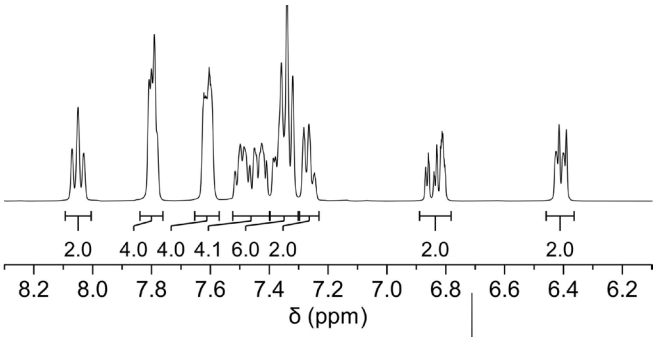

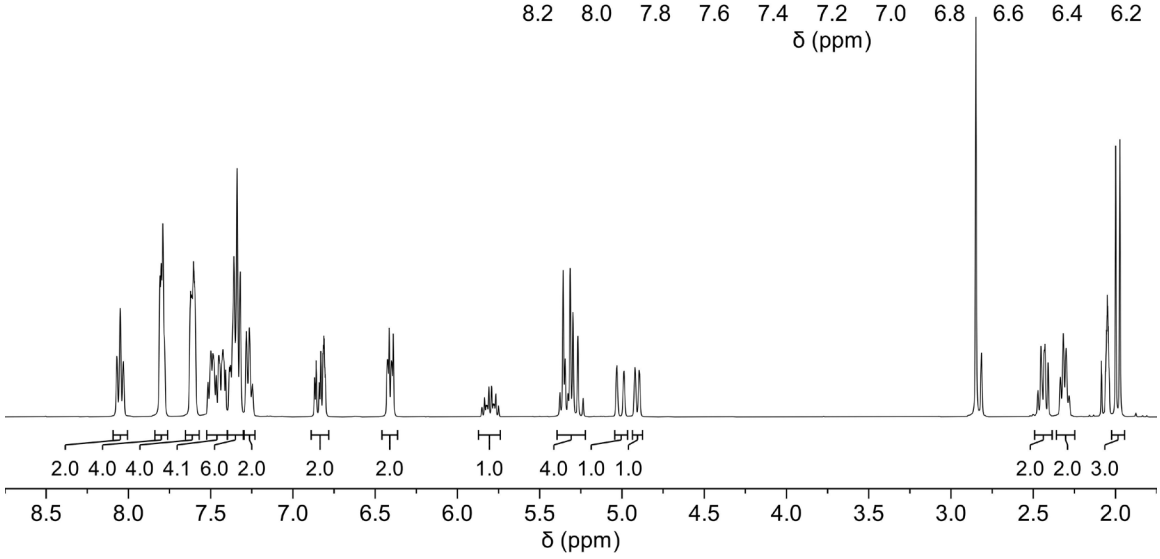

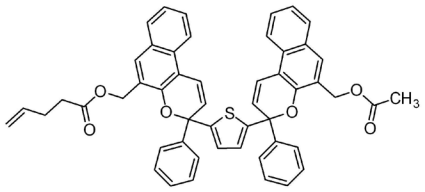

Control

^{13}C (101 MHz,acetone-d_6)

References

(1) Li, J.; Nagamani, C.; Moore, J. S. Polymer Mechanochemistry: From Destructive to Productive. *Acc. Chem. Res.* **2015**, *48*, 2181–2190.

(2) Beyer, M. K.; Clausen-Schaumann, H. Mechanochemistry: The Mechanical Activation of Covalent Bonds. *Chem. Rev.* **2005**, *105*, 2921–2948.

(3) Caruso, M. M.; Davis, D. A.; Shen, Q.; Odom, S. A.; Sottos, N. R.; White, S. R.; Moore, J. S. Mechanically-Induced Chemical Changes in Polymeric Materials. *Chem. Rev.* **2009**, *109*, 5755–5798.

(4) Robb, M. J.; Kim, T. A.; Halmes, A. J.; White, S. R.; Sottos, N. R.; Moore, J. S. Regioisomer-Specific Mechanochromism of Naphthopyran in Polymeric Materials. *J. Am. Chem. Soc.* **2016**, *138*, 12328–12331.

(5) Davis, D. A.; Hamilton, A.; Yang, J.; Cremar, L. D.; Van Gough, D.; Potisek, S. L.; Ong, M. T.; Braun, P. V.; Martínez, T. J.; White, S. R.; Moore, J. S.; Sottos, N. R. Force-Induced Activation of Covalent Bonds in Mechanoresponsive Polymeric Materials. *Nature* **2009**, *459*, 68–72.

(6) Zhang, H.; Gao, F.; Cao, X.; Li, Y.; Xu, Y.; Weng, W.; Boulatov, R. Mechanochromism and Mechanical-Force-Triggered Cross-Linking from a Single Reactive Moiety Incorporated into Polymer Chains. *Angew. Chem. Int. Ed.* **2016**, *55*, 3040–3044.

(7) Qian, H.; Purwanto, N. S.; Ivanoff, D. G.; Halmes, A. J.; Sottos, N. R.; Moore, J. S. Fast, Reversible Mechanochromism of Regioisomeric Oxazine Mechanophores: Developing In Situ Responsive Force Probes for Polymeric Materials. *Chem.* **2021**, *7*, 1080–1091.

(8) Imato, K.; Kanehara, T.; Ohishi, T.; Nishihara, M.; Yajima, H.; Ito, M.; Takahara, A.; Otsuka, H. Mechanochromic Dynamic Covalent Elastomers: Quantitative Stress Evaluation and Autonomous Recovery. *ACS Macro Lett.* **2015**, *4*, 1307–1311.

(9) Imato, K.; Irie, A.; Kosuge, T.; Ohishi, T.; Nishihara, M.; Takahara, A.; Otsuka, H. Mechanophores with a Reversible Radical System and Freezing-Induced Mechanochemistry in Polymer Solutions and Gels. *Angew. Chem. Int. Ed.* **2015**, *54*, 6168–6172.

(10) Wang, Z.; Ma, Z.; Wang, Y.; Xu, Z.; Luo, Y.; Wei, Y.; Jia, X. A Novel Mechanochromic and Photochromic Polymer Film: When Rhodamine Joins Polyurethane. *Adv. Mater.* **2015**, *27*, 6469–6474.

(11) Wang, T.; Zhang, N.; Dai, J.; Li, Z.; Bai, W.; Bai, R. Novel Reversible Mechanochromic Elastomer with High Sensitivity: Bond Scission and Bending-Induced Multicolor Switching. *ACS Appl. Mater. Interfaces* **2017**, *9*, 11874–11881.

(12) McFadden, M. E.; Barber, R. W.; Overholts, A. C.; Robb, M. J. Naphthopyran Molecular Switches and Their Emergent Mechanochemical Reactivity. *Chem. Sci.* **2023**, *14*, 10041–10067.

(13) McFadden, M. E.; Robb, M. J. Generation of an Elusive Permanent Merocyanine via a Unique Mechanochemical Reaction Pathway. *J. Am. Chem. Soc.* **2021**, *143*, 7925–7929.

(14) Osler, S. K.; McFadden, M. E.; Robb, M. J. Comparison of the Reactivity of Isomeric 2*H*- and 3*H*-Naphthopyran Mechanophores. *J. Polym. Sci.* **2021**, *59*, 2537–2544.

(15) Sun, Y.; McFadden, M. E.; Osler, S. K.; Barber, R. W.; Robb, M. J. Anomalous Photochromism and Mechanochromism of a Linear Naphthopyran Enabled by a Polarizing Dialkylamine Substituent. *Chem. Sci.* **2023**, *14*, 10494–10499.
(16) Osler, S. K.; Ballinger, N. A.; Robb, M. J. The Role of Torsion on the Force-Coupled Reactivity of a Fluorenyl Naphthopyran Mechanophore. *J. Am. Chem. Soc.* **2025**, *147*, 3904–3911.
(17) Versaw, B. A.; McFadden, M. E.; Husic, C. C.; Robb, M. J. Designing Naphthopyran Mechanophores with Tunable Mechanochromic Behavior. *Chem. Sci.* **2020**, *11*, 4525–4530.
(18) Kim, D.; Kwon, M. S.; Lee, C. W. Mechanochromic Polymers with a Multimodal Chromic Transition: Mechanophore Design and Transduction Mechanism. *Polym. Chem.* **2022**, *13*, 5177–5187.
(19) McFadden, M. E.; Robb, M. J. Force-Dependent Multicolor Mechanochromism from a Single Mechanophore. *J. Am. Chem. Soc.* **2019**, *141*, 11388–11392.
(20) Osler, S. K.; McFadden, M. E.; Zeng, T.; Robb, M. J. Mechanochemical Reactivity of a Multimodal 2*H*-Bis-Naphthopyran Mechanophore. *Polym. Chem.* **2023**, *14*, 2717–2723.
(21) McFadden, M. E.; Osler, S. K.; Sun, Y.; Robb, M. J. Mechanical Force Enables an Anomalous Dual Ring-Opening Reaction of Naphthodipyran. *J. Am. Chem. Soc.* **2022**, *144*, 22391–22396.
(22) Kosuge, T.; Zhu, X.; Lau, V. M.; Aoki, D.; Martinez, T. J.; Moore, J. S.; Otsuka, H. Multicolor Mechanochromism of a Polymer/Silica Composite with Dual Distinct Mechanophores. *J. Am. Chem. Soc.* **2019**, *141*, 1898–1902.
(23) Ishizuki, K.; Aoki, D.; Otsuka, H. Mechanochromic Polymers That Recognize the Duration of the Mechanical Stimulation via Multiple Mechanochromism. *Macromol. Rapid Commun.* **2021**, *42*, 2000429.
(24) Wang, T.; Wang, H.; Shen, L.; Zhang, N. Multicolor Mechanochromism of a Multinetwork Elastomer that can Distinguish Between Low and High Stress. *Polym. Chem.* **2021**, *12*, 3832–3841.
(25) Ishizuki, K.; Takahashi, A.; Otsuka, H. Multicolor Mechanochromic Polymer Blends That Can Distinguish between Tensile–Stress States. *Macromol. Rapid Commun.* **2025**, *46*, 2400812.
(26) Raisch, M.; Maftuhin, W.; Walter, M.; Sommer, M. A Mechanochromic Donor-Acceptor Torsional Spring. *Nat. Commun.* **2021**, *12*, 4243.
(27) Hertel, R.; Maftuhin, W.; Walter, M.; Sommer, M. Conformer Ring Flip Enhances Mechanochromic Performance of *ansa*-Donor–Acceptor–Donor Mechanochromic Torsional Springs. *J. Am. Chem. Soc.* **2022**, *144*, 21897–21907.
(28) Kotani, R.; Yokoyama, S.; Nobusue, S.; Yamaguchi, S.; Osuka, A.; Yabu, H.; Saito, S. Bridging Pico-to-Nanonewtons with a Ratiometric Force Probe for Monitoring Nanoscale Polymer Physics Before Damage. *Nat. Commun.* **2022**, *13*, 303.
(29) Yamakado, T.; Saito, S. Ratiometric Flapping Force Probe That Works in Polymer Gels. *J. Am. Chem. Soc.* **2022**, *144*, 2804–2815.
(30) Hu, H.; Cheng, X.; Ma, Z.; Sijbesma, R. P.; Ma, Z. Polymer Mechanochromism from Force-Tuned Excited-State Intramolecular Proton Transfer. *J. Am. Chem. Soc.* **2022**, *144*, 9971–9979.

(31) Zhao, W.; Carreira, E. M. A Smart Photochromophore Through Synergistic Coupling of Photochromic Subunits. *J. Am. Chem. Soc.* **2002**, *124*, 1582–1583.
(32) Zhao, W.; Carreira, E. M. Oligothiophene-Linked Bisnaphthopyrans: Sequential and Temperature-Dependent Photochromism. *Chem. Eur. J.* **2007**, *13*, 2671–2685.
(33) Lu, X.; Dong, Q.; Dong, X.; Zhao, W. Synthesis and Sequential Photochromism of Thiophene-Linked Bis-Pyrans. *Tetrahedron* **2015**, *71*, 4061–4069.
(34) May, P. A.; Munaretto, N. F.; Hamoy, M. B.; Robb, M. J.; Moore, J. S. Is Molecular Weight or Degree of Polymerization a Better Descriptor of Ultrasound-Induced Mechanochemical Transduction? *ACS Macro Lett.* **2016**, *5*, 177–180.
(35) Benzo and Naphthopyrans (Chromenes). In *Organic Photochromic and Thermochromic Compounds*; Springer: Boston, MA, 2002; pp 111–140.
(36) Lee, C. K.; Davis, D. A.; White, S. R.; Moore, J. S.; Sottos, N. R.; Braun, P. V. Force-Induced Redistribution of a Chemical Equilibrium. *J. Am. Chem. Soc.* **2010**, *132*, 16107–16111.
(37) Lloyd, E. M.; Vakil, J. R.; Yao, Y.; Sottos, N. R.; Craig, S. L. Covalent Mechanochemistry and Contemporary Polymer Network Chemistry: A Marriage in the Making. *J. Am. Chem. Soc.* **2023**, *145*, 751–768.
(38) Klein, I. M.; Husic, C. C.; Kovács, D. P.; Choquette, N. J.; Robb, M. J. Validation of the CoGEF Method as a Predictive Tool for Polymer Mechanochemistry. *J. Am. Chem. Soc.* **2020**, *142*, 16364–16381.
(39) Beyer, M. K. The Mechanical Strength of a Covalent Bond Calculated by Density Functional Theory. *J. Chem. Phys.* **2000**, *112*, 7307–7312.
(40) Gossweiler, G. R.; Hewage, G. B.; Soriano, G.; Wang, Q.; Welshofer, G. W.; Zhao, X.; Craig, S. L. Mechanochemical Activation of Covalent Bonds in Polymers with Full and Repeatable Macroscopic Shape Recovery. *ACS Macro Lett.* **2014**, *3*, 216–219.
(41) Zhao, W.; Carreira, E. M. Facile One-Pot Synthesis of Photochromic Pyrans. *Org. Lett.* **2003**, *5*, 4153–4154.